

AD-A153 682

TIME-AVERAGED AND TIME-DEPENDENT COMPUTATIONS OF  
ISOTHERMAL FLOWFIELDS IN. (U) DAYTON UNIV OH RESEARCH  
INST L KRISHNAMURTHY ET AL. DEC 84 UDR-TR-84-88

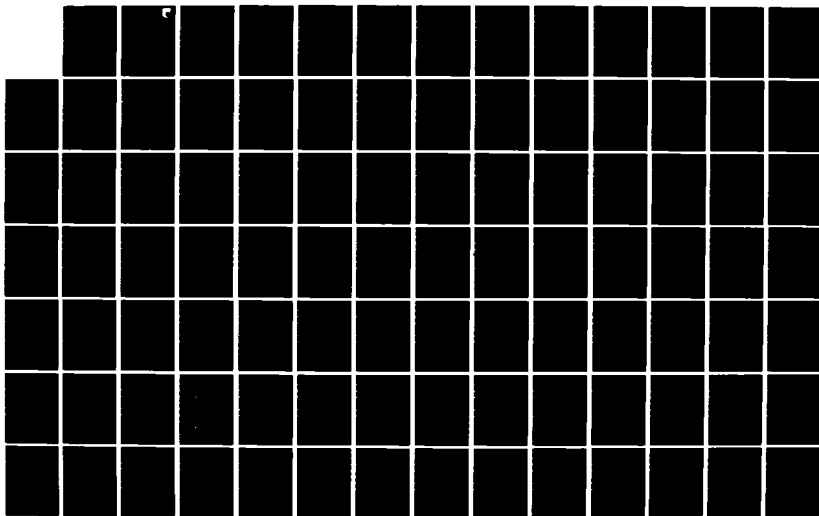
1/3

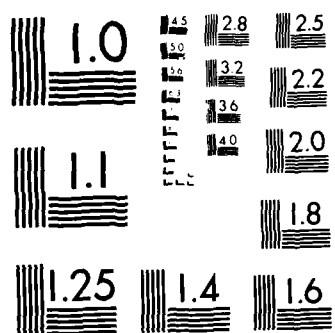
UNCLASSIFIED

AFWAL-TR-84-2081 F33615-82-K-2252

F/G 28/4

NL

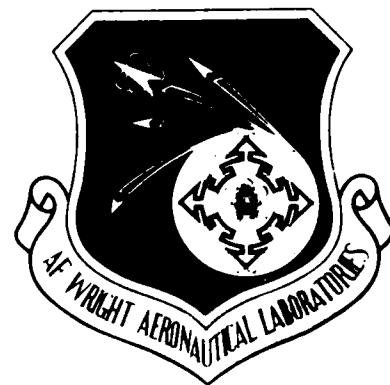




MICROCOPY RESOLUTION TEST CHART  
NATIONAL BUREAU OF STANDARDS 1963 A

AD-A153 682

AFWAL-TR-84-2081



TIME-AVERAGED AND TIME-DEPENDENT COMPUTATIONS OF  
ISOTHERMAL FLOWFIELDS IN A CENTERBODY COMBUSTOR

L. Krishnamurthy, M. S. Raju, M. J. Creed, and J. N. Memering  
University of Dayton  
Research Institute  
Dayton, Ohio 45469

December 1984

FINAL REPORT FOR PERIOD 15 JUNE 1982 TO 15 JUNE 1984

Approved for Public Release, Distribution Unlimited

AERO PROPULSION LABORATORY  
AIR FORCE WRIGHT AERONAUTICAL LABORATORIES  
AIR FORCE SYSTEMS COMMAND  
WRIGHT-PATTERSON AIR FORCE BASE, OH 45433-6563

DTIC FILE COPY

6

# NOTICE

"When Government drawings, specifications, or other data are used for any purpose other than in connection with a definitely related government procurement operation, the United States Government thereby incurs no responsibility nor any obligation whatsoever; and the fact that the Government may have formulated, furnished, or in any other way supplied the said drawings, specifications, or other data, is not to be regarded by implication or otherwise as in any manner licensing the holder or any other person or corporation, or conveying any rights or permission to manufacture, use, or sell any patented invention that may in any way be related thereto."

This report has been reviewed by the Office of Public Affairs (ASD/PA) and is releasable to the National Technical Information Service (NTIS). At NTIS, it will be available to the general public, including foreign nations.

This technical report has been reviewed and is approved for publication.

*W. M. Roquemore*

W.M. ROQUEMORE

Project Engineer, Fuels Branch

*Arthur V. Churchill*

ARTHUR V. CHURCHILL, Chief

Fuels Branch

FOR THE COMMANDER

*Benito P. Botteri*

BENITO P. BOTTERI, Assistant Chief

Fuels and Lubrication Division

"If your address has changed, if you wish to be removed from our mailing list, or if the addressee is no longer employed by your organization, please notify AFWAL/POSF, W-PAFB, OH 433-6563 to help us maintain a current mailing list."

Copies of this report should not be returned unless return is required by security considerations, contractual obligations, or notice on a specific document.

Unclassified

SECURITY CLASSIFICATION OF THIS PAGE

## REPORT DOCUMENTATION PAGE

1a. REPORT SECURITY CLASSIFICATION Unclassified			1b. RESTRICTIVE MARKINGS N/A		
2a. SECURITY CLASSIFICATION AUTHORITY N/A			3. DISTRIBUTION/AVAILABILITY OF REPORT Approved for Public Release, Distribution Unlimited		
2b. DECLASSIFICATION/DOWNGRADING SCHEDULE N/A					
4. PERFORMING ORGANIZATION REPORT NUMBER(S)  UDR-TR-84-88			5. MONITORING ORGANIZATION REPORT NUMBER(S)  AFWAL-TR-84-2081		
6a. NAME OF PERFORMING ORGANIZATION University of Dayton Research Institute		6b. OFFICE SYMBOL (If applicable)	7a. NAME OF MONITORING ORGANIZATION Aero Propulsion Laboratory (AFSC) Air Force Wright Aeronautical Laboratories		
6c. ADDRESS (City, State and ZIP Code)  Dayton, Ohio 45469			7b. ADDRESS (City, State and ZIP Code) Wright-Patterson Air Force Base Ohio 45433-6563		
8a. NAME OF FUNDING/SPONSORING ORGANIZATION		8b. OFFICE SYMBOL (If applicable) AFWAL/POSF	9. PROCUREMENT INSTRUMENT IDENTIFICATION NUMBER  F33615-82-K-2252		
8c. ADDRESS (City, State and ZIP Code)			10. SOURCE OF FUNDING NOS.		
			PROGRAM ELEMENT NO. 61102F	PROJECT NO. 2308	TASK NO. S7
					WORK UNIT NO. 11
11. TITLE (Include Security Classification) Time-Averaged and Time-Dependent Computations of Isothermal Flowfields in a Centerbody Combustor (U)					
12. PERSONAL AUTHOR(S) Krishnamurthy, L., Raju, M.S., Creed, M.J., and Memering, J.N.					
13a. TYPE OF REPORT Final Report		13b. TIME COVERED FROM 6/15/82 to 6/15/84		14. DATE OF REPORT (Yr., Mo., Day) December 1984	
				15. PAGE COUNT 186	
16. SUPPLEMENTARY NOTATION					
17. COSATI CODES			18. SUBJECT TERMS (Continue on reverse if necessary and identify by block number)		
FIELD	GROUP	SUB GR			
2102	2104	2105	Bluff-Body Near Wake Isothermal Flows Shear-Layer Instability, Coflowing Streams, Recirculating Flows, Unsteady Flow Confined Turbulent Flows Reynolds-Averaged Predictions Vortex Shedding		
19. ABSTRACT (Continue on reverse if necessary and identify by block number)					
<p>A numerical investigation of the near-wake region in a ducted bluff-body combustor by finite-difference computations is reported. The numerical predictions are based upon (a) the Reynolds-averaged Navier-Stokes equations and the k-<math>\epsilon</math> turbulence model; and (b) the time-dependent, compressible Navier-Stokes equations. The standard k-<math>\epsilon</math> turbulence model has been modified to account for the effect of streamline curvature and for the preferential influence of normal stresses.</p> <p>The time-averaged calculations have addressed the turbulent mixing under isothermal conditions in (a) the large- and small-scale centerbody combustor configurations, due to annular air flow and central CO<sub>2</sub> flow, and (b) the two-dimensional mixing-layer configuration, due to two streams of nitrogen at different velocities. The time-dependent calculations have addressed the near-wake flowfield of the large- (See reverse)</p>					
20. DISTRIBUTION/AVAILABILITY OF ABSTRACT  UNCLASSIFIED/UNLIMITED <input checked="" type="checkbox"/> SAME AS RPT <input type="checkbox"/> DTIC USERS <input type="checkbox"/>			21. ABSTRACT SECURITY CLASSIFICATION  Unclassified		
22a. NAME OF RESPONSIBLE INDIVIDUAL  W.M. Roquemore			22b. TELEPHONE NUMBER (Include Area Code) (513) 255-6813		22c. OFFICE SYMBOL  AFWAL/POSF

## BLOCK 19 (continued):

scale centerbody combustor configuration with only the annular air stream present.

The Reynolds-averaged predictions have examined the influence of the turbulence-model corrections and geometric scale under varying annular and central flows on (a) the axial and radial distributions of the mean and fluctuating components of the axial and radial velocities and of the mean  $\text{CO}_2$  concentrations and (b) the axial and radial locations of the vortex center, as well as the magnitude and location of the minimum centerline mean axial velocity. Comparison of the predicted results with the experimental data emphasizes and clarifies the complex flowfield interactions of the recirculating near-wake region.

The time-dependent computations have entailed a comprehensive examination of the influence of the inflow and outflow boundary conditions on the solution of subsonic, internal flowfields characterized by the centerbody combustor. The unsteady flow research has focused on the ability of the time-dependent formulation to describe the dynamic features of the centerbody combustor flowfield. Of particular importance to this investigation is the computational simulation of the vortex shedding process downstream of the bluff body.

The Reynolds-averaged predictions are consistent with the experimental evaluations in both the confined two-dimensional mixing layer and the centerbody combustor. The quantitative comparisons with the measured results are generally good for the mean components and fair to poor for the fluctuating components. Corrections to the  $k-\epsilon$  model exhibit a parametric dependence on the geometric scale and flow rates in the centerbody configuration. The computations with the time-dependent equations have demonstrated the capability of numerically simulating some of the unsteady flow features in the centerbody configuration. However, the physical realism of the predicted behavior is not firmly established. Nevertheless, the results clarify and emphasize the importance of properly specifying the inflow and outflow boundary conditions for the numerical simulation of the unsteady behavior in the centerbody configuration.

Present time-averaged and time-dependent computations have served to refine the understanding of the nonreacting turbulent flowfields in the centerbody combustor configuration and to suggest fruitful avenues for future research.

## PREFACE

This final report was submitted by the University of Dayton, under Contract No. F33615-82-K-2252. The research project was sponsored by the Air Force Wright Aeronautical Laboratories, Aero Propulsion Laboratory, Wright-Patterson Air Force Base, Ohio, under Project No. 2308, Task S7, Work Unit 11, and Project No. 3066, Task 05. Dr. William M. Roquemore, AFWAL/POSF, was Project Engineer. Dr. L. Krishnamurthy of the University was Principal Investigator and Project Director.

Dr. L. Krishnamurthy expresses his appreciation to:

- Drs. L. Huff and E. H. Gerber, UDRI, for their encouragement and support;
- Dr. W. M. Roquemore, Dr. James S. Petty, and Mr. Dale A. Hudson for their interest and fruitful discussions;
- Drs. W. L. Hankey, Jr. and J. S. Shang, AFWAL/FIMM, for their interest and helpful suggestions;
- Drs. E. J. Mularz and C. J. Marek, NASA-Lewis Research Center, for their interest and support of our computing activities on the NASA CRAY computer and especially Dr. Marek, for his unstinted help;
- Professors G. S. Samuelson of the University of California, Irvine and C. T. Bowman of Stanford University, for providing their experimental data;
- The members of his technical team (see Appendix A), for their technical contributions to the numerical computing activities (see Appendix B); and his present co-authors and Dr. S. O. Park, in particular, for the technically productive and personally rewarding association during this research;
- The Dayton-Cincinnati Section of the American Institute of Aeronautics and Astronautics and, in particular, Dr. D. L. Quam, for the Best Undergraduate Student Paper Award given to Ms. J. N. Memering during the 10th Annual Mini-Symposium; and
- Ms. Ellen Bordewisch, UDRI, for preparing this report, and Ms. A. Cochran, UDRI for technical editing.

# TABLE OF CONTENTS

SECTION	PAGE
I. INTRODUCTION	1
1. Background	1
2. Objectives	3
3. Scope of Present Work	4
4. Outline of Report	6
II. REYNOLDS-AVERAGED COMPUTATIONS	7
1. Confined Two-Dimensional Mixing Layer	7
a. Introduction	7
(1) Background	7
(2) Experimental Details	8
(3) Scope of Computations	10
b. Numerical Computations	10
(1) Governing Equations	11
(2) Computational Details	13
(3) Boundary Conditions	15
c. Results and Discussion	17
(1) Influence of Inlet Velocity Profile	17
(2) Influence of Turbulence Length Scale, Differencing Scheme, and Streamline Curvature	22
(3) Other Effects	23
d. Conclusions	23
2. Large- and Small-Scale CBCC's	30
a. Centerbody Combustor Configuration	31
(1) Background and Objectives	33
(2) Scope of Computations	34
b. Numerical Computations	34
(1) Computational Details	34
(2) Turbulence Model	37
c. Results and Discussion	38
(1) Pertinent Results from SS and KP	38
(2) UCI Configuration	40
(3) APL Configuration	43
d. Conclusions	51
3. Vortex-Center Characteristics	51
a. Recirculation-Zone Structure	54
(1) Preliminary Studies	54
(2) Objectives of Present Study	61
(3) Scope	61
b. Results and Discussion	62
(1) APL Configuration	62
(2) UCI Configuration	68
(3) Comparative Study	72
c. Conclusions	77



# TABLE OF CONTENTS (Concluded)

SECTION	PAGE
III. TIME-DEPENDENT COMPUTATIONS	78
1. Introduction	78
2. Boundary Conditions	79
a. Inflow Boundary Conditions	79
(1) Boundary Conditions due to Serra	79
(2) A Minor Variant of Serra's Conditions	80
(a) Rigorous Implementation	80
(b) An Alternative Formulation	81
(3) Boundary Conditions Due to Oliger and Sundstrom	82
(4) Boundary Conditions Due to Fedorchenko	82
b. Outflow Boundary Conditions	83
(1) Non-Reflecting Condition	83
(2) Constant Pressure Condition	84
(3) Split Boundary Condition	85
(a) Rigorous Implementation	85
(b) Alternative Implementation	85
(4) Relaxation Boundary Condition	86
(5) Boundary Condition for Reverse-Flow Exit	86
c. Solid-Wall Boundary Conditions	86
d. Centerline Boundary Conditions	86
e. Acoustic Characteristics of Boundary Conditions	87
3. Computational Details	89
4. Results and Discussion	92
IV. CONCLUSIONS AND RECOMMENDATIONS	173
1. Conclusions	173
2. Recommendations	176
References	179
Appendix A	184
Appendix B	185

# LIST OF ILLUSTRATIONS

FIGURE	TITLE	PAGE
1.	Schematic of the Mixing Layer.	9
2.	Computational Domain and Grid Point Distribution.	14
3.	Profiles of Mean and rms Streamwise Velocity Components at $x = 5$ cm.	18
4.	Profiles of Mean and rms Streamwise Velocity Components at $x = 12$ cm.	19
5.	Profiles of Mean and rms Streamwise Velocity Components at $x = 15$ cm.	20
6.	Profiles of Mean and rms Streamwise Velocity Components at $x = 18$ cm.	21
7.	Influence of Turbulence Length Scale, Differencing Scheme and Curvature on the rms Velocity Predictions at $x = 5$ cm.	24
8.	Influence of Turbulence Length Scale, Differencing Scheme and Curvature on the rms Velocity Predictions at $x = 12$ cm.	25
9.	Influence of Turbulence Length Scale, Differencing Scheme and Curvature on the rms Velocity Predictions at $x = 15$ cm.	26
10.	Influence of Turbulence Length Scales, Differencing Scheme and Curvature on the rms Velocity Predictions at $x = 18$ cm.	27
11.	Influence of Curvature and Exit Plane Location on the Mean Velocity Predictions at $x = 18$ cm.	28
12.	Influence of Curvature and Exit Plane Location on the rms Velocity Predictions at $x = 18$ cm.	29
13.	Schematic of CBCC.	32
14.	Computational Domain for CBCC.	35

LIST OF ILLUSTRATIONS  
(Continued)

FIGURE		PAGE
15.	Measured and Predicted Centerline Stagnation Points for APL CBCC.	39
16.	Measured (Brum et al. <sup>4</sup> ) and Predicted Centerline Mean Axial Velocity for UCI CBCC.	41
17.	Measured (Brum et al. <sup>4</sup> ) and Predicted Centerline rms Axial Velocity for UCI CBCC	42
18.	Measured (Brum et al. <sup>4</sup> ) and Predicted Mean Axial Velocity Radial Profiles for UCI CBCC.	44
19.	Measured (Brum et al. <sup>4</sup> ) and Predicted rms Axial Velocity Radial Profiles for UCI CBCC.	45
20.	Measured (Brum et al. <sup>4</sup> ) and Predicted Centerline Mean and rms Axial Velocity for UCI CBCC.	46
21.	Measured (Lightman et al. <sup>2</sup> ) and Predicted Centerline Mean and rms Axial Velocity For APL CBCC.	47
22.	Measured (Lightman et al. <sup>2</sup> ) and Predicted Centerline Mean and rms Axial Velocity for APL CBCC.	48
23.	Measured (Lightman et al. <sup>2</sup> ) and Predicted Centerline Mean and rms Axial Velocity for APL CBCC.	49
24.	Measured (Bradley et al. <sup>30</sup> ) and Predicted Centerline CO <sub>2</sub> Mole Fraction for APL CBCC.	52
25.	Measured (Bradley et al. <sup>30</sup> ) and Predicted Centerline CO <sub>2</sub> Mole Fraction for APL CBCC.	53
26.	Velocity Vector Plots for APL CBCC.	55
27.	Zero Mean Axial Velocity Contour and Mean Radial Velocity Distribution Thereon.	56
28.	Distribution of Turbulence Kinetic Energy on Zero Axial Velocity Contour.	58
29.	Radial Distribution of Turbulence Kinetic Energy at Different Axial Locations.	59
30.	Normalized Locations of Air Vortex Center.	60
31.	Radial Coordinate Variation with CO <sub>2</sub> Flow (APL CBCC).	64

LIST OF ILLUSTRATIONS  
(Continued)

FIGURE		PAGE
32.	Axial Coordinate of Vortex Center and Minimum Centerline Velocity Variation with CO <sub>2</sub> Flow (APL CBCC).	65
33.	Axial and Radial Coordinates of Vortex Center Variation with Air Flow (APL CBCC).	67
34.	Radial Coordinate Variation with CO <sub>2</sub> Flow (UCI CBCC) - PCE Model.	69
35.	Axial Coordinate of Vortex Center and Minimum Centerline Velocity Variation with CO <sub>2</sub> Flow (UCI CBCC) - PCE Model.	70
36.	Radial Coordinate of Vortex Center Variation with Air Flow (UCI CBCC) - PC Model.	71
37.	Axial Coordinate of Vortex Center Variation with Air Flow (UCI CBCC) - PC Model.	73
38.	Relationship of Minimum Centerline Velocity and Central Jet Flow (APL and UCI CBCC) - PC Model.	74
39.	Relationship of Axial Location of Minimum Centerline Velocity and Central Jet Flow (APL and UCI CBCC) - PCE Model.	75
40.	Schematic of the APL CBCC and Physical (60 x 46) Finite-Difference Mesh.	90
41.	Physical (80 x 46) Finite-Difference Mesh.	94
42.	Velocity-Vector and Vorticity-Contour Plots for Case 1 of Table 7.	98
43.	(a)-(b) Temporal Variation in Combustor Mass Flow and $\Delta T_{CFL}$ for Case 2 of Table 7.	100-101
44.	Velocity-Vector, Vorticity-Contour and Pressure-Contour Plots for Case 2 of Table 7.	102
45.	Velocity-Vector, Vorticity-Contour and Pressure-Contour Plots for Case 3a of Table 7.	103
46.	(a)-(b) Temporal Variation in Combustor Mass Flow and $\Delta T_{CFL}$ for Case 3b of Table 7.	104-105

LIST OF ILLUSTRATIONS  
(Continued)

FIGURE		PAGE
47a.	Velocity-Vector Plots for Case 3b of Table 7.	106
47b.	Vorticity-Contour Plots for Case 3b of Table 7.	107
47c.	Pressure-Contour Plots for Case 3b of Table 7.	108
48.	(a)-(c) Temporal Variation in Combustor Mass Flow for Case 4 of Table 7.	110-112
49.	(a)-(b) Velocity Vector Plots for Case 4 of Table 7.	113-114
49.	(c)-(d) Vorticity-Contour Plots for Case 4 of Table 7.	115-116
50.	(a)-(b) Temporal Variation in Combustor Mass Flow and $\Delta T_{CFL}$ for Case 5 of Table 7.	118-119
51.	(a)-(b) Velocity-Vector Plots for Case 5 of Table 7.	120-121
51.	(c)-(d) Vorticity-Contour Plots for Case 5 of Table 7.	122-123
51.	(e)-(f) Pressure-Contour Plots for Case 5 of Table 7.	124-125
52.	Temporal Variation in Combustor Mass Flow and $\Delta T_{CFL}$ for Case 6a of Table 7.	127
53.	(a)-(b) Velocity-Vector Plots for case 6a of Table 7.	128-129
53c.	Vorticity-Contour Plots for Case 6a of Table 7.	130
54.	(a)-(b) Temporal Variation in Combustor Mass Flow and $\Delta T_{CFL}$ for case 6b of Table 7.	131-132
55.	(a)-(b) Velocity-Vector Plots for Case 6b of Table 7.	133-134
55.	(c)-(d) Vorticity-Contour Plots for Case 6b of Table 7.	135-136

LIST OF ILLUSTRATIONS  
(Continued)

FIGURE		PAGE
55e.	Pressure-Contour Plots for Case 6b of Table 7.	137
56.	(a)-(b) Temporal Variation in Combustor Mass Flow and $\Delta T_{CFL}$ for Case 6c of Table 7.	139-140
57.	(a)-(b) Velocity-Vector Plots for Case 6c of Table 7.	141-142
57.	(c)-(d) Vorticity-Contour Plots for Case 6c of Table 7.	143-144
57.	(e)-(f) Pressure-Contour Plots for Case 6c of Table 7.	145-146
58.	(a)-(b) Temporal Variation of Combustor Mass Flow and $\Delta T_{CFL}$ for Case 7a of Table 7.	147-148
59.	(a)-(b) Velocity-Vector Plots for Case 7a of Table 7.	149-150
59.	(c)-(d) Vorticity-Contour Plots for Case 7a of Table 7.	151-152
60.	(a)-(b) Temporal Variation in Combustor Mass Flow and $\Delta T_{CFL}$ for Case 7b of Table 7.	154-155
61a.	Velocity-Vector Plots Common to both Cases 7b and 8a of Table 7.	156
61b.	Vorticity-Contour Plots Common to both Cases 7b and 8a of Table 7.	157
61c.	Vorticity-Contour and Velocity-Vector Plots for Case 7b of Table 7.	158
62.	(a)-(d) Temporal Variation of Combustor Mass Flow and $\Delta T_{CFL}$ for Case 8a of Table 7.	159-162
63.	Superposition of Two Different Simple Harmonic Waves	163
64a.	Velocity-Vector Plots for Case 8a of Table 7.	164
64b.	Vorticity-Contour Plots for Case 8a of Table 7.	165
65.	(a)-(b) Temporal Variation in Combustor Mass Flow and $\Delta T_{CFL}$ for Case 8b of Table 7.	166-167
66.	(a)-(b) Velocity-Vector Plots for Case 8b of Table 7.	168-169

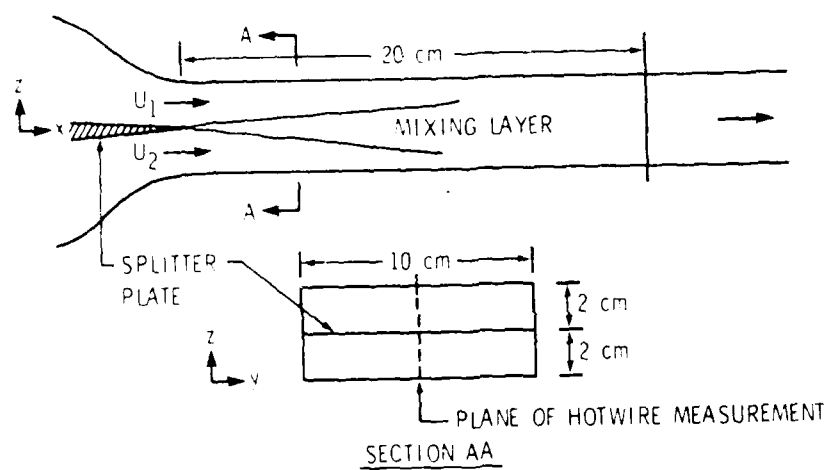


Figure 1. Schematic of the Mixing Layer.

Navier-Stokes equations and the two-equation turbulence model (for the turbulence kinetic energy  $k$  and its rate of dissipation  $\epsilon$ ), the numerical simulation of the Stanford mixing layer became of interest.

Our computational investigations have been examining turbulent recirculating flowfields characteristic of the CBCC (see, e.g., Krishnamurthy, et al.<sup>3</sup>) by means of the TEACH<sup>10</sup> code which involves elliptic flowfields. The mixing-layer development, however, is an example of an evolving flow (without flow recirculation) which is governed by parabolic equations. Strictly speaking, a numerical modeling based upon an elliptic formulation is not necessary to address the mixing-layer problem. Although the experimental configuration<sup>19</sup> does not involve recirculating flow, it does represent a confined flowfield, for which the TEACH procedure is appropriate. The availability of comprehensive data from the Stanford mixing layer, therefore, constitutes a useful means of model validation.

## (2) Experimental Details

As seen schematically in Figure 1, the Stanford mixing-layer experiment involves a flow facility which consists of a 4-cm-high, 10-cm-wide and 20-cm-long test section. Upstream of the test section is a well-designed two-dimensional contraction in which is located a splitter plate, midway between the confining walls at the top and bottom. A mixing layer is formed downstream of the trailing edge of the splitter plate, with unequal velocities in the initially separate upper and lower streams. Nitrogen is the carrier gas in both streams flowing continuously at free stream velocities of up to 20 m/s. Reacting flow experiments have employed dilute concentrations of NO in one stream and O<sub>2</sub>/O<sub>3</sub> in the other. The hot-wire anemometry measurements of present interest were made in nonreacting flows in the x-z plane located midway along the width of the test section (see Figure 1). The available data correspond to initial velocities of 6 m/s in the upper and 3 m/s in the lower streams.



## SECTION II

### REYNOLDS-AVERAGED COMPUTATIONS

This section deals with the numerical modeling of isothermal turbulent flowfields through the framework of Reynolds-averaged Navier-Stokes equations. Included are: the predictive results of the two-dimensional mixing layer and a comparison of these with the experimental data; the numerical modeling of the CBCC flowfields; and a description of the predictions of the vortex-center characteristics in the CBCC.

#### 1. CONFINED TWO-DIMENSIONAL MIXING LAYER

The numerical simulation of the Stanford mixing-layer experiment<sup>19</sup> is described below.

##### a. Introduction

The plane turbulent mixing layer formed downstream of a splitter plate separating two uniform and initially parallel streams represents one of the simplest and most extensively studied flows. The most basic flowfield in this configuration is the classic mixing layer arising from two streams of unequal velocities but of the same species. Apart from its intrinsic interest, such a mixing layer is often adopted in experimental studies of turbulent mixing in nonreacting and reacting flows. The recent absorption measurement<sup>19</sup> of a conserved scalar in a reacting flow under fast chemistry (due to two initially unmixed reactants of trace concentration present in inert carrier streams) is a good example.

##### (1) Background

Extensive hot-wire anemometry data of the mean and fluctuating velocity components in nonreacting flows (when one or both of the reactant species are absent) were available from the Stanford University experiment.<sup>19</sup> In view of our ongoing flowfield computations employing the Reynolds-averaged

behavior of the CBCC. However, within the scope of the present program, that investigation was not made. Instead, attention was focused on the influence of boundary conditions, numerical parameters, and computational grid on the CBCC flowfield predictions when only the annular stream is present.

#### 4. OUTLINE OF REPORT

The Reynolds-averaged computations of the CBCC flowfields are reported in Section II. Section III first discusses briefly the preliminary results of the time-dependent calculations which led to the shedding-like behavior and then reports the results of the comprehensive examination of the unsteady-flow modeling. The conclusions of the present modeling research program and the recommendations in light of these conclusions are outlined in Section IV.

Dynamics Laboratory (AFWAL/FIMM) vectorized, compressible, time-dependent code. Since the ability of the time-dependent calculations to provide physically acceptable solutions of the CBCC flowfield depended on the successful implementation of the boundary conditions appropriate to the modeling of confined, subsonic flowfields, this subject formed the main aspect of the research. The examination of the boundary conditions and of the question of acoustic interactions from the exit-plane boundary was to be made for two simpler flow situations of the CBCC. These corresponded to the CBCC with only the annular flow and with only the central jet. Successful implementation of the necessary boundary conditions to establish the dynamic behavior in the two cases was to be followed by the numerical investigation of the CBCC with both annular and central flows present.

The actual scope of the unsteady-flow modeling research, however, entailed a comprehensive examination of the influence of the inflow and outflow boundary conditions on the existence of the bluff-body vortex shedding or the lack thereof. This is easy to see. In the AFWAL/POSF experiments on the CBCC, there is at present no reason to suspect that the initial and boundary conditions are time dependent. The interior flowfield, however, does exhibit certain time-dependent features. Indeed the preliminary computations with the AFWAL/FIMM code appeared to indicate that the solution of the time-dependent governing equations produced a time-dependent flowfield in the CBCC interior. That such a situation may not be unique became apparent when under certain boundary conditions the time-dependent equations failed to generate a time-dependent solution in the interior and, in fact, the temporal behavior was damped out after several time steps. Of course, such a situation is common when the physical problem possesses a steady solution and often the time-dependent formulation is employed to yield the steady solution asymptotically for large times. It became important, therefore, to ascertain whether such was the case with the CBCC flowfield. In this context, a computational investigation involving time-dependent boundary conditions would have been helpful to elucidate the

flowfield. Other potential contributors of perhaps minor significance were thought to be the large-scale structures in the boundary layers of the confining duct and the centerbody surface, and the duct acoustics.

Irrespective of the source of the unsteadiness, its presence in itself raised important questions with respect to the numerical modeling. For example, is the CBCC flowfield inherently unsteady? If so, how relevant and useful is the prediction based on Reynolds-averaged formulation? To the extent that the latter appeared to show reasonable agreement with the time-averaged measurements, how would these compare with the results from the time averaging of the time-dependent solutions? The unsteady flow modeling with the aid of time-dependent Navier-Stokes equations was expected to provide answers to at least some of these questions.

### 3. SCOPE OF PRESENT WORK

The work reported here deals with the time-averaged and time-dependent calculations of the isothermal flowfields in the CBCC. The former involved the AFWAL/PORT version of the TEACH program and the modifications implemented during this research. The investigations examined the large- and small-scale CBCC's and compared the predictions with the experimental data. In addition to the centerline (axial) distributions and the radial distributions (at various axial locations) of the mean and fluctuating fields, the computations addressed the characteristics of the vortex centers. Also, the Reynolds-averaged calculations examined the two-dimensional, mixing-layer experiment at Stanford University. While this configuration is not directly relevant to the CBCC flowfields, this numerical simulation served to test several modeling aspects. No computational investigation with the improved TEACH code recently available to the Air Force<sup>18</sup> was made within the scope of this program.

The time-dependent computations involved the axisymmetric version of the Air Force Wright Aeronautical Laboratories, Flight

be adequately described and understood in terms of a time-mean flow." The implications of Richardson's suggestion, that the predictions must be based on an unsteady-flow model for comparison with and interpretation of experimental data in the near-wake region, were discussed earlier<sup>17</sup> for the CBCC flowfields. No time-dependent predictions of the CBCC were available, however, for an examination of the validity of the Reynolds-averaged predictions of the flowfield.

## 2. OBJECTIVES

Accordingly, the numerical modeling of the centerbody combustor flowfields was considered with twofold objectives. First, the Reynolds-averaged computations with the TEACH code addressed additional refinements in CBCC predictions with improved physical and numerical models. Improvements in physics were concerned with the modifications to the standard  $k-\epsilon$  model to account for streamline curvature and the preferential influence of normal stresses in the dissipation equation. The refinements in the area of numerics dealt with the differencing schemes and included the incorporation of power-law differencing schemes and modifications of the hybrid-upwind differencing schemes.

While the steady-state predictions were expected to show better agreement with the measured results because of the improvements in the physical and numerical models, a crucial aspect missing in the Reynolds-averaged computations was accounting for the observed dynamic behavior of the CBCC flowfield. Thus, the second objective of this research was concerned with the computational investigation of the unsteady flows. It seemed that the flowfield unsteadiness could arise from several possible causes. Thus, the vortex shedding off the centerbody trailing face, large-scale entrainment structures in the shear layer between the annular and central streams, and the coherent structures in the central jet could all either singly or in combination impart temporal characteristics to the CBCC

The Reynolds-averaged predictions of the CBCC flowfields appeared to provide reasonable approximations to the experimental results, especially for the mean flowfields under isothermal conditions. The quantitative accuracy of the predictions of the fluctuating fields was generally poor. Several possible sources for this discrepancy have been identified, as discussed below.

The TEACH procedure utilizes the hybrid-upwind differencing scheme for the convective terms.<sup>3,12</sup> This scheme is known to suffer from numerical diffusion problems.<sup>6</sup> The CBCC flowfield is characterized by large streamline curvature and is a good example of the complex turbulent flow defined by Bradshaw,<sup>13</sup> due to the extra strain rates associated with the streamline curvature. It is known that the turbulent shear stress and the degree of anisotropy between the normal stresses are very sensitive to curvature. Since the standard "k- $\epsilon$  model" does not account for streamline curvature effects, this was considered to be partly responsible for the discrepancy between the predicted and the measured recirculation lengths. Moreover, as noted by Leschziner and Rodi,<sup>14</sup> the dissipation ( $\epsilon$ ) equation in the standard k- $\epsilon$  model requires modification in recirculating flows to account for the preferential influence of the normal stresses on the turbulence transport. Finally, the CBCC flowfield appeared to exhibit certain flow unsteadiness associated with the bluff-body near wake.

The applicability of Reynolds-averaged description to flowfields possessing large-scale unsteadiness has been a subject of much debate. It is known that the separated shear layers and the recirculation regions downstream of a bluff body are inherently unsteady. Indeed, high-speed photographs of combustion in the CBCC<sup>15</sup> have revealed the propagation of large-scale toroidal vortices, with successive flame bursts and relative quiescence of random nature. As pointed out by Richardson, in a discussion of the results of the axisymmetric wake behind a disk by Carmody,<sup>16</sup> "it appears unlikely that a flow possessing distinct and large-scale periodic characteristics can

## SECTION I

### INTRODUCTION

This final report documents the computational fluid dynamic research performed for the Air Force Wright Aeronautical Laboratories, Aero Propulsion Laboratory (AFWAL/PO), by the University of Dayton. The computational investigations had two overall objectives: (a) conducting the steady-state predictive modeling of the confined turbulent mixing in the near-wake region of the AFWAL/POSF centerbody combustor configuration and (b) performing the time-dependent computations of the centerbody combustor flowfields.

#### 1. BACKGROUND

The confined recirculating flow involving dual coaxial streams in the near-wake region of an axisymmetric bluff body has been the focus of an ongoing diagnostic and predictive research program <sup>1-3</sup> at the Aero Propulsion Laboratory (APL). A 1/5-scale model of the APL centerbody combustor configuration (CBCC) is in operation at the University of California, Irvine (UCI).<sup>4</sup>

Numerical predictions of the CBCC flowfields have been the subject of several research studies in the recent past.<sup>3-9</sup> These studies dealt with the steady-state flowfield computations based on the Reynolds-averaged Navier-Stokes equations. The numerical calculations employed the well known Teaching Elliptic Axisymmetric Characteristics Heuristically (TEACH)<sup>10</sup> procedure. The modeling of turbulence necessitated by the Reynolds averaging was based on an eddy viscosity computed by the two-equation model for the turbulence kinetic energy  $k$  and the rate of its dissipation  $\epsilon$ .<sup>11</sup>

LIST OF SYMBOLS  
(Concluded)

SUBSCRIPTS

e	Exit plane of the computational domain
eff	Effective value
in	Inlet plane of the computational domain
KL,j	Last grid points at exit boundary
t	Turbulent (Section II) Stagnation values (Section III)
w	Wall condition
1	Upper stream (Section II)
1, j	First grid points at inlet boundary
2	Lower stream (Section II)

SUPERSCRIPITS

n	Time step or time index
—	Time-mean value (Reynolds Averaging)
'	Fluctuating component (Reynolds Averaging)



LIST OF SYMBOLS  
(Continued)

$S_\phi$	Source term for the variable $\phi$ in Equation (1)
$t$	Time
$T$	Temperature
$u$	Streamwise rms velocity component
$U$	Velocity component along $x$
$V$	Velocity component along $z$ (Section II) Velocity component along $r$ (Section III)
$x, z$	Rectangular coordinates
$\alpha$	Parameter appearing in Equation (38)
$\beta$	Reflection coefficient
$\gamma$	Ratio of specific heats
$\Gamma_\phi$	Exchange coefficient for the $\phi$ in Equation (2)
$\epsilon$	Dissipation rate of $k$
$\zeta, \xi$	Transformed coordinates
$\eta$	Direction normal to the boundary
$\lambda$	Inlet turbulence length scale parameter (Section II) $-2/3\mu$ second viscosity coefficient (Section III)
$\mu$	Molecular viscosity coefficient
$\rho$	Density
$\sigma_\phi$	Effective Prandtl number for $\phi$ in Equation (2)
$\tau$	Shear stress or "computational effort" (i.e., CPU time per iteration per grid point)
$\tau_w$	Wall shear stress
$\phi$	General dependent variable in Equation (1) (Section I) Additional unspecified physical variable (Section III)
$\omega$	Frequency

# LIST OF SYMBOLS

a	Speed of sound
C	Damping parameter
CPU	Central processing unit
$c_\mu, C_1, C_2$	Constants in the "Standard" k- $\epsilon$ model
DT	Time steps
e	Specific internal energy
E	Dependent variable
F, G	Vector fluxes in mean flow equations
h	Half height of channel (= 2 cm)
H	Source term [See Equation (60)]
k	Turbulent kinetic energy
$\ell$	Turbulent length scale (= $\lambda h$ )
$L_c$	Length of the centerbody
$L_d$	Length of the duct
M	Mach number
N	Number of time steps
p	Static pressure
P	Static Pressure
Pr	Prandtl number
$P_k$	Rate of generation of k in Table 1
Q	Conductance
r	Radial direction
R	Gas constant
$R_c$	Radius of centerbody
$R_d$	Radius of duct

# LIST OF TABLES

TABLE	TITLE	PAGE
1.	Governing Equations	12
2.	Boundary Conditions	16
3.	Flowfield Conditions	36
4.	Flowfield Conditions	63
5.	Axial Coordinate of Vortex Center (APL CBCC)	76
6.	Details of Various Cases Modeled with Different Combinations of Inflow and Outflow Boundary Conditions (--- Cases Not Run)	93
7.	Details of Numerical Computations for the Different cases of Table 6.	95-96

LIST OF ILLUSTRATIONS  
(Concluded)

FIGURE		PAGE
66	(c)-(d) Vorticity-Contour Plots for Case 8b of Table 7.	170-171
67	Velocity-Vector and Vorticity-Contour Plots for Case 9 of Table 7.	172

For these conditions, the nonuniformities in the inlet mean velocities were less than 1 percent. The streamwise turbulence intensities ( $u/U$ ) in the inlet were below 0.5 percent. The  $z$ -profiles of the streamwise components of the mean ( $U$ ) and the rms ( $u$ ) velocities were measured at the four streamwise stations of 5, 12, 15, and 18 cm downstream of the trailing edge of the splitter plate.

### (3) Scope of Computations

The predictive calculations have employed the standard features of the TEACH-type numerics, such as the "hybrid" upwind differencing<sup>12</sup> and the  $k$ - $\epsilon$  turbulence model<sup>11</sup> (which uses a constant value of 0.09 for the parameter  $c_\mu$ ). Additional features considered in the present calculations are the power-law differencing scheme<sup>3,20</sup> (which retains the diffusive effects for a larger cell-Peclet number range, viz.,  $-10 < Pe < 10$ , than the "hybrid" upwind scheme) and the streamline-curvature correction<sup>14</sup> which introduces a curvature-dependent (and thus nonconstant)  $c_\mu$  in the  $k$ - $\epsilon$  model. The corrections for the effect of streamline curvature are obtained with and without a modification of the  $\epsilon$ -equation.<sup>14</sup> Present computations also examine the influences of nonuniform inlet profiles and the exit-plane location of the computational domain. The sensitivity of the numerical predictions to different aspects of the modeling is noted by a comparison of predicted and measured results.

#### b. Numerical Computations

The TEACH code describes a finite-difference computational procedure to solve the Reynolds-averaged Navier-Stokes equations. This procedure involves the primitive (pressure and velocity) variables instead of the stream function-vorticity formulation and thus entails a direct solution of the velocity and pressure fields. A special procedure called the SIMPLE<sup>21</sup> algorithm is employed for this purpose. Further details concerning the underlying theory and the computational procedure are available in References 3 and 10.

## (1) Governing Equations

For the mixing-layer problem of interest here, the governing equations are formulated in the planar two-dimensional geometry.  $U$  and  $V$  are the time-mean velocity components in the longitudinal ( $x$ ) and the transverse ( $z$ ) directions. Present calculations deal with the isothermal, nonreacting flow of the carrier (nitrogen) gas. Therefore, it is not necessary to consider the species and energy conservation equations. The only other dependent variables of interest are  $k$  and  $\epsilon$ . The governing equations for all the dependent variables can be expressed in the general form

$$\frac{\partial}{\partial x} (\rho \bar{U} \bar{\phi}) + \frac{\partial}{\partial z} (\rho \bar{V} \bar{\phi}) - \frac{\partial}{\partial x} (\Gamma_{\phi} \frac{\partial \bar{\phi}}{\partial x}) - \frac{\partial}{\partial z} (\Gamma_{\phi} \frac{\partial \bar{\phi}}{\partial z}) = S_{\phi} \quad (1)$$

where  $\phi$  denotes any dependent variable (time-mean value). In Eq.(1)  $S_{\phi}$  is the source term for the variable  $\phi$  which includes true source terms (such as those due to chemical reactions) as well as the terms not covered by the first four terms (representing the convective and diffusive contributions).  $\Gamma_{\phi}$  is the effective exchange coefficient for the transport of the variable  $\phi$  and is given by

$$\Gamma_{\phi} = \mu_{eff} \bar{\epsilon} / \sigma_{\phi} \quad (2)$$

where  $\mu_{eff}$  is the effective viscosity in the flowfield and  $\sigma_{\phi}$  is the appropriate effective Prandtl/Schmidt number for each  $\phi$ . Table 1 summarizes the relevant information for all the dependent variables.

The effective viscosity  $\mu_{eff}$  appearing in Eq. (2) is given by

$$\mu_{eff} = \mu + \mu_t \quad (3)$$

where  $\mu$  is the laminar viscosity and  $\mu_t$  is the turbulent eddy viscosity. The latter is obtained from

$$\mu_t = c_{\mu} \rho k^2 / \epsilon \quad (4)$$

TABLE 1  
GOVERNING EQUATIONS

Equation	$\bar{\phi}$	$\Gamma_{\phi}$	$S_{\phi}$
Continuity	1	0	0
Axial (Mean) Momentum	$\bar{U}$	$\nu_{eff}$	$-\frac{\partial \bar{p}}{\partial x} + \frac{\partial}{\partial x} (\nu_{eff} \frac{\partial \bar{U}}{\partial x}) + \frac{\partial}{\partial z} (\nu_{eff} \frac{\partial \bar{V}}{\partial x})$
Radial (Mean) Momentum	$\bar{V}$	$\nu_{eff}$	$-\frac{\partial \bar{p}}{\partial z} + \frac{\partial}{\partial x} (\nu_{eff} \frac{\partial \bar{U}}{\partial z}) + \frac{\partial}{\partial z} (\nu_{eff} \frac{\partial \bar{V}}{\partial z})$
Turbulence Kinetic Energy	k	$\nu_{eff}/\sigma_k$	$P_k - \rho \epsilon$
Turbulence Energy Dissipation	$\epsilon$	$\nu_{eff}/\sigma_{\epsilon}$	$C_1(\epsilon/k)P_k - C_2 \rho \epsilon^2/k$

$\sigma_k$	$\sigma_{\epsilon}$	$C_1$	$C_2$
1	1.3	1.44	1.92

$$P_k \equiv \nu_{eff} \left\{ 2 \left[ \left( \frac{\partial \bar{U}}{\partial x} \right)^2 + \left( \frac{\partial \bar{V}}{\partial z} \right)^2 \right] + \left( \frac{\partial \bar{U}}{\partial z} + \frac{\partial \bar{V}}{\partial x} \right)^2 \right\}$$

where  $c_\mu$  is usually taken to be a constant equal to 0.09. The above procedure involves the introduction of two partial differential equations for  $k$  and  $\epsilon$  which are solved together with the conservation equations for mass, momentum, and energy. We note that the inclusion of these additional equations has been anticipated in the general formulation of Eq. (1) and in Table 1. The "standard"  $k$ - $\epsilon$  model<sup>11</sup> does not account for streamline curvature effects. Following Leschziner and Rodi,<sup>14</sup> ad hoc modifications have been introduced by us to incorporate curvature effects in the flowfield modeling of the centerbody configuration.<sup>3</sup> Although streamline-curvature effect is not expected to be significant in the mixing-layer problem, present calculations examined this question also.

## (2) Computational Details

Figure 2 shows the computational domain and the grid-point distribution initially adopted in the numerical calculations. The chosen grid consists of 41 longitudinal nodes and 42 lateral nodes with grid spacings that are nonuniform longitudinally and uniform laterally. The location of the exit boundary at 22.5 cm from the trailing edge of the splitter plate is arbitrary. The experimental details of the region downstream of the 20-cm-long test section are not known. To find the sensitivity of the results to the location of the exit boundary, calculations were also carried out with a different grid consisting of 51 longitudinal nodes and with the exit-plane located at a distance of 31.5 cm.

In the TEACH computational procedure all the salient locations such as the top and bottom walls, the trailing edge of the splitter plate, and the exit boundary are located midway between the adjacent grid nodes. Moreover, a staggered-grid arrangement is employed in the formulation of the finite-difference equations. All the dependent variables, except  $U$  and  $V$ , are referred to at the grid nodes.  $U$  and  $V$  are calculated at locations midway between the grid nodes.



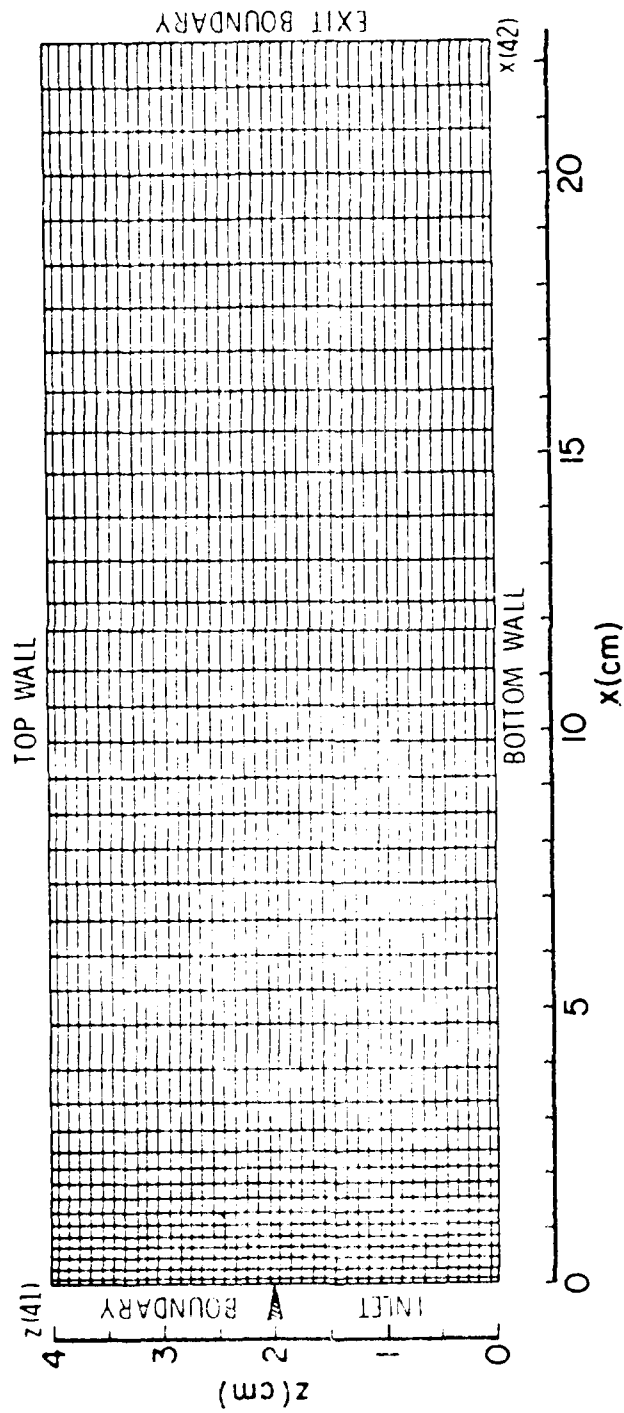


Figure 2. Computational Domain and Grid Point Distribution.

### (3) Boundary Conditions

Table 2 summarizes the boundary conditions employed in the numerical calculations. In view of the elliptic formulation of Eq. (1), the boundary conditions are prescribed on all the boundaries of the computational domain. The top and bottom boundaries are the confining walls and the dependent variables  $U$ ,  $k$  and  $\epsilon$  are prescribed by wall-function formulation.  $V$  vanishes on these boundaries. The right boundary is the outflow boundary at which the streamwise derivatives of all the dependent variables are set to zero. The left boundary represents the inflow boundary. The inlet profiles of  $U$  correspond to experimental conditions (e.g.,  $U_{in}$  is 6 m/s in the upper stream and 3 m/s in the lower stream). With well designed inlets, the transverse velocity  $V$  is close to zero and is treated as such. Numerical calculations have been performed for both uniform and nonuniform inlet distributions of  $U$ .

The specification of  $k$  and  $\epsilon$  at the inlets requires some elaboration. The inlet profile of  $k$  is obtained from

$$k = \text{TURBIN} \times U_{in}^2 \quad (5)$$

where  $U_{in}$  denotes the mean longitudinal velocity at the inlet and TURBIN is the parameter (FORTRAN variables in the TEACH code) which remains to be specified. We note that the experimental data on the turbulence intensity measurements in the inlet provide a basis for selecting the appropriate value of TURBIN. Furthermore, in the absence of turbulence intensity measurements in all three orthogonal coordinate directions, the determination of  $k$  from the intensity results in one or two directions (e.g., the Stanford mixing-layer data provide  $u/U$  only) requires the assumption of isotropy.

The inlet distribution of  $\epsilon$  is specified through the prescription of the inlet turbulence length scale, according to

$$\epsilon = k^{1.5}/\ell, \quad (6)$$

TABLE 2  
BOUNDARY CONDITIONS

$\bar{\phi}$	Top and Bottom Boundaries (Walls)	Left Boundary (Inlets)	Right Boundary (Outflow)
$\bar{U}$	Law of the Wall to Relate the Wall Shear Stress $\tau_w$	$\bar{U}$ Specified $\bar{U} = U_{in}$ ( $U_1$ and $U_2$ )	Overall mass Conservation
$\bar{V}$	$\bar{V} = 0$	$\bar{V} = 0$	$\frac{\partial \bar{V}}{\partial x} = 0$
$k$	Given by Wall Functions	$k$ Specified (TURBIN) ( $U_{in}$ ) <sup>2</sup>	$\frac{\partial k}{\partial x} = 0$
$\epsilon$		$\epsilon = k^{1.5}/l$ $l = 0.56 h$ $l = 0.05 h$	$\frac{\partial \epsilon}{\partial x} = 0$

where  $\ell$  is the inlet turbulence length scale. For the two-dimensional mixing layer,  $\ell$  is taken as

$$\ell = \lambda h, \quad (7)$$

where  $\lambda$  is a parameter (FORTRAN variable in the TEACH code is ALAMDA) and  $h$  is the half height of the channel ( $h = 2$  cm). The value of 0.56 for  $\lambda$  used in the present calculations is based upon earlier studies.<sup>3,14</sup> In addition, the sensitivity of the predictions has been checked for  $\lambda = 0.05$ .

### c. Results and Discussion

Present numerical investigations have considered several aspects of the mixing-layer flowfield. The results reported here correspond to initial velocities of 6 and 3 m/s in the upper and lower streams of nitrogen. The Reynolds number  $Re_x$  [based upon the distance  $x$  from the trailing edge of the splitter plate and defined as  $Re_x = 0.5 (U_1 + U_2) x / \nu$ , where  $\nu$  is the kinematic viscosity] considered ranges from 14,300 for  $x = 5$  cm to 52,000 for  $x = 18$  cm. The numerical predictions are presented here and compared with experimental data.

#### (1) Influence of Inlet Velocity Profile

The predicted results of the mean and rms streamwise velocity components in the mixing layer are shown in Figures 3 through 6 for the four  $x$  locations of 5, 12, 15, and 18 cm respectively. The predictions corresponding to both uniform and nonuniform inlet distributions of  $U$  and  $k$  are compared with the hot-wire data. Since the available experimental data at the inlet sections do not go all the way to the splitter plate and to the top and bottom walls, some minor arbitrariness arises concerning the rapid changes in  $U$  and  $u$  close to these boundaries. While the rapid decay of the mean velocity to zero does not pose problems, the rapid increase first and then the rapid decrease of the rms velocity to zero at the boundaries cause some difficulty in prescribing the nonuniform inlet profile for the numerical calculations.

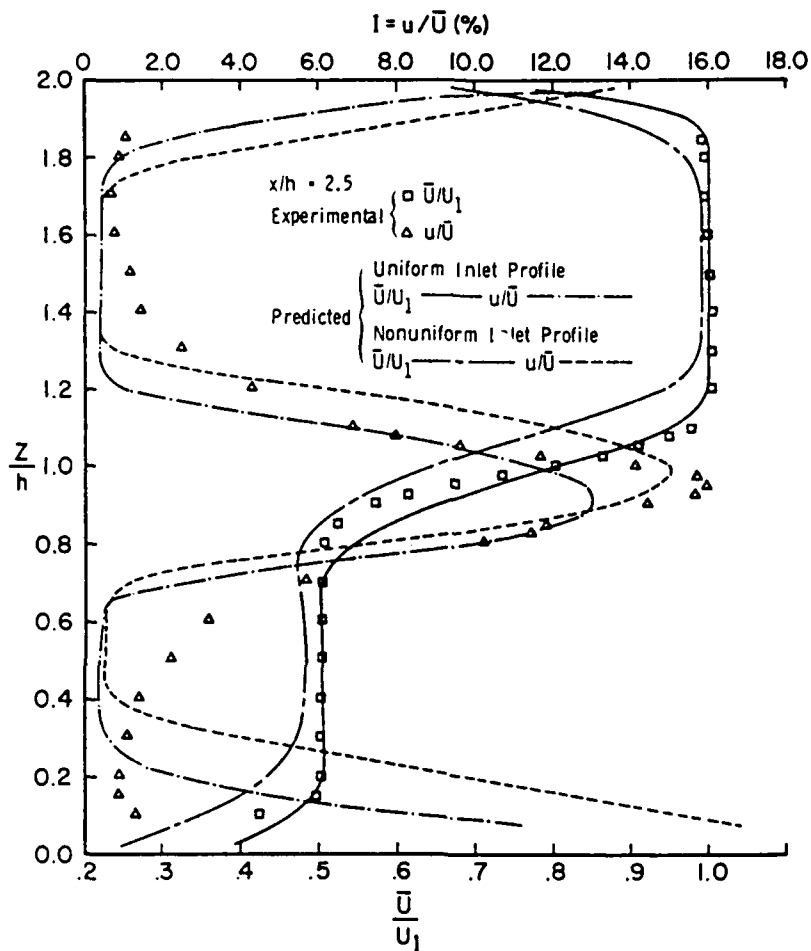


Figure 3. Profiles of Mean and rms Streamwise Velocity Components at  $x = 5$  cm.

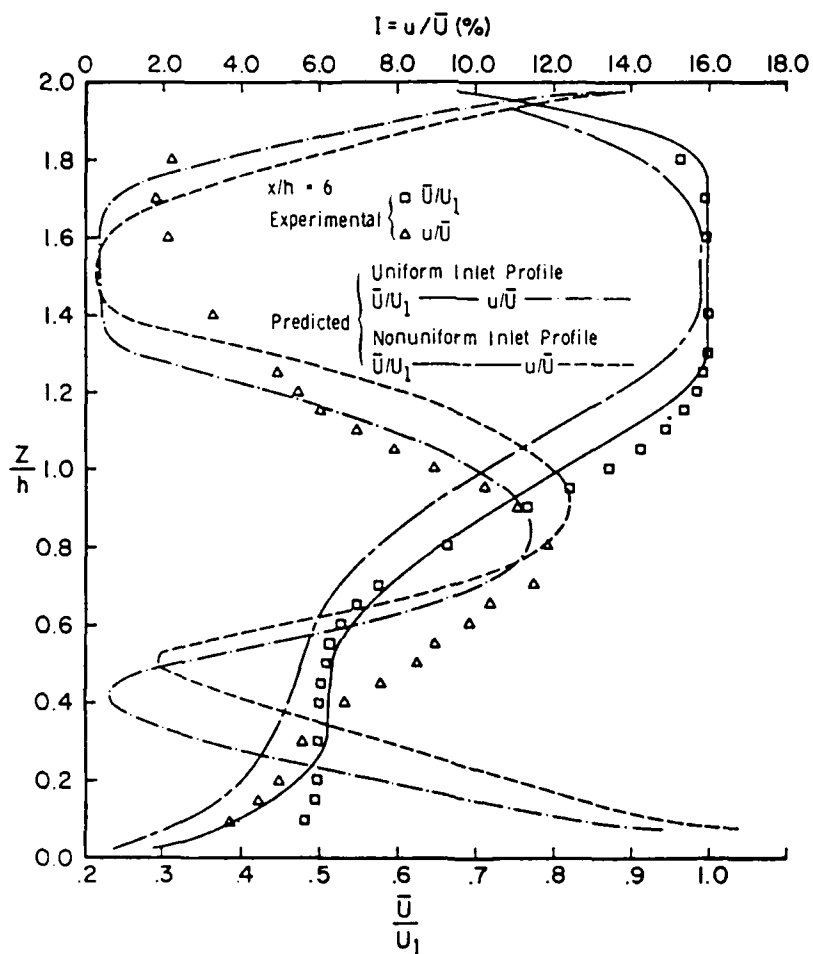


Figure 4. Profiles of Mean and rms Streamwise Velocity Components at  $x = 12$  cm.

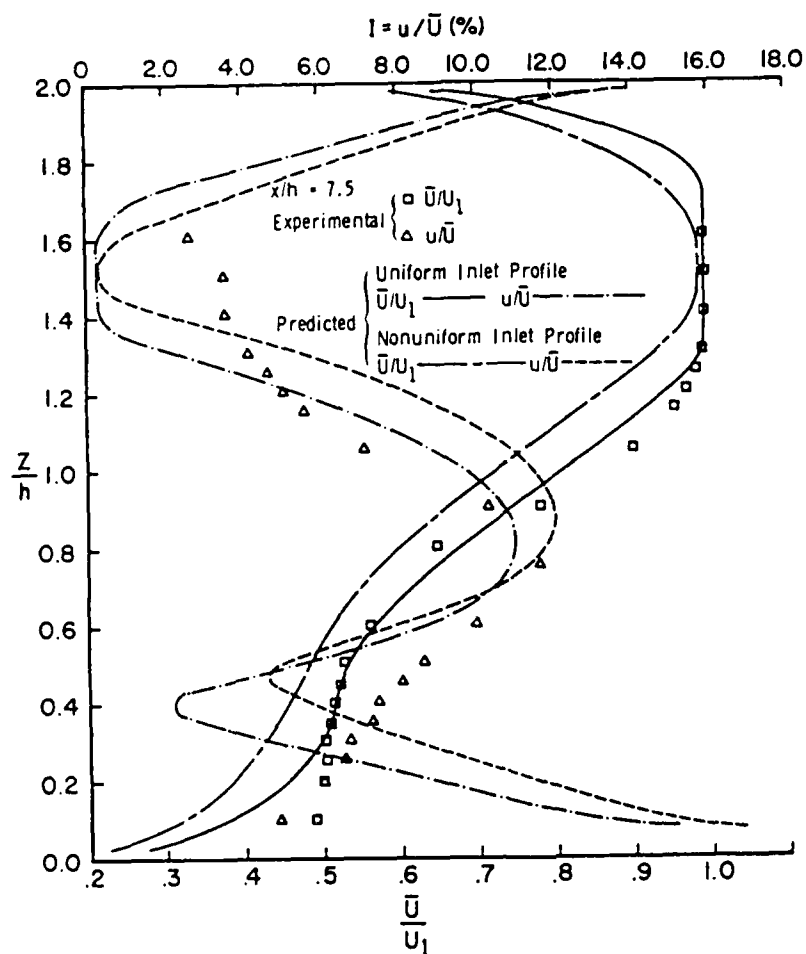


Figure 5. Profiles of Mean and rms Streamwise Velocity Components at  $x = 15$  cm.

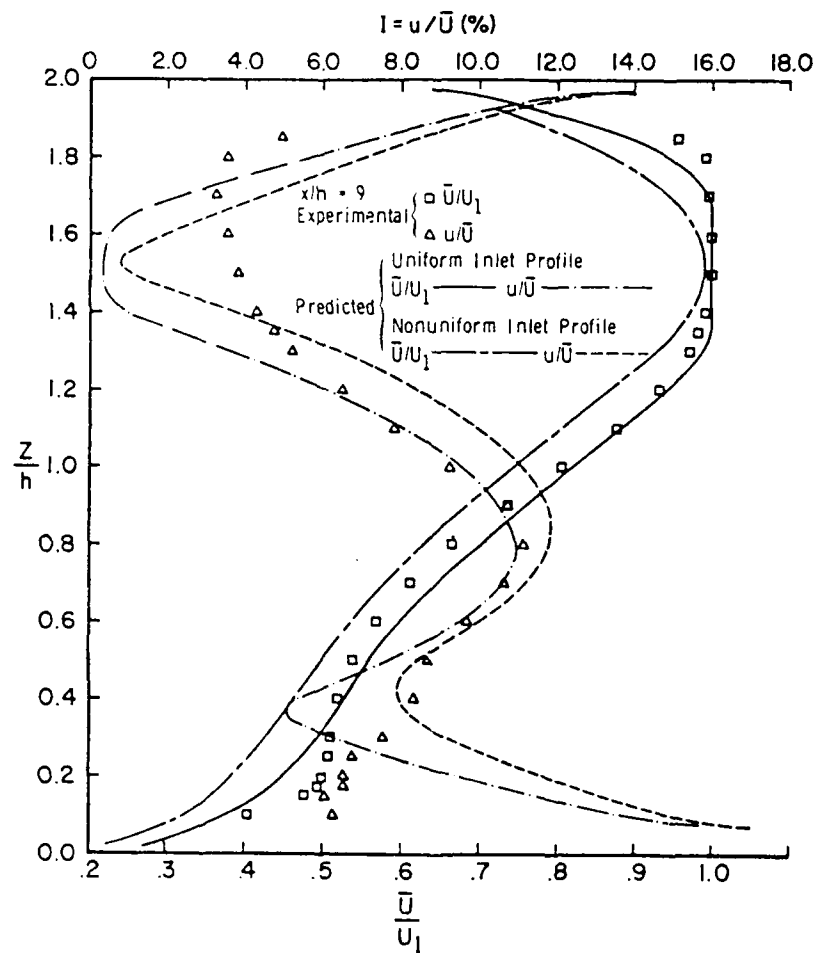


Figure 6. Profiles of Mean and rms Streamwise Velocity Components at  $x = 18$  cm.



An examination of the results indicates that the agreement between the predictions and measurements is much better for the mean velocity component than for the rms component. For the mean velocity component, the predicted results with uniform inlet profiles show very good agreement with the experimental data. Calculations with nonuniform inlet profiles underpredict the measurements at the four streamwise locations. For the rms velocity component, the predictions show that the overall trend in the mixing layer conforms to the experimental trend. Quantitative agreement for the magnitude and location of the peak turbulence intensity, however, is generally poor. We note that the calculations overpredict the turbulent mixing rate, especially near the origin of the mixing layer. Farther downstream, predictions tend to indicate better agreement with the measured data inside the mixing layer and in this case also the calculations with uniform inlet velocity profiles are clearly superior to those employing nonuniform profiles. The poor agreement between the measurements and predictions outside the mixing layer may be, in part, due to the assumption of isotropy in the numerical modeling [ $u$  is computed as  $(2k/3)^{0.5}$ ], the validity of which is not established in the experiments. Also, the very rapid rise in the intensity predictions near the top and bottom walls is a consequence of the normalization with respect to the local mean velocity  $U$  (which vanishes at the walls).

(2) Influence of Turbulence Length Scale, Differencing Scheme, and Streamline Curvature

The predictive calculations discussed earlier were based upon the "hybrid" upwind differencing scheme and the "standard"  $k-\epsilon$  model without the correction for the streamline curvature. The inlet turbulence length scale parameter  $\lambda$  was taken as 0.56. Additional computations were completed to investigate the effect of the changes in these areas of modeling on the predictions. The calculations showed that there is no discernible difference in the mean velocity profile at all four  $x$  locations between: (a)  $\lambda = 0.56$  and  $\lambda = 0.05$ , (b) upwind and power-law differencing

schemes, and (c) the results with and without the correction for streamline curvature.

Figures 7 through 10 show the results of the turbulence intensity profiles at the four streamwise locations. It appears that the variations in both the inlet turbulence length scale and the differencing schemes do not have significant influence on the rms velocity field at the four  $x$  locations. The curvature correction shows no discernible influence on the rms velocity predictions at the first two streamwise locations. Farther downstream (at  $x = 15$  and  $18$  cm), however, a small but noticeable effect is seen inside the mixing layer.

### (3) Other Effects

All the foregoing results were obtained from calculations that employed the computational domain with the exit-plane located at  $x = 22.5$  cm. Moreover, the streamline curvature correction did not involve the dissipation-equation modification of Reference 14. Therefore, a parametric examination of the effect of a different exit-plane location ( $x = 31.5$  cm) and a  $\epsilon$ -equation modification was completed. These calculations showed no difference in the mean and rms predictions at the first three  $x$  locations. Figure 11 which presents the mean-velocity profile at  $x = 18$  cm indicates that there is no discernible effect inside the mixing layer. The turbulence intensity profile at  $x = 18$  cm seen in Figure 12 shows a very small effect in the mixing layer.

### d. Conclusions

- The numerical calculations employing the TEACH-type numerics and the  $k-\epsilon$  turbulence model provide physically correct predictions of the two-dimensional, isothermal mixing layer.
- The numerical predictions of the mean streamwise velocity profile at different downstream locations show good agreement with the hot-wire data from the Stanford mixing-layer experiment.

## (2) Turbulence Model

The turbulent eddy viscosity  $\mu_t$  (the effective viscosity  $\mu_{eff}$  appearing in the governing equations is given by  $\mu_t + \mu$  where  $\mu$  is the laminar viscosity) in the  $k-\epsilon$  model is obtained from  $\mu_t = c_\mu \rho k^2 / \epsilon$ , where  $\rho$  is the mass density and  $c_\mu$  is a constant equal to 0.09.

Isotropy is assumed in obtaining  $k$  from the rms velocity components, according to  $k = (3/2)w^2$ , where  $w$  is the axial rms velocity component. The inlet profile of  $k$  is given by  $0.03 w^2$  for the annular jet and by  $0.03 W^2$  for the central jet (see SS and KP). The required inlet profile for  $\epsilon$  is specified as discussed below.

Inlet Turbulence-Length Scale. As in KP, we obtain the inlet profile of  $\epsilon$  from  $\epsilon = k^{3/2}/\ell$ , where the inlet turbulence-length scale  $\ell$  is given by  $\ell = \lambda \delta$ . Here  $\lambda$  is a specified constant and  $\delta$  is a characteristic reference length given by  $(D_d - D)/2$  for the annular jet and  $d/2$  for the central jet. KP used 0.3333 and 0.5556 for  $\lambda$ . The former value is equivalent to 0.03 used in SS (since they employ  $\epsilon = c_\mu k^{3/2}/\ell$ ) and the latter value is used in LR. Present results are based upon  $\lambda = 0.5556$ .

Streamline Curvature Correction. Curvature modifications to turbulence models have been attempted by a number of researchers (e.g., see LR; Humphrey and Pourahmadi;<sup>31</sup> Rodi and Scheuerer;<sup>32</sup> and the references cited in them). A majority of these modifications have been concerned with the  $k-\epsilon$  model. Present numerical investigation has introduced a curvature-dependent (and hence nonconstant)  $c_\mu$  into the standard  $k-\epsilon$  model. Following LR, we have

$$c_\mu = -K_1 K_2 / [1 + 8K_1^2 (k/\epsilon)^2 \left( \frac{\partial w}{\partial n} \frac{s}{R_c} + \frac{w}{R_c} \right) \frac{w}{R_c} ],$$

where  $R_c$  is the local radius of curvature of a streamline,  $s$  and  $n$  denote the coordinates along and normal to the streamline, and

TABLE 3  
FLOWFIELD CONDITIONS

CBCC	Temp. K	$\bar{W}_d$ m/s	$\bar{W}_A$ m/s	Air Mass Flow kg/s $\times 10^2$	Re <sub>A</sub> $\times 10^{-5}$	$\bar{W}_F$ m/s	CO <sub>2</sub> Mass Flow kg/s $\times 10^5$	Re <sub>F</sub> $\times 10^{-4}$
APL	300	32.91	46.7	200	3.08	51.19 136.5	167 444	2.44 6.50
UCI	300	7.5 15.0	11.68 23.35	1.86 3.72	0.153 0.306	24.82	5.93	0.32



data<sup>2,30</sup> to elucidate the distinctions between the small- and large-scale CBCC. This was necessary in view of the differing nature of the predictions.

## (2) Scope of Computations

This study deals with the isothermal flow-field predictions. As in SS and KP, present work employs the TEACH computational procedure (Gosman and Ideriah<sup>10</sup>), and the standard features of the numerics thereof. An additional feature considered here is the power-law differencing scheme<sup>20</sup> in place of the hybrid upwind scheme.<sup>12</sup> While both the APL and the UCI configurations were studied, only a limited parametric range of the flowfield conditions investigated is reported.

### b. Numerical Computations

The details concerning the application of the TEACH procedure to the CBCC flowfields are available in Krishnamurthy et al.<sup>3</sup> and therefore are not repeated here.

### (1) Computational Details

Figure 14 shows the present computational domain and the grid-point distribution. The grid consists of 41 axial nodes and 39 radial nodes with a nonuniform spacing in both directions to ensure adequate spatial resolution in flowfield regions with large gradients of the flow variables. The calculations with this grid require about 170,000g words of memory on the CDC CYBER computer. The converged solutions are attained in less than 900 iterations, with each iteration taking less than a second of computer time.

The results herein correspond to the conditions shown in Table 3, with uniform inlet profiles for the mean axial velocity, corresponding to  $\bar{W}_A$  in the annular jet and  $\bar{W}_F$  in the central jet. The Reynolds number  $Re_A$  of the air flow is based upon  $D$  and the reference velocity  $\bar{W}_d$  in the duct. The Reynolds number  $Re_F$  of the  $CO_2$  flow is based upon  $d$  and  $\bar{W}_F$ .

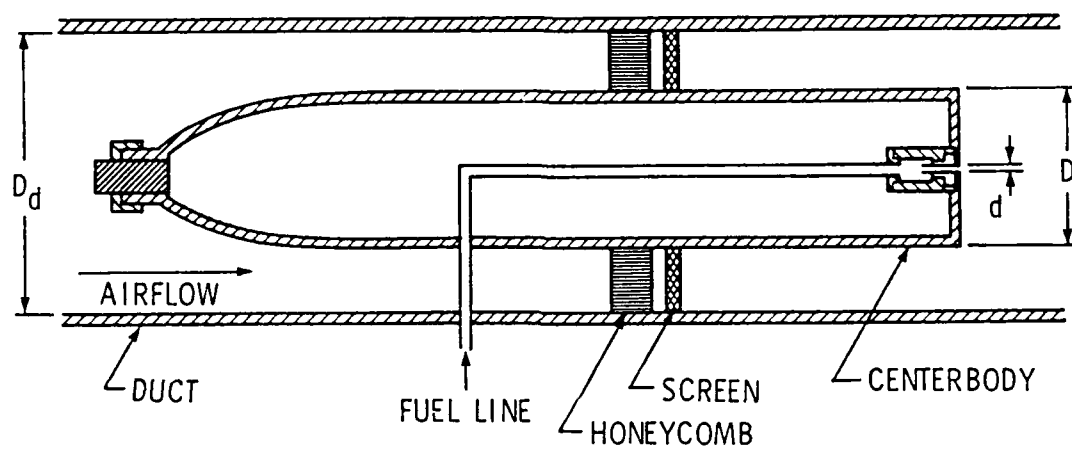
## (1) Background and Objectives

SS and KP employed the two-equation model for the turbulent kinetic energy  $k$  and its dissipation rate  $\epsilon$ .<sup>11</sup> This model in its standard version does not account for streamline curvature effects. Its predictions overestimated the extent of the recirculation region in the APL CBCC compared with the laser Doppler anemometry (LDA) data of Lightman et al.<sup>23-24</sup> This was in contrast to the experience of several previous studies of turbulent recirculating flows where significant underprediction was observed (e.g., see Pope and Whitelaw;<sup>25</sup> Militzer et al.;<sup>26</sup> Gosman et al.;<sup>27</sup> Durst and Rastogi<sup>28</sup>). Also, SS and KP overpredicted the central jet  $\text{CO}_2$  mass flow rate required in the experiments<sup>24</sup> to eliminate the centerline reverse air flow. Another aspect in which the prediction was deficient concerned the axial distribution of the centerline rms axial velocity component.

It is known that the turbulent shear stress and the degree of anisotropy between the normal stresses are very sensitive to streamline curvature.<sup>29</sup> Thus, the presence of large curvature in the CBCC may have contributed in part to the discrepancy between the measurement and prediction. Accordingly, the main objective of the present study was to examine the influence of curvature corrections in the prediction. Recent availability of extensive isothermal LDA data from UCI, as well as LDA (Lightman et al.<sup>2</sup>) and  $\text{CO}_2$  concentration (Bradley et al.<sup>30</sup>) data from APL has facilitated this inquiry.

When calculations were made for the UCI CBCC with the standard  $k-\epsilon$  model, the centerline recirculation length was underpredicted in line with the experience of other researchers.

The introduction of a curvature correction, along the lines suggested by Leschziner and Rodi<sup>14</sup> (hereafter denoted by LR), resulted in only a partial improvement of the prediction. Therefore, the second objective was to examine the impact of the diffusion-equation modification considered in LR. A final objective was the comparison of the predictions with the newer APL



APL  
COMBUSTOR

$D_d = 25.4$  cm  
 $D = 14.0$  cm  
 $d = 4.80$  mm  
 $L = 30.2$  cm

UCI  
COMBUSTOR

$D_d = 5.10$  cm  
 $D = 3.05$  cm  
 $d = 1.30$  mm  
 $L = 22.6$  cm

Figure 13. Schematic of CRCC.



the predicted and measured results of the axial and radial distributions of the mean and rms axial velocity, the centerline stagnation points, and the axial decay of the centerline CO<sub>2</sub> concentration.

a. Centerbody Combustor Configuration

The centerbody combustor represents a complex turbulent flowfield. As noted by Bradshaw,<sup>13</sup> a complex turbulent flow is one which cannot be predicted with acceptable accuracy by methods developed in classical thin shear layers. The assumptions inherent in the thin-shear-layer approximation are often invalidated in realistic flowfields by the presence of several features (e.g., interacting shear layers or high rates of strain associated with large streamline curvature). Figure 13 shows schematically the large- and small-scale CBCC. This involves confined turbulent mixing of an annular air stream and a central gas (CO<sub>2</sub> in isothermal experiments and C<sub>3</sub>H<sub>8</sub> in combustor experiments) jet in the near-wake region downstream of a bluff body. Figure 13 shows that the ratio D/d is rather large (29 for the APL and 23 for the UCI configurations). Indeed, the present interjet separation is much larger than that studied in typical coaxial jet mixing of both confined and unconfined flowfields in the literature. The wide separation between the jets and the concomitant presence of the toroidal recirculating bluff-body wake in the mixing region have raised some interesting flowfield ramifications addressed only recently in numerical predictions (e.g., see Krishnamurthy;<sup>5</sup> Sturgess and Syed,<sup>6</sup> hereafter denoted by SS; and Krishnamurthy et al.,<sup>3</sup> hereafter denoted by KP). Depending on the strength of the annular and central jets, the CBCC flowfield exhibits wake-like and jet-like characteristics under isothermal conditions (e.g., see Krishnamurthy, Wahrer, and Cochran<sup>9</sup>). Nevertheless, the juxtaposition of the two streams with the near-wake region in a confined configuration renders the CBCC flowfield a highly "complex turbulent flow," in the sense of Bradshaw.<sup>13</sup> In addition to the interacting shear layers, large streamline curvature is present.

- The numerical predictions of the turbulence (streamwise) intensity are consistent with the experimental trends and show fair to poor quantitative agreement.
- Both the mean and rms velocity predictions are not significantly affected by parametric changes in the numerical modeling involving inlet turbulence length scale, differencing scheme, streamline curvature correction in the  $k-\epsilon$  model, and the location of the computational domain exit plane.
- Predictions based on uniform inlet-velocity profiles show better agreement with the measurements than the predictions based on nonuniform profiles.
- The mixing layer appears to exhibit some interactions with the boundary layers at the top and bottom walls (being greater for the latter than for the former) at large distances downstream. These interactions may explain, in part, the noted differences between the predicted and measured rms velocity results, when there is excellent agreement for the mean velocity. Indeed, this conclusion is consistent with the recent observations of Wood and Bradshaw.<sup>22</sup> They report significant changes in the turbulence structure (with the mean-velocity profile remaining unaltered) when the mixing layer is influenced by a solid surface. While their mixing layer had to contend with only a bottom boundary layer, they emphasize that "...similar, and perhaps even larger, changes will occur in a two-stream mixing layer confined by a tunnel roof as well as the floor."

## 2. LARGE- AND SMALL-SCALE CBCC'S

The confined turbulent recirculating flowfield due to the isothermal mixing of dual coaxial streams in the near-wake region of the CBCC is described below. The finite-difference computations examine modifications to the turbulence model to account for the effects of streamline curvature and for the preferential influence of normal stresses on turbulence dissipation. This examination is facilitated by a comparison of

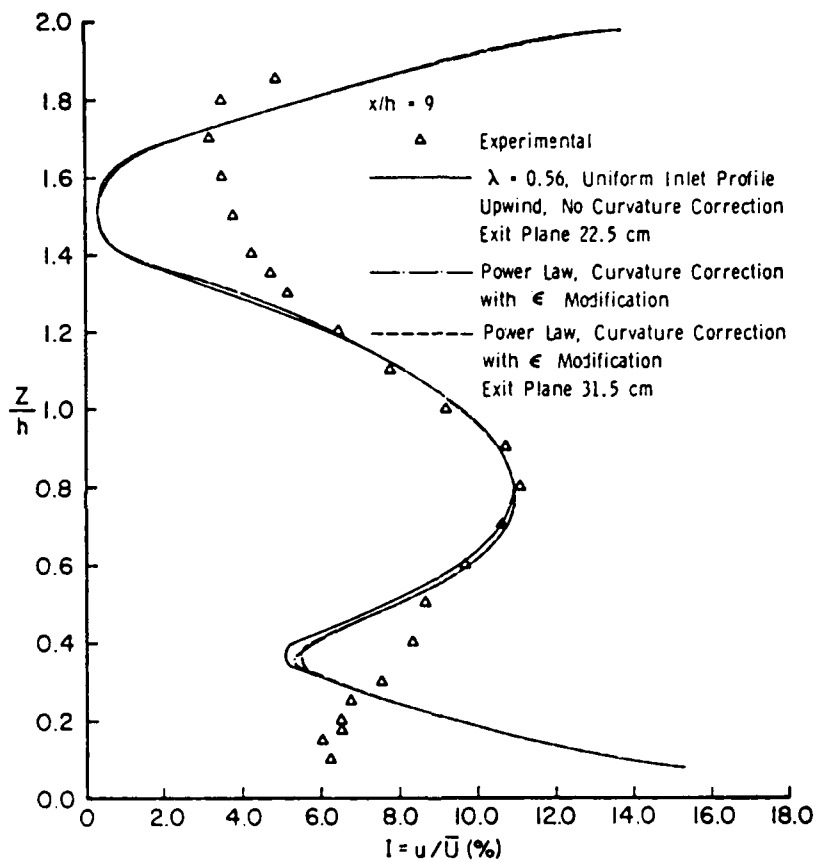


Figure 12. Influence of Curvature and Exit Plane Location on the rms Velocity Predictions at  $x = 18$  cm.

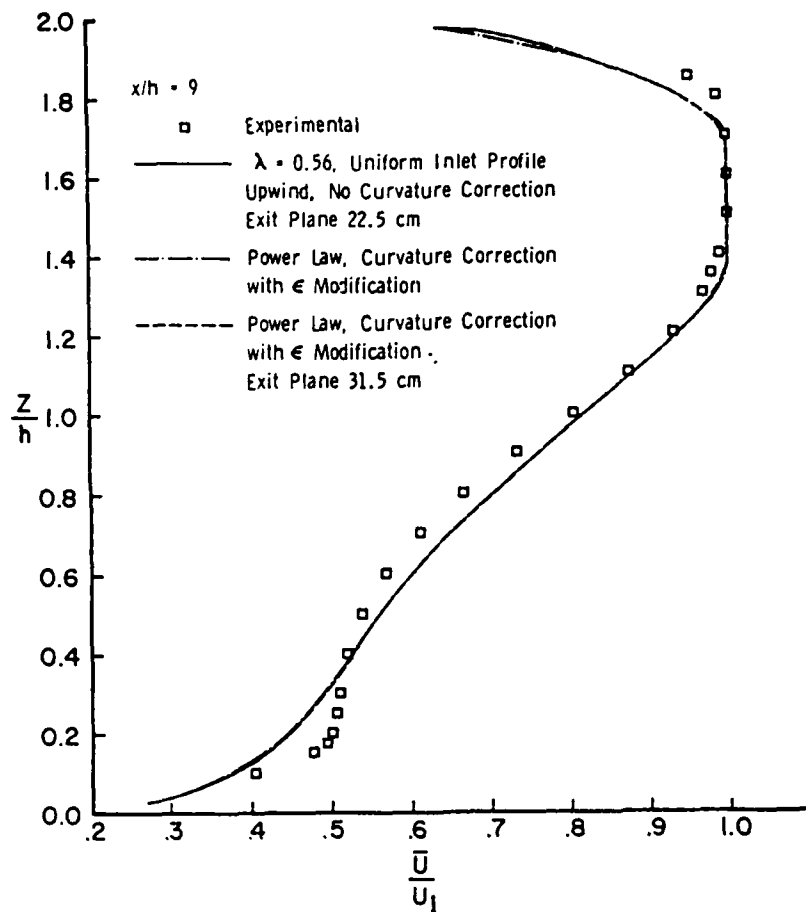


Figure 11. Influence of Curvature and Exit Plane Location on the Mean Velocity Predictions at  $x = 18$  cm.

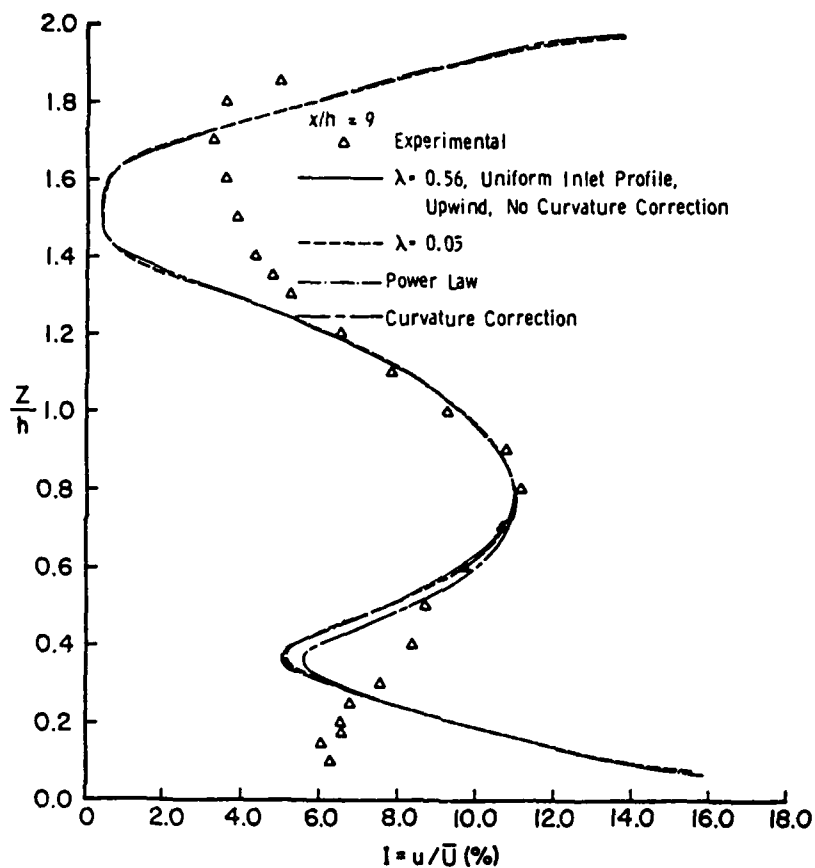


Figure 10. Influence of Turbulence Length Scale, Differencing Scheme and Curvature on the rms Velocity Predictions at  $x = 18$  cm.

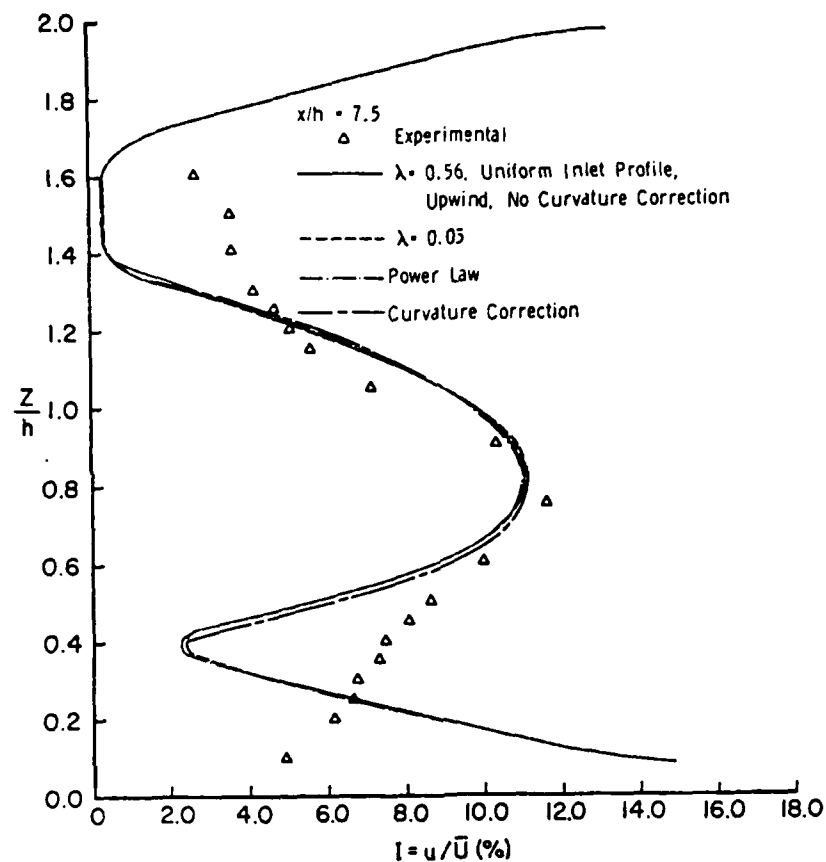


Figure 9. Influence of Turbulence Length Scale, Differencing Scheme and Curvature on the rms Velocity Predictions at  $x = 15$  cm.

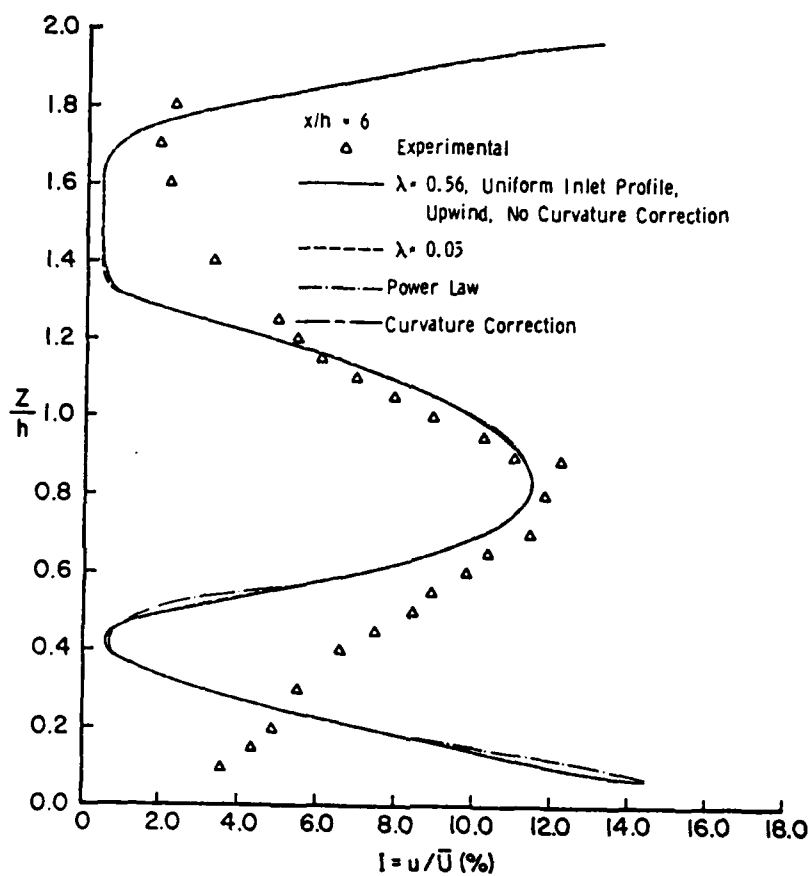


Figure 8. Influence of Turbulence Length Scale, Differencing Scheme and Curvature on the rms Velocity Predictions at  $x = 12$  cm.

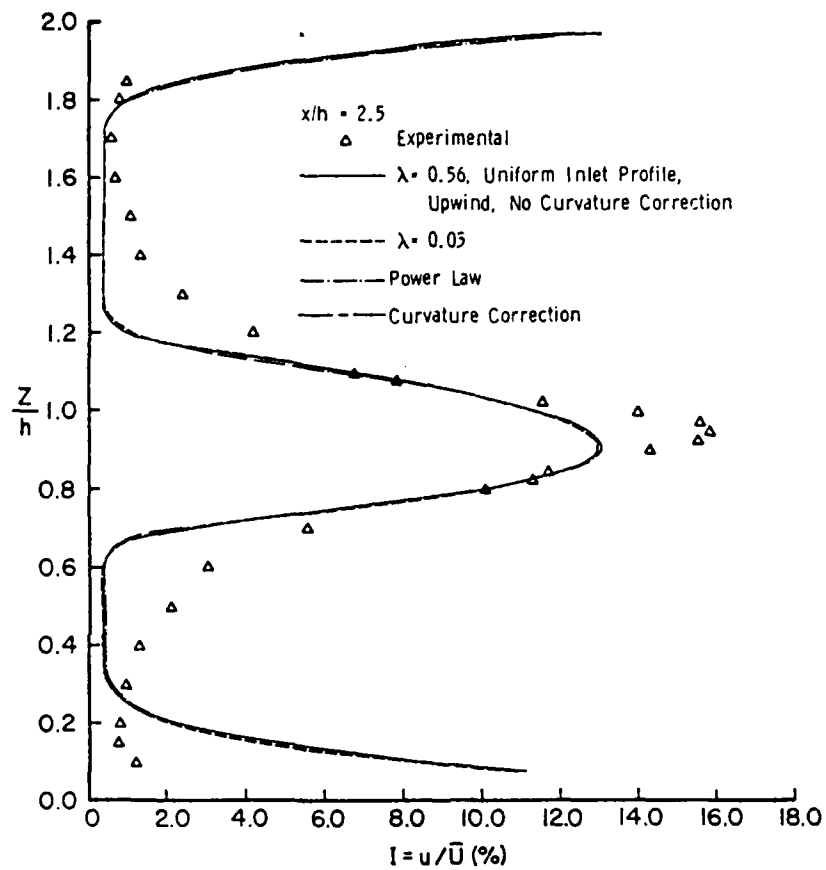


Figure 7. Influence of Turbulence Length Scale, Differencing Scheme and Curvature on the rms Velocity Predictions at  $x = 5$  cm.



$K_1$  and  $K_2$  are constants equal to 0.267 and -0.489 respectively. Although an element of arbitrariness in LR was noted in Reference 3, the discussion therein emphasizes the utility of the formulation of LR which is retained here. Also, as in LR, the calculations impose an arbitrary positive lower bound of 0.025 on  $c_\mu$ .

e Modification. We employ the preferential modification of dissipation proposed in LR for recirculating flowfields. Although additional work is necessary in view of the ad hoc nature of this modification, its inclusion throws some light on the observed distinction between the small- and large-scale CBCC.

### c. Results and Discussion

#### (1) Pertinent Results from SS and KP

To set the present results in context, we show in Figure 15 the earlier results from SS and KP. With identical values of  $\lambda$  (0.03 in SS), the two (grid A in KP) show good agreement in their degrees of underprediction of the forward stagnation points (FSP) and overprediction of the rear stagnation points (RSP) (the FSP occurs where the central jet loses its forward momentum entirely and the RSP is the usual end of the recirculation zone).

The measurements<sup>23-24</sup> showed that for  $\bar{W}_A = 47$  m/s and  $\bar{W}_F = 135$  m/s (corresponding respectively to an air mass flow of 2 kg/s and CO<sub>2</sub> mass flow of 16 kg/hr in the APL CBCC),  $\bar{W}$  was non-negative on the centerline. Indeed, the minimum CO<sub>2</sub> mass flow which eliminated the centerline-flow reversal was inferred from the measurements to be 14.7 kg/hr in SS. The predictions, however, indicate the occurrence of the centerline reverse flow (with both stagnation points present) at 16 kg/hr.

Curvature Correction. The preliminary results in KP for streamline curvature correction are shown for two CO<sub>2</sub> flow rates (viz., 4 and 8 kg/hr). It must be noted that the increase in  $\lambda$  from 0.3333 to 0.5556 has masked the effect of the correction.

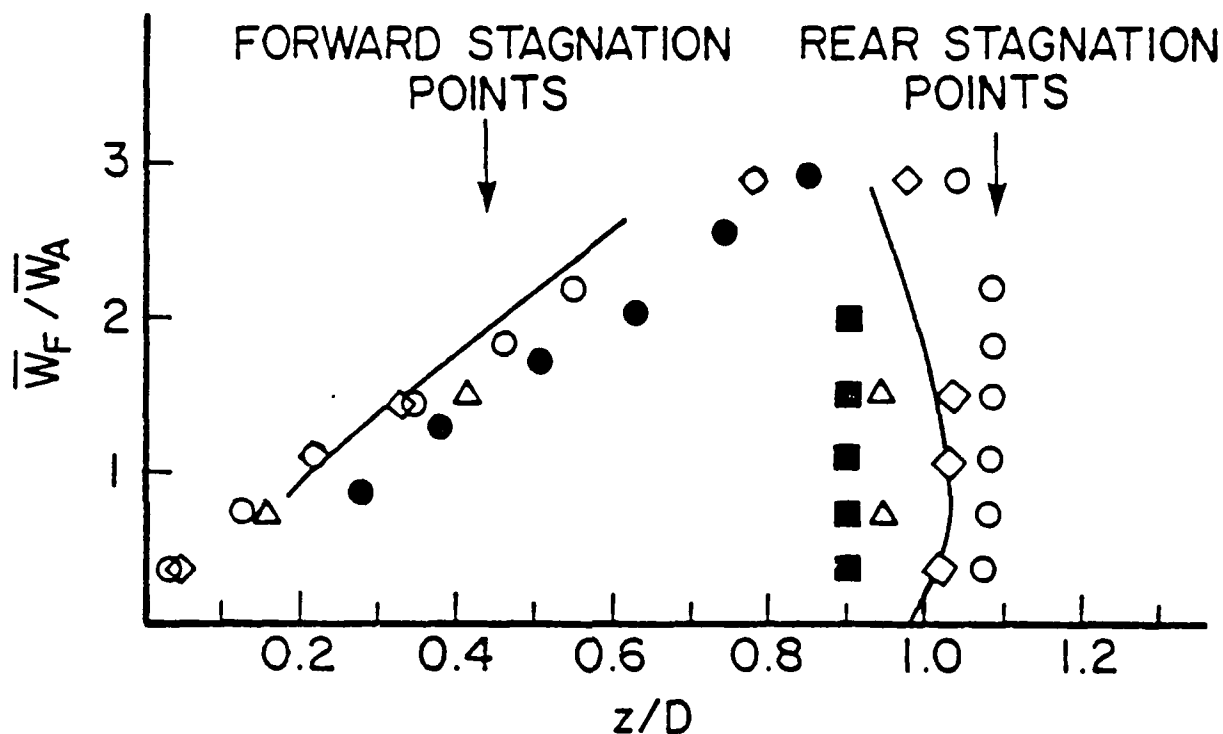


Figure 15. Measured and Predicted Centerline Stagnation Points for APL CBCC.  $\bullet$ ,  $\blacksquare$  LDA Results: Lightman et al.<sup>23,24</sup> The Predictions are Based upon Hybrid Upwind Differencing Scheme.  $\text{---}$  : SS (39 x 39),  $\lambda = 0.3333$ ;  $\diamond$  : KP, Grid A (41, 34),  $\lambda = 0.3333$ ;  $\circ$  : KP, Grid B (41, 34),  $\lambda = 0.3333$ ;  $\Delta$  : KP, Grid B (41, 34),  $\lambda = 0.5556$ , with Curvature Corrections. Grid B had More Nodes in the Annular Region than Grid A.

SS and KP have observed, however, that the increase in  $\lambda$  (without the correction) moves monotonically both the stagnation points upstream, thereby resulting in greater underprediction of the FSP. With the correction, the FSP moves farther downstream towards the measured value. The degree of overprediction of the RSP is seen greatly reduced with the larger  $\lambda$  and the curvature correction. Finally, the prediction with the correction has eliminated the centerline-flow reversal at the CO<sub>2</sub> flow of 16 kg/hr.

Unlike the good agreement for the centerline stagnation points, the centerline peak negative mean axial velocity  $\bar{W}_m$  was overpredicted with the curvature correction. Since KP had not isolated the influence of  $\lambda$ , hybrid upwind differencing (and the propensity for numerical diffusion therein), and the arbitrarily modified grid B, it was essential to examine the effect of the curvature correction more systematically.

## (2) UCI Configuration

Figure 16 compares the present predictions with the measurements. We note that the standard model underpredicts both the stagnation points by about 30 percent, a result in agreement with other studies. Considerable improvement is seen when the curvature correction to  $c_\mu$  is introduced. However, the stagnation points and  $\bar{W}_m$  are still underpredicted. With the  $\epsilon$ -equation modification in addition to the curvature correction, excellent agreement is seen for  $0 < z/D < 1.6$ . Farther downstream the measured recovery is greater than given by all the predictions.

Comparison of rms Velocity. The results seen in Figure 17 do not confirm the good agreement observed for the mean axial velocity. In fact, the predictions are very poor especially for  $z/D < 1.3$ . The somewhat better agreement seen for  $2 < z/D < 3$  is not consistent with the greater disparity noted for the mean velocity. Of course, a major problem in the predictions is the assumption of isotropy, which is known to be invalid in the near wake. Furthermore, good agreement for  $\bar{W}$  and poor agreement for  $w$

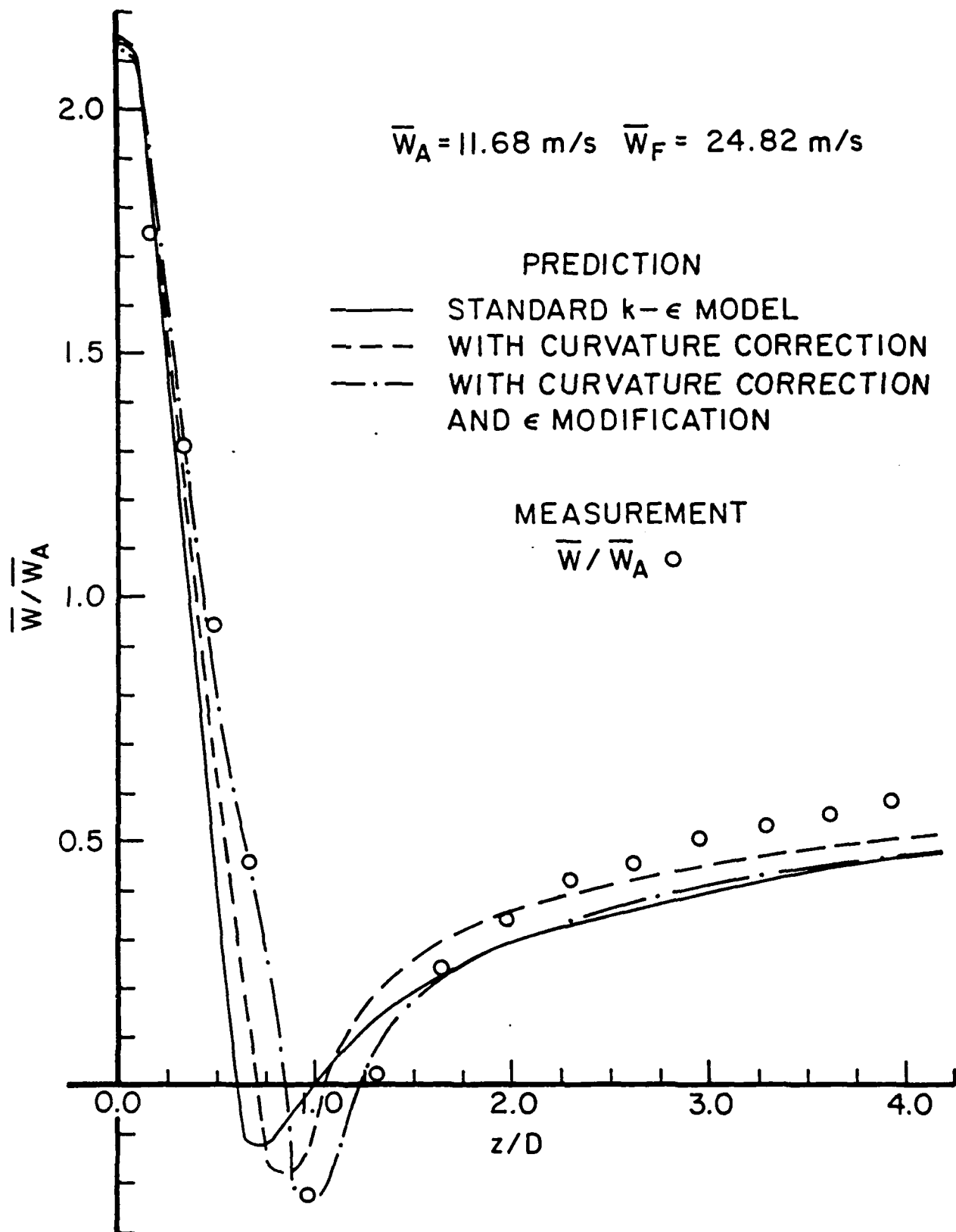


Figure 16. Measured (Brum et al.<sup>4</sup>) and Predicted Centerline Mean Axial Velocity for UCI CBCC.

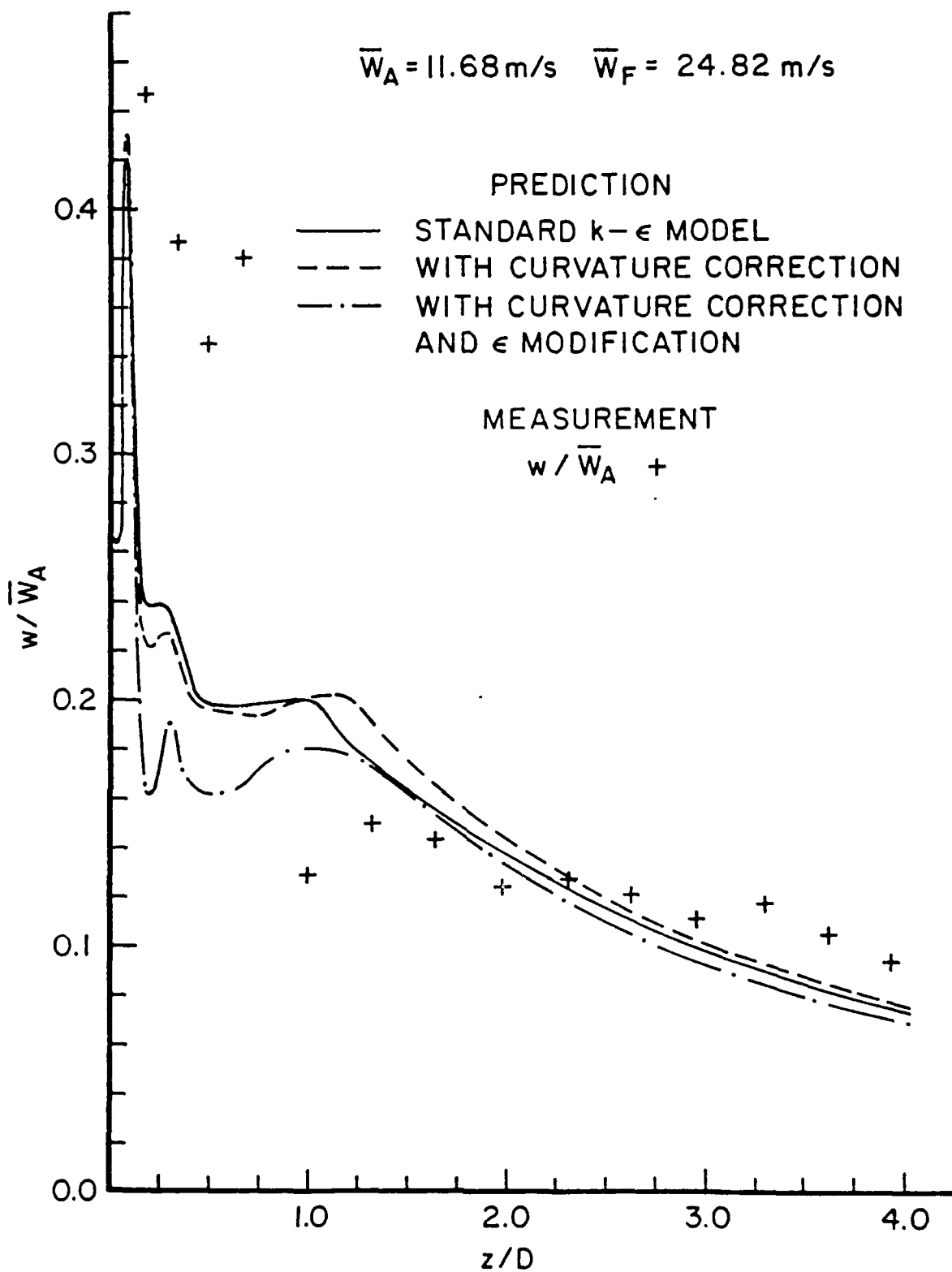


Figure 17. Measured (Brum et al.<sup>4</sup>) and Predicted Centerline rms Axial Velocity for UCI CBCC.

appear to be characteristic of complex turbulent flows (e.g., see Wood and Bradshaw<sup>22</sup>).

Radial Distributions. The predicted radial profiles at four axial locations in Figures 18 and 19 include both the  $c_\mu$  and  $\epsilon$  modifications. Good agreement is seen and the comparison is particularly striking at the axial location well within the recirculation region ( $z/D \sim 0.17$ ) and at the one near the RSP ( $z/D \sim 1.31$ ).

Flowfield Without the Central Jet. There is a marked difference in Figure 20 where the central jet is absent. The RSP is underpredicted by about 10% but the predicted magnitude and the axial location of  $\bar{W}_m$  differ by a factor of 2 from the measured values. The rms component, however, shows better agreement between the prediction and the measurement. This behavior is clearly different from that of the nonzero central jet seen in Figures 16 and 17. A parametric dependence emerging from these observations appears to emphasize the ad hoc nature of the modifications examined.

### (3) APL Configuration

The centerline profiles of  $\bar{W}$  and  $w$  for the large-scale CBCC are seen in Figures 21 through 23 for three different values of  $\bar{W}_p$ . The predictions of the standard  $k-\epsilon$  model and those with the correction for curvature (with and without the  $\epsilon$  modification) are compared with the LDA data of Lightman et al.<sup>2</sup>

Measurements. The experimental data for the mean velocity differ from the earlier results (Lightman et al.<sup>23,34</sup>). The locations of the RSP are at a  $z/D$  of 1 instead of 0.9 (see Figure 15). Figure 23 indicates a small region of centerline-flow reversal ( $0.75 \leq z/D \leq 0.975$ ). The newer data thus show better agreement with the predictions in SS and KP. Indeed, for the case of zero  $CO_2$  flow, the RSP result of SS even shows a small underprediction.

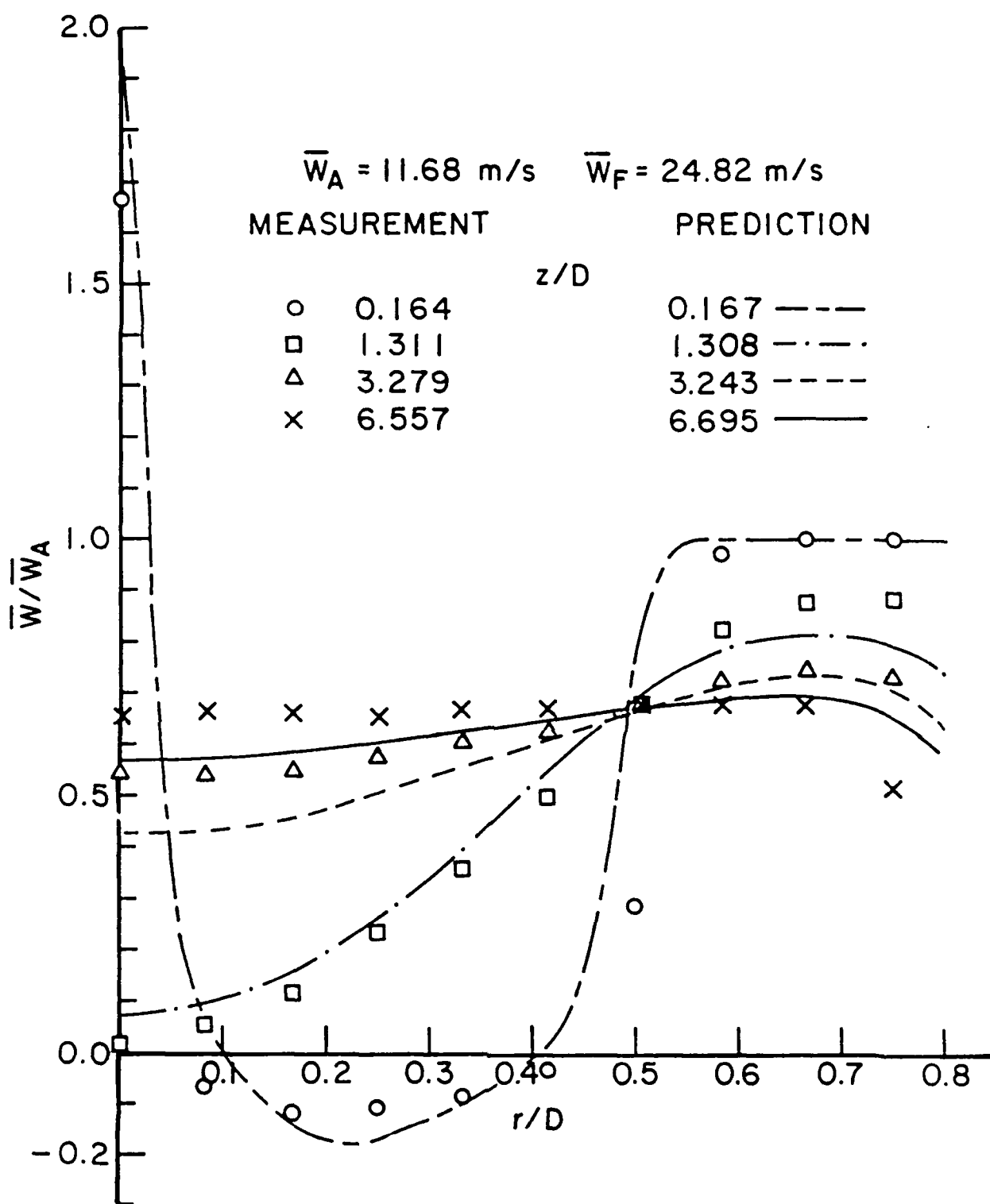


Figure 18. Measured (Brum et al.<sup>4</sup>) and Predicted Mean Axial Velocity Radial Profiles for UCI CRCC.

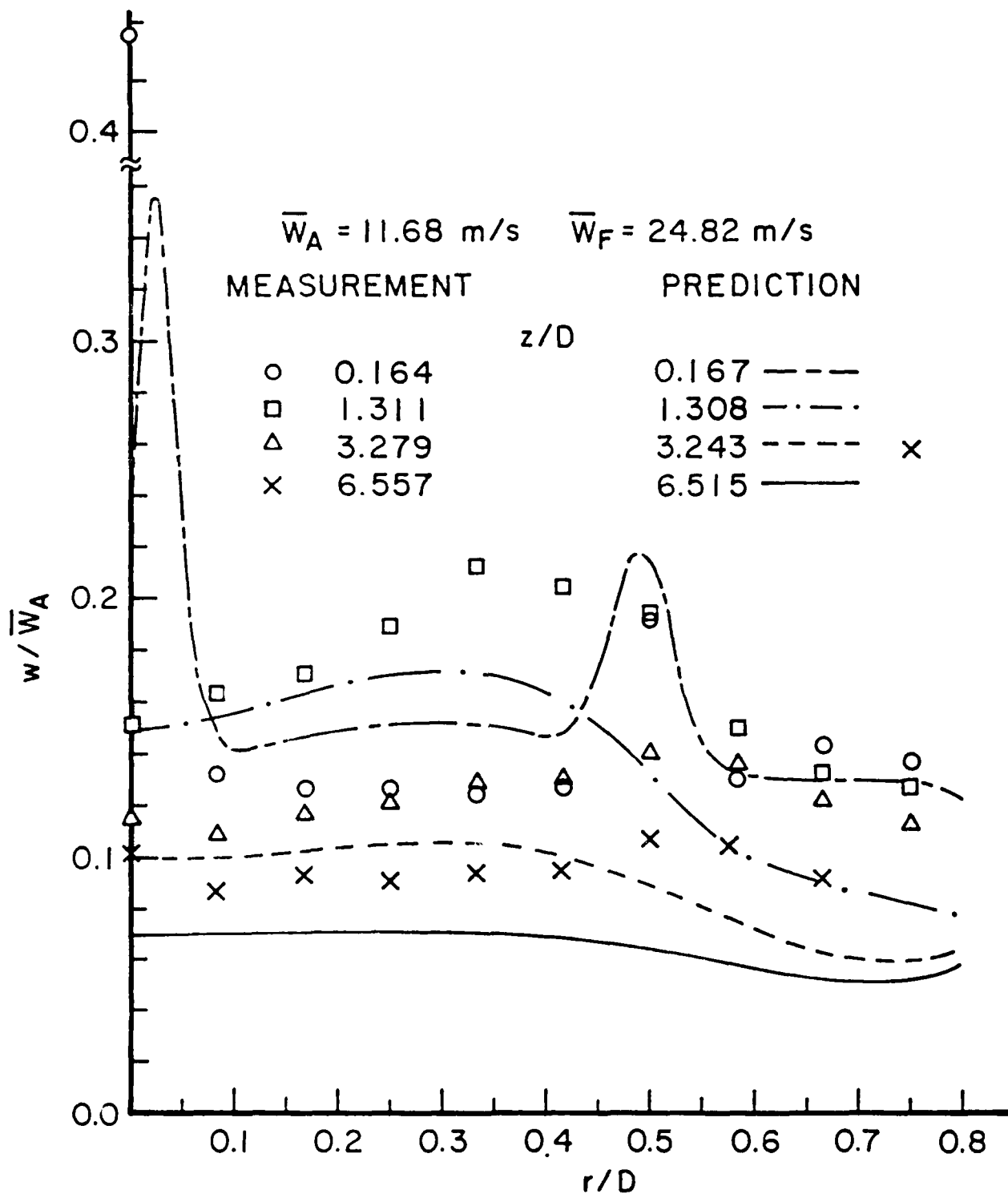


Figure 19. Measured (Brum et al.<sup>4</sup>) and Predicted rms Axial Velocity Radial Profiles for UCI CBCC.



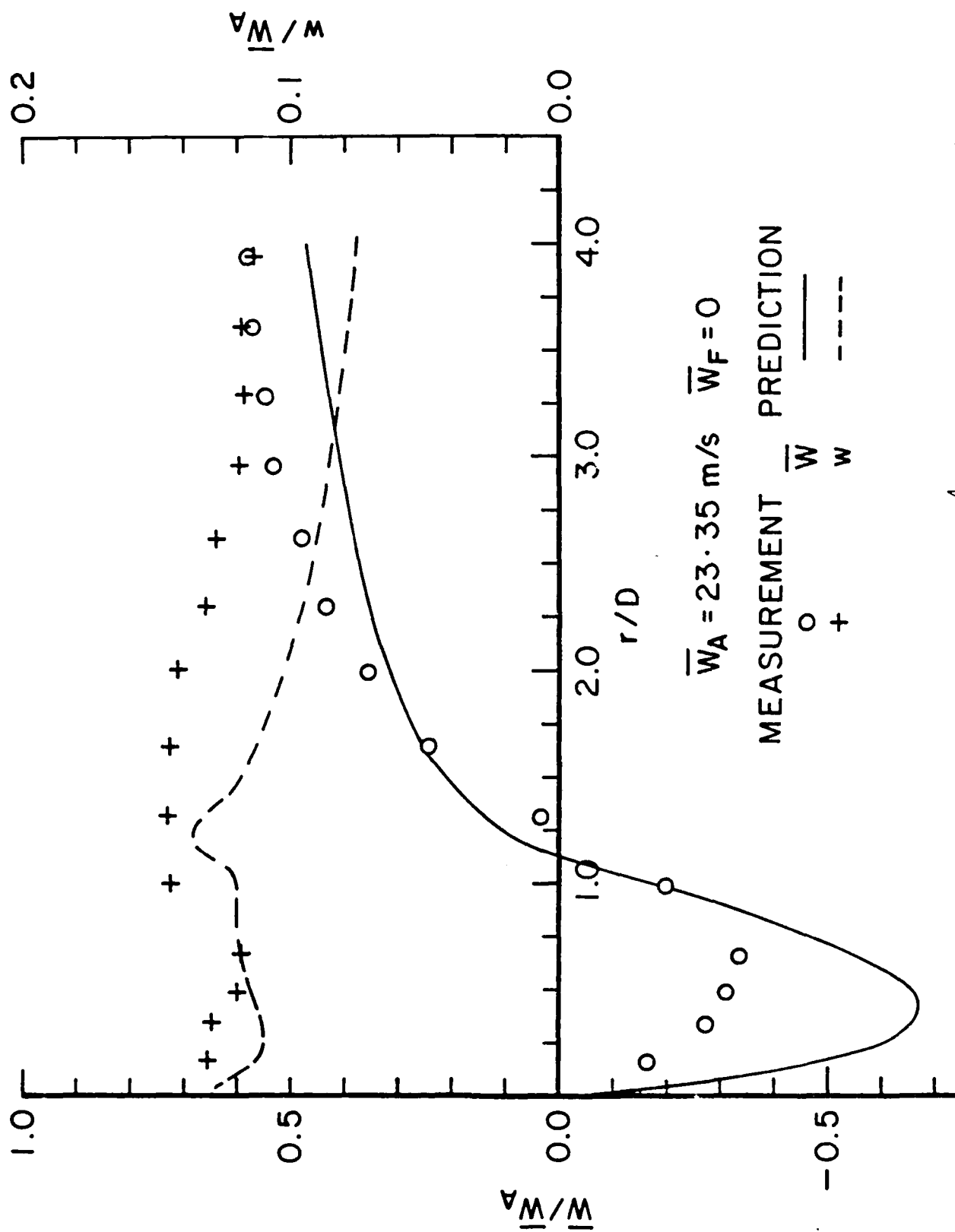


Figure 20. Measured (Brum et al.<sup>4</sup>) and Predicted Centerline Mean and rms Axial Velocity for UCI CBCC.

$$\bar{W}_A = 46.76 \text{ m/s} \quad \bar{W}_F = 0$$

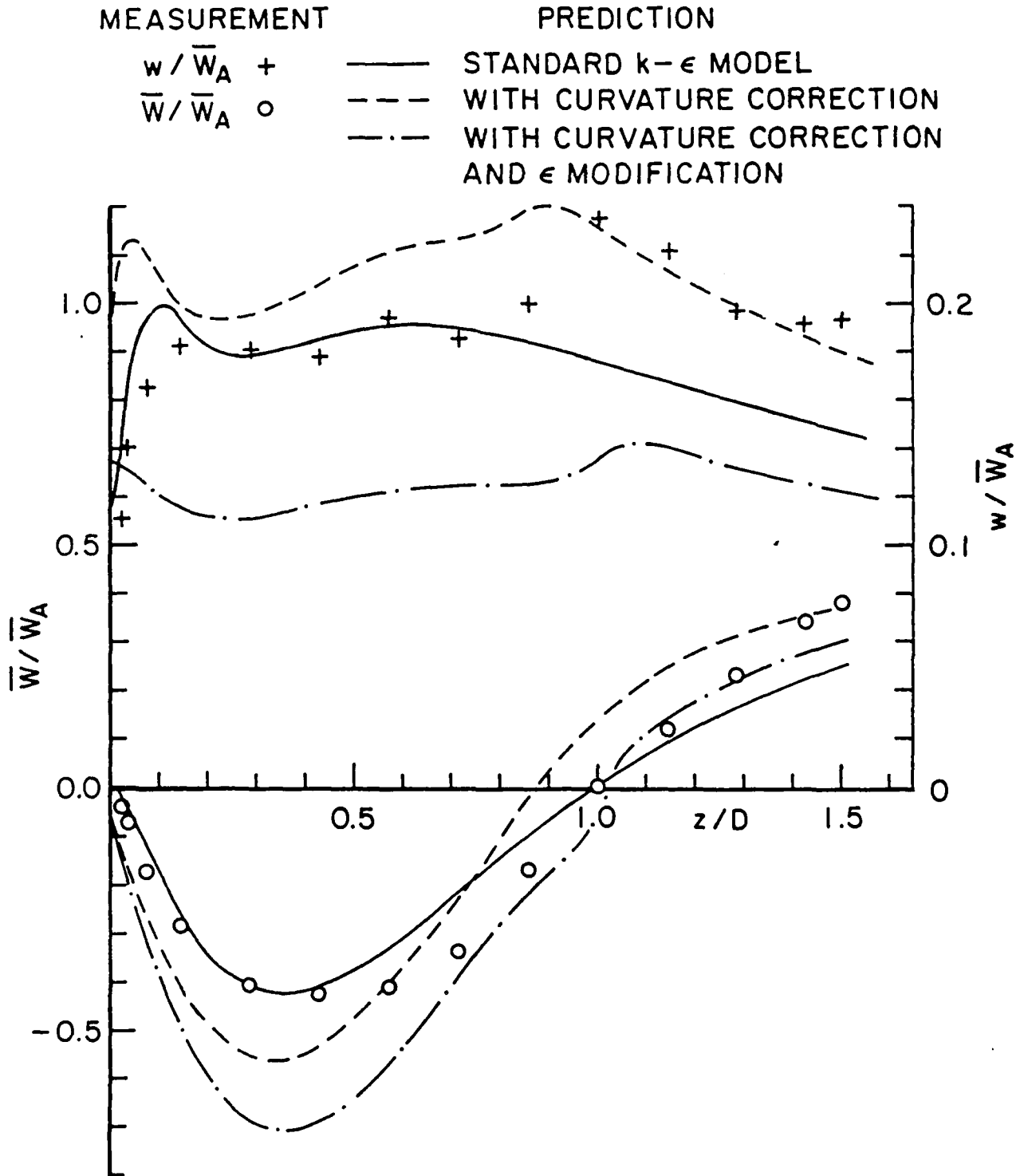


Figure 21. Measured (Lightman et al.<sup>2</sup>) and Predicted Centerline Mean and rms Axial Velocity for APL CBCC. Air Flow 2 kg/s and Zero CO<sub>2</sub> Flow.

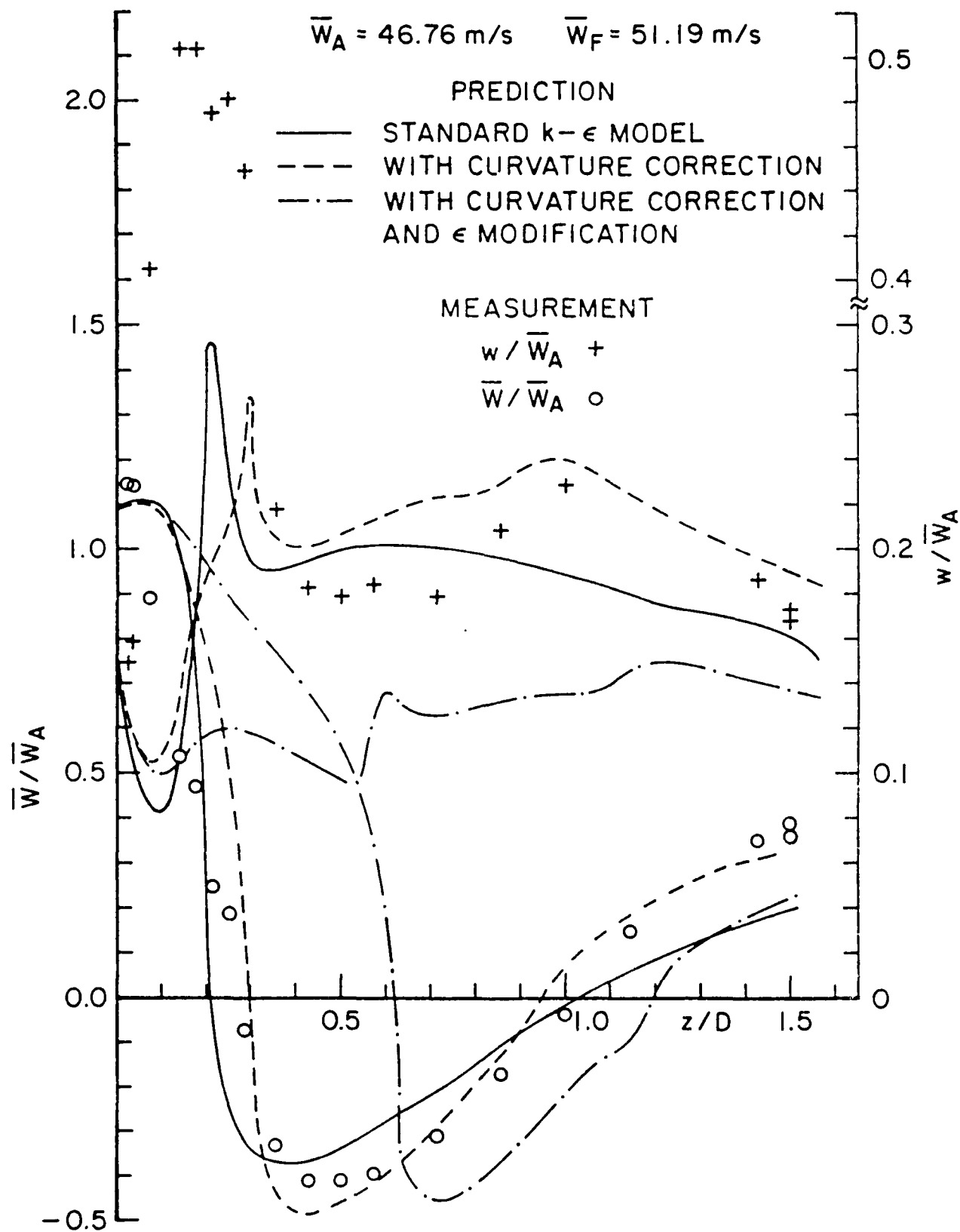


Figure 22. Measured (Lightman et al.<sup>2</sup>) and Predicted Centerline Mean and rms Axial Velocity for APL CBCC. Air Flow 2 kg/s and CO<sub>2</sub> Flow 6 kg/hr.

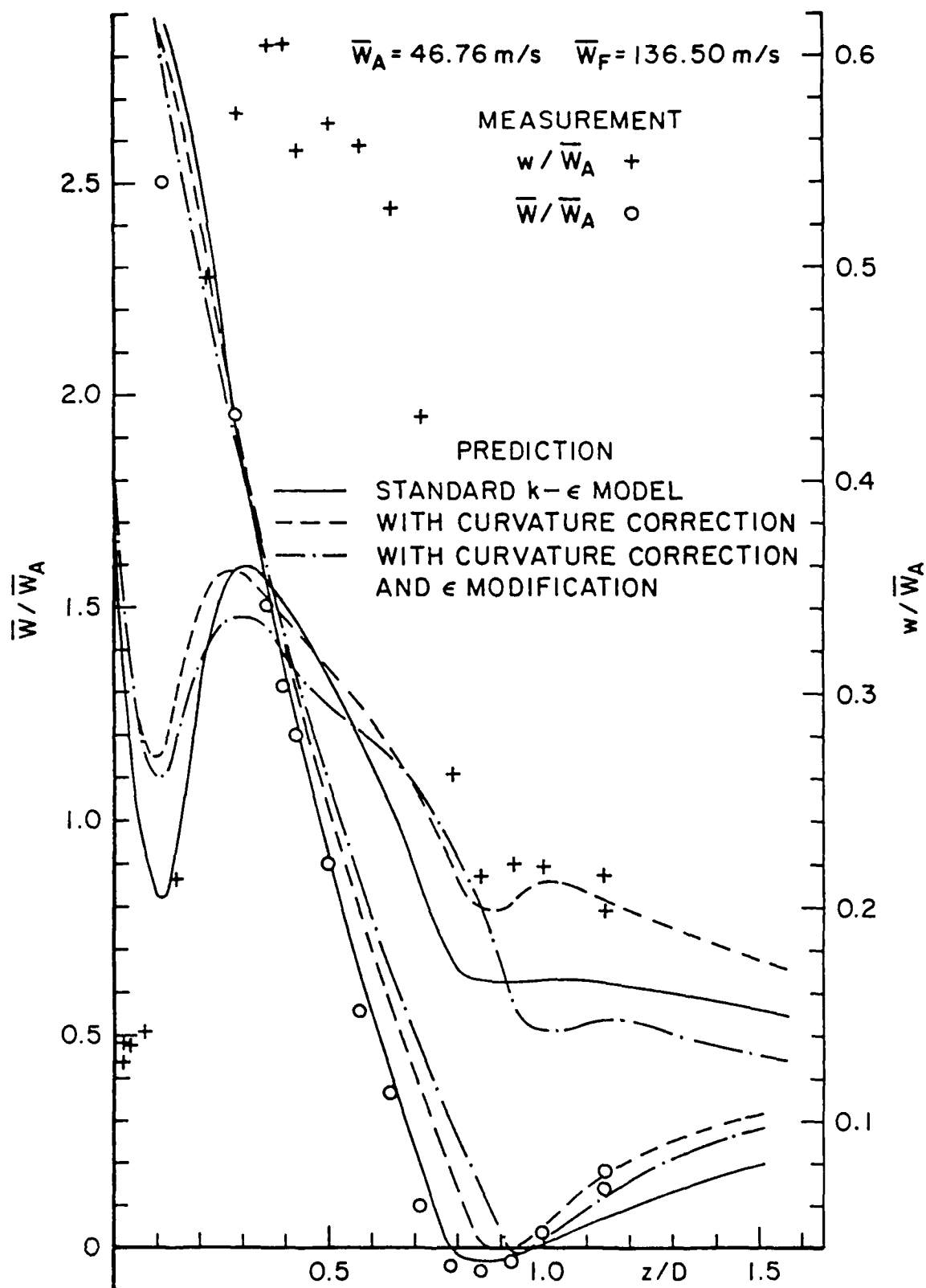


Figure 23. Measured (Lightman et al.<sup>2</sup>) and Predicted Centerline Mean and rms Axial Velocity for APL CBCC. Air Flow 2 kg/s and CO<sub>2</sub> Flow 16 kg/hr.

Figure 22 shows the FSP to occur at  $z/D = 0.28$  which more closely agrees with SS and KP in Figure 15 than did the earlier experimental data. A crucial difference in the two measurements which contributes to the appreciable difference in the observed FSP location is the central-jet exit configuration. Recent experiments employed a well-designed nozzle, thereby ensuring a uniform  $\bar{w}_F$ . Earlier experiments involved a straight tube 15 diameters in length upstream of the exit plane, resulting in a nonuniform  $\bar{w}_F$ . While this difference accounts for the decrease in the FSP location, the reason for the increase in the RSP location is not clear.

Predictions. In terms of the present predictions, a number of observations can be made. Calculations with  $c_u$  and  $\epsilon$  modifications are clearly inferior for all three  $\text{CO}_2$  flows in all respects. The fact that the three predictions do not differ significantly for 16 kg/hr reflects that the central jet essentially breaks through the recirculation region and does not suffer the large streamline curvature effects associated with the recirculating flow. At the lower  $\text{CO}_2$  flows, the dissipation modification significantly decreases the rms velocity. For the mean velocity, the zero  $\text{CO}_2$  case shows good agreement for the RSP and very poor agreement for the velocity profile in the reverse-flow region. For the 6 kg/hr  $\text{CO}_2$  case, while the magnitude of  $\bar{w}_m$  agrees reasonably well with the measured value, its location, as well as the locations of FSP and RSP, are all considerably overpredicted.

The differences in the predictions based upon standard  $c_u$  and curvature-corrected  $c_u$  are not clear cut. At 16 kg/hr, the uncorrected prediction for  $\bar{w}$  is superior, while the correction yields better  $w$  prediction, especially near the RSP (as may be anticipated). At 6 kg/hr, the correction again predicts  $w$  better near the RSP. For  $\bar{w}$ , except for the location of the RSP, the curvature correction appears to show better agreement with the measurement than the standard model. Both calculations underpredict the location of  $\bar{w}_m$ ; the magnitude is underpredicted by the standard model and overpredicted by the curvature

correction. For the zero CO<sub>2</sub> flow case, the uncorrected prediction appears to be better overall.

CO<sub>2</sub> Concentrations. Comparison of the predictions with the measurements (Bradley et al.)<sup>30</sup> of CO<sub>2</sub> mole fractions seen in Figures 24 and 25 leads to similar conclusions regarding the calculations. The prediction of the standard model is clearly superior at the higher flow rate. At 6 kg/hr, the standard model and the curvature correction do not appear to differ appreciably from each other. The predictions with the modifications of  $c_\mu$  and  $\epsilon$  show much slower decay of CO<sub>2</sub> centerline concentration than do the measurements and other predictions. This behavior is consistent with the significant underprediction of  $w$  and the slower decay of  $\bar{W}$  (noted especially for 6 kg/hr in Figure 22).

#### d. Conclusions

The numerical computations based upon the Reynolds-averaged equations and  $k-\epsilon$  turbulence model have demonstrated that the CBCC represents a highly complex turbulent flow. The predictions with the standard  $k-\epsilon$  model, as well as ad hoc modifications to account for the streamline curvature and the preferential influence of normal stresses on dissipation are compared with the measurements in a large-scale and a small-scale CBCC. Significant differences between the predictions are noted, especially for the dissipation-equation modification which results in much greater dissipation in the large-scale CBCC. The introduction of the curvature-corrected  $c_\mu$  results in better predictions for certain flowfield regions but exhibits a dependence on the annular and central flow rates.

### 3. VORTEX-CENTER CHARACTERISTICS

The time-averaged characteristics of the vortex center in the near-wake recirculation region in the CBCC by finite-difference computations are examined. The numerical predictions under isothermal conditions examine the influence of the turbulence-model corrections under varying annular air and central CO<sub>2</sub> flows on the axial and radial locations of the vortex

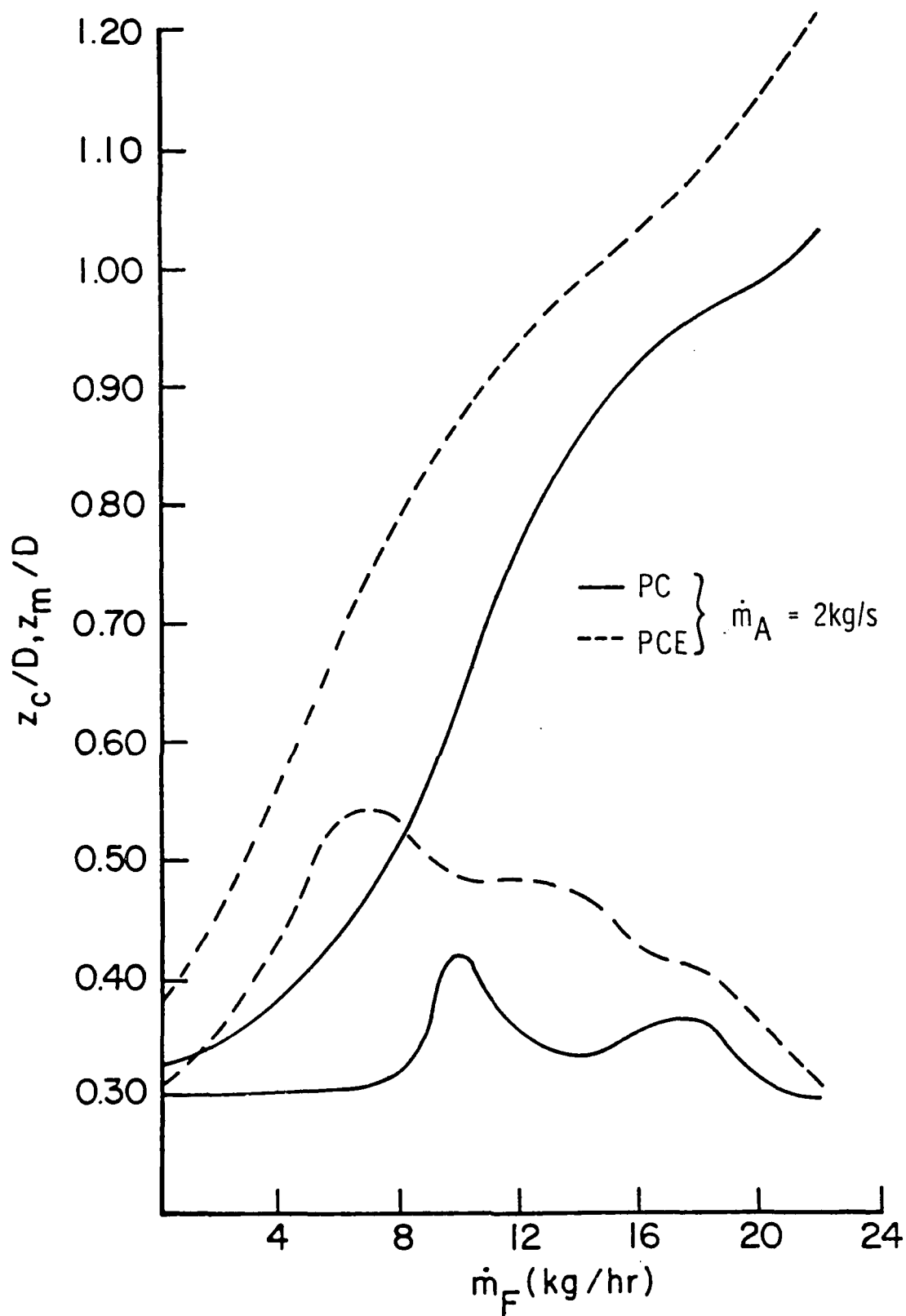


Figure 32. Axial Coordinate of Vortex Center and Minimum Centerline Velocity Variation with  $\text{CO}_2$  Flow (APL CRCC).

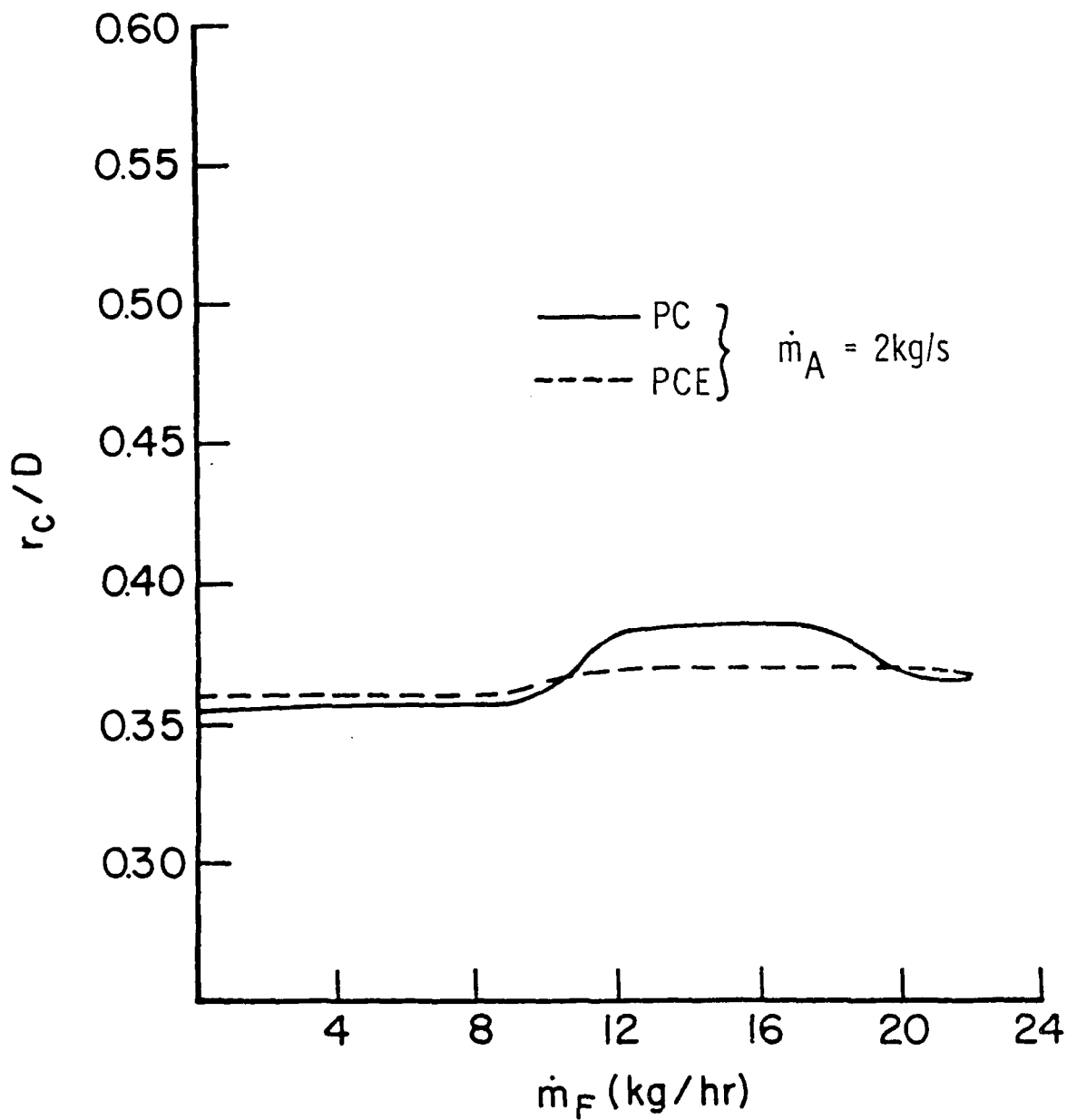


Figure 31. Radial Coordinate Variation with  $\text{CO}_2$  Flow (APL CBCC).



TABLE 4  
FLOWFIELD CONDITIONS

UCI			APL		
$\dot{m}_A \times 10^2$	$\bar{w}_A$	$Re_A \times 10^{-4}$	$\dot{m}_A \times 10^2$	$\bar{w}_A$	$Re_A \times 10^{-4}$
1.24	7.78	1.07	100	23.38	17.8
1.86	11.67	1.60	200	46.76	35.7
2.48	15.57	2.13	300	70.14	53.5
3.10	19.46	2.67	400	93.52	71.3
3.72	23.35	3.20	500	116.9	89.1
$(\dot{m}_F/\dot{m}_A) \times 10^3$	$\bar{w}_F/\bar{w}_A$	$Re_F/Re_A$	$\dot{m}_F \times 10^5$	$\bar{w}_F$	$Re_F \times 10^{-3}$
0.00	0.00	0.00	0	0.0	0.0
0.80	0.53	0.05	111	34.1	16.3
1.59	1.06	0.10	167	51.2	24.4
2.39	1.59	0.15	222	68.2	32.5
3.20	2.13	0.20	278	85.3	40.6
3.98	2.66	0.25	333	102.4	48.8
4.78	3.19	0.30	389	119.4	56.9
5.58	3.72	0.35	444	136.5	65.0
6.37	4.25	0.40	500	153.6	73.2
			556	170.6	81.3
			611	187.7	89.4

streamline-curvature corrections, and dissipation modifications [see Paragraph II.2.b(2)]. The range of the annular and central flow rates investigated for both the large- and small-scale CBCC's corresponds to all the flow regimes depicted in Figure 26. Table 4 lists the various characteristics of the flowfield for both the APL and UCI CBCC. The Reynolds number for the air flow  $Re_A$  is based on  $D$  and the reference velocity  $\bar{W}_d$  in the duct; the  $d$  and  $\bar{W}_F$  (See Figure 13). Variation in the  $CO_2$  flow conditions is due to the input parameters which were varied in the actual experiments (i.e., for UCI, the ratio  $\dot{m}_F/\dot{m}_A$  was varied, whereas for APL,  $\dot{m}_F$  was varied).

## b. Results and Discussion

### (1) APL Configuration

Figure 31 shows the relation between the normalized radial coordinate of the vortex center and  $CO_2$  flow rate. In what follows, the turbulence model with curvature correction is denoted as PC and the one with both curvature correction and dissipation modification is denoted as PCE. For both the PC and PCE models, the radial position stays approximately fixed at a value around 0.36. This is consistent with the preliminary results in Paragraph II.3.a(1) (which noted that for  $CO_2$  flow rates of 0 to 8 kg/hr and air flow rate of 2 kg/s the normalized radial coordinate is a constant of approximately 0.35). At a flow rate near 11 kg/hr, however, both models exhibit a slight increase in distance from the centerline. This move could be a result of the growing prominence of the central jet at  $CO_2$  rates of 12 to 16 kg/hr. (Reverse mass flow on the centerline disappears at 16 kg/hr with an annular flow rate of 2 kg/s.)

The slight movement of the radial coordinate is insignificant in comparison to the migration of the axial coordinate  $z_c$ , shown in Figure 32. In the region of centerline reverse flow, the axial coordinate moves gradually downstream with increasing  $CO_2$  flow, then migrates back toward the centerbody. The peak value of  $z_c$  occurs for a flow rate of

of zero central flow is 0.3 in both calculations. At the highest CO<sub>2</sub> flow rate, the FREP result is about 20 percent higher than the TEACH result. Since the TEACH calculations are based upon the physically more realistic k- $\epsilon$  turbulence model than the constant eddy viscosity model used in the FREP calculations, present results for the axial location of the vortex center may be more accurate. The identical value for the radial location, however, implies that the details of turbulence model do not have much effect on how far the vortex center is displaced off the centerline. This conclusion is consistent with the observation of Ko and Chan<sup>36</sup> that the radial position of the vortex center in their unconfined annular jet study was essentially independent of the momentum flux of the annular jet and hence the pressure available for the entrainment behind the centerbody face. For further implications of our results vis-a-vis those of Ko and Chan,<sup>36</sup> we recall our discussion in Reference 5.

## (2) Objectives of Present Study

The foregoing results were limited to the APL CBCC and only a small range of the central CO<sub>2</sub> flow rates for a fixed annular air flow rate was considered. Although these calculations dealt with isothermal flowfields, a detailed examination of the vortex center characteristics could offer additional insights into the phenomenon of flame stabilization. Accordingly, the main objective of the present study is a parametric investigation of the vortex center for varying air and CO<sub>2</sub> flow rates under different turbulence-model corrections in both APL and UCI CBCC's. A second objective is to examine the influence of the variations in flow rates, turbulence-model parameters, and combustor scaling on the magnitude and location of the minimum (which is negative when centerline flow reversal is present) centerline axial velocity.

## (3) Scope

This study deals with the time-averaged flowfield predictions and is based on certain modifications to the standard TEACH numerics. These include a power-law differencing scheme,

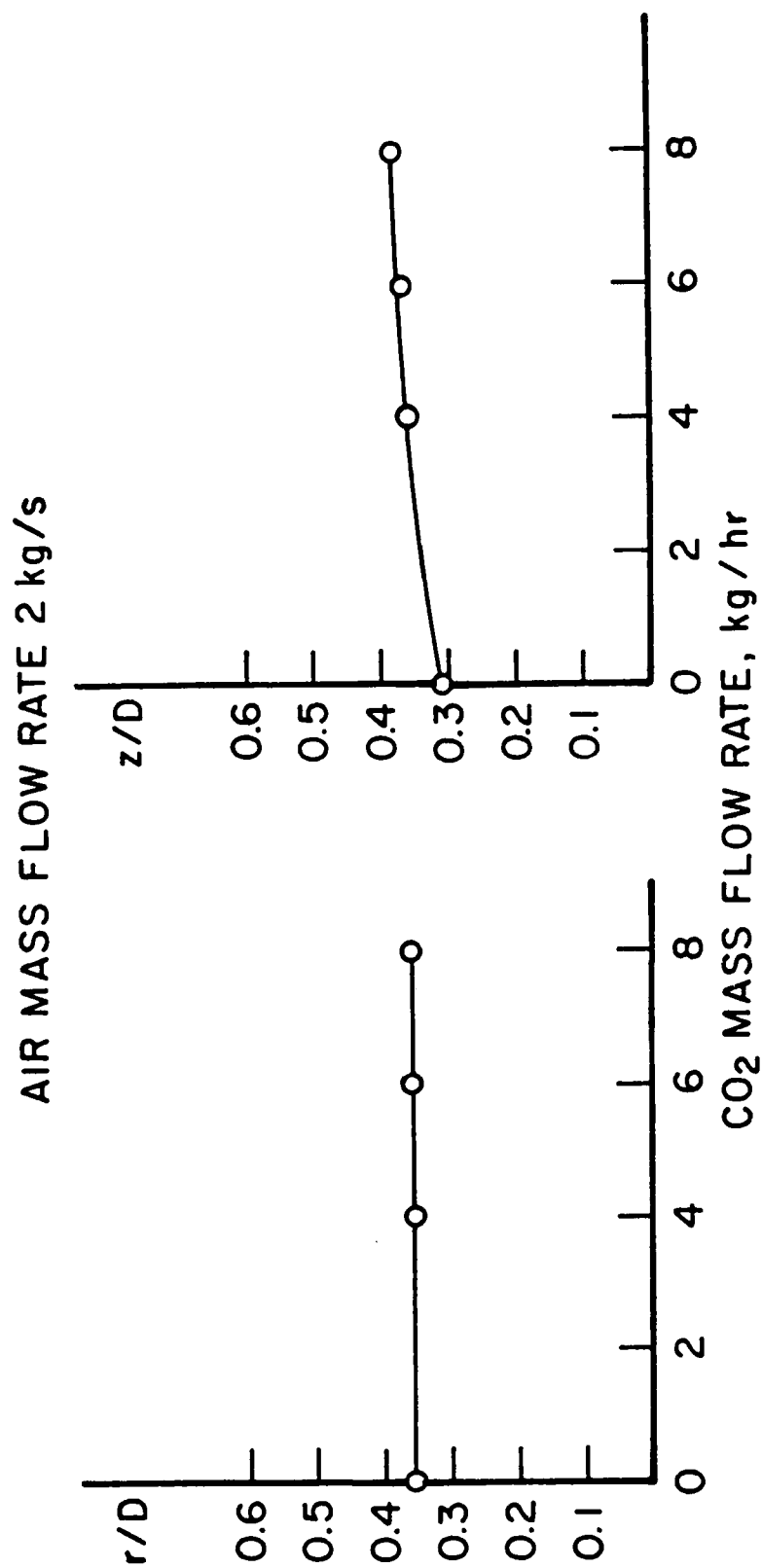


Figure 30. Normalized Locations of Air Vortex Center.

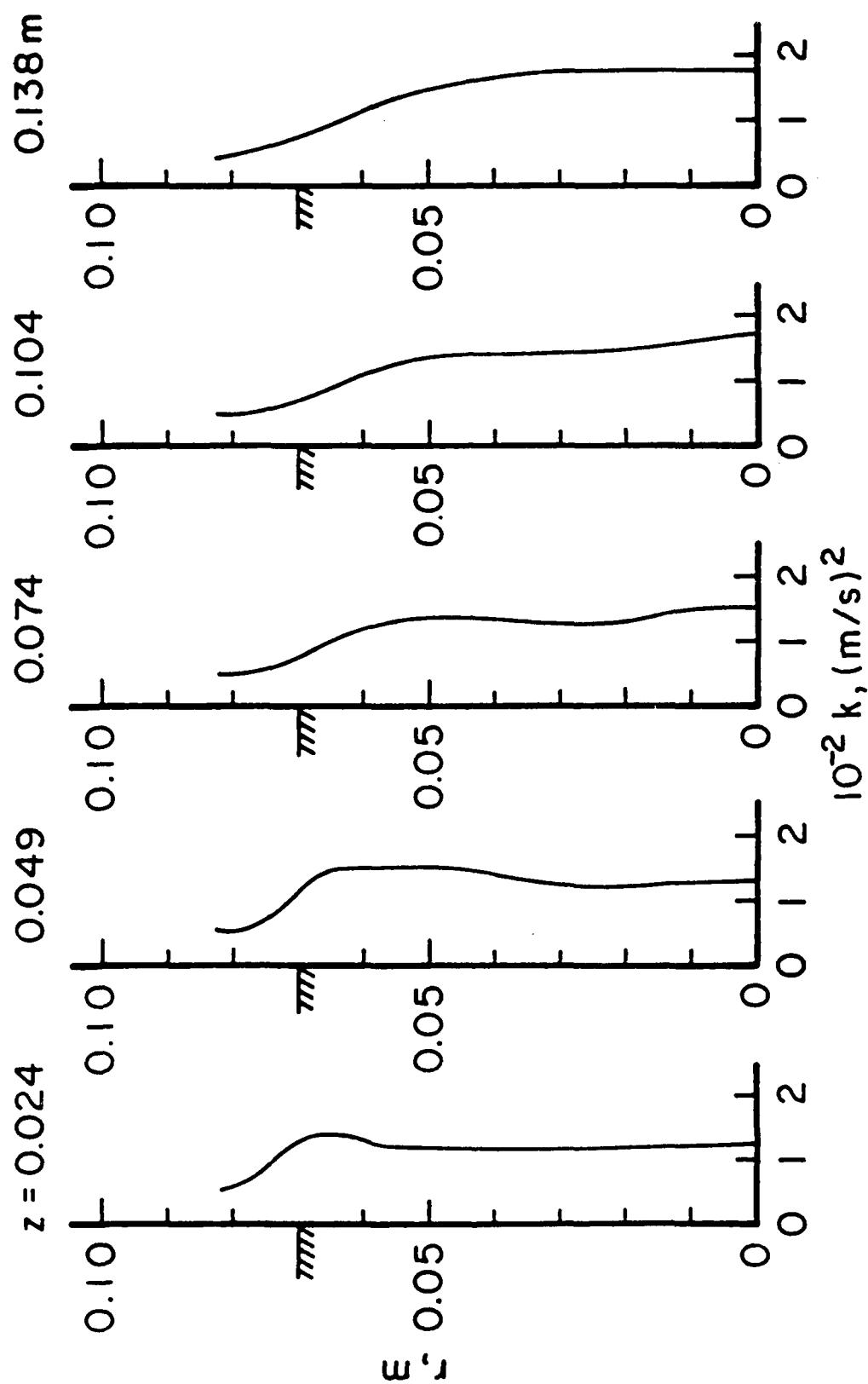


Figure 29. Radial Distribution of Turbulence Kinetic Energy at Different Axial Locations.



Figure 28. Distribution of Turbulence Kinetic Energy on Zero Axial Velocity Contour.

flux represents the positive axial flux contained between the zero velocity contour and the time-averaged separated streamline. In other words, the radially outward flux cannot cross the time-averaged separated streamline into the annular main flow.

The distribution of the turbulence kinetic energy on the zero velocity contour is shown in Figure 28. It is seen that the local maximum of the kinetic energy on the contour within the recirculation region occurs at the vicinity of the vortex center. An examination of the radial distribution of the kinetic energy at five axial locations shown in Figure 29 indicates that except for the axial location closest to the centerbody face, the turbulence kinetic energy peaks near the zero velocity contour. These observations appear to indicate that the time-averaged turbulence activity is highest along the zero axial velocity contour inside the recirculation region. It is physically reasonable to expect that the region of highest turbulence activity would represent the region of optimum mixing. Although the numerical computations reported here correspond to isothermal flowfields and do not necessarily apply to reacting flowfields, our current viewpoint has interesting implications for bluff-body flame stabilization.<sup>33-35</sup> It is tempting to associate the vortex center with a local hot spot (and temperature peak) and the zero velocity contour with the optimal region of flame propagation.

Time-Averaged Vortex Center. The radial and axial coordinates (normalized with respect to the centerbody diameter) of the vortex center for different central CO<sub>2</sub> flow rates are shown in Figure 30. We note that the radial location of the vortex center is invariant with CO<sub>2</sub> flow rate. The axial coordinate, however, is seen to increase slowly with CO<sub>2</sub> flow rate. A comparison of these results with those of our previous study<sup>5</sup> with the FREP code (which employed a constant value of turbulent eddy viscosity) shows the somewhat intriguing result that the predicted locations of the vortex center in both TEACH and FREP modeling are not much different. Indeed, the radial location is predicted as 0.35 by both codes. The axial location for the case

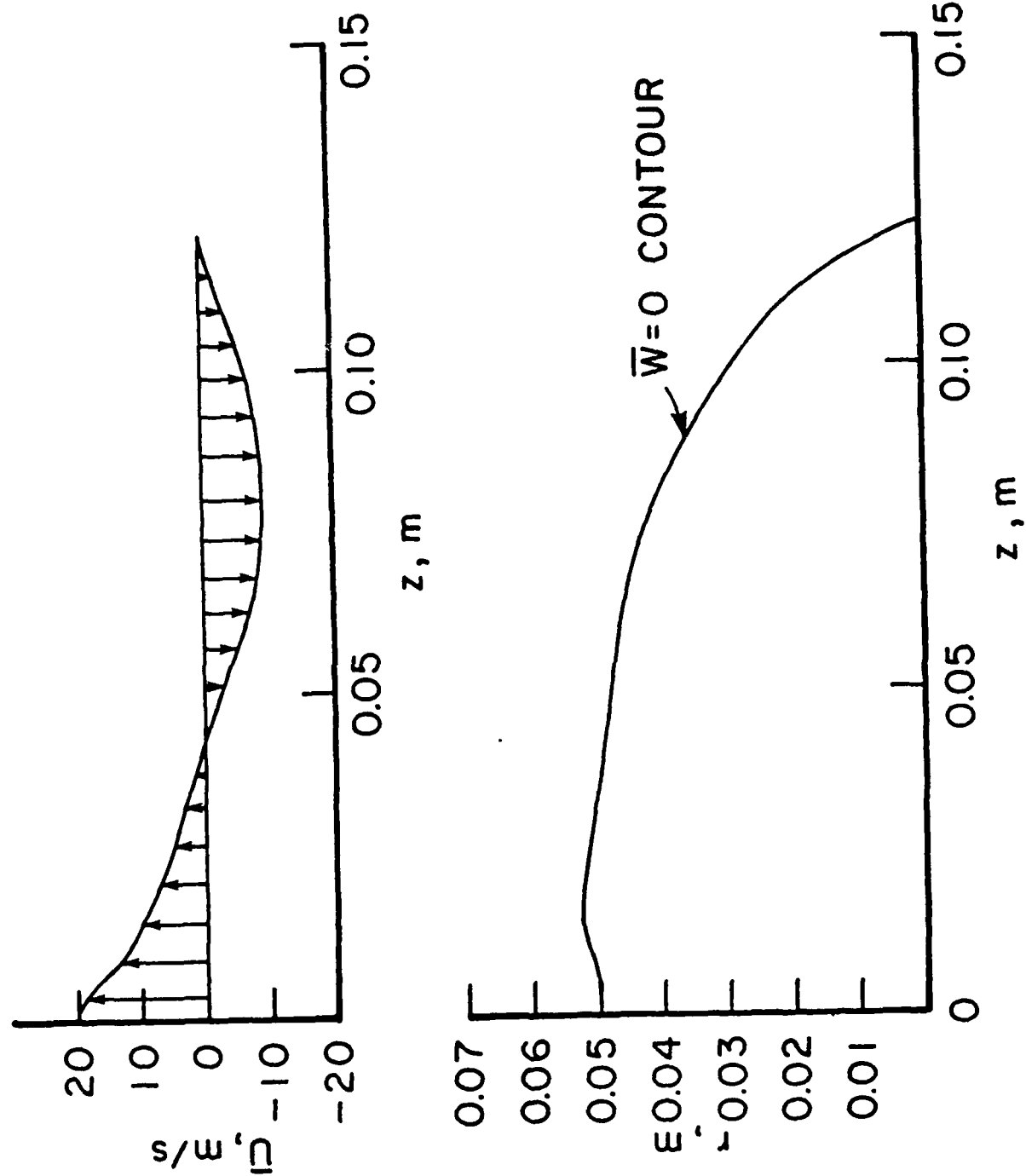


Figure 27. Zero Mean Axial Velocity Contour and Mean Radial Velocity Distribution Thereon.



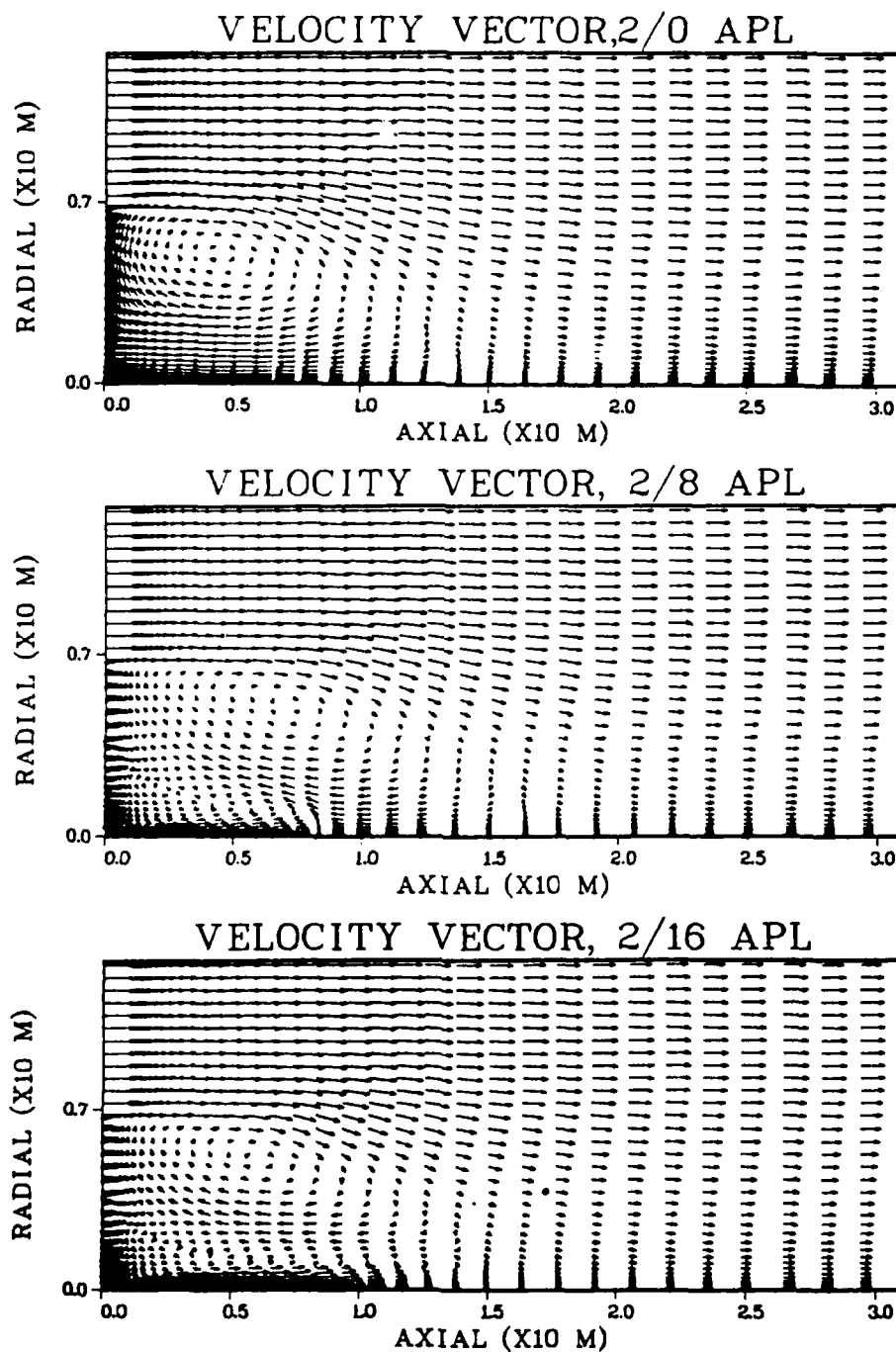


Figure 26. Velocity Vector Plots for APL CBCC.

center, as well as on the magnitude and location of the minimum centerline axial velocity. These results emphasize and clarify the complex flowfield interactions of the annular and central streams in the near-wake region.

a. Recirculation-Zone Structure

The nature of the toroidal recirculating vortex in the CBCC is illustrated in Figure 26 which shows the computed velocity field in the APL CBCC. The computations involve annular air flow and central CO<sub>2</sub> flow, with the figure depicting the flowfields corresponding to (a) no central flow, (b) small central flow, and (c) large central flow. The recirculation region comprises two toroidal vortices: a primary vortex and a smaller secondary vortex near the central jet. The relative sizes of these vortices and the locations of the vortex centers are dependent upon the annular and central flow rates and the resulting degree of mixing and entrainment present in the system. At zero or small central flow, the annular flow is dominant, entraining the CO<sub>2</sub> flow and causing a flow reversal along the centerline. As the strength of the central jet increases, it gradually overcomes the centerline reverse flow, and the secondary vortex grows relative to the primary vortex. Eventually the central jet becomes strong enough to eliminate the centerline reverse flow entirely and starts to entrain the annular flow. Off centerline reverse flow and primary vortex are still present, the latter at diminished strength however.

(1) Preliminary Studies

Associated with the primary vortex is the time-averaged contour of zero mean axial velocity. Figure 27 presents this contour and the mean radial velocity ( $\bar{U}$ ) distribution thereon for the case of zero central flow. The point of zero radial velocity on the contour is the vortex center. As may be expected on physical grounds, the flow is radially outward to the left and radially inward to the right of the vortex center on the zero velocity contour. Note, however, that the radially outward mass

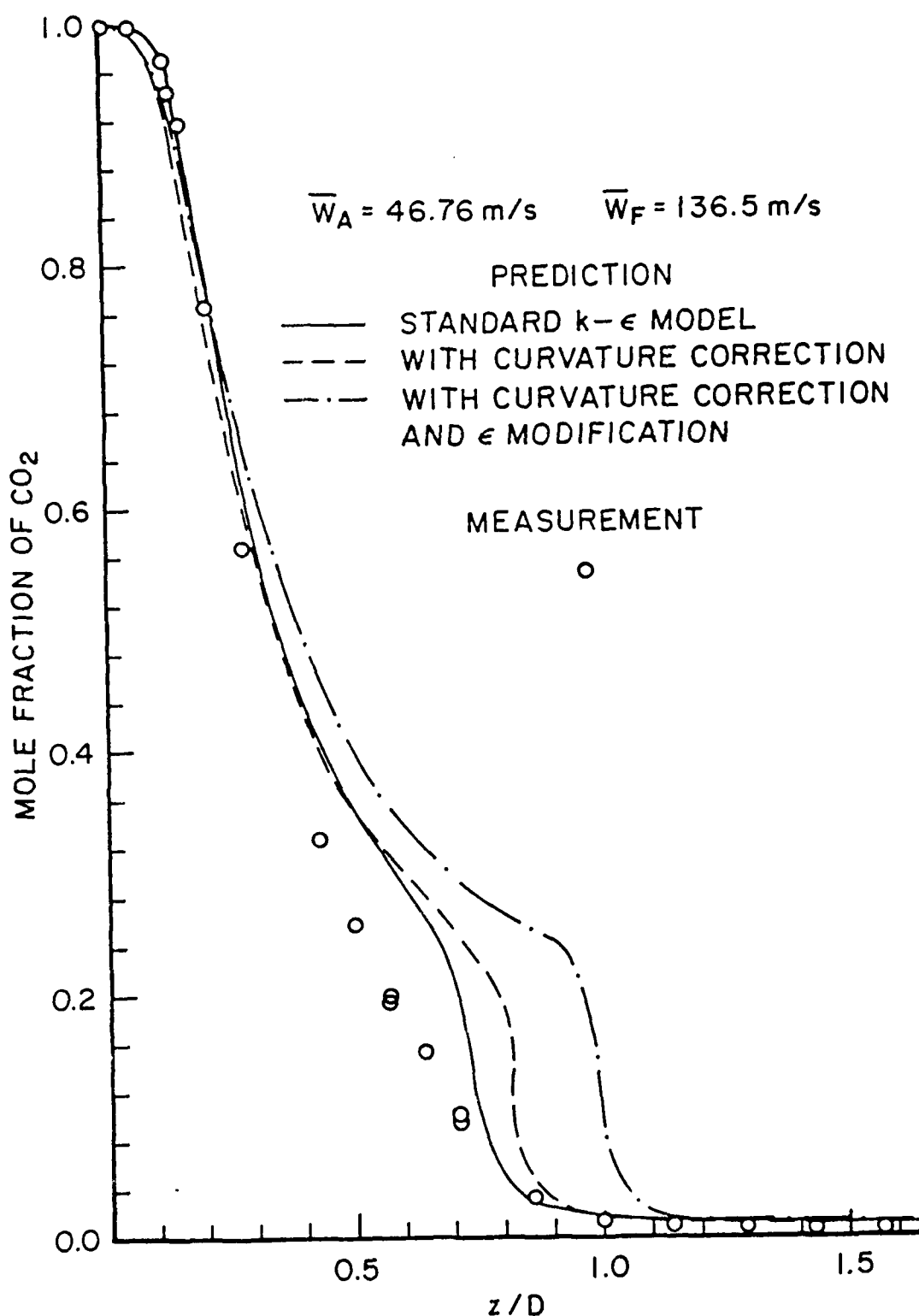


Figure 25. Measured (Bradley et al.<sup>30</sup>) and Predicted Centerline CO<sub>2</sub> Mole Fraction for APL CBCC. Air Flow 2 kg/s and CO<sub>2</sub> Flow 16 kg/hr.

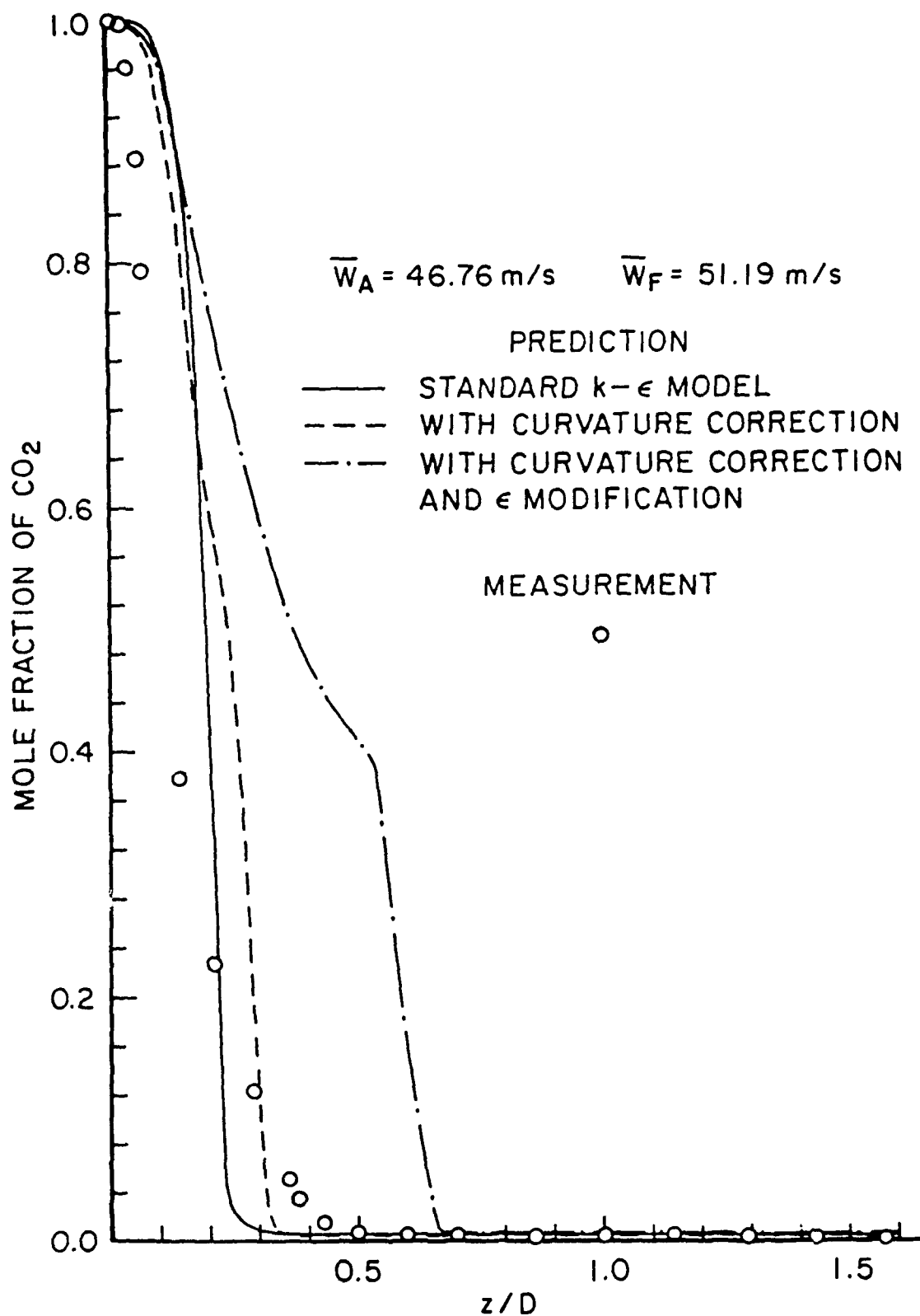


Figure 24. Measured (Bradley et al.<sup>30</sup>) and Predicted Centerline CO<sub>2</sub> Mole Fraction for APL CBCC. Air Flow 2 kg/s and CO<sub>2</sub> Flow 6 kg/hr.

7 kg/hr for PCE and 10 kg/hr for PC. This result can be explained by the competition between the annular and central flows. As the dominance of the central flow increases, the entrainment by the annular flow gradually diminishes and eventually the annular flow begins to get entrained by the central flow rather than the converse, which is true at low CO<sub>2</sub> flows. It is here that  $z_c$  peaks and the primary vortex (and its center) is pushed downstream. When entrainment of the annular flow begins, the primary vortex is pulled toward the centerbody. Near the point at which negative centerline flow disappears (around 16 kg/hr), a secondary peak is also found for  $z_c$ . It appears that the detachment of the primary vortex from the centerline promotes a small downstream motion of the vortex center. After this peak is reached, all increases in CO<sub>2</sub> flow draw the primary vortex center toward the centerbody.

While the general trend of the path of the vortex center is consistent between the PC and PCE models, the actual magnitude of the axial coordinates and the precise location of the peaks vary. The PCE model tends to predict values further downstream than the PC model. This same trend is evident in the location of the minimum centerline velocity ( $z_m$ ). This location steadily moves downstream with increasing CO<sub>2</sub> flow, although the actual magnitude of  $z_m$  is dependent upon the presence of the dissipation modification. According to Paragraph II.2.c(3), the PC model tends to predict the minimum velocity location and magnitude more accurately for the APL CBCC.

If air flow rate is varied, holding CO<sub>2</sub> flow rate constant, the radial coordinate of the vortex center again remains fixed near 0.36 at CO<sub>2</sub> flow rates of 0 and 6 kg/hr (see Figure 33). This result is consistent with the findings of Ko and Chan<sup>36</sup> that in their unconfined annular jet the radial position of the vortex center is not dependent on the annular momentum flux. In fact, the radial coordinate normalized by the duct diameter is 0.19 and this compares very well with the value of 0.18 reported by Ko and Chan. Their results for no central flow and increasing annular

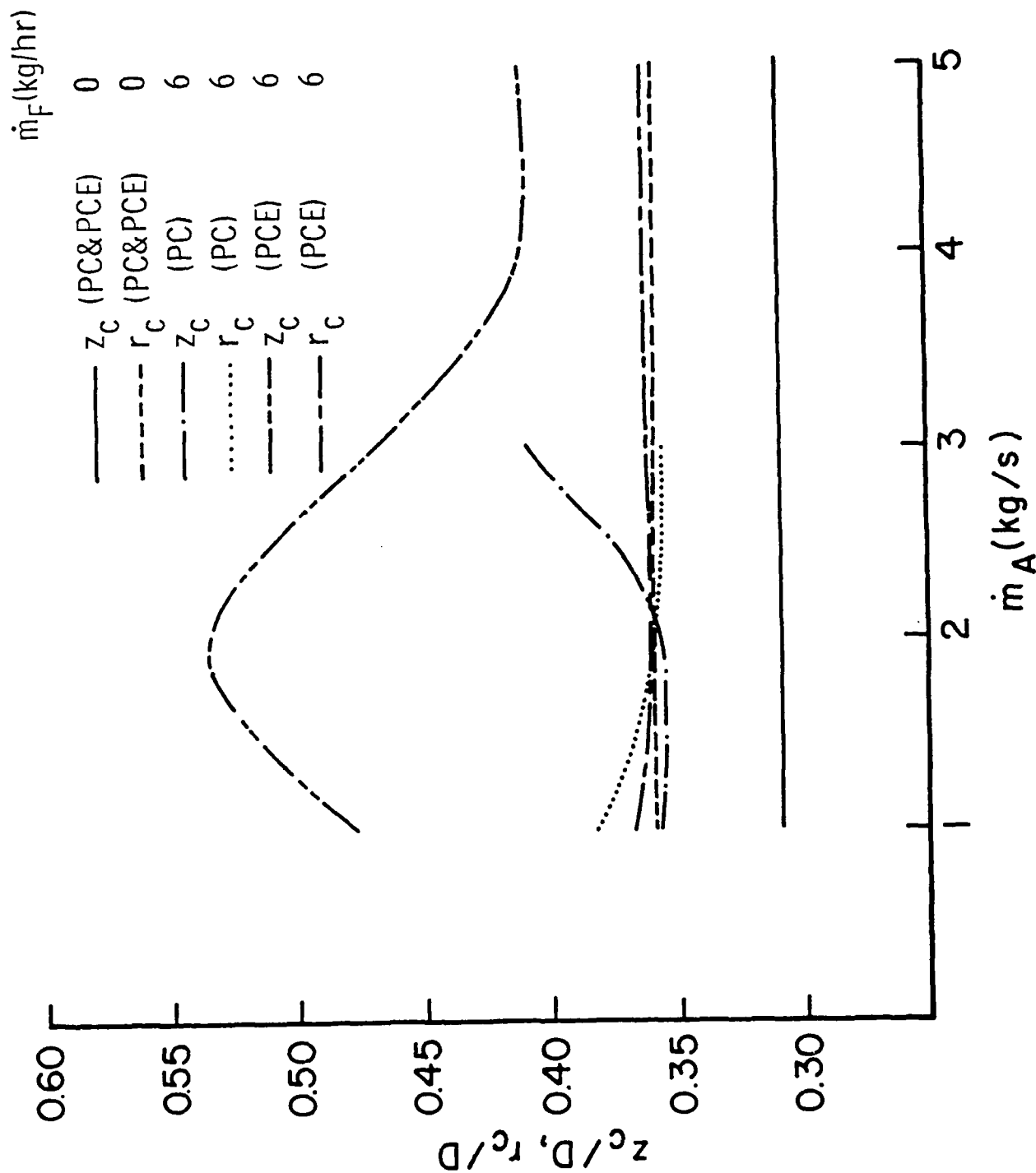


Figure 33. Axial and Radial Coordinates of Vortex Center Variation with Air Flow (APL CRCC).

flow, however, show a shift of the vortex center toward the centerbody. This study, on the other hand, demonstrates no change in the axial position of the vortex center with increasing air flow and no CO<sub>2</sub> flow. The differences may be explained by noting that Ko and Chan used an unconfined jet. Such a configuration allows for ambient air entrainment at the annular jet, something which a ducted CBCC cannot provide. With the addition of the central jet, however, the extra potential for entrainment is present, thus giving results similar to those of Ko and Chan (i.e., a movement of the axial coordinate toward the centerbody with increased annular flow). At lower annular flows, entrainment of the annular jet by the central jet is a more prominent feature, thus causing the vortex center to be located upstream of the vortex center at higher air flows.

## (2) UCI Configuration

Figures 34 and 36 reinforce the APL results [discussed in II.3.b(1)] in that the radial coordinate of the vortex center is essentially fixed at approximately 0.36, regardless of CO<sub>2</sub> and air flow rates. Once again, a slight increase in distance from the centerline is observed as the CO<sub>2</sub> flow rate approaches the point of elimination of negative centerline velocity. This shift could be caused by the elongation and lifting of the primary vortex from the centerline.

Figure 35 shows that the variation of the axial coordinates as predicted by the PCE model follows the same trend as in the APL case. The first peak occurs consistently (for both APL and UCI PCE models) at a  $\bar{W}_F/\bar{W}_A$  ratio of approximately 1.3. The secondary peak occurs at a  $\bar{W}_F/\bar{W}_A$  ratio of approximately 2.6. The uniformity at this point is not as strong, however. The general trend for the variance of  $z_c$  with  $\dot{m}_F$  is that with increasing air flow, the peak values of  $z_c$  are less pronounced, due to the increased prominence of the annular jet. Results from the PC model (not shown) concur with those of the PCE model. The values for the location of the minimum centerline

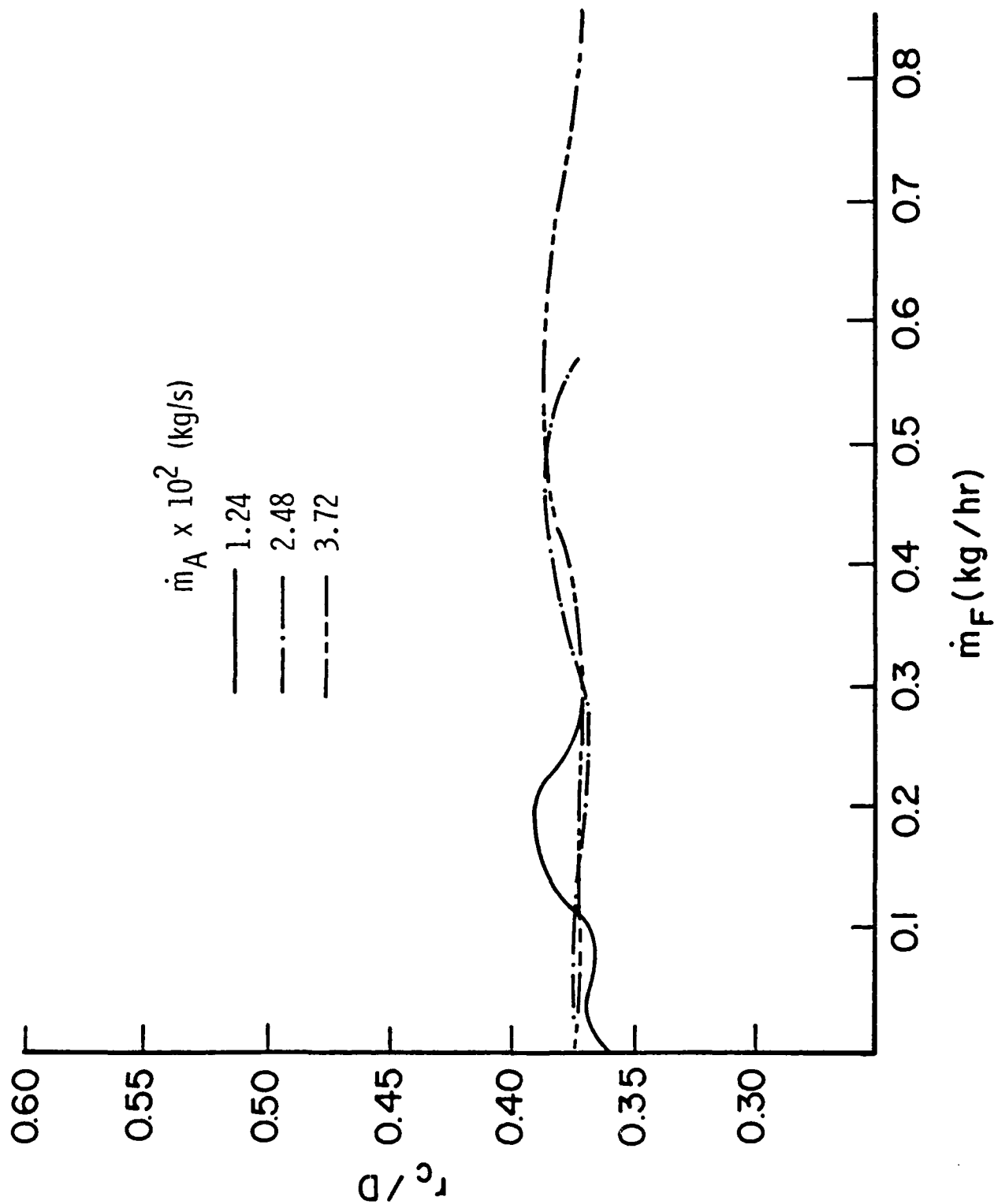


Figure 34. Radial Coordinate Variation with CO<sub>2</sub> Flow (UCI CRCC)  
 - PCF Model.



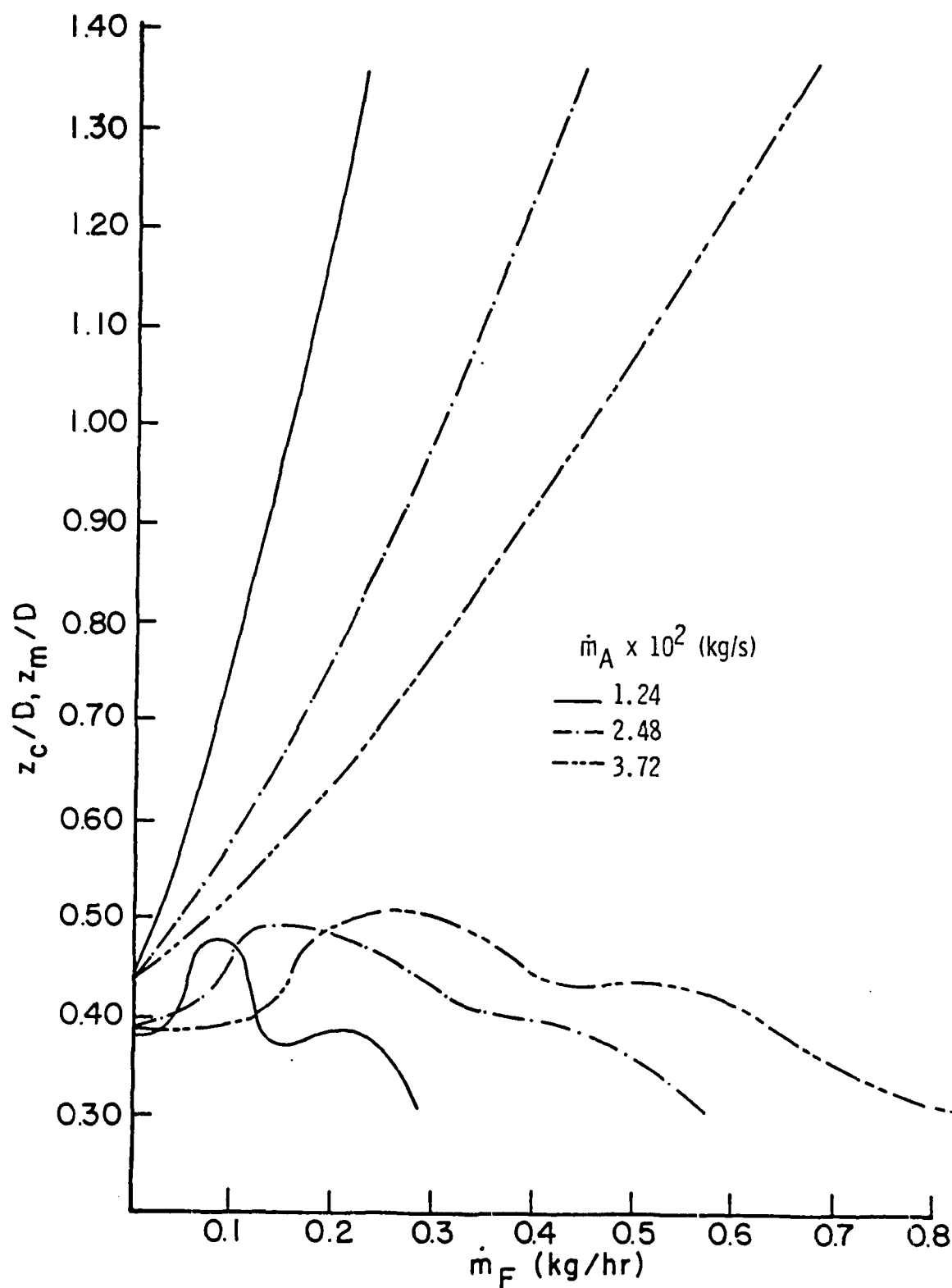


Figure 35. Axial Coordinate of Vortex Center and Minimum Centerline Velocity Variation with CO<sub>2</sub> Flow (UCI CBCC) - PCE Model.

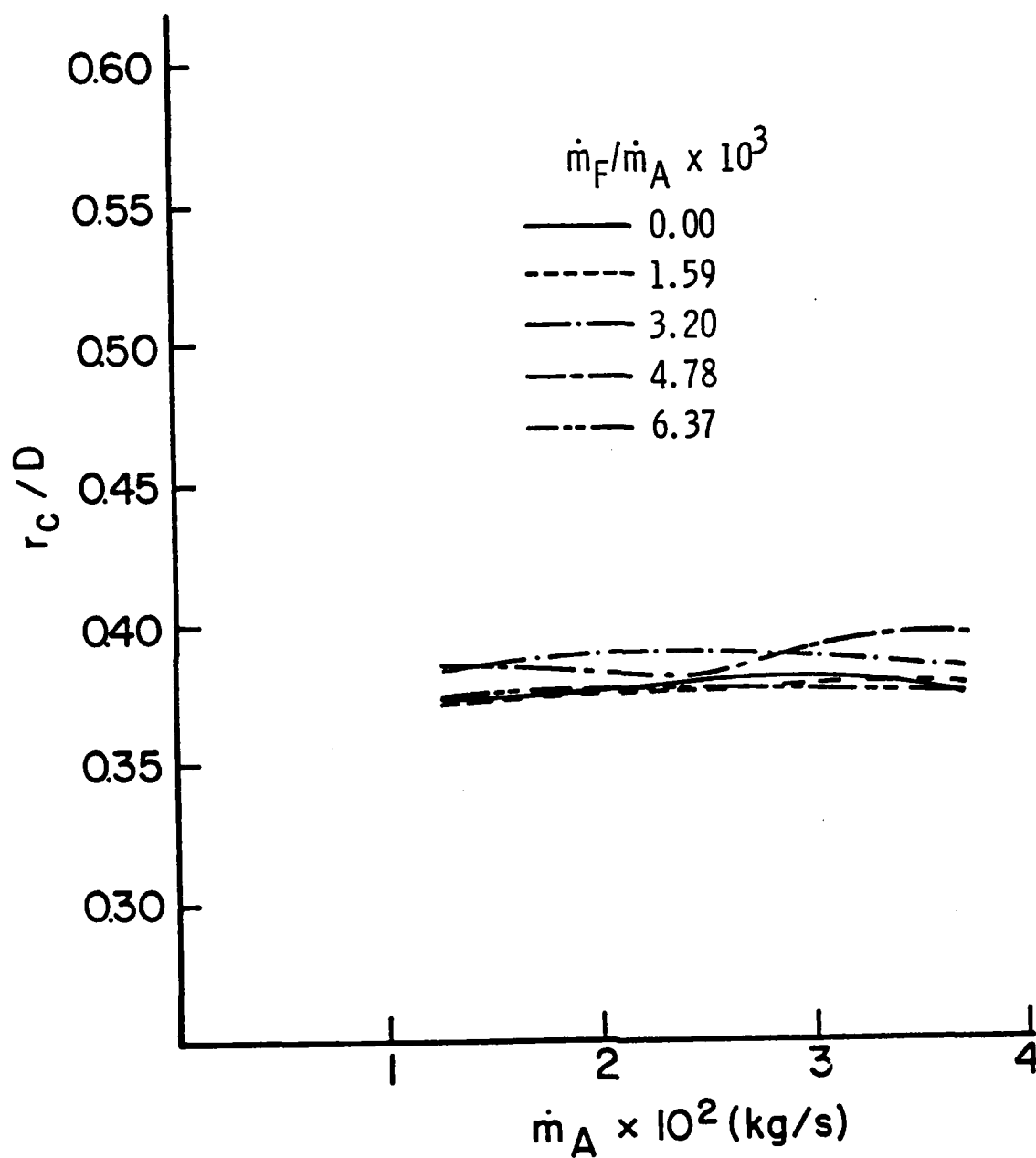


Figure 36. Radial Coordinate of Vortex Center Variation with Air Flow (UCI CRCC) - PC Model.

velocity, also shown in Figure 34, confirm the APL results in that  $z_m$  is nearly linearly dependent upon the  $\text{CO}_2$  flow rate. An increase in annular flow, as expected, pushes the  $z_m$  value closer to the centerbody. A graph of  $z_m/D$  versus  $\bar{W}_F/\bar{W}_A$  (not shown) would reveal that the results for all the three air flows (7.8, 15.6, and 23.4 m/s) essentially coincide.

Figure 37 presents the variation of the axial coordinate of the vortex center with annular air flow. The  $z_c$  value is essentially constant for low  $\text{CO}_2$  rates, analogous to the 0 kg/hr  $\text{CO}_2$  flow in APL (see Figure 32), but at a higher value of 0.38 compared to 0.36 for APL. At higher  $\text{CO}_2$  flow rates, the trends are not similar to those of the APL CBCC. One possible explanation is the difference in the  $\bar{W}_F/\bar{W}_A$  ratios. In the APL configuration, the ratios ranged from 0.44 to 0.73 in the region which exhibited a decrease in  $z_c$  with increased air flow. The one point which appeared to be dominated by central flow had a  $\bar{W}_F/\bar{W}_A$  of 2.19. All of the points of the UCI curves at the three higher  $\text{CO}_2$  flows have the  $\bar{W}_F/\bar{W}_A$  values of 2.13 or higher.

### (3) Comparative Study

Figures 38 and 39 demonstrate the correlation between the APL and three  $\text{CO}_2$  flow rates of UCI. The normalized minimum centerline velocity as a function of normalized central flow has, for the most part, a constant relationship in all runs (see Figure 38). The ratio between  $z_m$  and  $z_c$ , shown in Figure 39, appears consistent among all runs when compared to the ratio of the inlet flow velocities, although these results do not coincide as well as those in Figure 38. Similar trends can be seen between the PC and PCE models in both correlations, though for each case only one model is shown. This relation between the minimum centerline velocity and vortex center location could prove helpful in experimental techniques where inlet flow rates and centerline velocities are easier to measure than is the vortex center location.

The results from this study extend the preliminary results in Figure 30 and, as noted in Paragraph II.3.a.(1), appear to

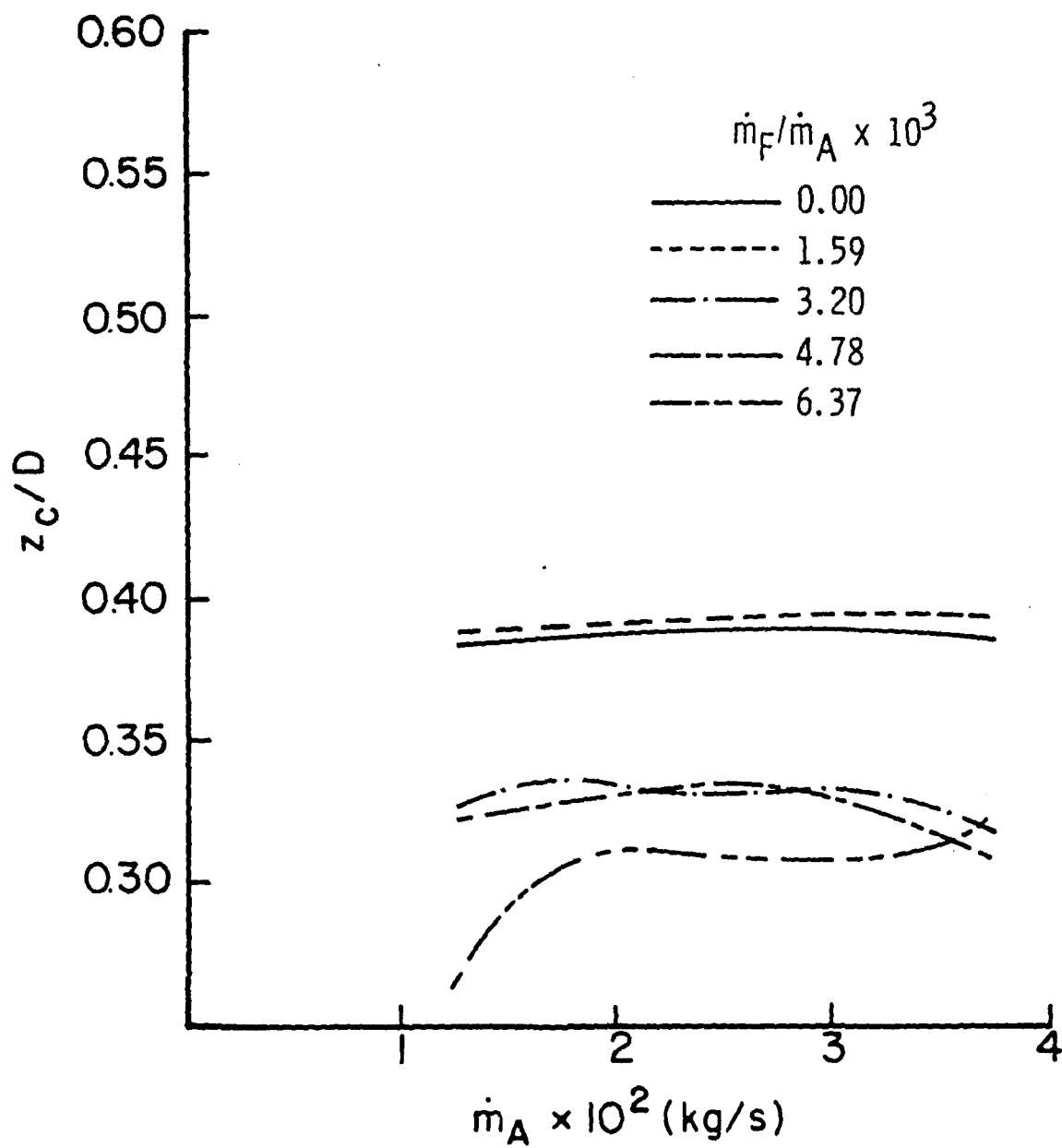


Figure 37. Axial Coordinate of Vortex Center Variation with Air Flow (UCI CBCC) - PC Model.

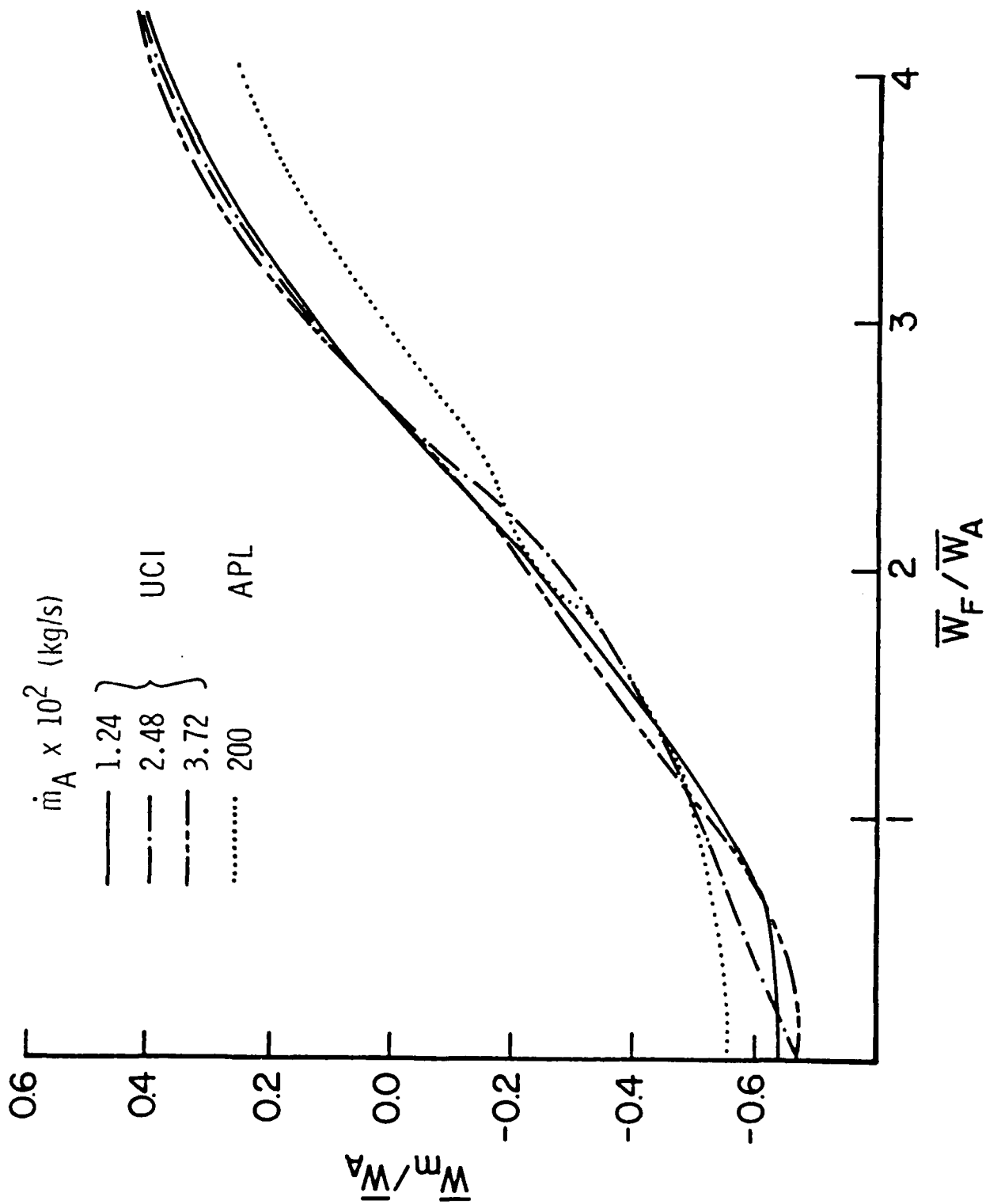


Figure 38. Relationship of Minimum Centerline Velocity and Central Jet Flow (APL and UCI CBCC) - PC Model.

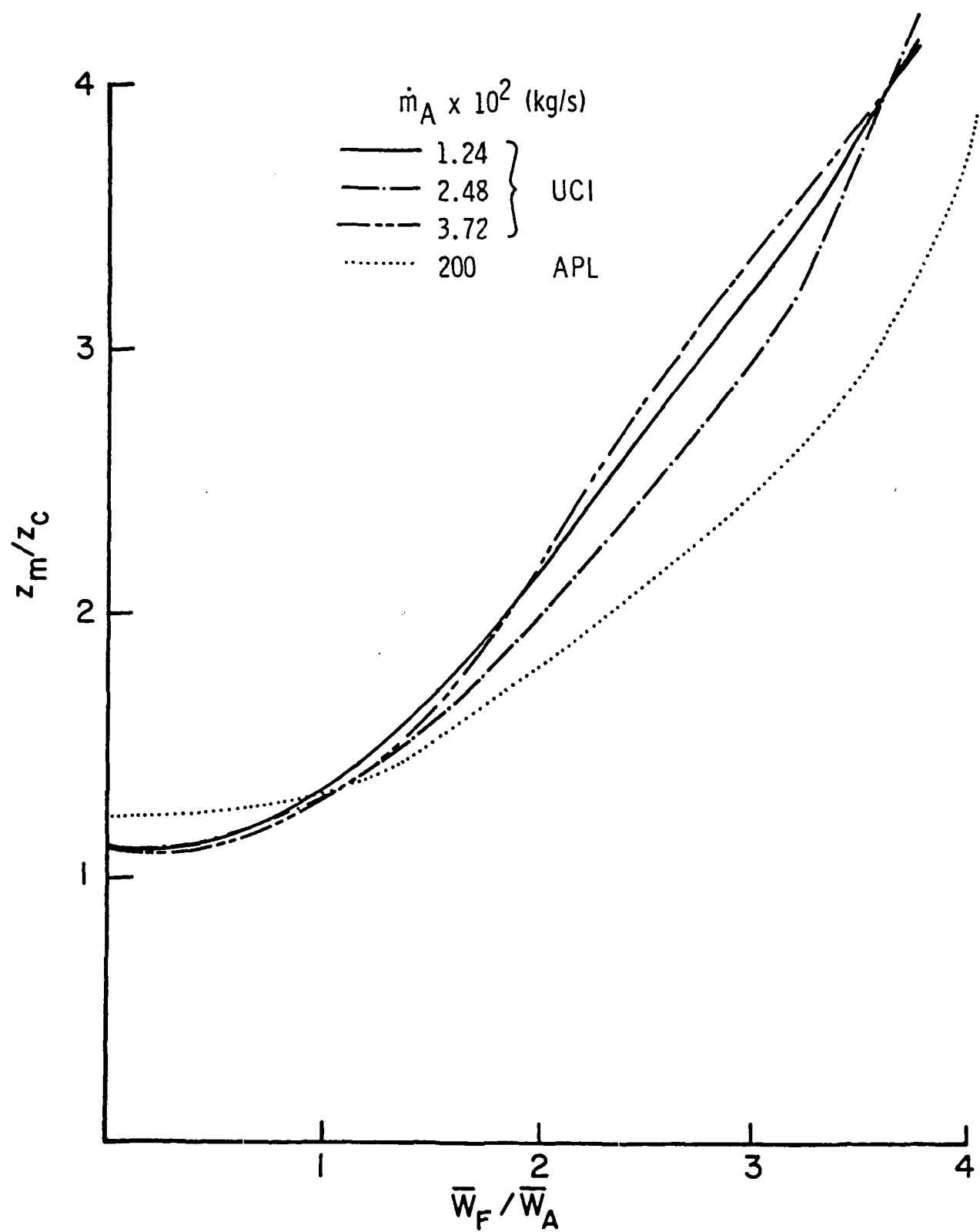


Figure 39. Relationship of Axial Location of Minimum Centerline Velocity and Central Jet Flow (APL and UCI CBCC) - PCE Model.

coincide with those of a previous study on primary vortex characteristics by Krishnamurthy.<sup>5</sup> Using the Field Relaxation Elliptic Procedure (FREP) Code, Krishnamurthy obtained the constant value of 0.35 for the normalized radial coordinate at various central jet flows. Also, the axial coordinate of the vortex center moved downstream with increased central flow in the range observed (0 to 8 kg/hr CO<sub>2</sub> flow and 2 kg/s air flow). In a later investigation, Krishnamurthy, et al.<sup>3</sup> compared the results of the standard TEACH code to the experimental results of Lightman, et al.<sup>2</sup> for annular flow of 2 kg/s and no central jet. The radial again was found to be consistent at a  $r/D$  value of 0.35, in agreement with present results. For the axial coordinate, however, the standard TEACH code considerably underpredicted the location of the vortex center as compared to the experimental data (see Table 5).

TABLE 5. AXIAL COORDINATE OF VORTEX CENTER IN VARIOUS MODELS (APL CBCC).

Model	Normalized Axial Location
Experiment <sup>2</sup>	0.43
FREP <sup>5</sup>	0.30
TEACH (standard) <sup>3</sup>	0.26
TEACH-PC	0.31
TEACH-PCE	0.31

All of the previous and present studies have underpredicted the axial location of the vortex center to some degree. Streamline-curvature correction and dissipation-equation modification have provided the closest approximations thus far to the experimental results. With the central jet added, the general trend has been that the PCE Model predicts a vortex center location further downstream than the PC model. This indicates that better agreement with experimental results for increased CO<sub>2</sub> flow is likely with the PCE model.

### c. Conclusions

The radial coordinate of the primary vortex center remains essentially constant regardless of air or CO<sub>2</sub> flow rates. The axial coordinate moves downstream with increasing central flow and constant annular flow until entrainment of air by CO<sub>2</sub> begins; then  $z_c$  migrates toward the centerbody. With changing air flow and zero CO<sub>2</sub> flow, the axial coordinate stays constant. The addition of central flow causes  $z_c$  to shift toward the centerbody, if the annular jet is dominant. The differences between the UCI and APL combustors are seen mostly in the magnitude of the variables; normalization shows the same overall trends preserved between the two, although not exactly.



## SECTION III

### TIME-DEPENDENT COMPUTATIONS

This section deals with the calculation of the CBCC flowfield by the solution of the time-dependent Navier-Stokes equations using the AFWAL/FIMM unsteady code.

#### 1. INTRODUCTION

Proper specification of boundary conditions is critical to the numerical solution of subsonic flowfields. This section presents a systematic study of the influence of various inflow and outflow boundary conditions for the numerical solution of the time-dependent Navier-Stokes equations. Combinations of several representative inflow and outflow boundary conditions are applied to obtain the solution of subsonic unsteady flow in a centerbody combustion chamber of finite computational domain. The absence of solutions of nonlinear boundary value problems of this class is explained both by the difficulties in constructing models of unsteady subsonic flows of a viscous gas in a finite region (due to the specific requirements imposed on the boundary conditions), and by the problem of correct resolution of the acoustic processes by the difference scheme. For subsonic flow, the propagation of disturbances upstream against the flow direction complicates the situation significantly and requires more care in the choice of inflow and outflow boundary conditions. Following the approach of Reference 37 the acoustic characteristics of various boundary conditions are investigated, which enables one to study their effect on the longitudinal oscillations in the domain of interest. In contrast to subsonic flow, supersonic flow leaves little choice in the selection of the boundary conditions and all physical variables should be specified at the inflow boundary and none at the outflow boundary.

At a subsonic inflow boundary, the Navier-Stokes equations require the specification of three boundary conditions and the

subsonic outflow boundary requires the specification of only one boundary condition. Therefore, in the numerical solution of the problem the variables at the boundary points must be calculated by introducing additional difference algorithms, containing to some degree elements of spatial extrapolation from the interior points of the domain. Various extrapolation procedures of the type  $(\partial\phi/\partial\eta)^{n+1} = 0$  or  $(\partial^2\phi/\partial\eta^2)^{n+1} = 0$  can be used to compute the additional unspecified physical variables required by the finite-difference scheme at the boundaries (here  $\eta$  is in the direction normal to the the boundary and  $n$  corresponds to the the time step). However, there is no rigorous mathematical theory available to justify such extrapolation procedures.

## 2. BOUNDARY CONDITIONS

In what follows various inflow boundary conditions and their finite-difference analogues are described and the boundary conditions are applied at both the predictor and corrector steps of MacCormack's finite-difference algorithm. The conditions are described only for the  $(n+1)$  corrector step. The procedure for the  $(n+1/2)$  predictor step is identical to the  $(n+1)$  corrector step, with the time step superscripts  $(n+1; n+1/2)$  replaced by  $(n+1/2; n)$ . The subscripts denote the  $x$  (axial) and  $r$  (radial) grid indices and  $KL$  is the last grid index in the  $x$  direction.

### a. Inflow Boundary Conditions

The following paragraphs discuss the various combinations of the boundary conditions at the inlet.

#### (1) Boundary Conditions due to Serra

Serra<sup>38</sup> suggests the use of total pressure, total temperature, and flow angle at the inflow boundary for successful modeling of internal gas flows.

$$P_t, T_t, V = 0 \text{ and } \frac{\partial U}{\partial x} = 0 \quad (8)$$

AD-A153 682

TIME-AVERAGED AND TIME-DEPENDENT COMPUTATIONS OF  
ISOTHERMAL FLOWFIELDS IN: (U) DAYTON UNIV OH RESEARCH  
INST L KRISHNAMURTHY ET AL. DEC 84 UDR-TR-84-88

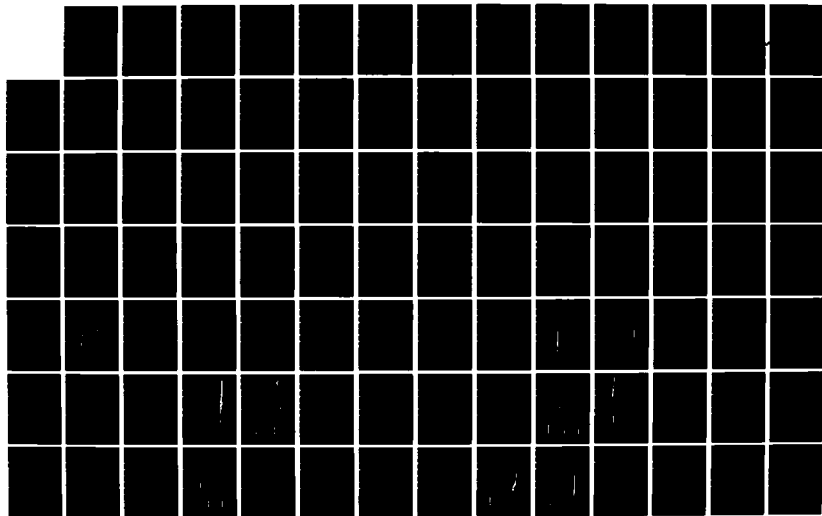
2/3

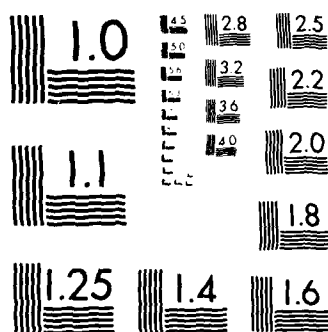
UNCLASSIFIED

AFWAL-TR-84-2081 F33615-82-K-2252

F/G 20/4

NL





MICROCOPY RESOLUTION TEST CHART  
NATIONAL BUREAU OF STANDARDS 1963-A

The finite-difference formulation of Eq. (8) is given by

$$T_{1,j}^{n+1} = T_t - (\gamma-1) [U_{1,j}^{n+1}]^2 / (2\gamma R) \quad (9)$$

$$P_{1,j}^{n+1} = P_t / \{ 1 + (\gamma-1) [U_{1,j}^{n+1}]^2 / (2\gamma R T_{1,j}^{n+1}) \}^{\gamma/\gamma-1} \quad (10)$$

$$V_{1,j}^{n+1} = 0.0 \quad (11)$$

$$U_{1,j}^{n+1} = U_{2,j}^{n+1} \quad (12)$$

$$\rho_{1,j}^{n+1} = P_{1,j}^{n+1} / (R T_{1,j}^{n+1}) \quad (13)$$

Knowing  $U_{1,j}^{n+1}$  and  $V_{1,j}^{n+1}$  from Eqs. (11) and (12)  $T_{1,j}^{n+1}$  is determined from Eq. (9) and  $P_{1,j}^{n+1}$ ,  $\rho_{1,j}^{n+1}$  follow from Eqs. (10) and (13), respectively.

## (2) A Minor Variant of Serra's Conditions

A slight variant of Serra's boundary conditions results if the condition  $\partial U / \partial x = 0$  is replaced by  $\partial \rho U / \partial x = 0$ . We have

$$P_t, T_t, V = 0, \text{ and } \frac{\partial \rho U}{\partial x} = 0 \quad (14)$$

The finite-difference formulation of Eq. (14) is the same as Eq. (9) to (13) except for Eq. (12) which is replaced by

$$\rho_{1,j}^{n+1} U_{1,j}^{n+1} = \rho_{2,j}^{n+1} U_{2,j}^{n+1} \quad (15)$$

### (a) Rigorous Implementation

Because of the nonlinearity in Eq. (15), Eqs. (9), (10), (13) and (15) form a set of coupled nonlinear equations whose solution

procedure is facilitated by the following method:

$$\rho_{1,j}^{n+1} = K_1 T_{1,j}^{n+1} / R \quad (16)$$

$$U_{1,j}^{n+1} = K / \rho_{1,j}^{n+1} \quad (17)$$

$$K_2 [T_{1,j}^{n+1}]^{2/\gamma-1} + T_{1,j}^{n+1} = T_t \quad (18)$$

where

$$K_1 = P_t / [T_t]^\gamma / \gamma^{-1}, \quad K = \rho_{2,j}^{n+1} U_{2,j}^{n+1}$$

and

$$K_2 = [(\gamma-1)R/2\gamma] [K/K_1]^2.$$

The solution of Eq. (18) is accomplished iteratively through quasilinearization as seen below:

$$\left[ T_{1,j}^{n+1} \right]_{i+1} = (T_t - 6K_2 / [T_{1,j}^{n+1}]_i^5) / (1 - 5K_2 / [T_{1,j}^{n+1}]_i^6) \quad (19)$$

#### (b) An Alternative Formulation

Scott and Hankey<sup>39</sup> implemented inflow boundary conditions given by Eq. (14) by the following procedure.

$$T_{1,j}^{n+1} = T_t - (\gamma-1) [U_{1,j}^{n+1/2}]^2 / (2\gamma R) \quad (20)$$

$$P_{1,j}^{n+1} = P_t / (1 + (\gamma-1) [U_{1,j}^{n+1/2}]^2 / (2\gamma R T_{1,j}^{n+1}))^{\gamma/\gamma-1} \quad (21)$$

$$V_{1,j}^{n+1} = 0.0 \quad (22)$$

$$\rho_{1,j}^{n+1} U_{1,j}^{n+1} = \rho_{2,j}^{n+1} U_{2,j}^{n+1} \quad (23)$$

$$\rho_{1,j}^{n+1} = P_{1,j}^{n+1} / (R T_{1,j}^{n+1}) \quad (24)$$

By making use of the predictor step values of  $U$  and  $V$  Eqs. (20) and (21) can be solved for  $p_{1,j}^{n+1}$  and  $T_{1,j}^{n+1}$ , independent of the updated values  $U_{1,j}^{n+1}$  and  $V_{1,j}^{n+1}$  obtained from Eqs. (22)

and (23). Density is obtained from Eq. (24). Though this approach reduces the program complexity, it is found to produce an entirely different solution from that due to the rigorous implementation of the inlet conditions as outlined by Eqs. (15 to 19) [See paragraph III.2.a(2a)].

### (3) Boundary Conditions Due to Oliger and Sundstrom

Oliger and Sundstrom<sup>40-41</sup> have shown that the specification of  $p$ ,  $U$ , and  $V$  at the inflow is well-posed for the linearized system of equations. We have

$$p, U, V = 0 \text{ and } \frac{\partial T}{\partial x} = 0. \quad (25)$$

The finite-difference analog of Eq. (25) is given by

$$p_{1,j}^{n+1} = f(t) \quad (26)$$

$$U_{1,j}^{n+1} = g(t) \quad (27)$$

$$V_{1,j}^{n+1} = 0.0 \quad (28)$$

$$T_{1,j}^{n+1} = T_{2,j}^{n+1} \quad (29)$$

$$p_{1,j}^{n+1} = R_{p,1,j}^{n+1} T_{1,j}^{n+1} \quad (30)$$

where  $f(t)$  and  $g(t)$  are given functions, which are fairly smooth and monotonic for  $t \in (t_1, t_2)$  and are practically unchanged within a characteristic period of oscillation  $t_p = 2\pi/\omega < t_2 - t_1$ .

### (4) Boundary Conditions Due to Fedorchenko

A. T. Fedorchenko<sup>37,42</sup> successfully modeled unsteady subsonic

flows of a viscous case with the inflow boundary conditions involving specification of  $T$ ,  $\rho U$ , and  $\rho V$ :

$$T, \rho U, \rho V = 0, \text{ and } \frac{\partial P}{\partial x} . \quad (31)$$

The finite-difference formulation is given by

$$T_{1,j}^{n+1} = \text{Constant} \quad (32)$$

$$\rho_{1,j}^{n+1} v_{1,j}^{n+1} = 0.0 \quad (33)$$

$$\rho_{1,j}^{n+1} U_{1,j}^{n+1} = f(t) \quad (34)$$

$$p_{1,j}^{n+1} = p_{2,j}^{n+1} \quad (35)$$

$$\rho_{1,j}^{n+1} = p_{1,j}^{n+1} / (RT_{1,j}^{n+1}). \quad (36)$$

#### b. Outflow Boundary Conditions

In what follows we describe different variants of essentially what amounts to the specification of exit pressure ( $P_e$ ) as the required outflow boundary condition.

##### (1) Non-Reflecting Condition

Rudy and Strikwerda<sup>43</sup> suggest the use of a non-reflecting boundary condition which is based on the outflow characteristic of the Euler equation of motion for application to viscous gases. The main purpose of the condition is to prevent upstream propagation of acoustic waves from the outflow boundary and thereby accomplish rapid convergence to the desired steady-state solution using time-dependent Navier-Stokes equations. Thus

$$\frac{\partial P}{\partial t} - \rho a \frac{\partial U}{\partial t} + \alpha (P - P_e) = 0, \quad \frac{\partial^2 U}{\partial x^2} = \frac{\partial^2 V}{\partial x^2} = \frac{\partial^2 T}{\partial x^2} = 0. \quad (37)$$

Because of the time dependence of the non-reflecting boundary condition it is necessary to describe the finite-difference formulation of both the predictor and corrector steps.



The Predictor Step:

$$\frac{\partial^2 \phi_{KL,j}^{n+1/2}}{\partial x^2} = 0 \quad (38)$$

where  $\phi = U, V,$  and  $T$

$$p_{KL,j}^{n+1/2} = p_{KL,j}^n + \rho_{KL,j}^n (\gamma R T_{KL,j}^n)^{1/2} (U_{KL,j}^{n+1/2} - U_{KL,j}^n) - \alpha \Delta T (p_{KL,j}^n - p_e) \quad (39)$$

The Corrector Step:

$$\frac{\partial^2 \phi_{KL,j}^{n+1}}{\partial x^2} = 0 \quad (40)$$

where  $\phi = U, V,$  and  $T$

$$p_{KL,j}^{n+1} = 0.5(p_{KL,j}^{n+1/2} + p_{KL,j}^n) + \rho_{KL,j}^{n+1/2} (\gamma R T_{KL,j}^{n+1/2})^{1/2} (U_{KL,j}^{n+1} - U_{KL,j}^{n+1/2}) - \alpha \Delta T (p_{KL,j}^{n+1/2} - p_e) \quad (41)$$

Instead of the vanishing second-order derivatives given by Eqs. (38) and (40), linear extrapolation of  $\phi = U, V,$  and  $T$  is incorporated at the exit, as seen below:

$$\phi_{KL,j} = [(x_{KL,j} - x_{KL-1,j}) / (x_{KL-1,j} - x_{KL-2,j})] (\phi_{KL-1,j} - \phi_{KL-2,j}) + \phi_{KL-1,j} \quad (42)$$

## (2) Constant Pressure Condition

The boundary condition most widely used in many gasdynamic applications involves the specification of constant pressure.

$$p = p_e, \quad \frac{\partial U}{\partial x} = \frac{\partial V}{\partial x} = \frac{\partial T}{\partial x} = 0 \quad (43)$$

$$p_{KL,j}^{n+1} = p_e, \quad U_{KL,j}^{n+1} = U_{KL-1,j}^{n+1}, \quad V_{KL,j}^{n+1} = V_{KL-1,j}^{n+1}, \\ T_{KL,j}^{n+1} = T_{KL-1,j}^{n+1} \text{ and } \rho_{KL,j}^{n+1} = p_{KL,j}^{n+1} / (R T_{KL,j}^{n+1}). \quad (44)$$

### (3) Split Boundary Condition

Hasen<sup>44</sup> suggested the use of a split condition for pressure as the outflow condition.

#### (a) Rigorous Implementation

$$\left. \begin{aligned} P &= P_e, & r &< R_c \\ \frac{\partial P}{\partial x} &= 0, & R_c &< r < R_d \\ \frac{\partial U}{\partial x} &= \frac{\partial V}{\partial x} = \frac{\partial T}{\partial x} = 0 \end{aligned} \right\} \text{split condition} \quad (45)$$

where  $R_c$  and  $R_d$  are the radii of the centerbody and duct wall of the combustor, respectively.

$$\begin{aligned} P_{KL,j}^{n+1} &= P_e & \text{if } r &< R_c \\ P_{KL,j}^{n+1} &= P_{KL-1,j}^{n+1} & \text{if } R_c < r < R_d \\ \phi_{KL,j}^{n+1} &= \phi_{KL-1,j}^{n+1}, \quad \rho_{KL,j}^{n+1} = P_{KL,j}^{n+1} / (RT_{KL,j}^{n+1}) \end{aligned} \quad (46)$$

where  $\phi = U, V, \text{ and } T$ .

#### (b) Alternative Implementation

Instead of evaluating density from the equation of state, Eq. (46), Scott and Hankey<sup>39</sup> used the following method:

$$\rho_{KL,j}^{n+1} = P_{KL,j}^{n+1} / (RT_{KL-1,j}^{n+1} [1 + \gamma(\gamma-1)M^2/2]_{KL-1,j}) \quad (47)$$

Furthermore, after the determination of the primitive variables, the programming of Reference 39 in the evaluation of the conservative variable,  $\rho e$ , is as follows:

$$[\rho e]_{KL,j}^{n+1} = \rho_{KL,j}^{n+1} \{ C_v T_{KL-1,j}^{n+1} + [U_{KL-1,j}^{n+1}]^2 + [V_{KL-1,j}^{n+1}]^2 \} \quad (48)$$

The implication of Eq. (48) is that more energy is added at the outflow boundary by an amount equal to  $1/2(U^2 + v^2)$  because specific internal energy is defined as  $e = C_v T + 1/2(U^2 + v^2)$ .

#### (4) Relaxation Boundary Condition

The following variant involving the specification of pressure at the exit is used in Reference 45 for the modeling of Kelvin-Helmholtz instability.

$$P_{KL,j}^{n+1} = P + (x_{KL} - x_{KL-1})(P_e - P)/R_d, \quad (49)$$

where  $P$  is obtained from the linear extrapolation; and

$$\frac{\partial^2 \phi}{\partial x^2} = 0, \quad \text{where } \phi = U, V, \text{ and } T.$$

#### (5) Boundary Conditions For Reverse-Flow Exit

A. T. Fedorchenko<sup>42</sup> suggests the use of specifying  $V$ ,  $T$ , and  $P$  if there is a flow reversal at the exit.

$$P = P_e, \quad \frac{\partial U}{\partial x} = \frac{\partial T}{\partial x} = \frac{\partial V}{\partial x} = 0$$

and (50)

$$V = 0, \quad T = T_e, \quad P = P_e \quad \text{and} \quad \frac{\partial \rho U}{\partial x} = 0 \quad \text{if} \quad U_{KL,j}^{n+1} < 0.$$

#### c. Solid-Wall Boundary Conditions

The centerbody and duct walls are treated as no-slip, isothermal surfaces, involving the specification of  $T_w$  and  $U_w = V_w = 0$ . The remaining thermodynamic variables  $P_w$  and  $\rho_w$  are evaluated from:

$$P_w = R \rho_w T_w, \quad \frac{\partial P}{\partial \eta} = 0 \quad (51)$$

or continuity equation, where  $\eta$  is in the direction normal to the wall.

d. Centerline Boundary Conditions

The boundary conditions on the axis of symmetry are given by

$$\frac{\partial U}{\partial r} = \frac{\partial P}{\partial r} = \frac{\partial T}{\partial r} = 0 \quad \text{and} \quad V = 0 \quad (52)$$

e. Acoustic Characteristics of Boundary Conditions

By linearizing the inflow and outflow boundary conditions it is possible to estimate the acoustic properties of the longitudinal oscillations in the domain of interest. Following the approach of A. T. Fedorchenko,<sup>37</sup> the relative value of normal conductance  $Q$  and reflection coefficient  $\beta$  can be estimated for the given inlet boundary by considering small adiabatic fluctuations:

$$U = \bar{U} + U', \quad V = \bar{V} + V', \quad \rho = \bar{\rho} + \rho', \quad \rho' \cong P'/\bar{a}^2, \quad \left| \frac{U'}{\bar{U}} \right| \ll 1$$

and  $\left| \frac{P'}{\bar{P}} \right| \ll 1.$  (53)

For the boundary conditions given by Eq. (8), it is possible to show that

$$Q = U' \bar{\rho} \bar{a} / P'$$

and  $\beta \cong (1+Q)/(1-Q).$  (54)

It is known that both  $Q$  and  $\beta$  are real and independent of the frequency of oscillation. From the definition of  $P_t$ , we have

$$P_t = P \left( 1 + \frac{(\gamma - 1) U^2}{2 a^2} \right)^{\gamma/\gamma - 1} \quad (55)$$

For small  $M$ , the above equation can be approximated by

$$P \cong P_t \left( 1 - \frac{U^2}{2RT} \right) \quad (56)$$

In terms of the small adiabatic oscillations, Eq. (56) becomes

$$P \cong P_t \left( 1 - \frac{\bar{U}^2}{2RT} \right) - \frac{P_t \bar{U} U'}{RT} \quad (57)$$

Substituting for  $P' = -\frac{P_t UU'}{RT}$  in Eq. (54), we have

$$Q \approx -\frac{\bar{\rho} \bar{a} RT}{P_t \bar{U}} \approx -\frac{\bar{a}}{\bar{U}} = -\frac{1}{M}$$

and

$$\beta \approx \frac{M - 1}{1 + M} \approx -1. \quad (58)$$

For the inflow conditions of Eq. (25),  $Q = 0$  and  $\beta = 1$  and they represent adiabatic solid wall boundary conditions involving specification of  $U$ ,  $V$ , and  $\partial T / \partial n = 0$ . The inflow conditions act as a perfect reflecting boundary, independent of  $M$ .

The analysis<sup>42</sup> of the inflow condition of Eq. (31) shows

$$Q \approx -M \quad \text{and} \quad \beta \approx \frac{1-M}{1+M} \approx 1. \quad (59)$$

For the exit boundary conditions ( $P = P_e$ ) of Eq. (43), Fedorchenko<sup>42</sup> showed that  $Q = \infty$  and  $\beta = -1$ , which indicates that the conditions act like a perfect reflecting boundary.

For the total transmission of the quasi-plane normal wave through the inlet and exit boundaries (that is,  $|\beta| \ll 1$ ), it is required that  $(Q)_{\text{inflow}} \approx -1$  or  $(Q)_{\text{outflow}} \approx 1$ . If, however,  $(Q)_{\text{inflow}} > 0$  or  $(Q)_{\text{outflow}} < 0$ , it may lead to the amplification of the longitudinal oscillations in the domain of interest.

The foregoing analysis does not take into account the radial oscillations arising from the inhomogeneous boundary conditions at the inlet and the exit (if  $\frac{\partial \rho U}{\partial r} \neq 0$ , then  $\frac{\partial \rho}{\partial r} \neq 0$ ), as well as the refraction effects in the vortex flow.<sup>42</sup>

It is useful to note that the reason for considering perfectly reflecting permeable boundary conditions at the exit [except for Eq. (37) from Rudy and Strikwerda<sup>43</sup>] is due to Hankey,<sup>46</sup> who suggested the need for a feedback mechanism to sustain the inherent unsteady behavior which is characteristic of the bluff-body shedding phenomenon at high Reynolds-number flows.

### 3. COMPUTATIONAL DETAILS

Using the time-dependent, axisymmetric, compressible Navier-Stokes equations of a perfect gas, solutions are obtained for the subsonic flowfield in the CBCC. Figure 40 shows schematically the APL CBCC and the physical domain which consists of 60 axial and 46 radial nodes. Although the dynamic behavior observed in the centerbody near wake<sup>15</sup> involved combustion due to the annular air stream and central fuel jet, present computations are directed towards obtaining a physically meaningful unsteady solution involving the flowfield due to the annular stream alone.

The equations describing the conservation of mass, momentum, and energy may be written in the following conservative form in physical space as

$$\frac{\partial E}{\partial t} + \frac{\partial F}{\partial x} + \frac{1}{r} \frac{\partial rG}{\partial r} = H \quad (60)$$

where

$$E = \begin{bmatrix} \rho \\ \rho U \\ \rho V \\ \rho e \end{bmatrix}, \quad F = \begin{bmatrix} \rho U \\ \rho U^2 - \tau_{xx} \\ \rho UV - \tau_{rx} \\ \rho Ue - U\tau_{xx} - V\tau_{xr} - K T_x \end{bmatrix}, \quad (61)$$

$$G = \begin{bmatrix} \rho V \\ \rho UV - \tau_{rx} \\ \rho V^2 - \tau_{rr} \\ \rho Ve - V\tau_{rr} - U\tau_{xr} - k T_r \end{bmatrix}, \quad H = \begin{bmatrix} 0 \\ 0 \\ -\tau_{\theta\theta}/r \\ 0 \end{bmatrix}$$

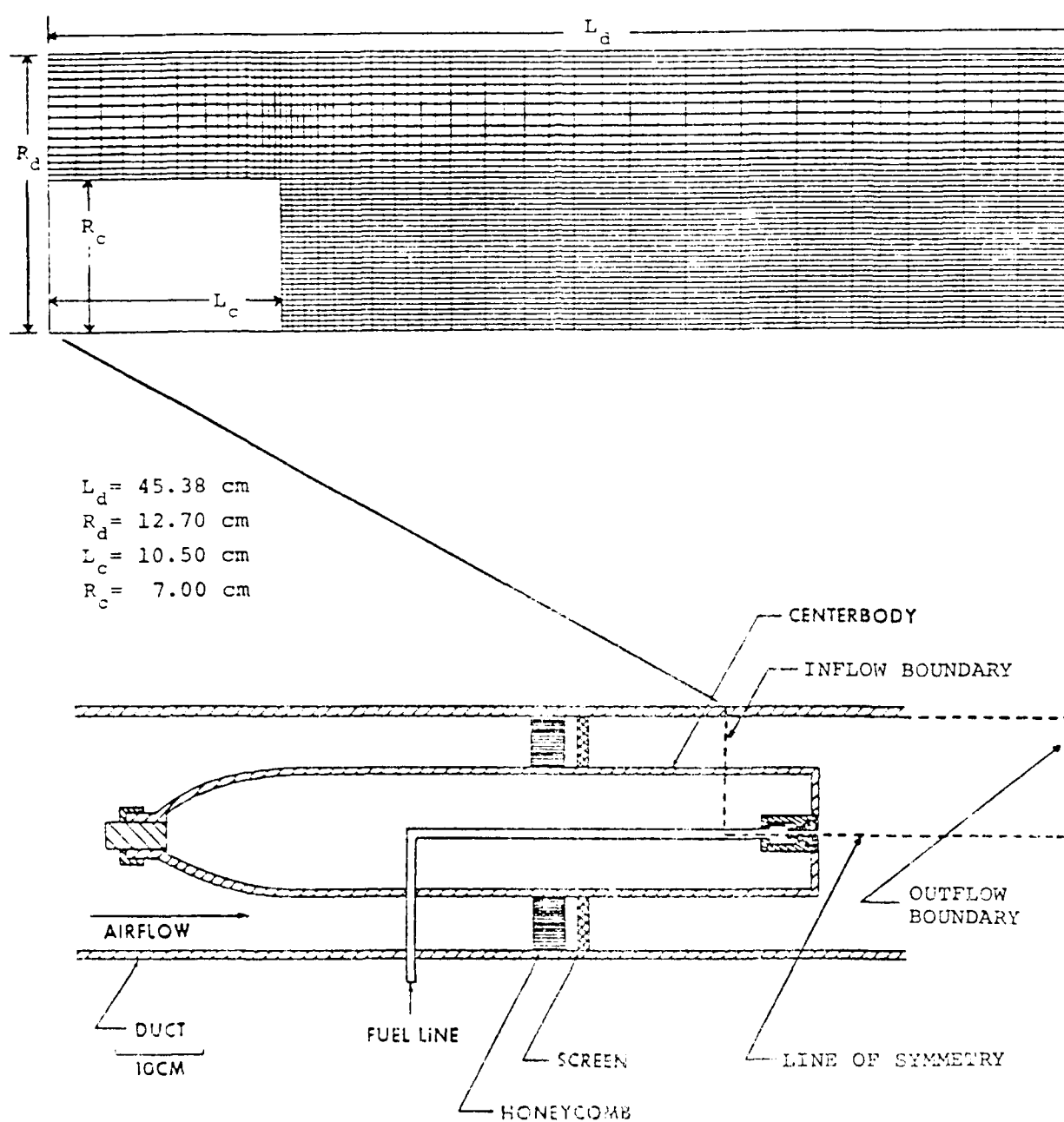


Figure 40. Schematic of the API CBCC and Physical (60 x 46) Finite-Difference Mesh.

and where

$$\tau_{xx} = (2\mu + \lambda) \frac{\partial U}{\partial x} + \lambda \left( \frac{V}{r} + \frac{\partial V}{\partial r} \right) - P \quad (62)$$

$$\tau_{rr} = (2\mu + \lambda) \frac{\partial V}{\partial r} + \lambda \left( \frac{V}{r} + \frac{\partial U}{\partial x} \right) - P \quad (63)$$

$$\tau_{\theta\theta} = (2\mu + \lambda) \frac{V}{r} + \lambda \left( \frac{\partial U}{\partial x} + \frac{\partial V}{\partial r} \right) - P \quad (64)$$

and

$$\tau_{xr} = \tau_{rx} = \mu \left( \frac{\partial U}{\partial r} + \frac{\partial V}{\partial x} \right) \quad (65)$$

The values of Prandtl number ( $Pr$ ) = 0.72 and ratio of specific heats ( $\gamma$ ) = 1.4 are specified. The molecular viscosity  $\mu$  is related to the temperature by Sutherland's law. Finally, the pressure is related to temperature by the equation of state

$$P = \rho RT. \quad (66)$$

These equations are advanced in time using the vectorized computer code of Shang<sup>47</sup> which employs MacCormack's explicit and unsplit algorithm.<sup>48</sup> A forward-predictor, backward-corrector operator sequence is used for each time step. Exponential grid stretching is used to adequately resolve the flowfield in the anticipated regions of large gradients. The physical domain is transformed into a computational domain of unit square with equal spatial step sizes,  $\Delta x$  and  $\Delta r$  ( $\Delta x \neq \Delta r$ ). The time step of compressible equations is limited by the Courant-Friedrichs-Lewy (CFL) condition. The maximum allowable time step in transformed coordinates is given by

$$\Delta T_{CFL} = 1 / \left[ \frac{U_{\xi}}{\Delta \xi} + \frac{U_{\zeta}}{\Delta \zeta} + a \left\{ \left( \frac{\zeta_x}{\Delta \zeta} + \frac{\xi_x}{\Delta \xi} \right)^2 + \left( \frac{\zeta_r}{\Delta \zeta} + \frac{\xi_r}{\Delta \xi} \right)^2 \right\} \right]^{1/2} \quad (67)$$

where

$$U_{\zeta} = \zeta_x U + \zeta_r V$$

$$U_{\xi} = \xi_x U + \xi_r V$$

$\xi(x)$  and  $\zeta(r)$  are the transformed variables needed for the transformation of the physical domain to the computational



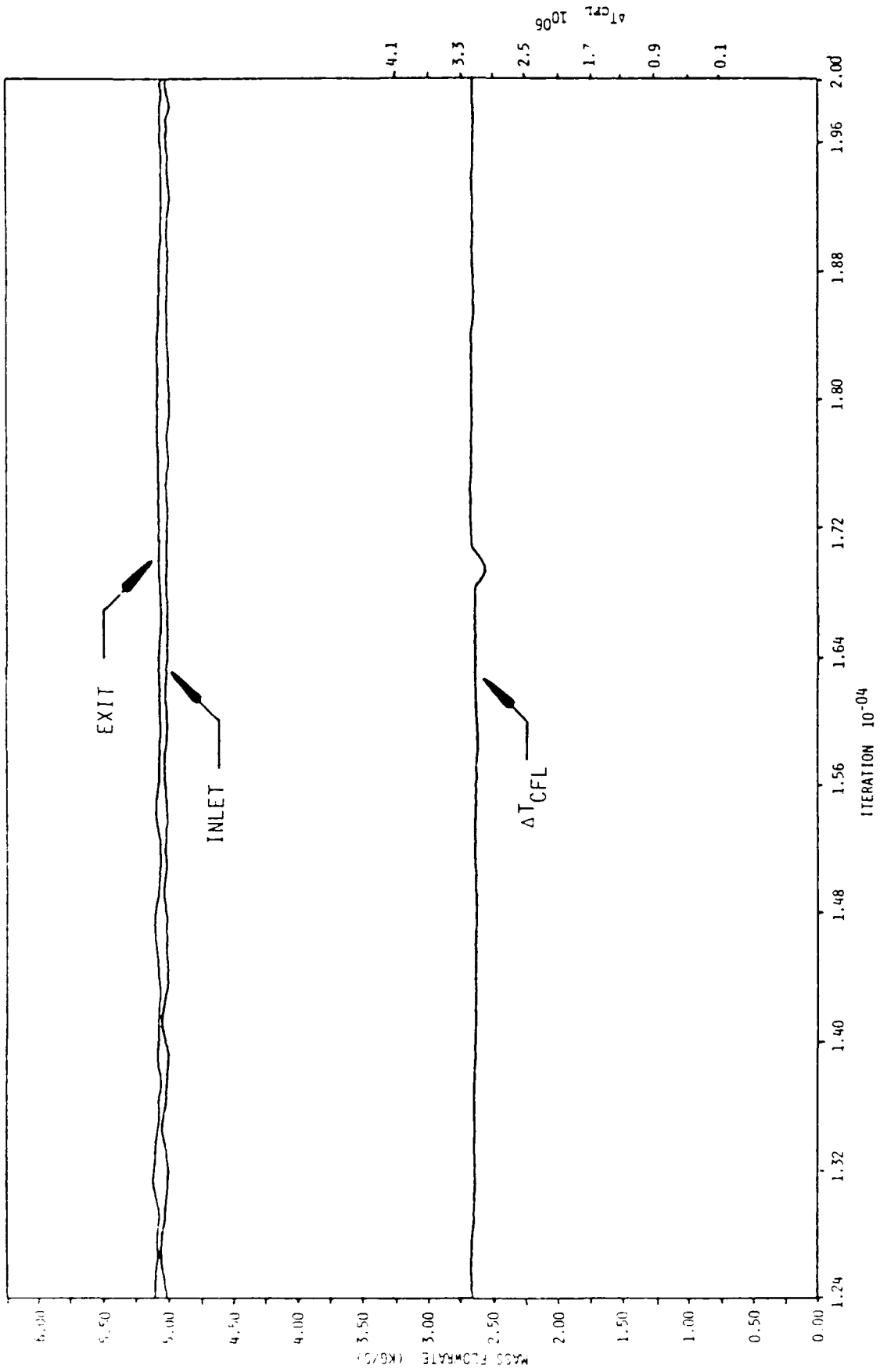


Figure 46b. Temporal Variation in Combustor Mass Flow and  $\Delta T_{CFL}$  for case 3b of Table 7.

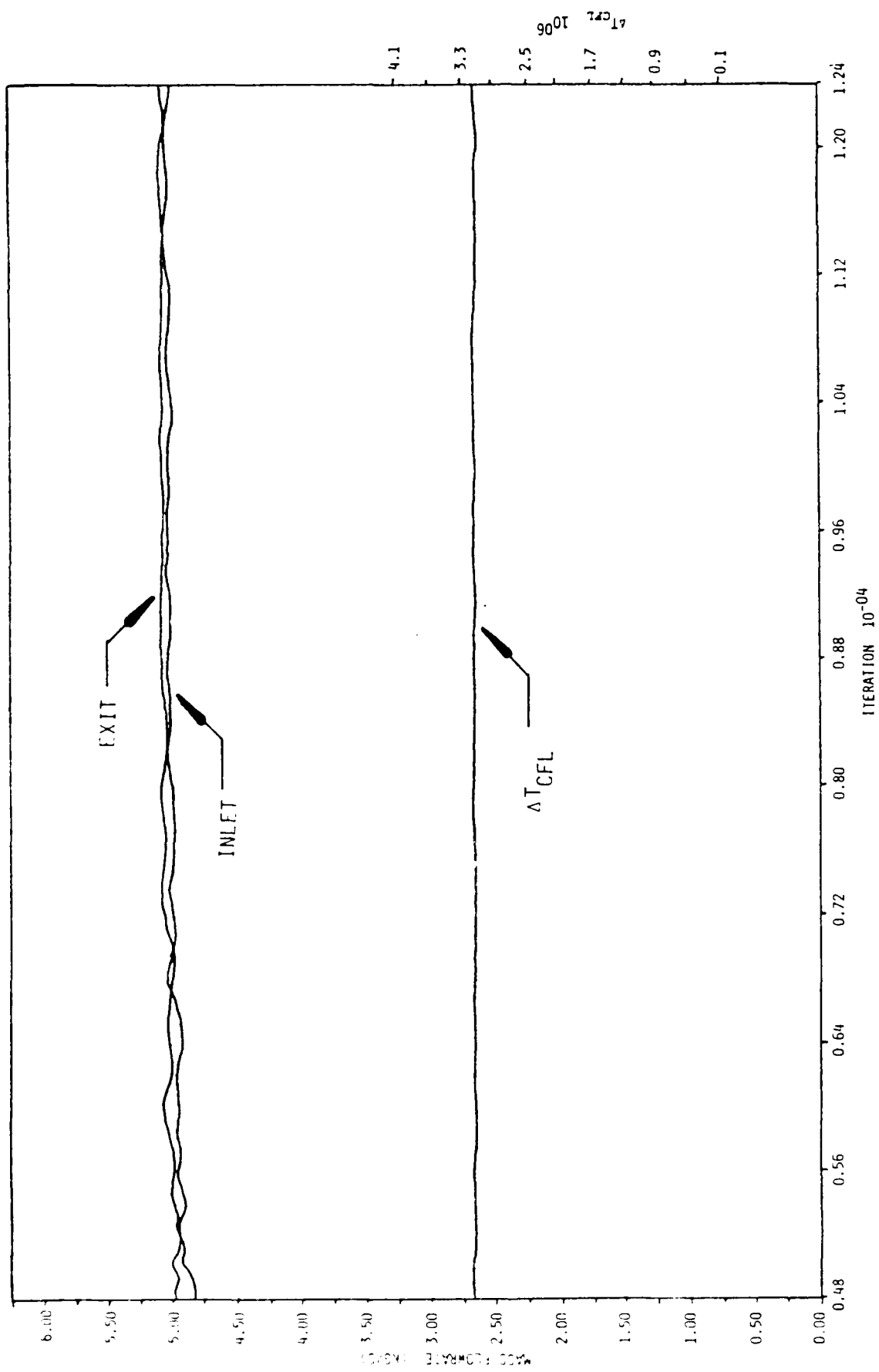
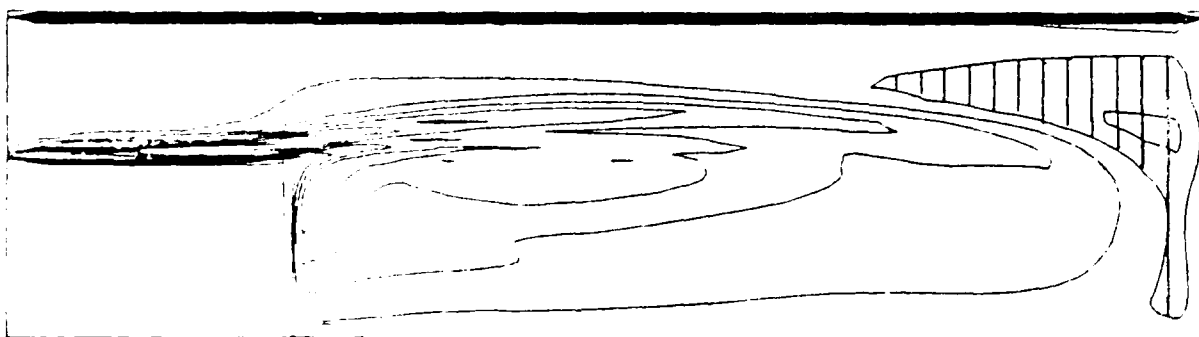
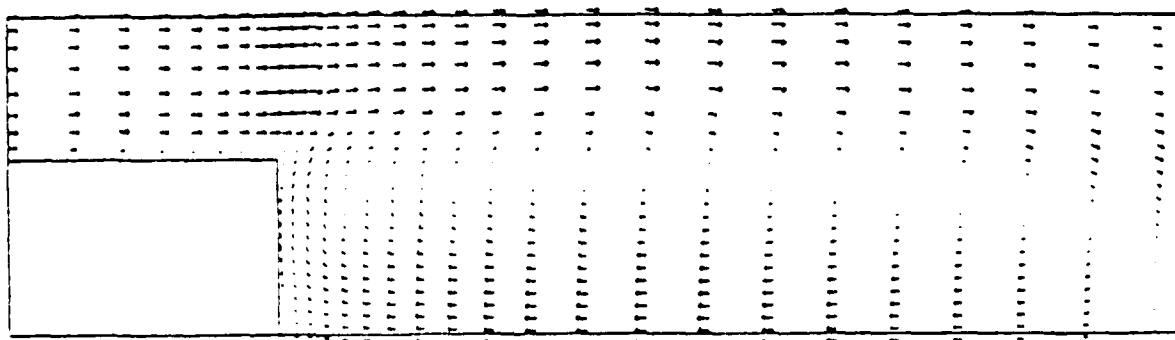


Figure 46a. Temporal Variation in Combustor Mass Flow and  $\Delta T_{CFL}$  for case 3b of Table 7.



$N = 10,500$

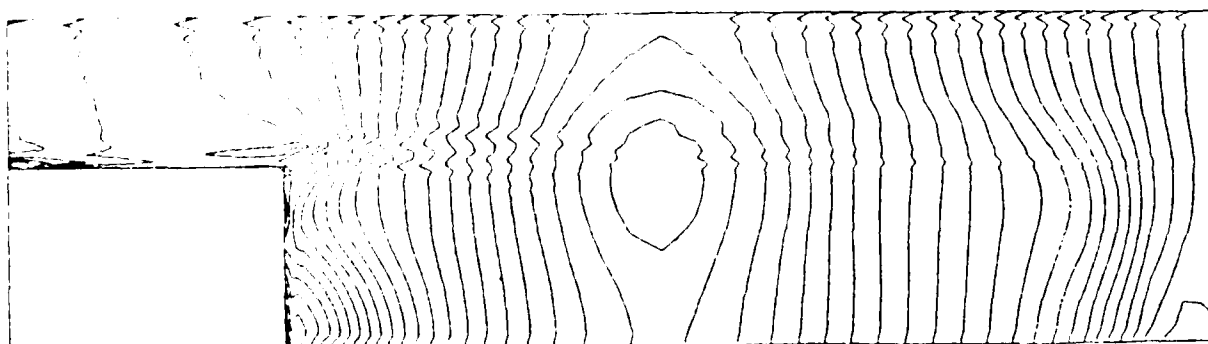
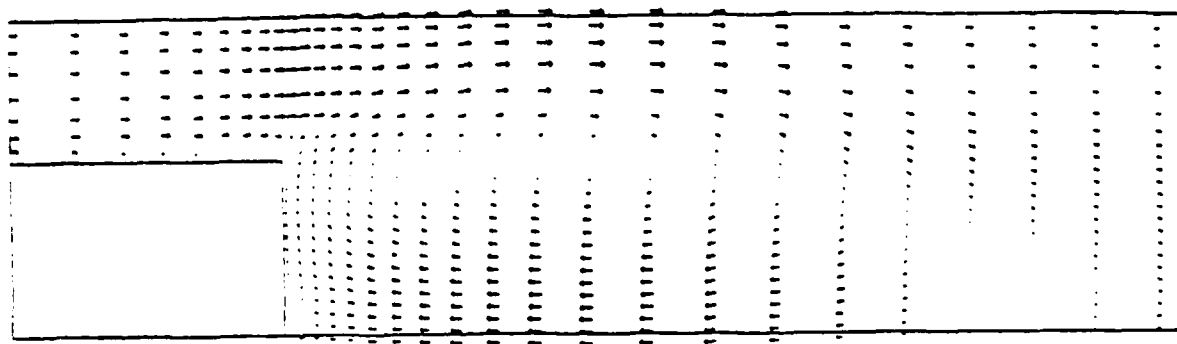


Figure 45. Velocity-Vector, Vorticity-Contour and Pressure-Contour Plots for Case 3a of Table 7.



$N = 26,000$

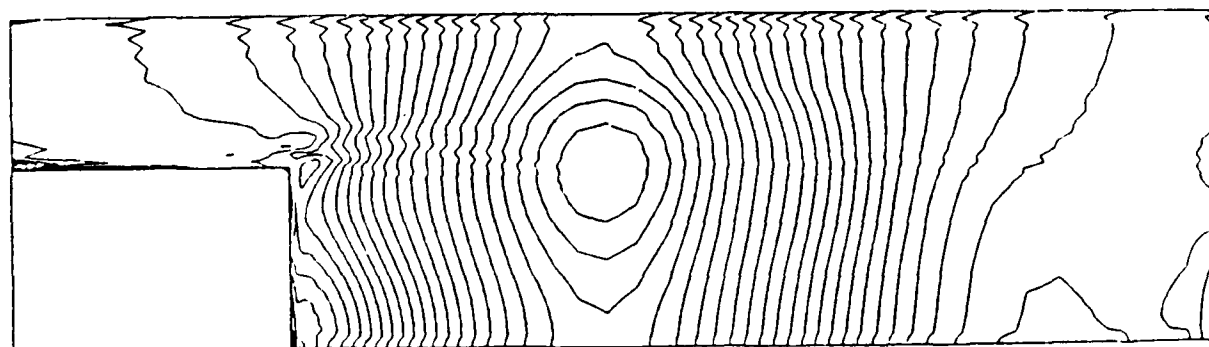


Figure 44. Velocity-Vector, Vorticity-Contour and Pressure-Contour Plots for Case 2 of Table 7.

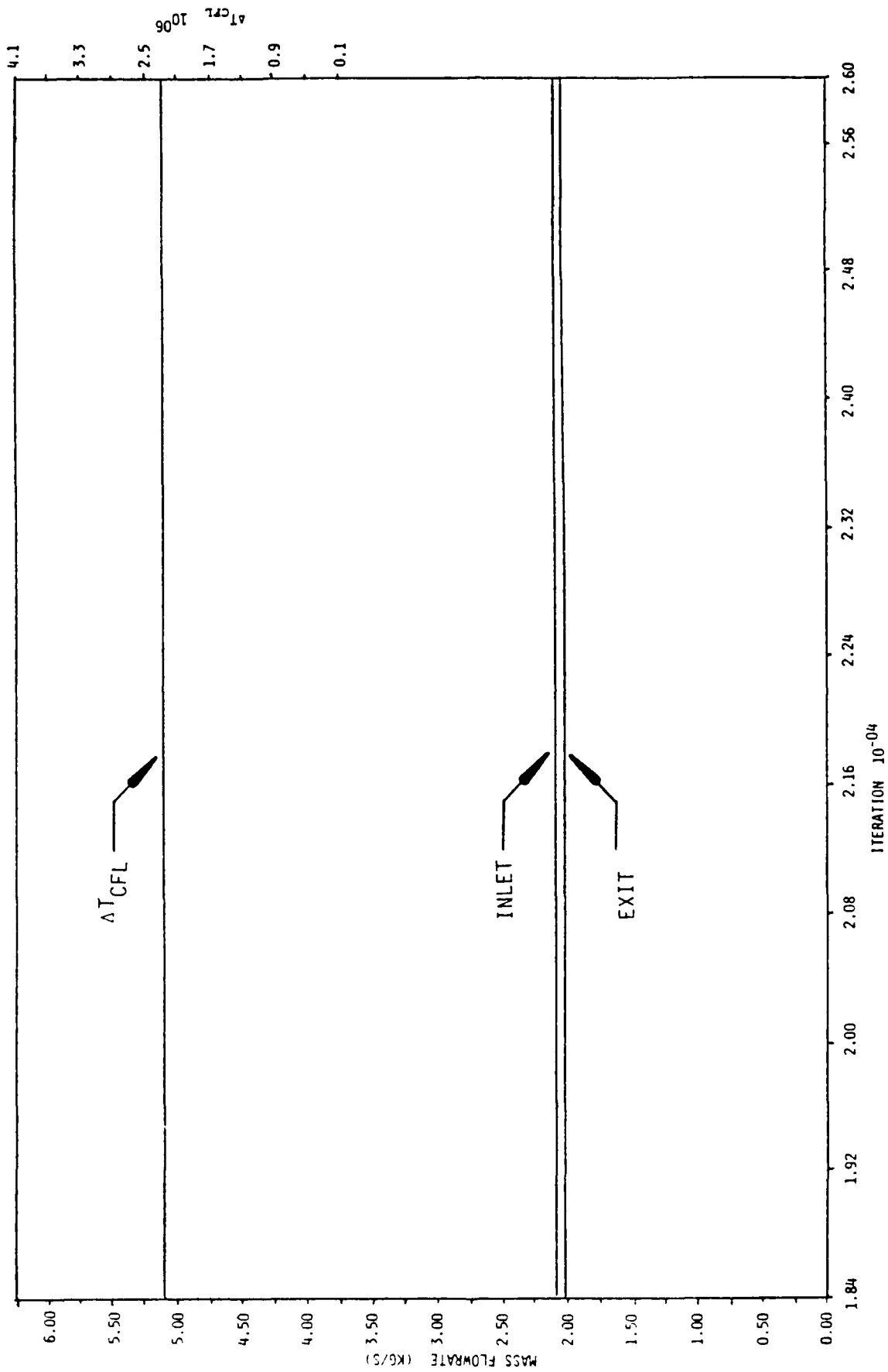


Figure 43b. Temporal Variation in Combustor Mass Flow and  $\Delta T_{CFL}$  for Case 2 of Table 7.

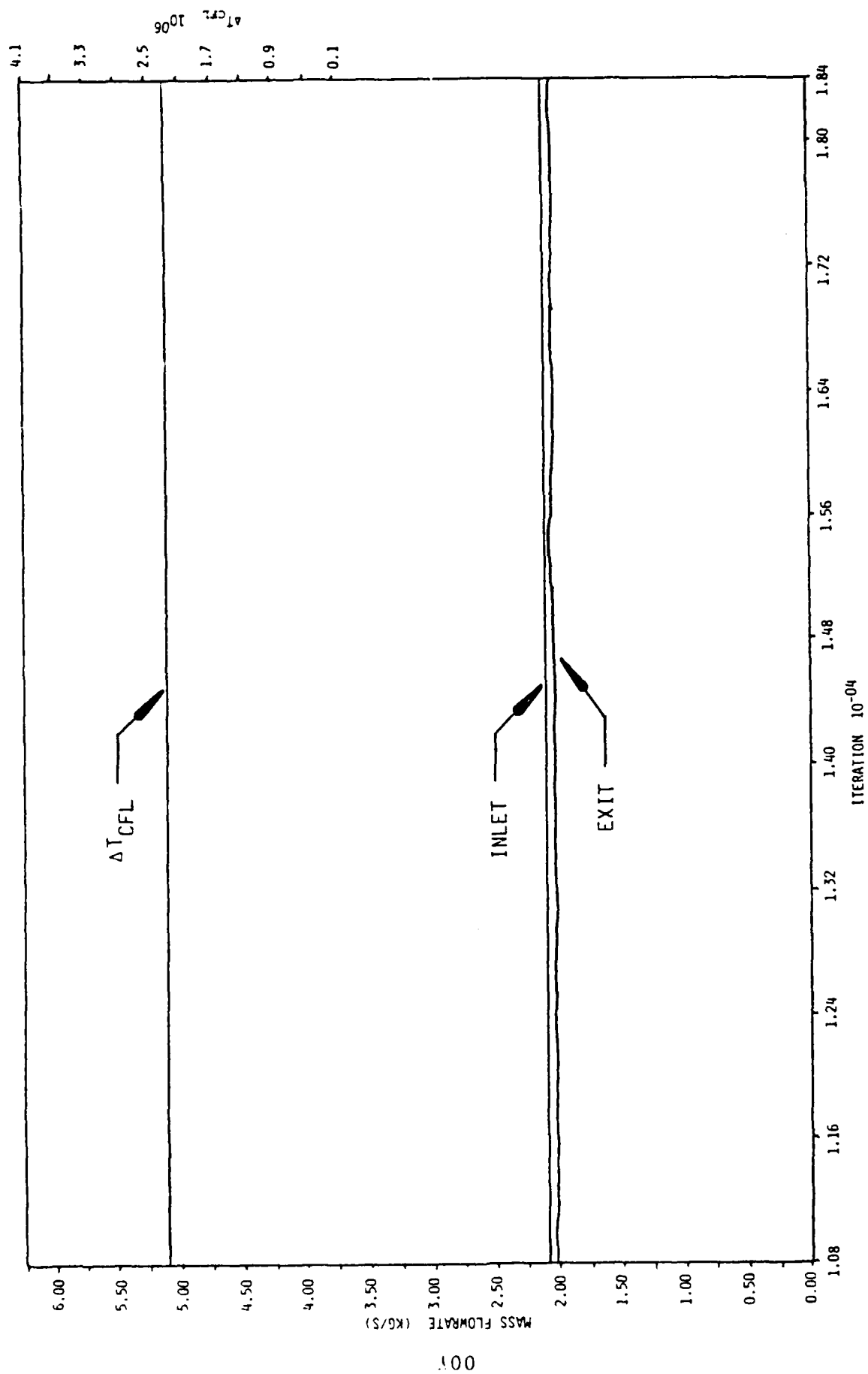
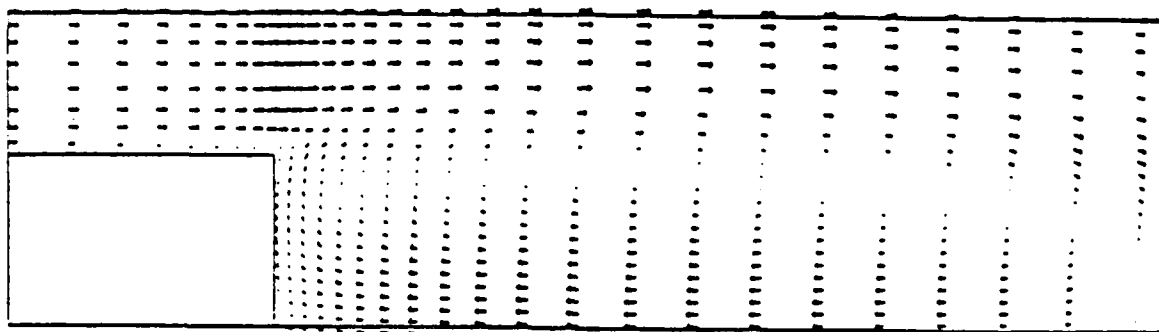


Figure 43a. Temporal Variation in Combustor Mass Flow and  $\Delta T_{CFL}$  for Case 2 of Table 7.

terbody diameter  $D_C$ ) are equal to 1.1 and 0.5 respectively. It is observed that the initial development of the flowfield is accompanied by the generation of longitudinal harmonic oscillations with a clearly defined dominant frequency  $\omega_{x1} \sim 182$  Hz which is close to the fundamental characteristic frequency of a one-dimensional quarter-wave resonator  $\omega_{x1} \sim a/4L_d \sim 191$  cycles/sec. In addition, resonance also occurs at all harmonics of the fundamental frequency, i.e.,  $\omega_{x2} = 2\omega_{x1}$ , ...,  $\omega_{xn} = n\omega_{x1}$ . The longitudinal oscillations attenuated in about 3,500 time steps which clearly corresponds to the time it takes for a particle entering the inflow boundary to reach the exit plane,  $L_d/U_{inflow} \sim 8$  milliseconds. The vorticity contours of Figure 42 show heavy concentration in the boundary layers of the duct wall and the centerbody wall. The positive vorticity contours corresponding to counterclockwise vorticity originating from the duct wall boundary layer are shown by hatching. The negative vorticity contours originating at the centerbody boundary layer are carried past into the centerbody near wake by convection. It is observed that the tail-end of the zero-vorticity contour extends in the axial direction towards the outflow boundary at a rate of 3 m/s. The stretching of the recirculation region is the only unsteady feature of the flowfield after the combustor mass flow reaches the steady state.

Figure 43 of Case 2 shows that there is no variation in the mass flow rate or in  $\Delta T_{CFL}$  of the flowfield with time. The pressure contour plot seen in Figure 44 clearly demonstrates the existence of a shear layer originating from the trailing edge of the centerbody and shows the location of the vortex center in this shear layer. Furthermore, as may be anticipated, the pressure minimum occurs at the vortex center and the pressure maximum at the centerline stagnation point of the centerbody. All other salient features of the flowfield are identical to the previously discussed Case 1.

Figures 45 to 47 correspond to Cases 3a and 3b. Case 3a corresponds to a mass flow rate of 2.5 kg/s and a Reynolds number of 106 on a (60 x 46) grid and Case 3b corresponds to a mass flow



$N = 27,000$

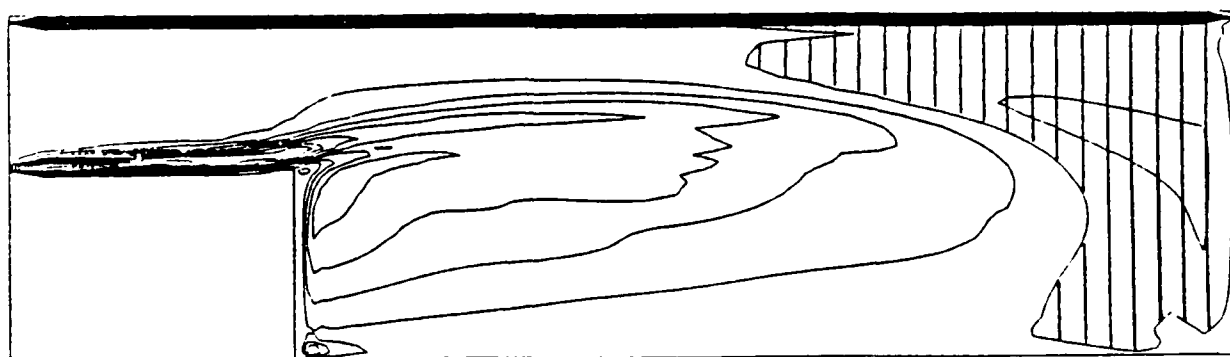


Figure 42. Velocity-Vector and Vorticity-Contour Plots for Case 1 of Table 7.



Reynolds number based on the duct diameter and the average Mach number of the flowfield based on the average inflow velocity. Table 7 also provides the details of the number of timesteps (iterations) and the corresponding total time in seconds over which the flowfield is computed. Quantities shown in parentheses in Table 7 must be interpreted with care. The asterisk denotes the data of Reference 39.

The numerical calculations are performed on the AFWAL CDC CYBER 750/175 computer and on the NASA Lewis Research Center CRAY-1 computer. The original AFWAL computer code has been optimized for the CBCC configuration by reducing the field-length of computer memory from the initial requirement of 363,000g words to 172,100g words for the baseline domain. The optimized version of the computer code requires a field-length of 216,240g words for the extended domain.

The relative computational efficiency, or the so-called "computational effort"  $\tau$  is defined as the CPU time required to advance the solution by one time step per spatial grid point; i.e.,  $\tau = \text{CPU in seconds} / \text{number of mesh points} \times \text{number of time steps}$ . For the present computer code  $\tau = 5.96 \times 10^{-4}$  seconds on the CYBER and  $\tau = 4.4 \times 10^{-5}$  seconds on the CRAY. All the numerical computations are performed for the (60 x 46) grid on the CYBER and for the (80 x 46) grid on the CRAY. For the solution to advance 10,000 time steps, the approximate CPU time required for the computer code is 4.5 hours on the CYBER and 0.45 hours on the CRAY.

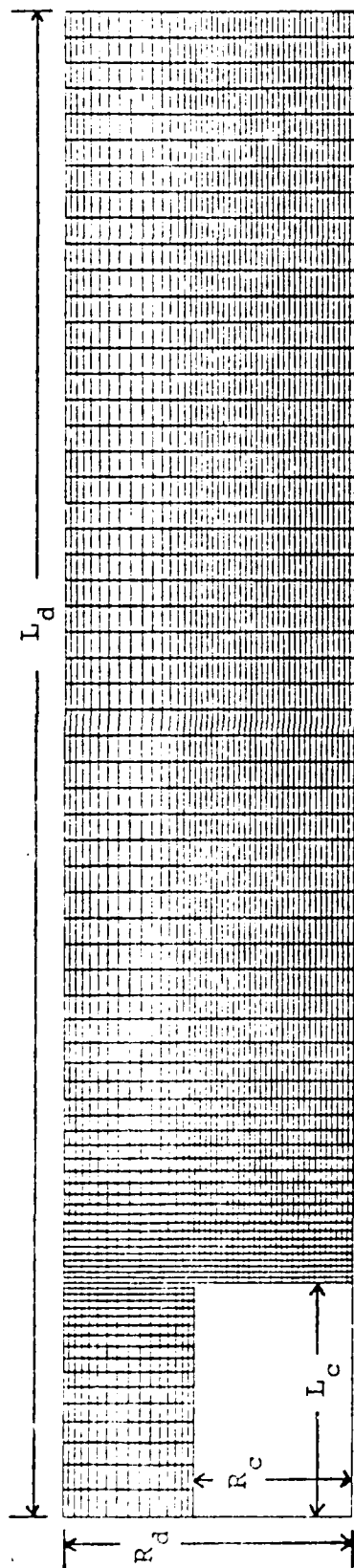
The numerical calculations of Cases 1 through 4 of Table 7 show that the flowfield attains a steady mass-flow rate and the time required for the flowfield to reach this converged mass-flow rate varied anywhere between  $L_d/U_{\text{inflow}}$  to  $4L_d/U_{\text{inflow}}$ . The velocity vector plot of Case 1, Figure 42, shows a stationary recirculation region in the centerbody near wake and does not indicate any evidence of vortex shedding. The centerline reattachment point extends all the way to the exit plane. The axial and radial coordinates of the vortex center (normalized by cen-

TABLE 7  
DETAILS OF NUMERICAL COMPUTATIONS FOR THE DIFFERENT CASES OF TABLE 6.

CASE	AVERAGE MASS FLOW (kg/s)	AVERAGE REYNOLDS NUMBER $\times 10^{-6}$ (based on duct diameter)	AVERAGE MACH NUMBER (based on average inflow velocity)	TOTAL TIME (s)	NUMBER OF TIME STEPS	INITIAL DISTRIBUTION OF THE FLOW FIELD
1	2.3	0.956	0.166	0.065	27000	Starting Flow Field Corresponds to 6000 Iteration of Case 2
2	2.0	0.835	0.145	0.063	26000	$U = 50.05$ m/s if $x \leq L_C$ $U = 34.85$ m/s if $x > L_C$ $P = P_a$ , $T = T_a$ , $\rho = \rho_a$ , $V=0$
3a	2.5	1.039	0.181	0.023	10500	Starting Flow Field Corresponds to 22000 Iteration of Case 2
3b	5.0	2.086	0.363	0.063	20000	$U = 100.6$ m/s if $x \leq L_C$ $U = 70.0$ m/s if $x > L_C$ $P = P_a$ , $T = T_a$ , $\rho = \rho_a$ , $V=0$
4	5.5	2.295	0.399	0.056	22000	Starting Flow Field Corresponds to 25700 Iteration of Case 6a
5	---	-----	-----	0.083	40000	Same as 3b
6a	(4.2)	(1.752)	(0.305)	0.068	25700	$U = 50.0$ m/s, $V = 0$ , $P = P_a$ , $T = T_a$ , $\rho = \rho_a$
6b	(4.75)	(1.982)	(0.345)	0.076	40000	Same as 3b
6c	(4.75)	(1.982)	(0.345)	0.099	40000	Same as 3b
7a	4.0	1.669	0.290	0.129	40000	Same as 3b
7	2.0	0.835	0.145	0.203	60000	Same as 2
8a	2.0	0.835	0.145	0.287	80000	Same as 2
8b	4.0	1.669	0.290	0.228	70000	Same as 3b
9	3.9	1.627	0.283	0.059	23000	Starting Flow Field Corresponds to 37000 Iteration of Case 6a

TABLE 7  
DETAILS OF NUMERICAL COMPUTATIONS FOR THE DIFFERENT CASES OF TABLE 6.

CASE	INFLOW PARAMETERS	OUTFLOW PARAMETERS	GRID SIZE	CFL NUMBER	DAMPING PARAMETERS	
					$C_x$	$C_r$
1	$P_t = 10388.3 \text{ kg}_f/\text{m}^2$ $T_t = 535.6 \text{ R}, V = 0$	$P_e = 10236.31 \text{ kg}_f/\text{m}^2$	60 x 46	0.5	2.0	2.0
2	$\rho = 1.1965 \text{ kg}/\text{m}^3$ $U = 50.05 \text{ m/s}, V = 0$	$P_e = 9762.81 \text{ kg}_f/\text{m}^2$	60 x 46	0.5	2.0	2.0
3a	Same as Case 1	Same as Case 1	60 x 46	0.5	0.5	0.5
3b	Same as Case 1	$P_e = 9821.39 \text{ kg}_f/\text{m}^2$	80 x 46	0.8	0.5	0.5
4	$P_t = 10441.3 \text{ kg}_f/\text{m}^2$ $T_t = 535.6 \text{ R}, V = 0$	$P_e = 9772.58 \text{ kg}_f/\text{m}^2$	60 x 46	0.65	2.0	2.0
5	Same as Case 1	Same as Case 3b	80 x 46	0.5	2.0	2.0
6a	Same as Case 4	Same as Case 2	60 x 46	0.5	2.0	2.0
6b	Same as Case 1	Same as Case 3b	80 x 46	0.5	2.0	2.0
6c	Same as Case 1	Same as Case 3b	80 x 46	0.8	2.0	2.0
7a	$\rho U = 120.3 \text{ kg}/\text{m}^2 \text{ s}$ $\rho V = 0, T = 533.4 \text{ R}$	Same as Case 3b	80 x 46	0.8	2.0	2.0
7b	$\rho U = 58.4 \text{ kg}/\text{m}^2 \text{ s}$ $\rho V = 0, T = 533.4 \text{ R}$	Same as Case 3b	80 x 46	0.8	2.0	2.0
8a	Same as Case 7b	$P_e = 9821.39 \text{ kg}_f/\text{m}^2$ ( $T_e = 533.36 \text{ R}, V = 0$ for reverse flow)	80 x 46	0.8	2.0	2.0
8b	Same as Case 7a	Same as Case 8a	80 x 46	0.8	2.0	2.0
9	Same as Case 1	$P_e = 9821.39 \text{ kg}_f/\text{m}^2$	60 x 46	0.65	2.0	2.0



$$\begin{aligned} L_d &= 67.05 \text{ cm} \\ R_d &= 12.70 \text{ cm} \\ L_c &= 10.50 \text{ cm} \\ R_c &= 7.00 \text{ cm} \end{aligned}$$

Figure 41. Physical (80 x 46) Finite-Difference Mesh.

TABLE 6  
 DETAILS OF VARIOUS CASES MODELED WITH DIFFERENT COMBINATIONS  
 OF INFLOW AND OUTFLOW BOUNDARY CONDITIONS (---CASES NOT RUN)

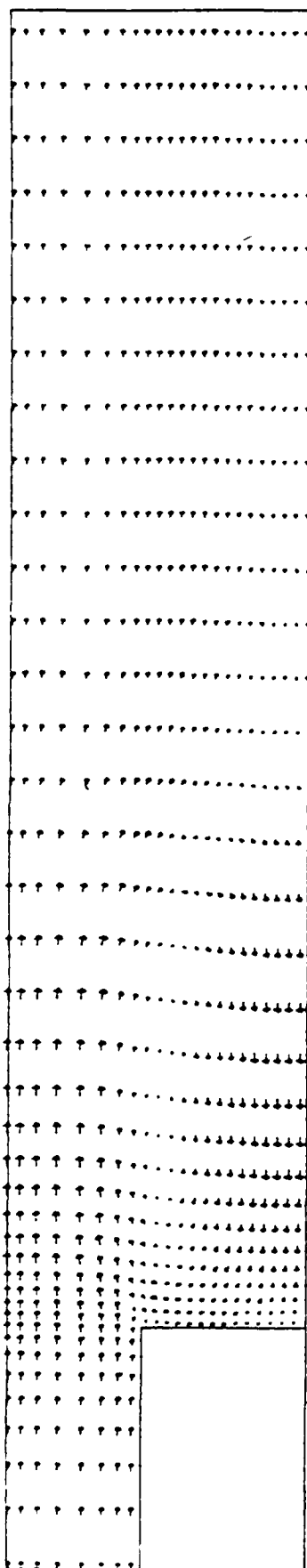
OUTFLOW CONDITIONS INFLOW CONDITIONS	(1)	(2)	(3a)	(3b)	(4)	(5)
	(1)	(2)	(3a)	(3b)	(4)	(5)
(1)	CASE 1	CASE 3	---	---	CASE 9	---
(2a)	---	---	CASE 4	---	---	---
(2b)	---	---	CASE 5	CASE 6	---	---
(3)	CASE 2	---	---	---	---	---
(4)	---	---	CASE 7	---	---	CASE 8

domain. The calculations are performed using third-order artificial damping parameters of Reference 49 to suppress spurious numerical oscillations.

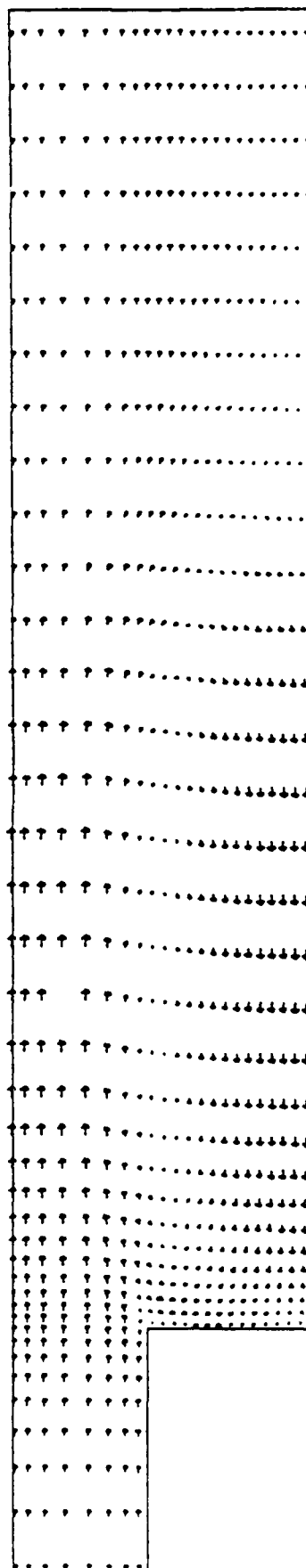
#### 4. RESULTS AND DISCUSSION

Table 6 shows the details of nine cases modeled with different combinations of several inflow and outflow boundary conditions. To identify the effect of the relative location of the inlet and exit boundaries on the reflection characteristics of the boundary conditions to be examined, two different finite-difference domains are considered. The baseline domain corresponding to Figure 40 consists of 60 nodes in the axial direction and 46 nodes in the radial direction. The domain represents a finite-cylindrical duct of length,  $L_d = 45.38$  cm and radius,  $R_d = 12.70$  cm and a centerbody of length,  $L_c = 10.50$  cm and radius,  $R_c = 7.00$  cm. The mesh is constructed with variable step sizes,  $\Delta x$  and  $\Delta r$  to provide a finer mesh at the near-wall regions of the centerbody and the duct, as well as in the recirculation zone of the centerbody near wake. Exponential stretching is used to construct the mesh with  $\Delta x$  varying between a maximum of 1.4 cm to a minimum of 0.24 cm and  $\Delta r$  varying between 0.505 cm to 0.24 cm. Figure 41 shows the extended domain, which consists of 80 nodes in the axial direction and 46 nodes in the radial direction. The physical dimensions of the two domains differ only in the axial length of the cylindrical duct ( $L_d$  is equal to 67.05 cm for the extended domain).

Table 7 shows the details of the numerical computations for modeling of the nine different cases of inflow and outflow boundary conditions given in Table 6. The table includes the values of the parameters to be specified for the inflow and outflow boundary conditions, CFL number, damping parameters ( $C_x$  and  $C_r$ ) and the initial distribution of the flowfield. In all the numerical computations, the values of the temperature and components of velocity to be specified at the centerbody and duct walls are kept constant at  $T_w = 536.6^\circ R$  and  $U_w = V_w = 0$ . Table 7 also includes the results of the numerical computations in terms of the average mass flow of the combustor flowfield, average

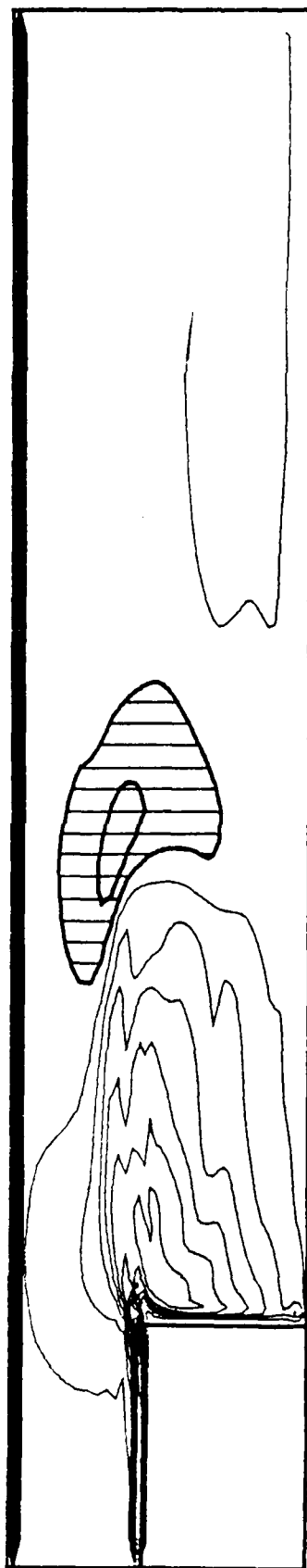


$N = 10,000$

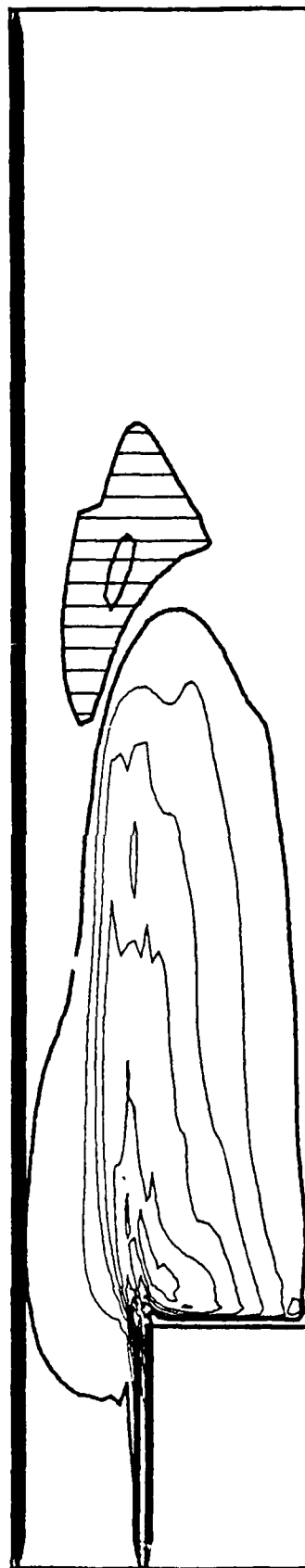


$N = 20,000$

Figure 47a. Velocity-Vector Plots for Case 3b of Table 7.



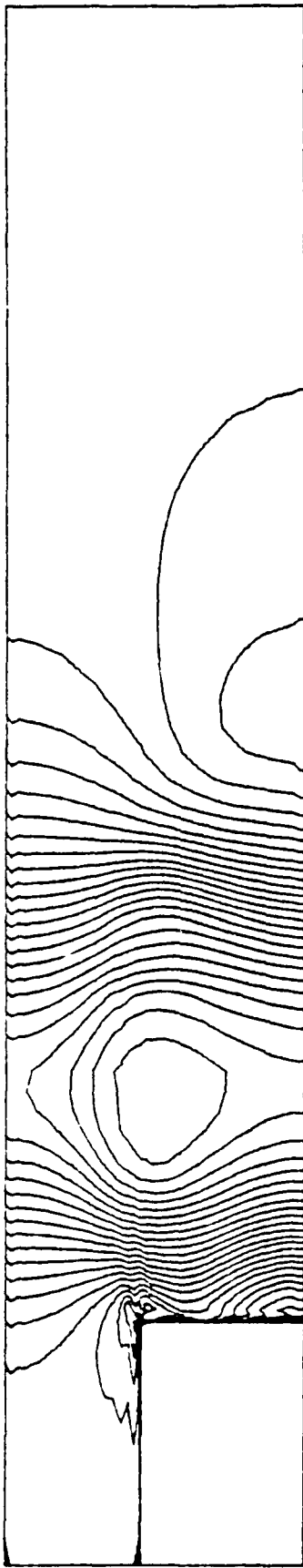
$N = 10,000$



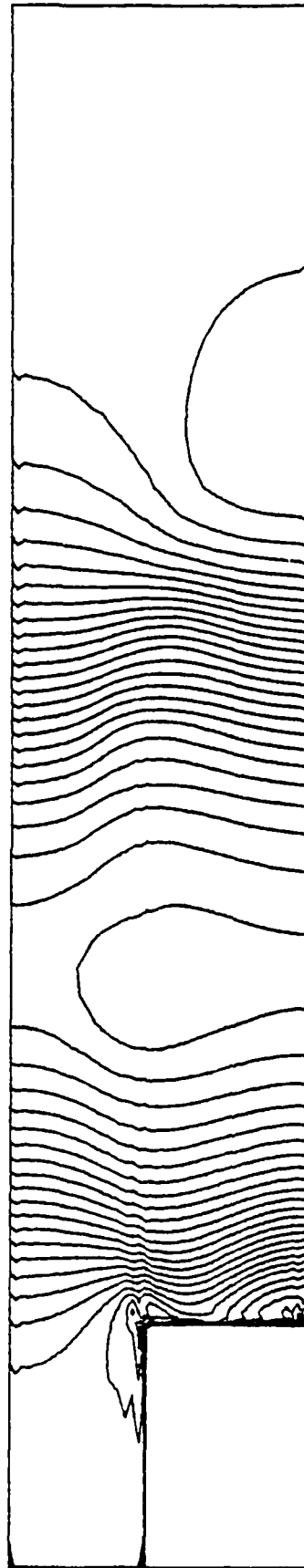
$N = 20,000$

Figure 47b. Vorticity-Contour Plots for Case 3b of Table 7.





$N = 10,000$



$N = 20,000$

Figure 47c. Pressure-Contour Plots for Case 3b of Table 7.

rate of 5.0 kg/s and a Reynolds number of  $2 \times 10^6$  on a (80 x 46) grid. Neither the increased Reynolds number nor the variation in the relative location of the inflow and outflow boundaries show any difference from the results of Cases 1 and 2. However, there are minor fluctuations in the mass flow rate with time, corresponding to a fundamental frequency of  $\omega_{x1} = a/4L_d = 128$  Hz for the numerical calculations performed on the (80 x 46) grid of Case 3b.

For the inflow boundary conditions involving the specification of total pressure, total temperature,  $V = 0$ ,  $\frac{\partial U}{\partial x}$  or  $\frac{\partial \rho U}{\partial x} = 0$ , it becomes practically impossible to specify at the inflow cross-section arbitrary profiles of  $U$  with characteristic values of the transverse gradients (especially with a definite value of mass flow at the inflow). When these inflow conditions are used in conjunction with the outflow conditions involving  $P = P_e$ , or the nonreflecting condition of Rudy and Strikwerda<sup>43</sup> for the flowfield with a steady-state solution, it becomes extremely difficult for the system to attain the desired mass flow rate. This difficulty is evident from the results of Cases 1, 3a, and 3b, where the average mass flow rates attained by the flowfield are given by 2.3 kg/s, 2.5 kg/s, and 5.0 kg/s, respectively. The situation becomes even worse for unsteady flowfields or when these inflow conditions are used in conjunction with outflow conditions involving the split condition of Hasen,<sup>44</sup> which permits variation of pressure with time at the outflow boundary.

The initial distribution of the flowfield for Case 4 corresponds to the solution of Scott and Hankey<sup>39</sup> at 25,700 DT. Figure 48 shows that the fluctuations in the mass flow persist for the first 8,000 DT. For the next 14,000 DT, both inflow and outflow mass flows reach essentially a constant value of 5.5 kg/s but with a slightly increasing monotonicity. The actual dynamics of this tendency to steady mass flow rate can be seen from the velocity vector plots of Figures 49a and 49b and the vorticity contour plots of Figures 49c and 49d. In Figures 49c and 49d, breaking up of the clockwise recirculation vortex occurs as a counterclockwise vortex originates at the centerline of the cen-

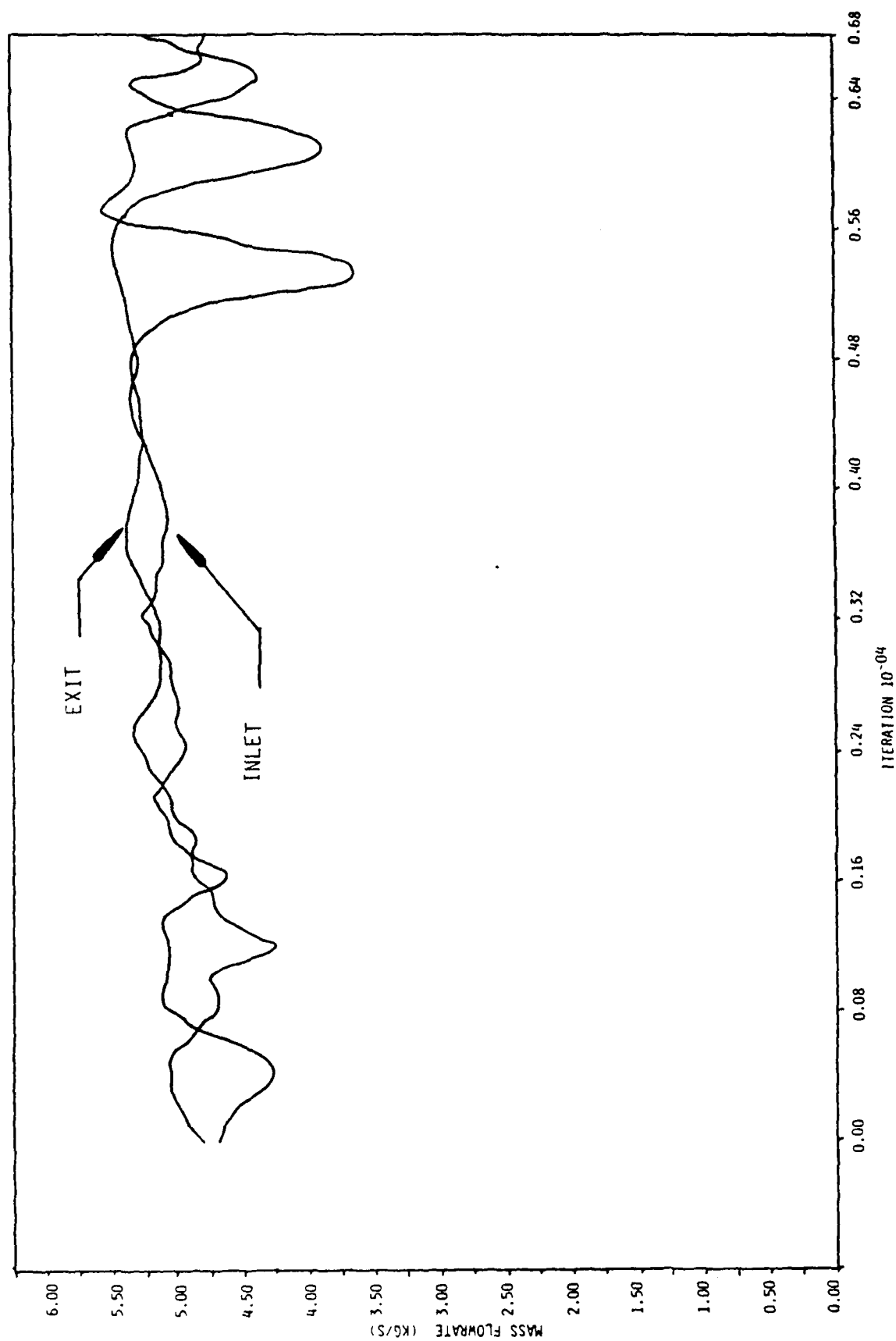


Figure 48a. Temporal Variation in Combustor Mass Flow for Case 4 of Table 7.

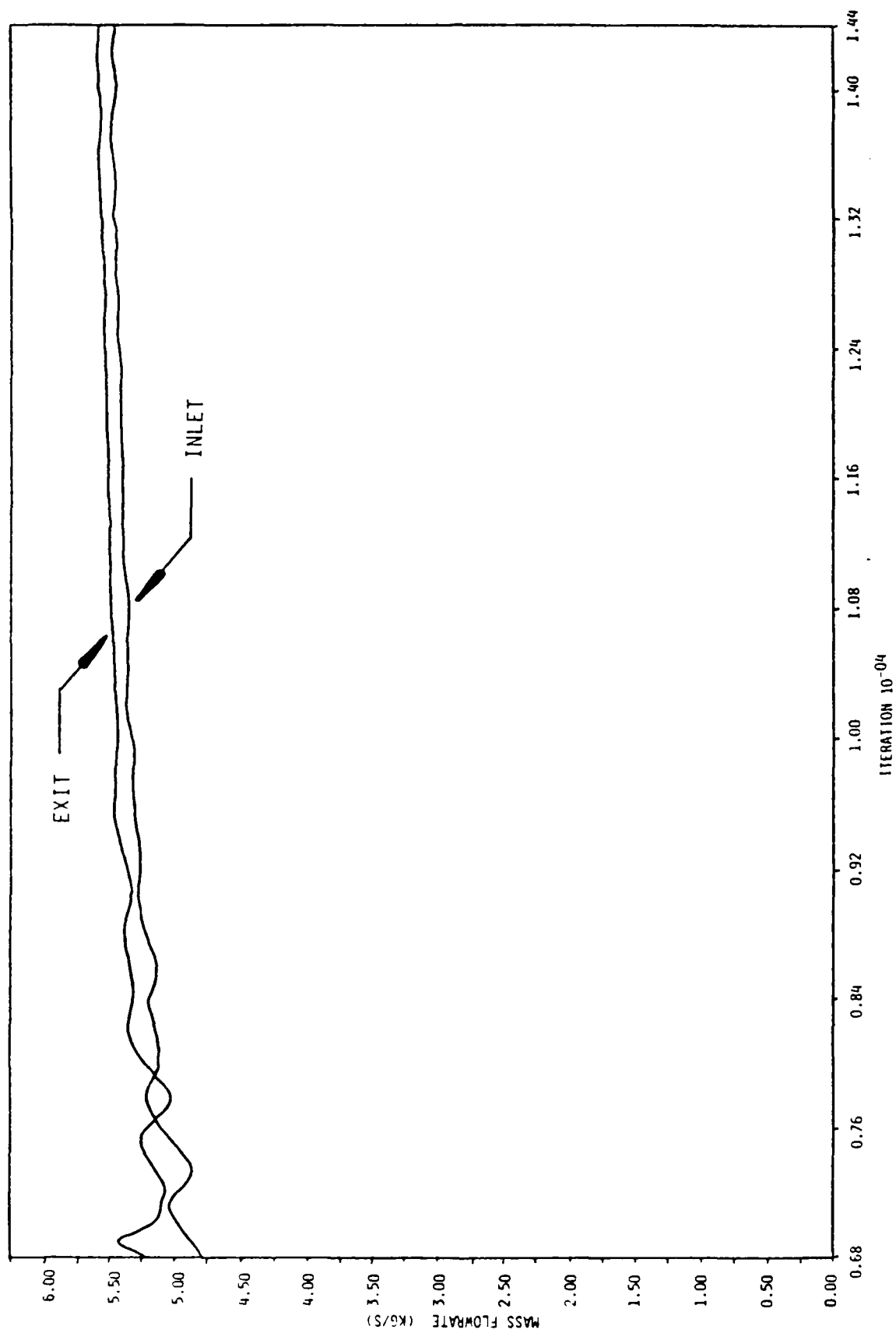


Figure 48b. Temporal Variation in Combustor Mass Flow for Case 4 of Table 7.

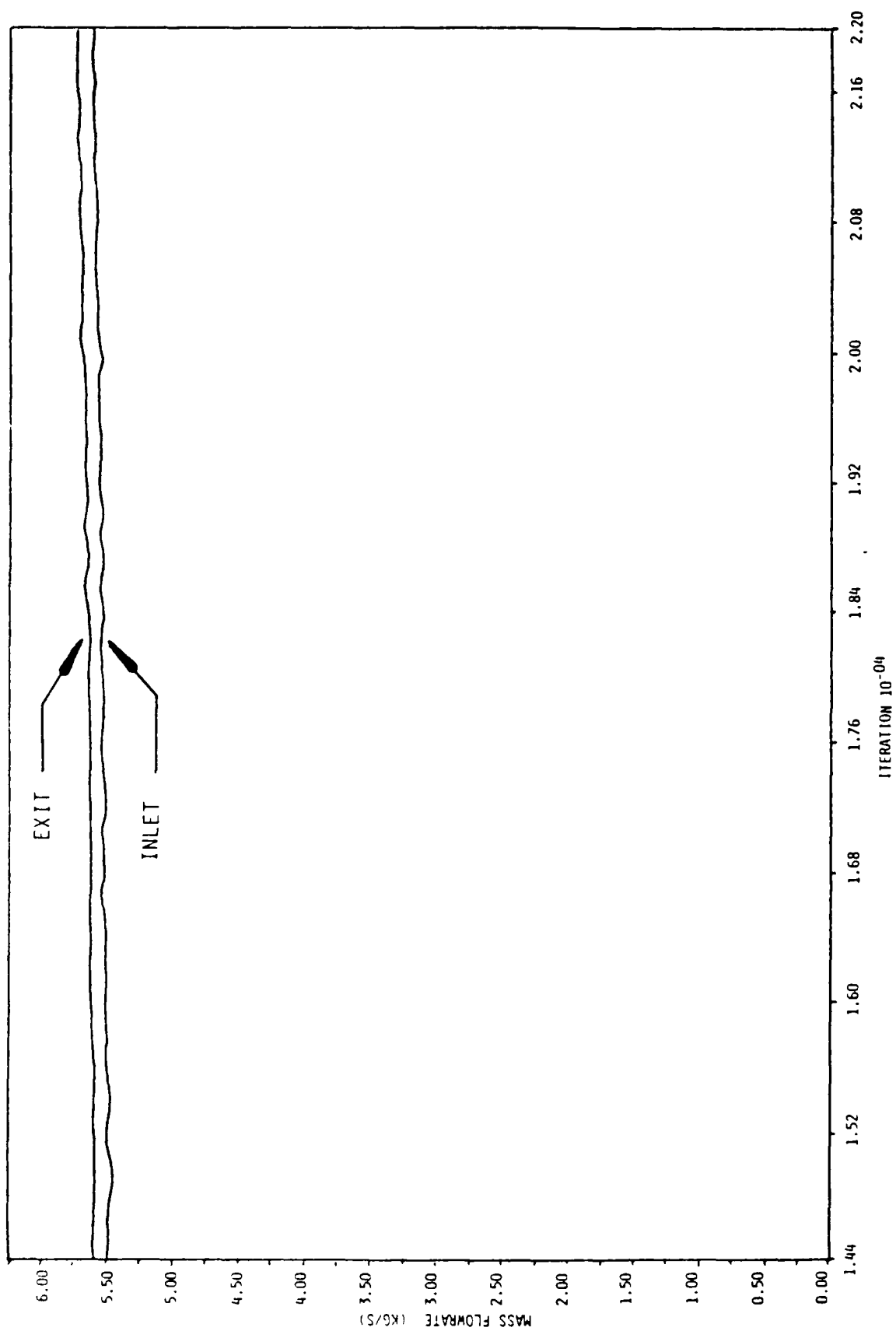
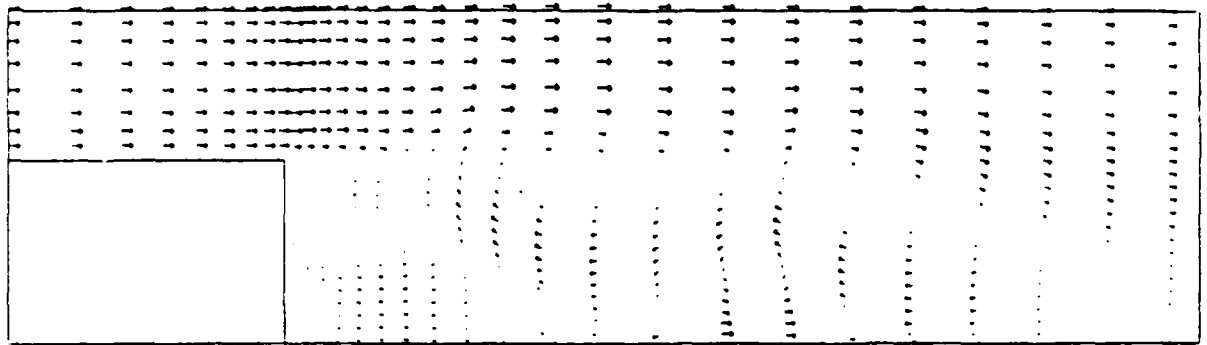
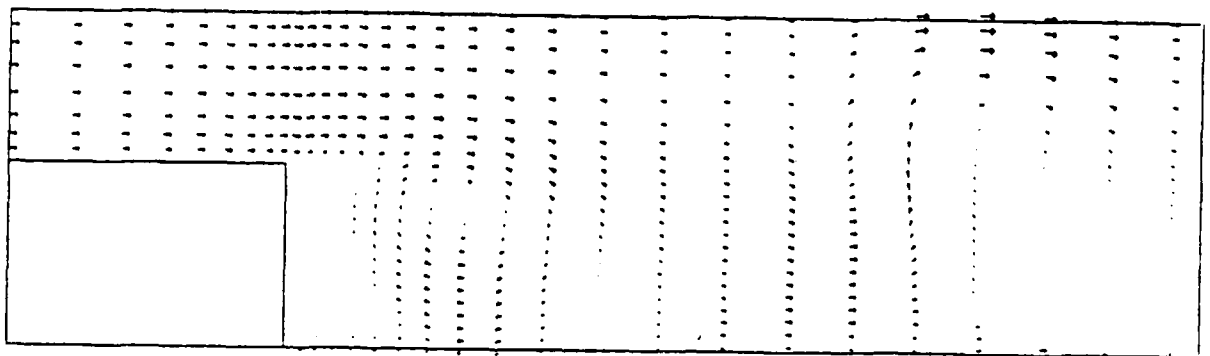


Figure 48c. Temporal Variation in Combustor Mass Flow for Case 4 of Table 7.

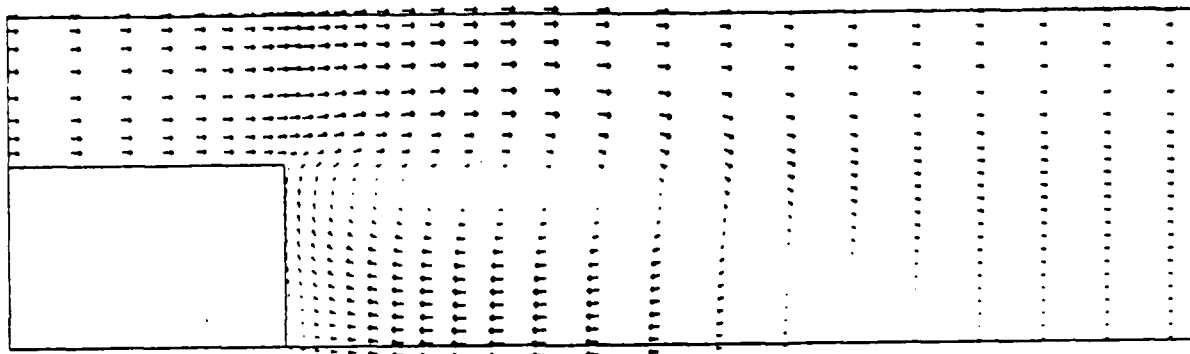


$N = 4,000$

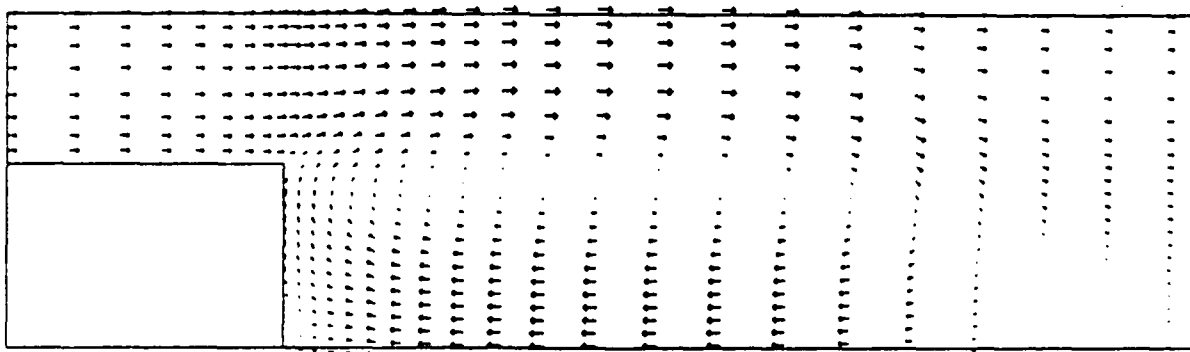


$N = 5,000$

Figure 49a. Velocity Vector Plots for Case 4 of Table 7.

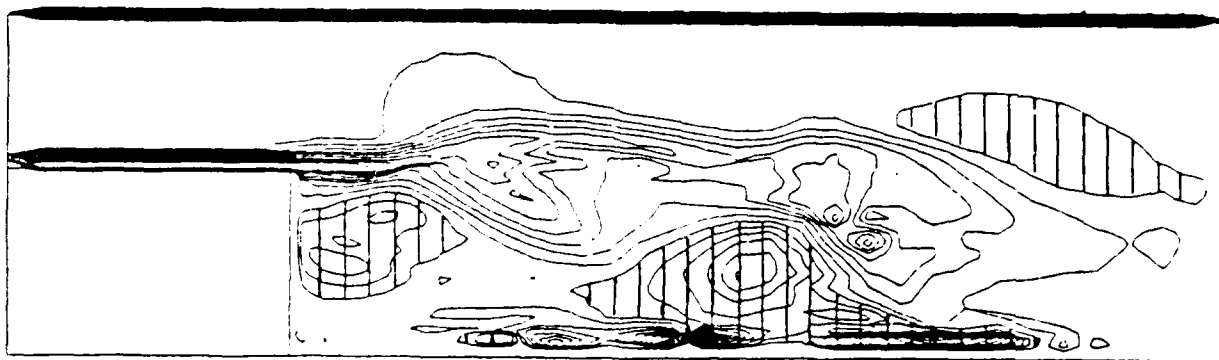


$N = 11,000$

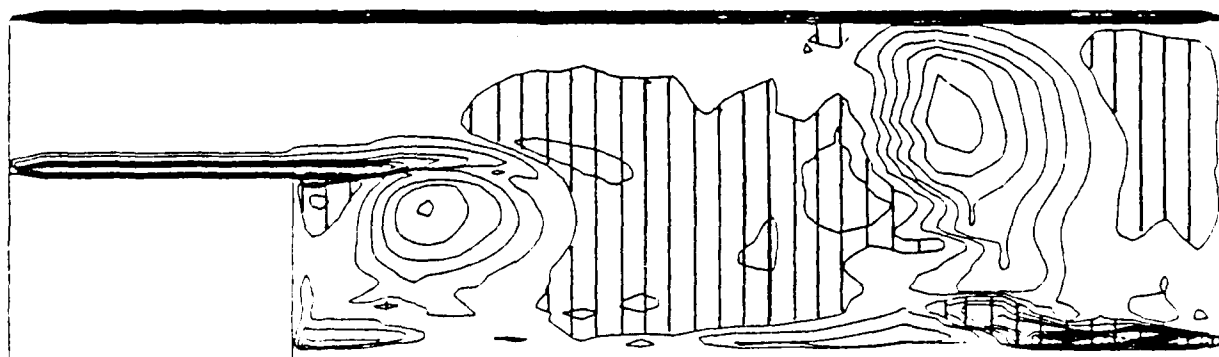


$N = 22,000$

Figure 49b. Velocity Vector Plots for Case 4 of Table 7.



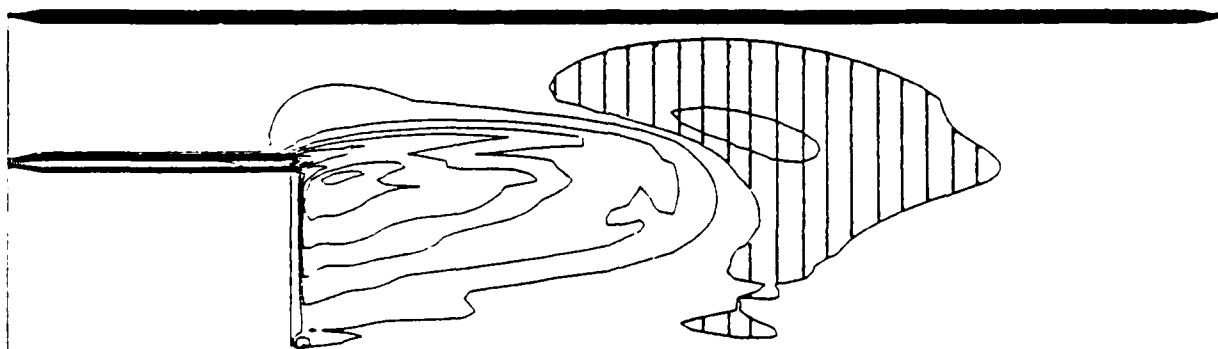
$N = 4,000$



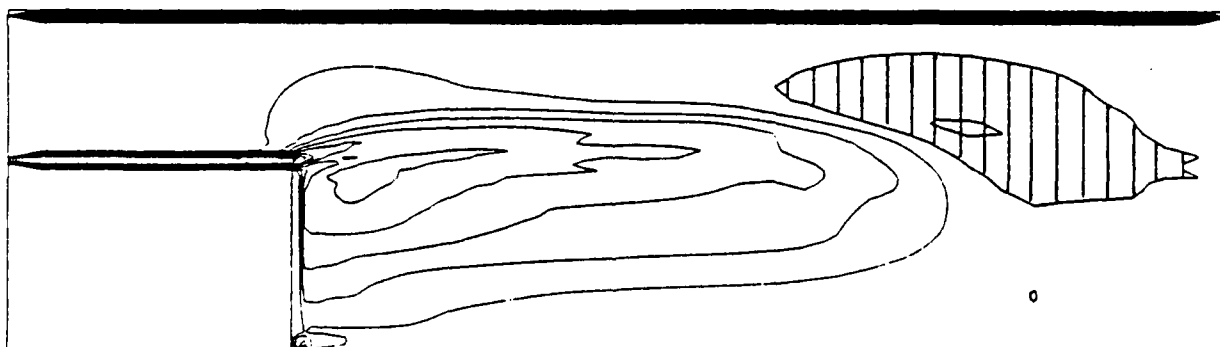
$N = 5,000$

Figure 49c. Vorticity-Contour Plots for Case 4 of Table 7.





$N = 11,000$



$N = 22,000$

Figure 49d. Vorticity-Contour Plots for Case 4 of Table 7.

terbody near wake, gains strength, and grows. At 5,000 DT, the figures show the remnant of the clockwise vortex which is about to be washed off downstream. From this point onwards the mass flow rates tend to their constant values, the clockwise recirculation vortex begins to grow, pushing the eddies towards the exit, and the final state resembles that of Figures 49b and 49d depicting the stretching of a stationary recirculation vortex, extending in the axial direction at a rate of 3m/sec. The large mass flow fluctuations of Figure 48 correspond to the time during which eddies are washed off the exit. Thus, approximately 8,000 DT are required for the initial transient fluctuations to disappear and the flow to attain a steady mass flow rate of 5.5 kg/s.

It is important to note that none of the calculations involving Cases 1 to 4 of Table 7 are continued long enough for the reverse flow to reach the outflow boundary, which would eventually happen due to the stretching of the recirculation zone in the axial direction. The rate at which the recirculation zone extends in the axial direction is found to be very slow at 3 m/s in all the cases considered.

Figures 50 and 51 correspond to Case 5 of Table 7. The inflow and outflow conditions are identical to Case 4, except for the inflow boundary conditions, which are programmed by the simplified procedure described in Paragraph III.2.a(2b). During the first 20,000 DT, after the initial attenuation of the longitudinal oscillations a steady mass flow rate is established as evidenced by Figures 51a, 51c, and 51e. Recall that three boundary conditions are to be specified when there is a reverse flow at the outflow boundary. As the extending recirculation vortex causes reverse flow at the outflow boundary around 22,000 DT, the split boundary condition involving the specification of only exit pressure cannot objectively handle the appropriate physics of the flowfield. As soon as this happens, reverse longitudinal oscillations are established, causing the domain to act as a

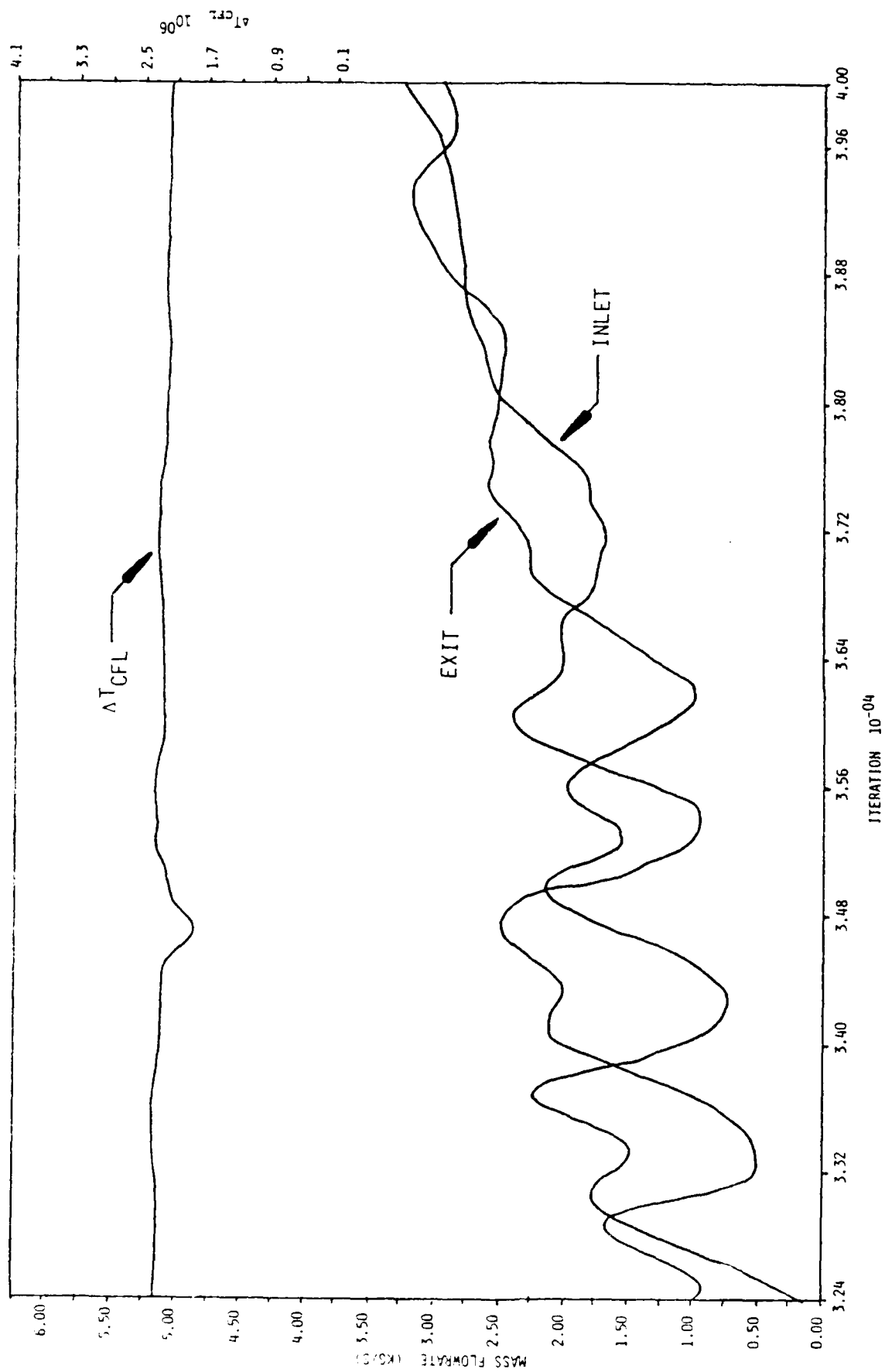


Figure 50a. Temporal Variation in Combustor Mass Flow and  $\Delta T_{CFL}$  for Case 5 of Table 7.

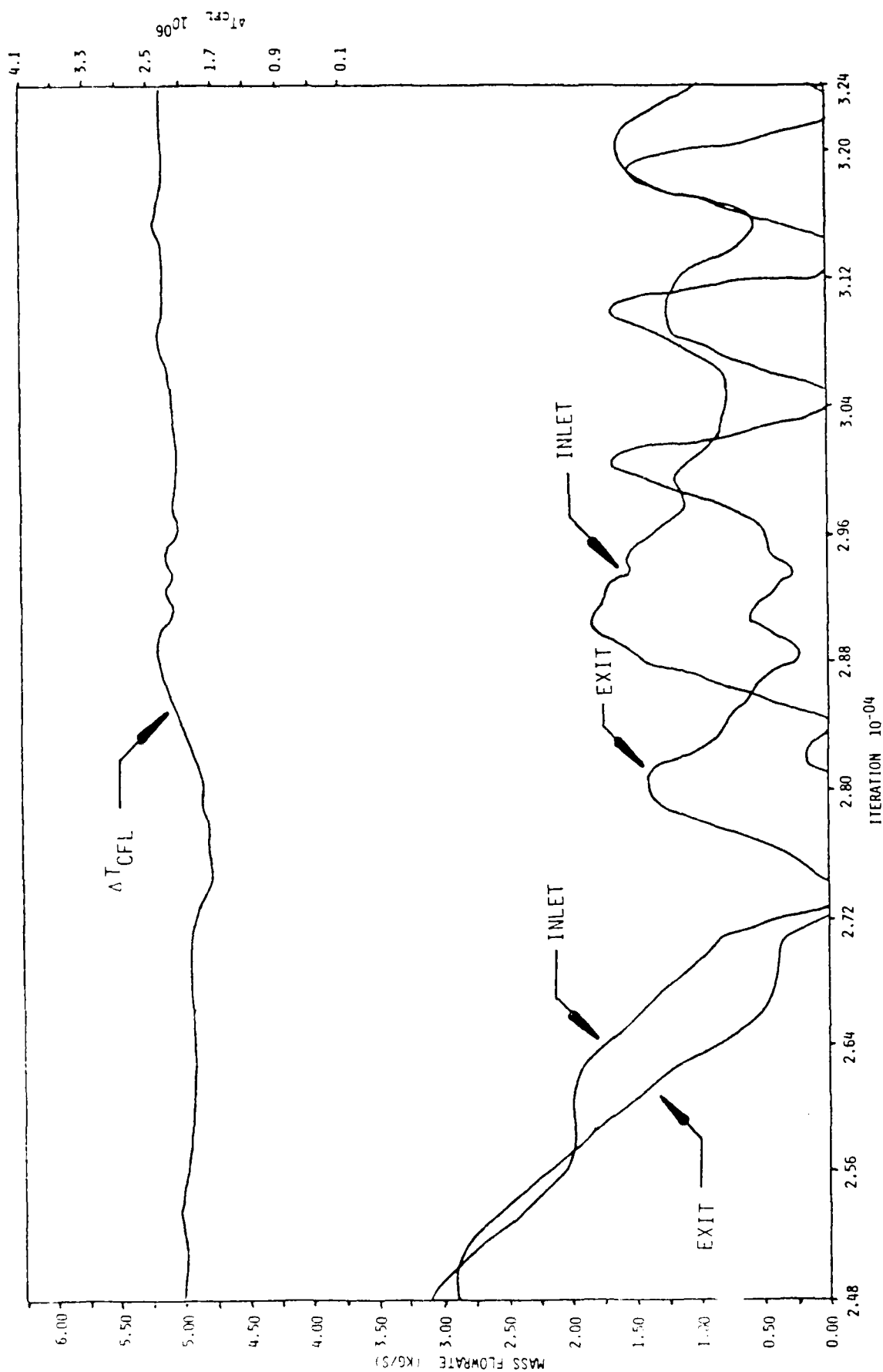
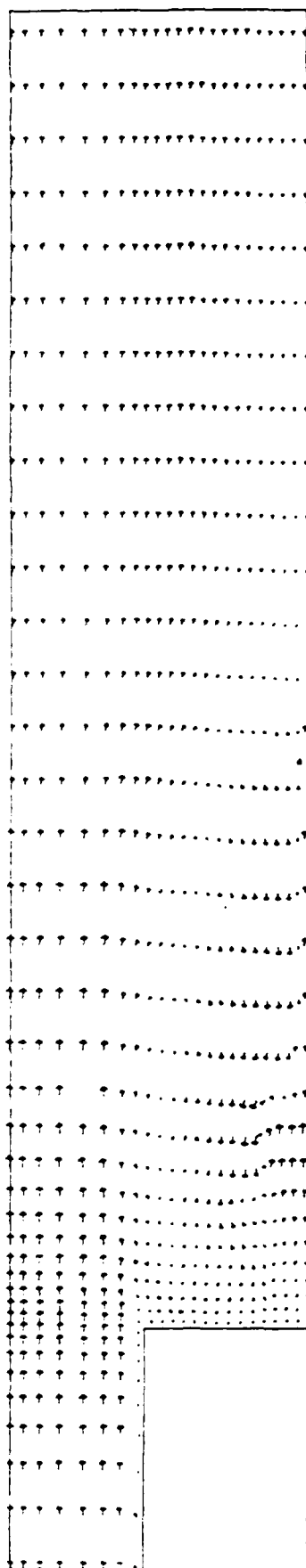
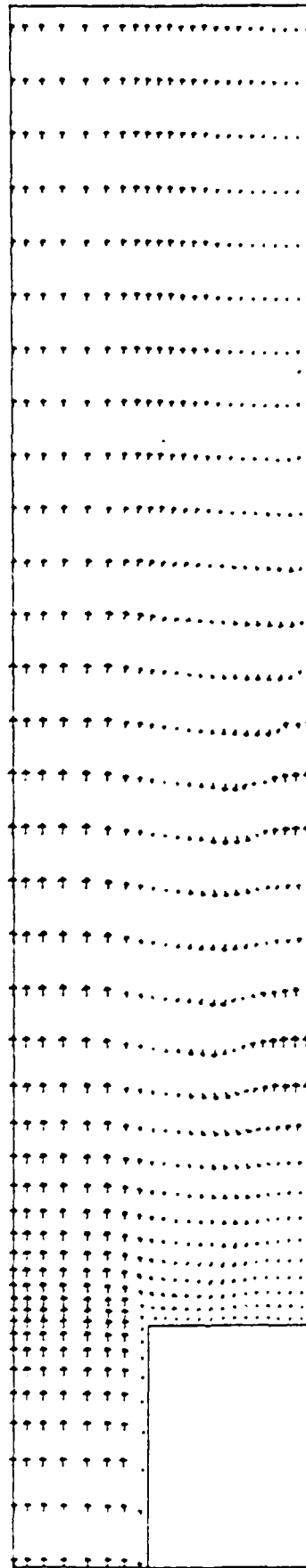


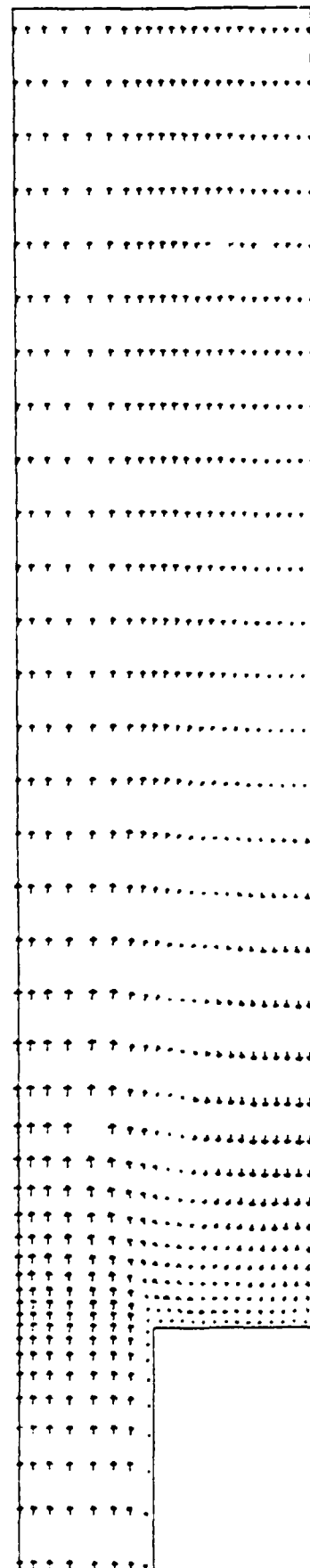
Figure 50b. Temporal Variation in Combustor Mass Flow and  $\Delta T_{CFL}$  for Case 5 of Table 7.



$N = 10,000$



$N = 20,000$



$N = 30,000$

Figure 55a. Velocity-Vector Plots for Case 6b of Table 7.

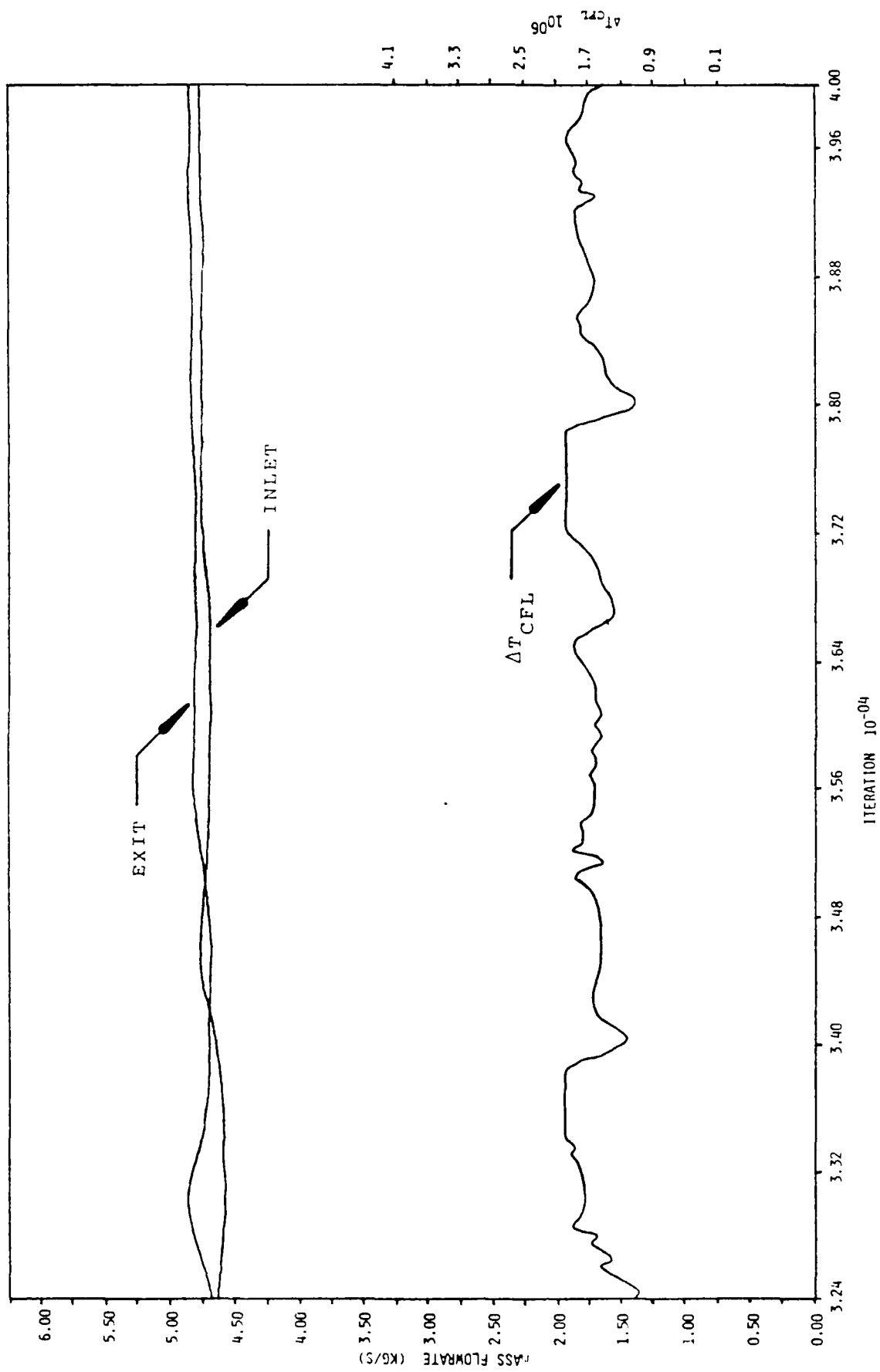


Figure 54b. Temporal Variation in Combustor Mass Flow and  $\Delta T_{CFL}$  for case 6b of Table 7.

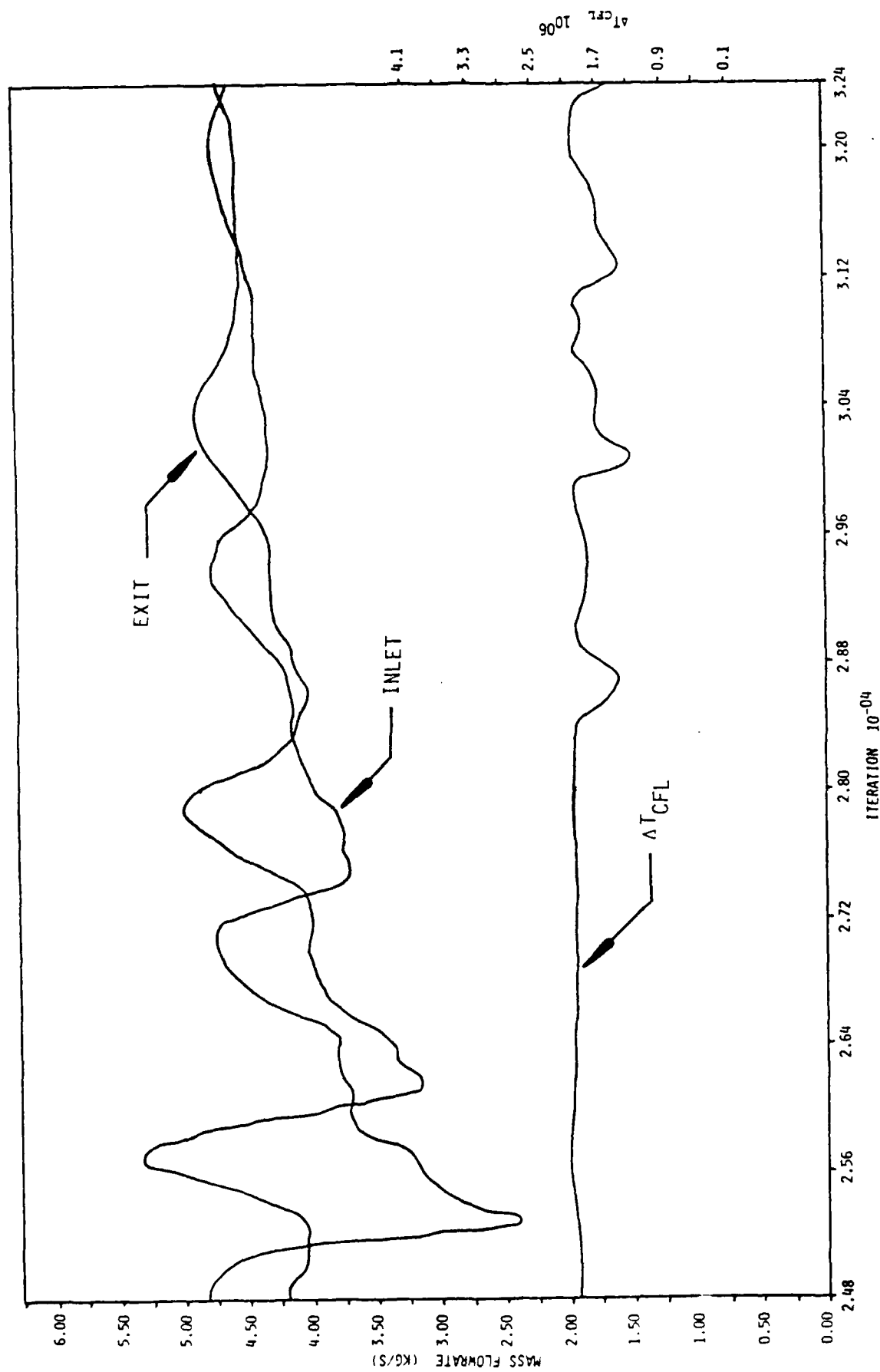


Figure 54a. Temporal Variation in Combustor Mass Flow and  $\Delta T_{CFL}$  for Case 6b of Table 7.

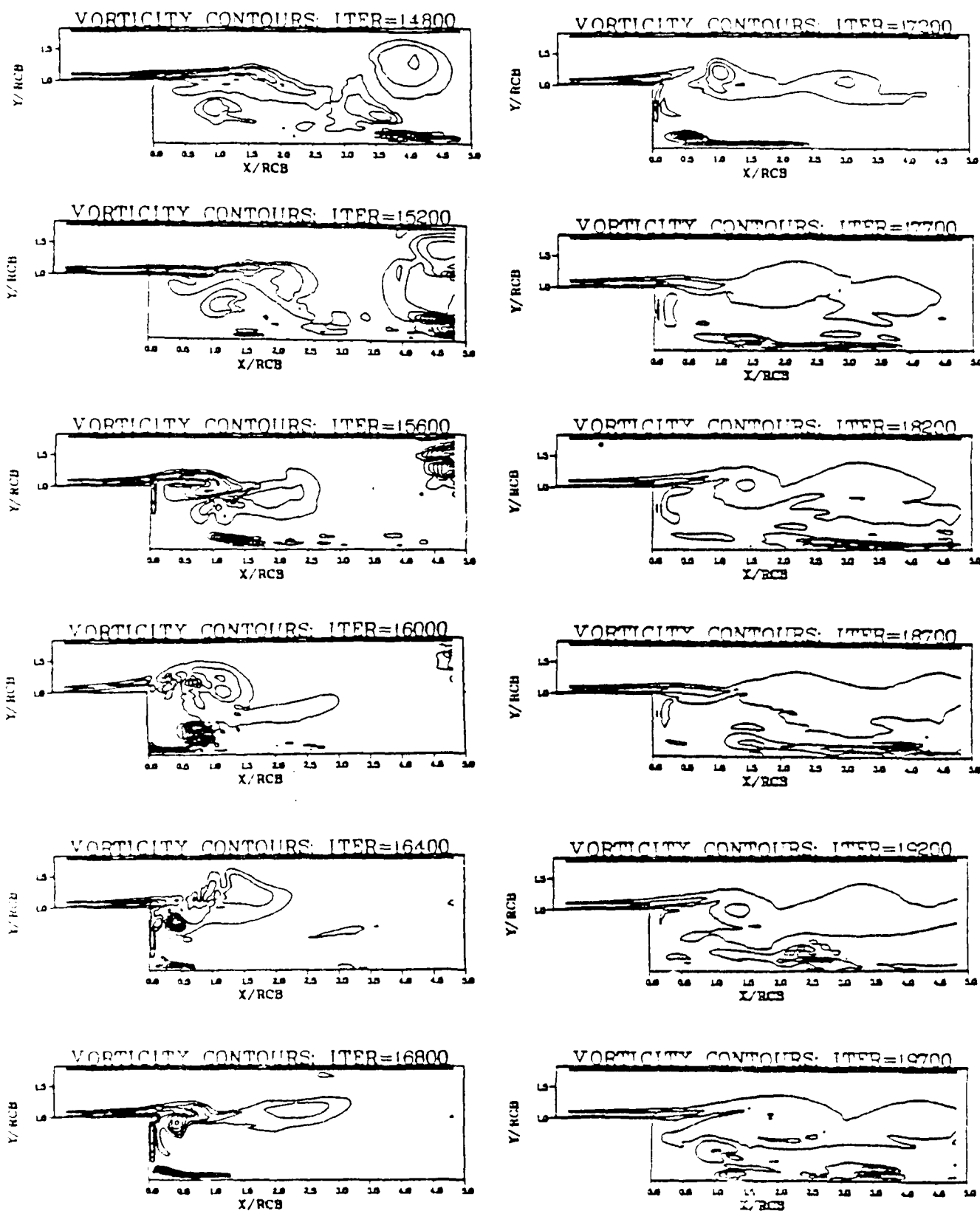


Figure 53a. Vorticity-Contour Plots for Case 6: of Table 7.  
(after Reference 39)



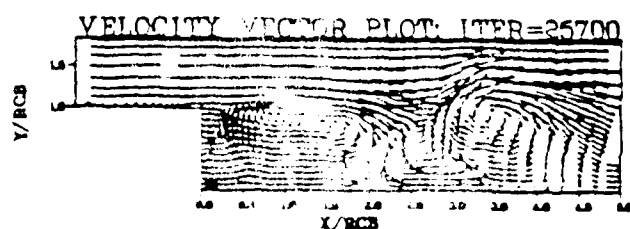
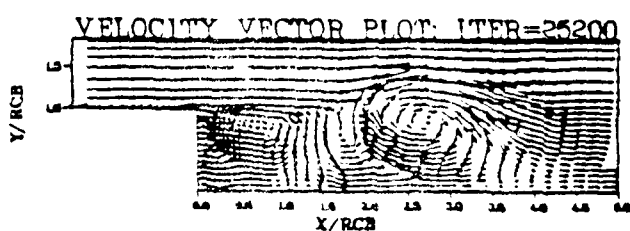
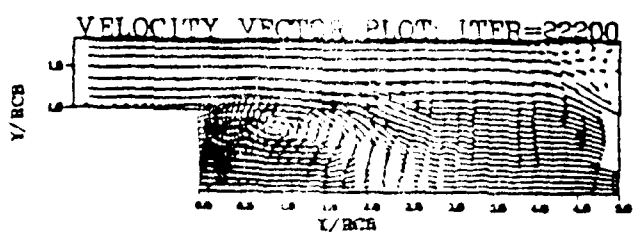
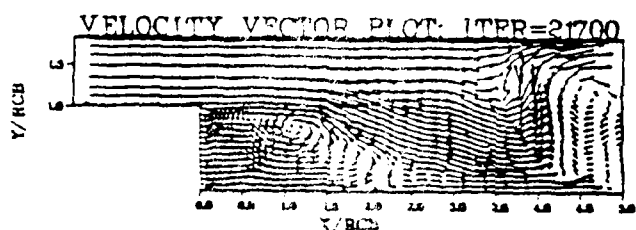
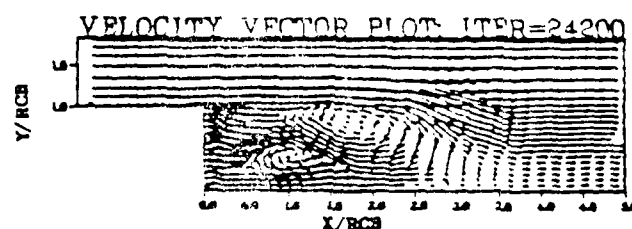
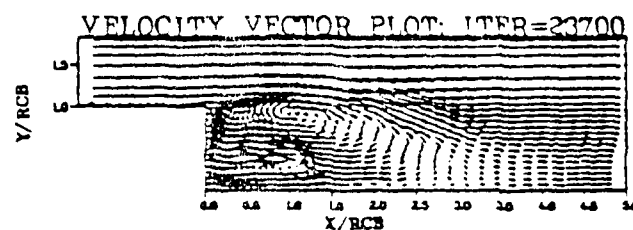
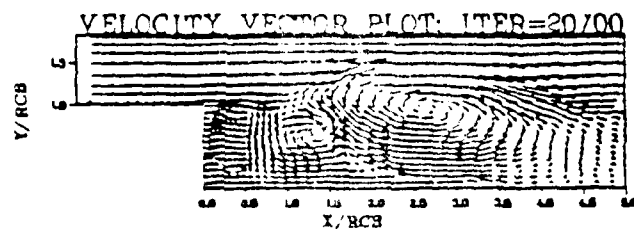
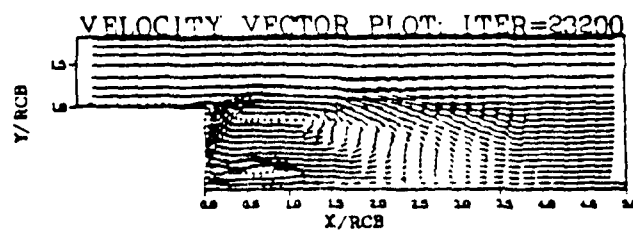
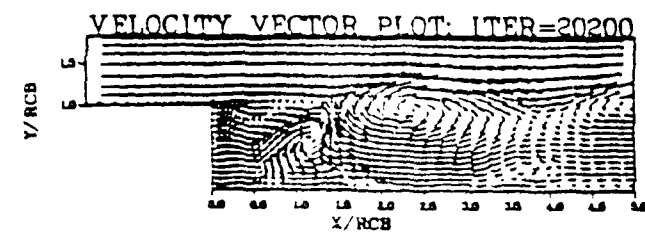


Figure 5. Velocity-Vector Plots for a series of Table 7.  
(after reference 39)

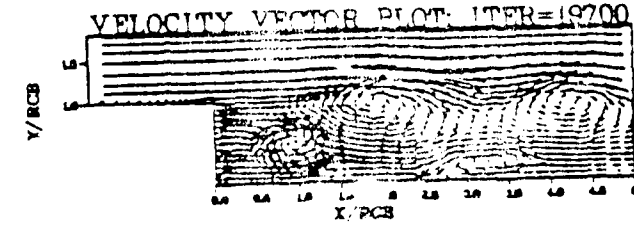
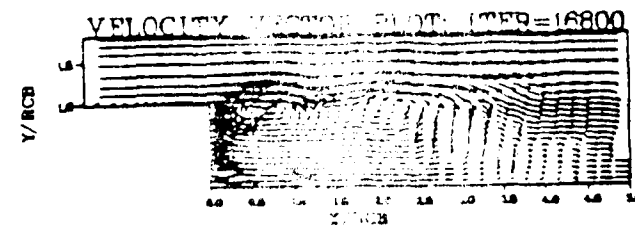
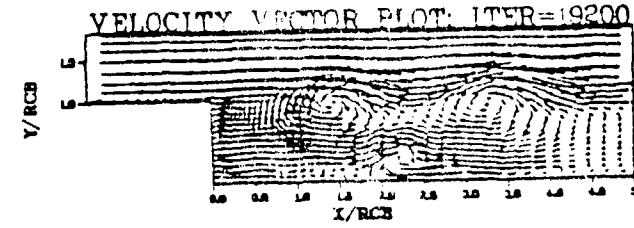
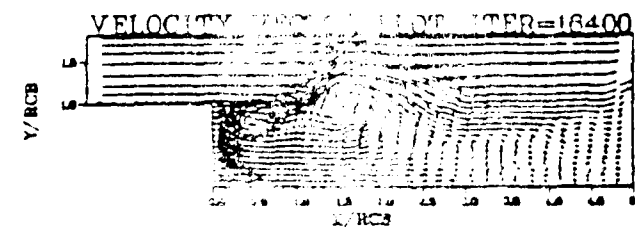
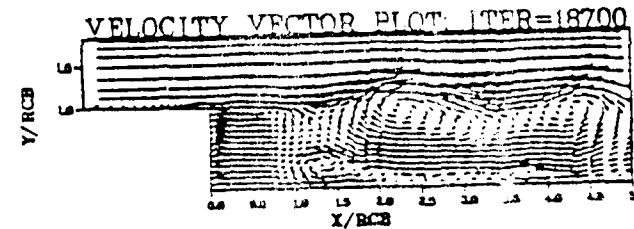
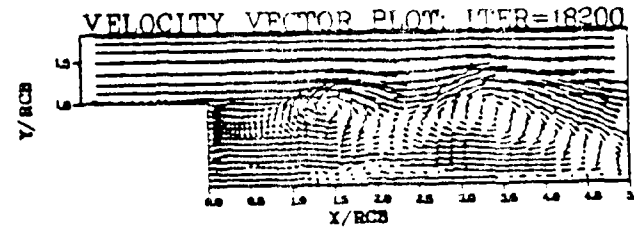
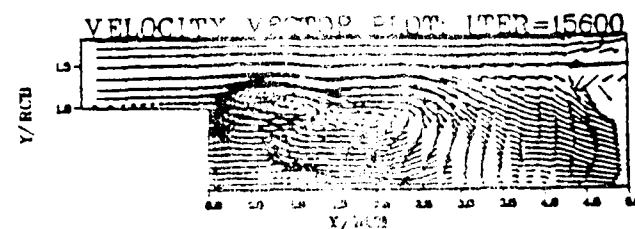
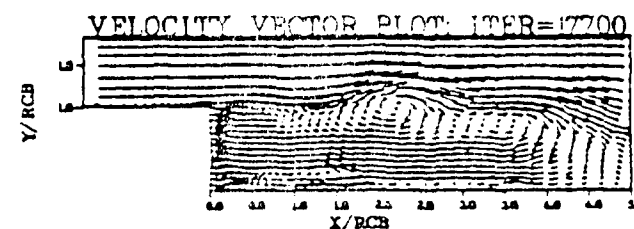
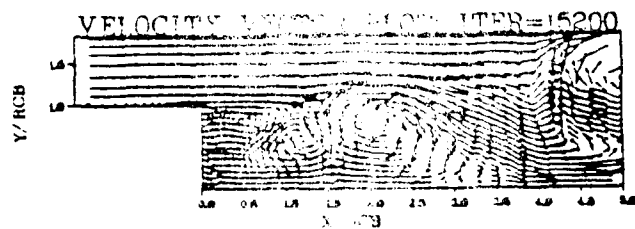
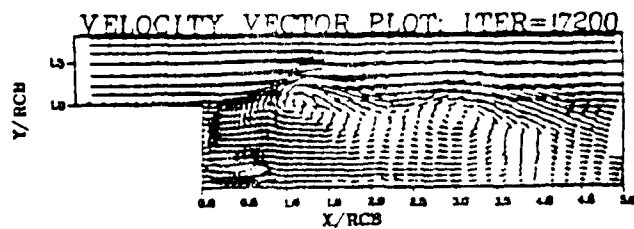


Fig. 7. Velocity-Vector Plots for case 6a of Table 7.  
(after Reference 39)

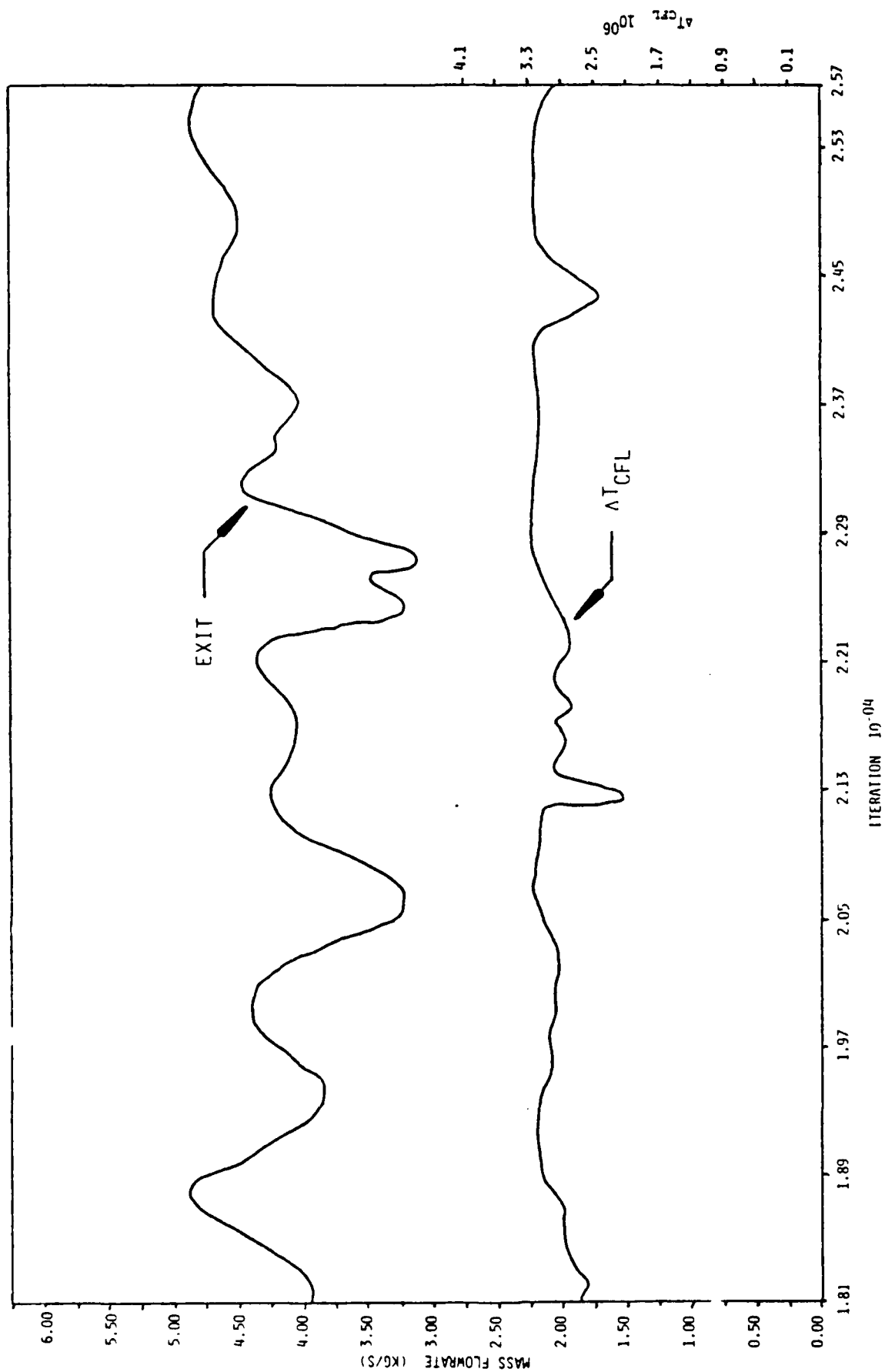
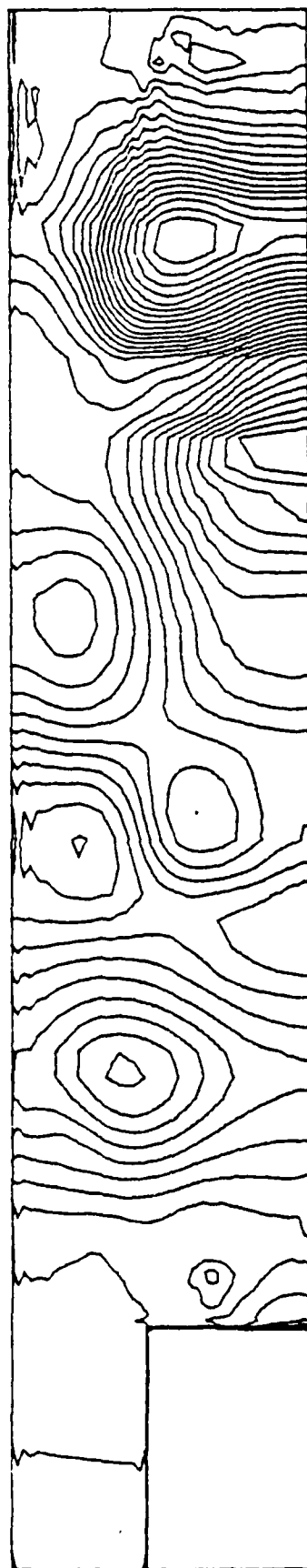


Figure 52. Temporal Variation in Combustor Mass Flow and  $\Delta T_{CFL}$  for Case 6a of Table 7.

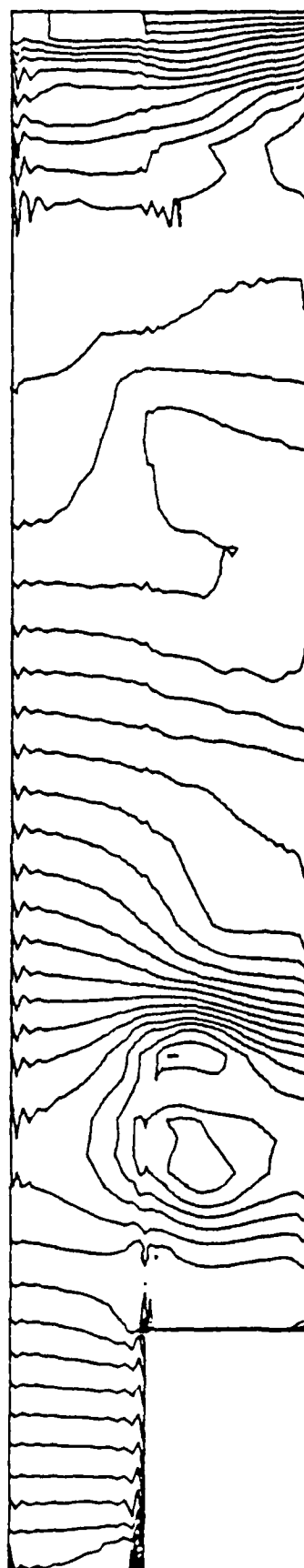
resonator with a fundamental frequency of the quarter-wave resonator. This process of acoustic interaction with the recirculation zone is accompanied by shedding-like phenomena seen in Figures 51b, 51d, and 51f. The mass-flow fluctuations of Figure 50 show that the amplification of the longitudinal oscillations result in a complete reversal of the mass flow at the inflow and outflow boundaries and the numerical solution becomes unstable and nonphysical.

Cases 6a, 6b, and 6c of Table 7 refer to the inflow and outflow conditions discussed in Paragraphs III.2.a(2b) and III.2.b(3b). Figures 52 and 53 are taken from Reference 39. Figure 52 shows that the mass flow varies between a maximum of 4.875 kg/s to a minimum of 3.125 kg/s and the variations in the  $\Delta T_{CFL}$  is a result of the temperature fluctuations in the flowfield as  $\Delta T_{CFL} \sim 1/\sqrt{T}$ . The numerical calculations of the isothermal flowfield showed temperature fluctuations ranging from 4,000°R to 250°R but the fluctuations are restricted to a very narrow band of the grid near the centerline of the reattachment point of the recirculation region. It appeared that these temperature fluctuations were caused by a violation of the CFL criterion due to an earlier discrepancy in the TIMESTEP subroutine. Figure 53 shows the velocity vector plots and vorticity contour plots. For a discussion of the results on the unsteady solution of Case 6a, the reader is referred to Reference 39.

For Case 6b, the numerical calculations are performed on a (80 x 46) grid with the corrected TIMESTEP subroutine. Figure 54 shows that the mass fluctuations persist for as long as 36,000 DT before establishing a steady mass-flow rate. However, the temporal variation of  $\Delta T_{CFL}$  and the associated temperature fluctuations ( $\Delta T_{CFL} \sim 1/\sqrt{T}$ ) are indications of nonphysical behavior of the solution as the calculations are performed under isothermal conditions. Figures 55a to 55e show the initial oscillatory flowfield before the establishment of a single recirculation vortex.

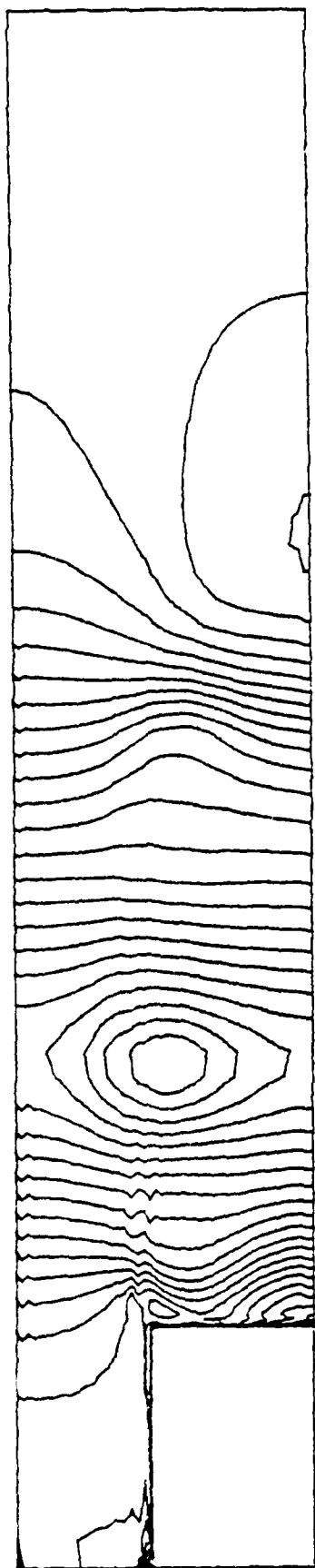


$N = 30,000$

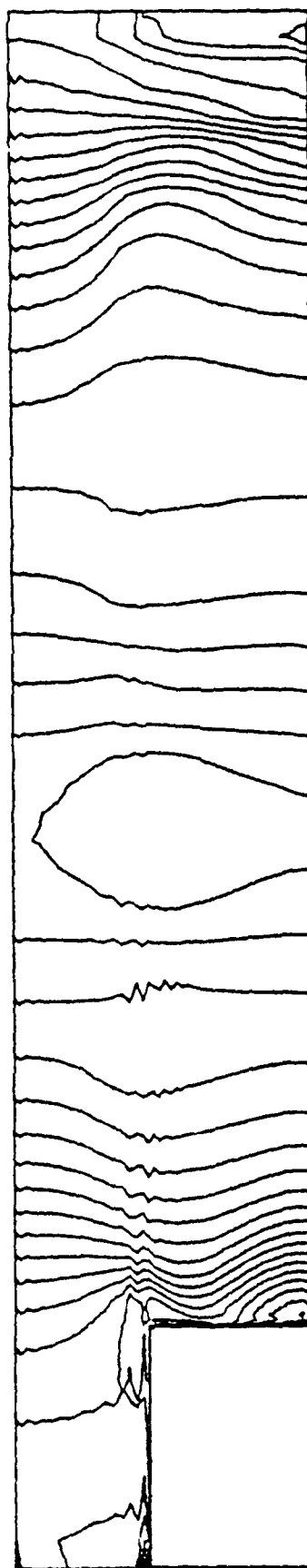


$N = 40,000$

Figure 5lf. Pressure-Contour Plots for Case 5 of Table 7.

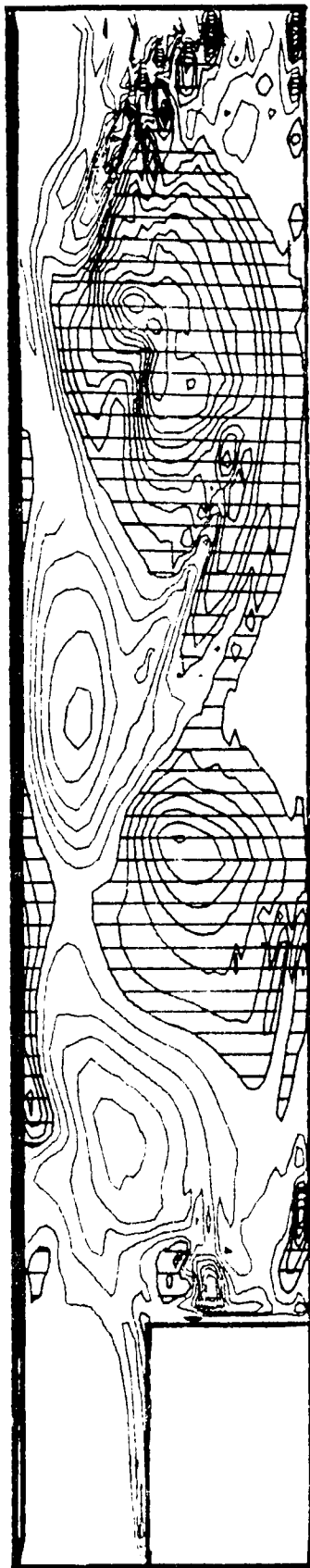


$N = 10,000$

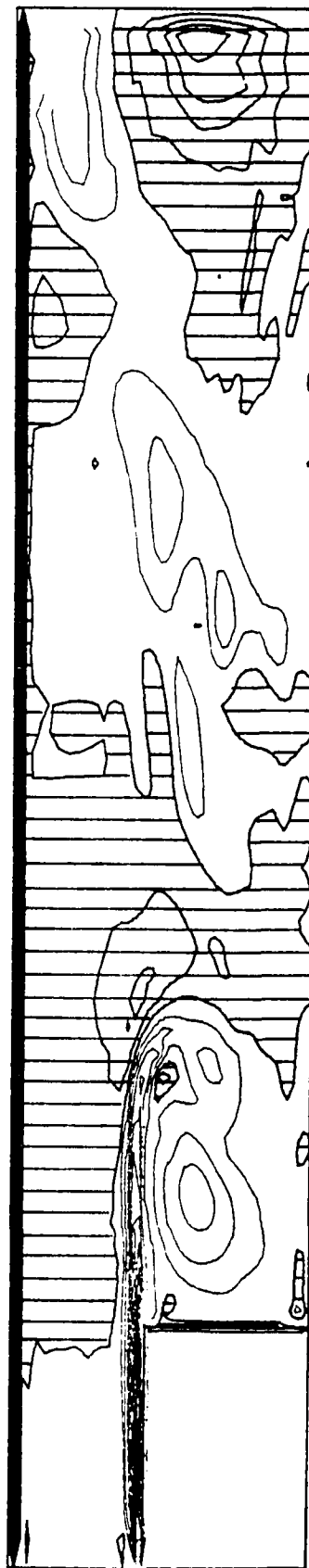


$N = 20,000$

Figure 5le. Pressure-Contour Plots for Case 5 of Table 7.

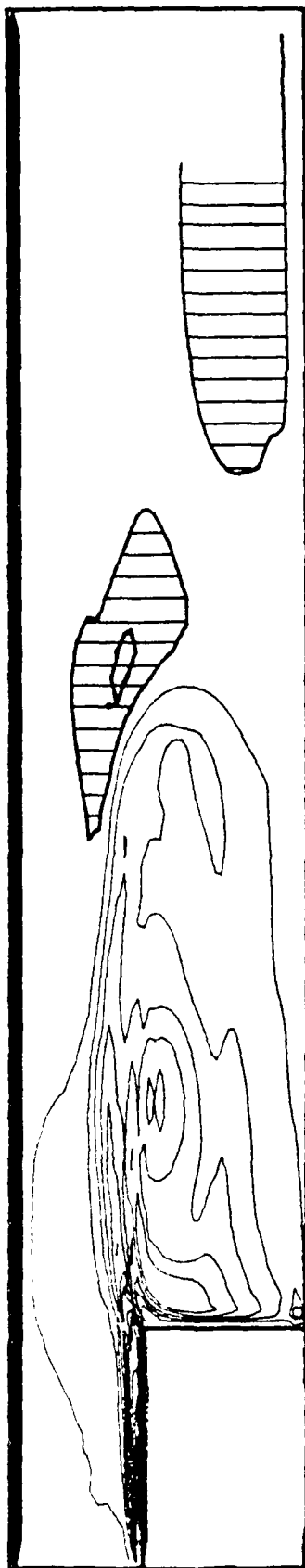


$N = 30,000$

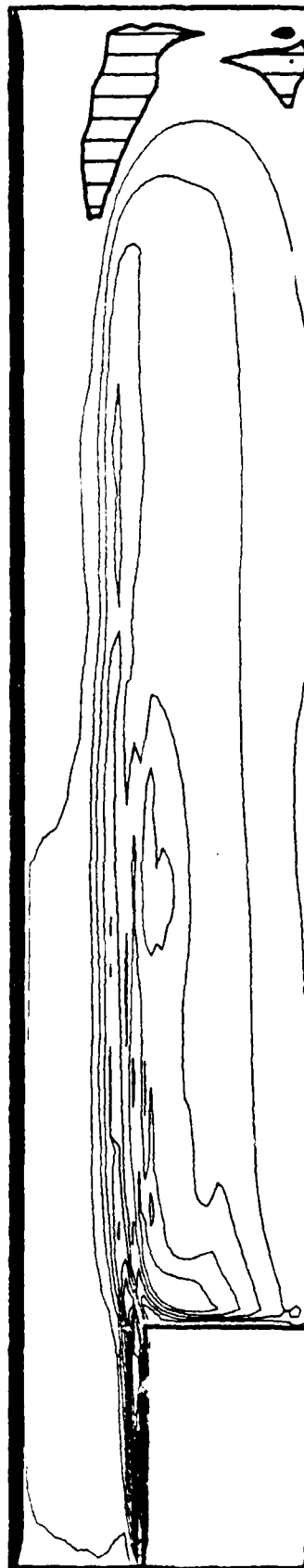


$N = 40,000$

Figure 5ld. Vorticity-Contour Plots for Case 5 of Table 7.



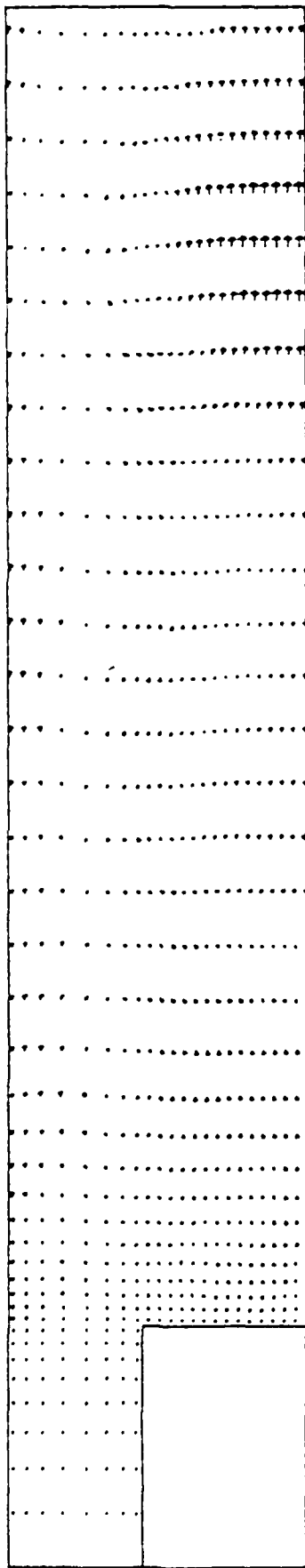
$N = 10,000$



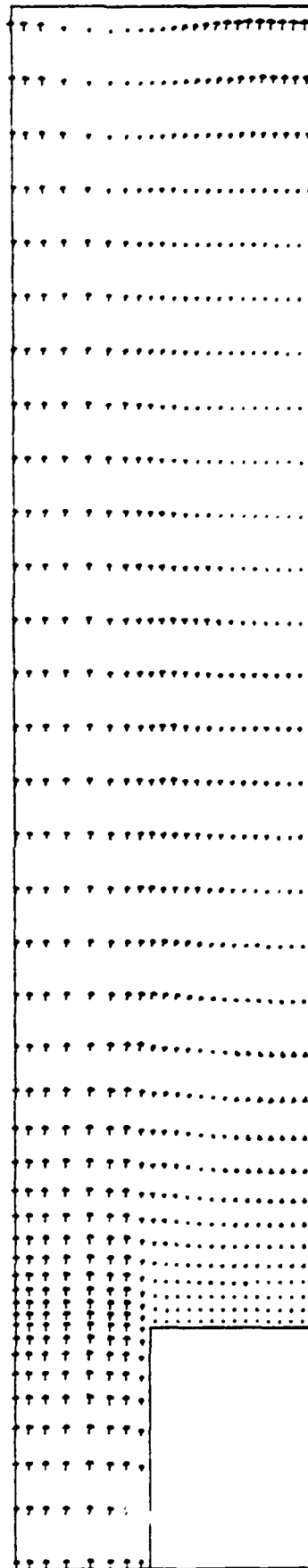
$N = 20,000$

Figure 51c. Vorticity-Contour Plots for Case 5 of Table 7.



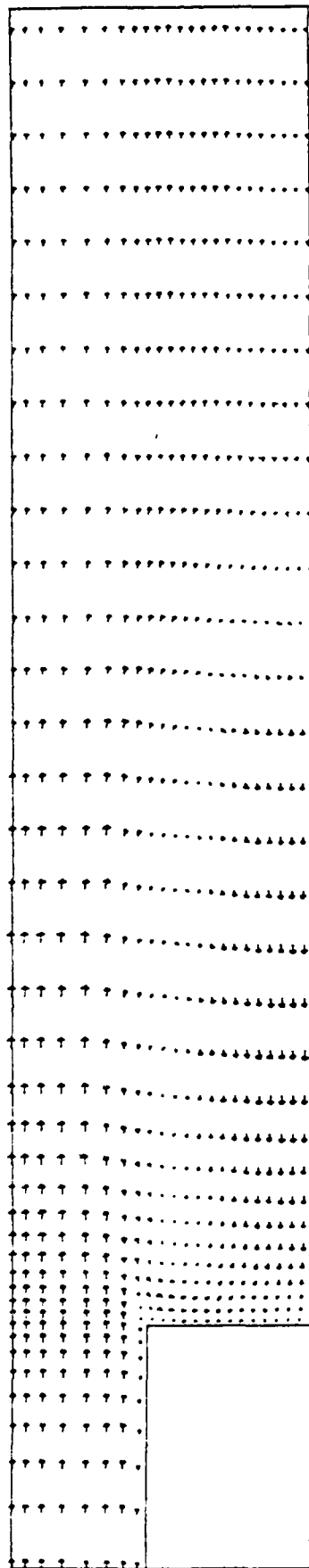


$N = 30,000$

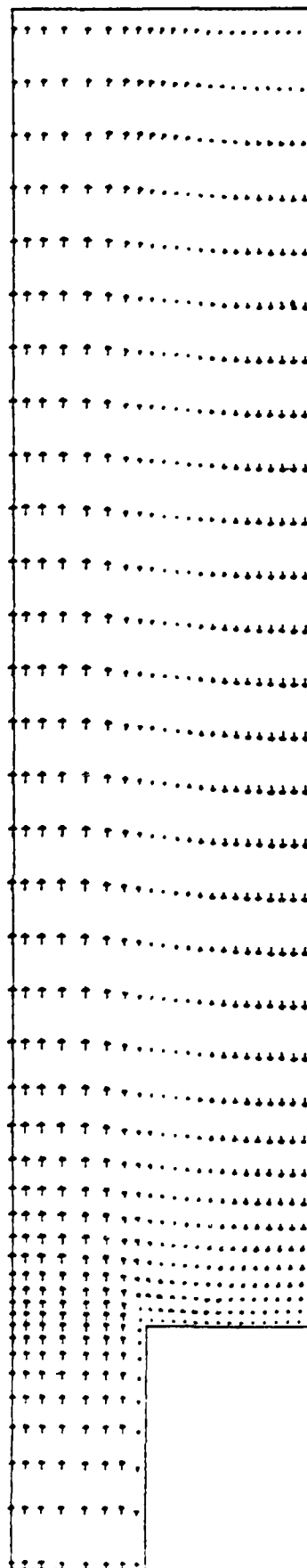


$N = 40,000$

Figure 5lb. Velocity-Vector Plots for Case 5 of Table 7.

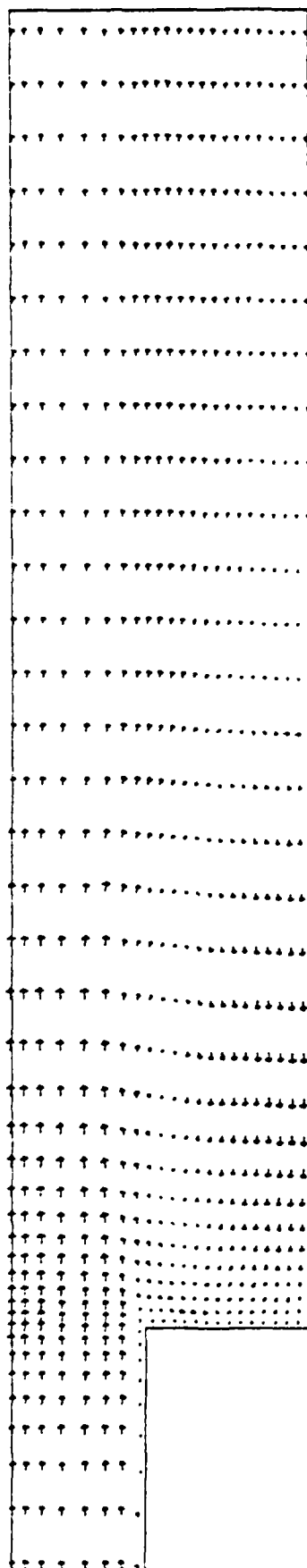


$N = 10,000$

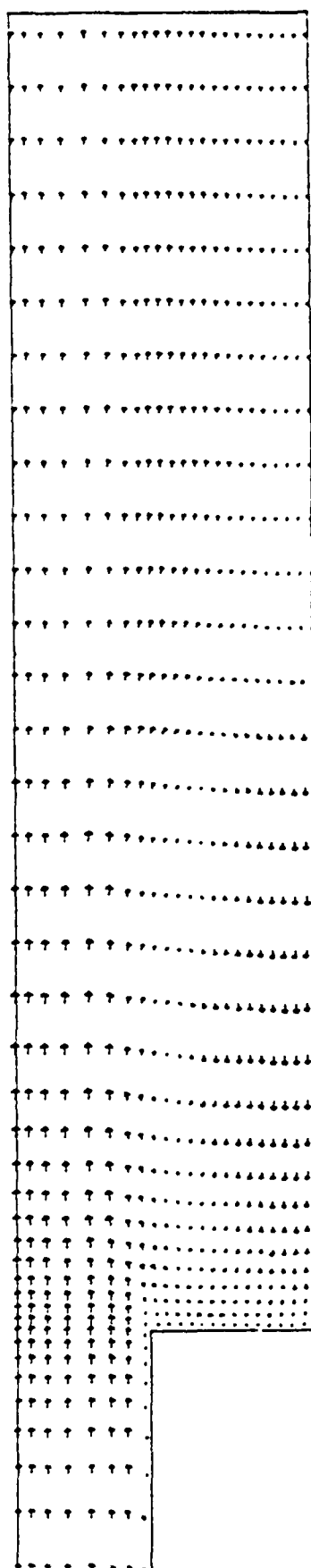


$N = 20,000$

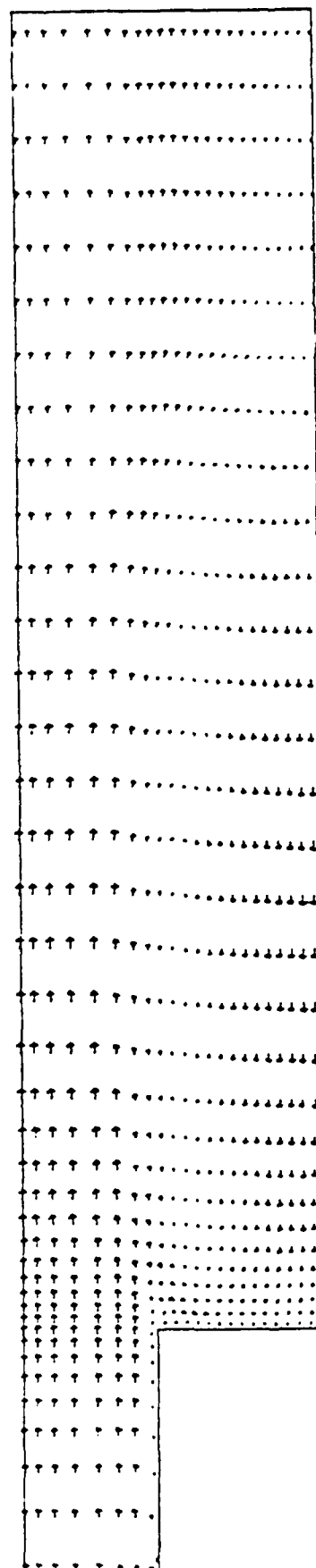
Figure 51a. Velocity-Vector Plots for Case 5 of Table 7.



$N = 32,000$

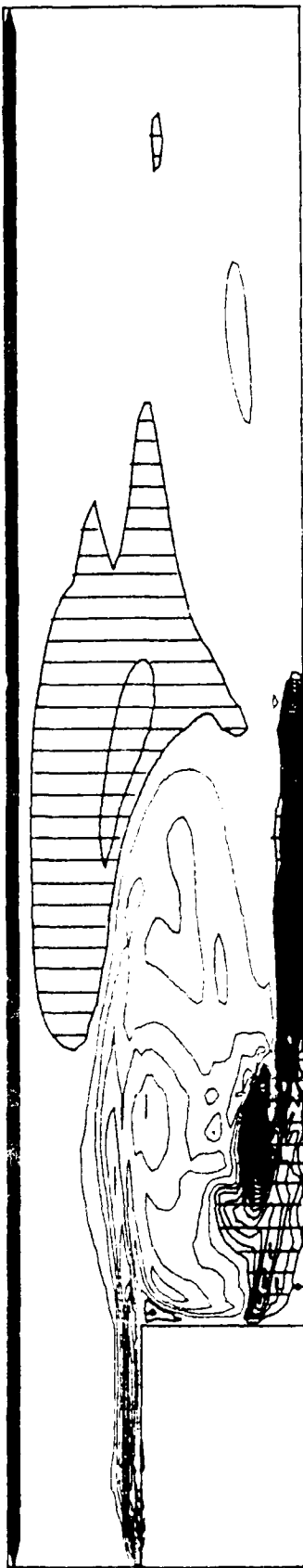


$N = 34,000$



$N = 40,000$

Figure 55b. Velocity-Vector Plots for Case 6b of Table 7.

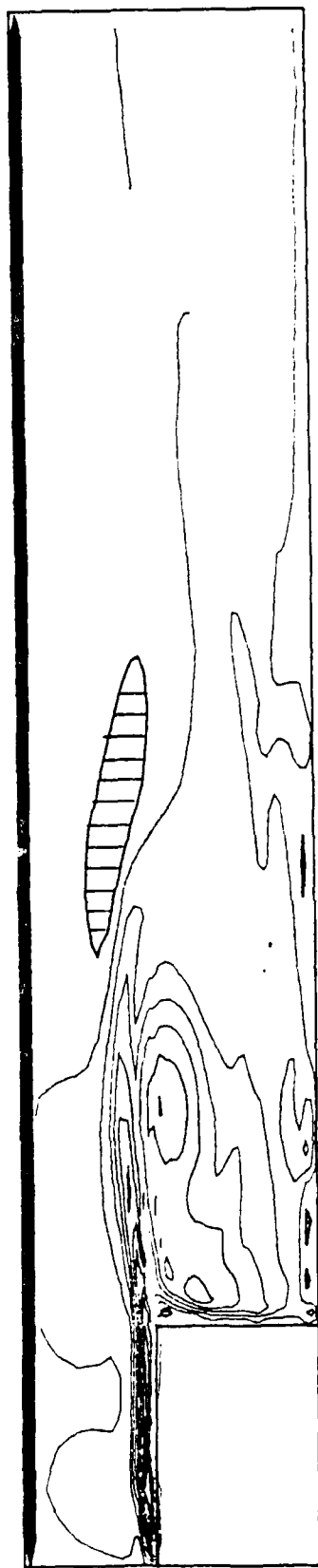


$N = 10,000$

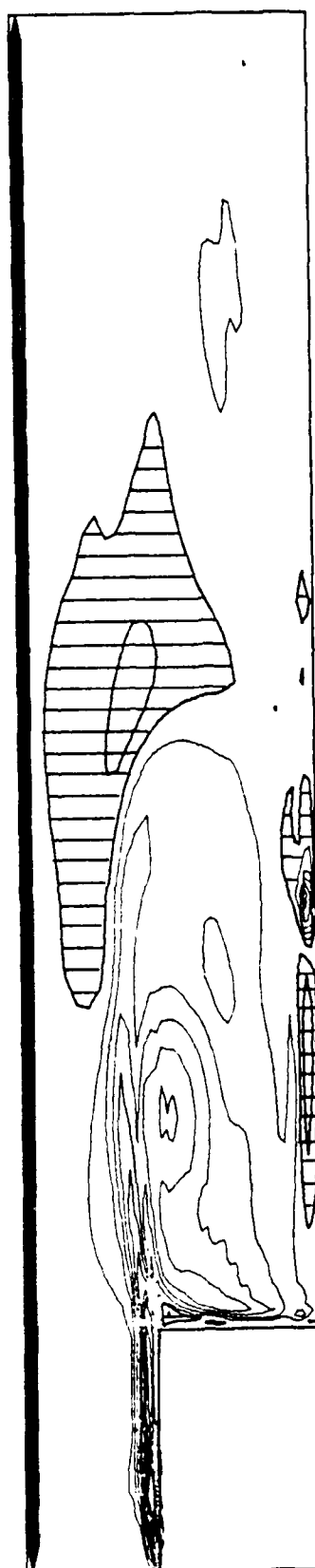


$N = 30,000$

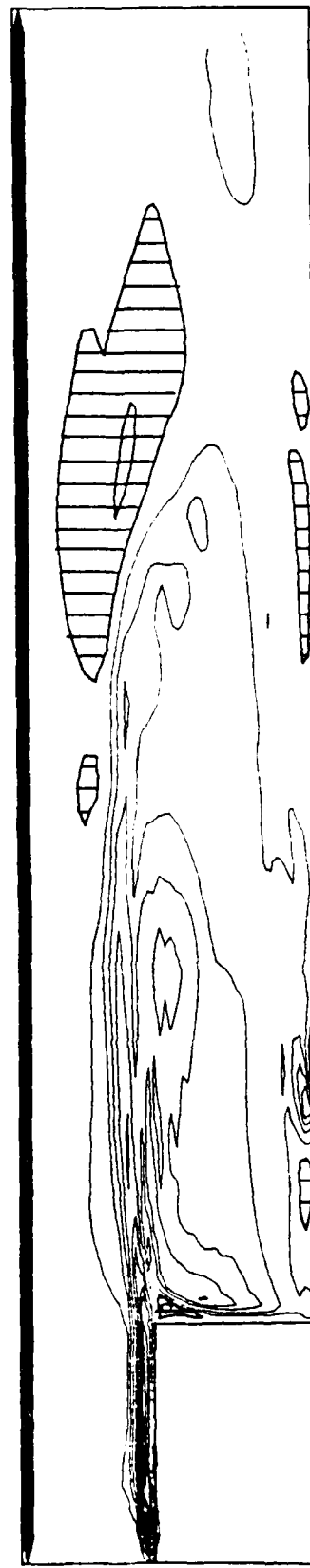
Figure 55c. Vorticity-Contour Plots for Case 6b of Table 7.



$N = 32,000$

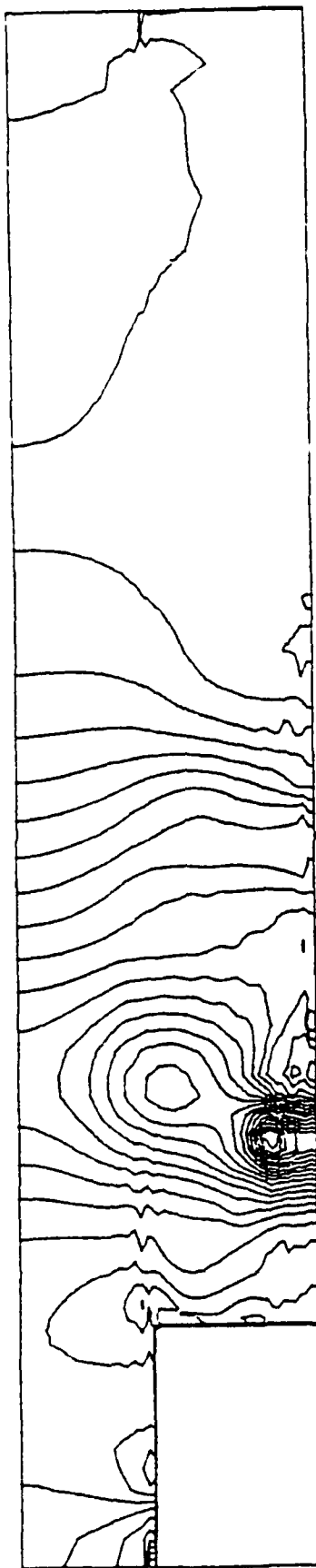


$N = 34,000$

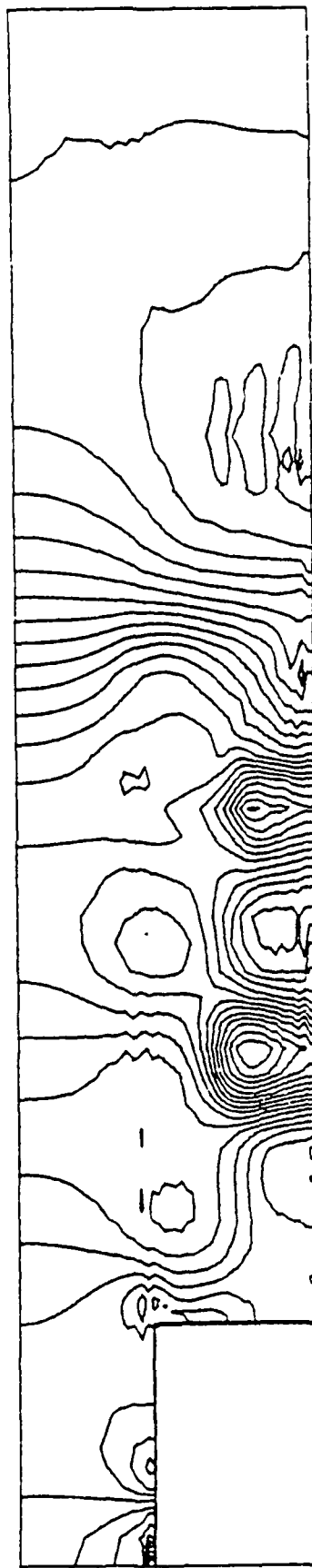


$N = 40,000$

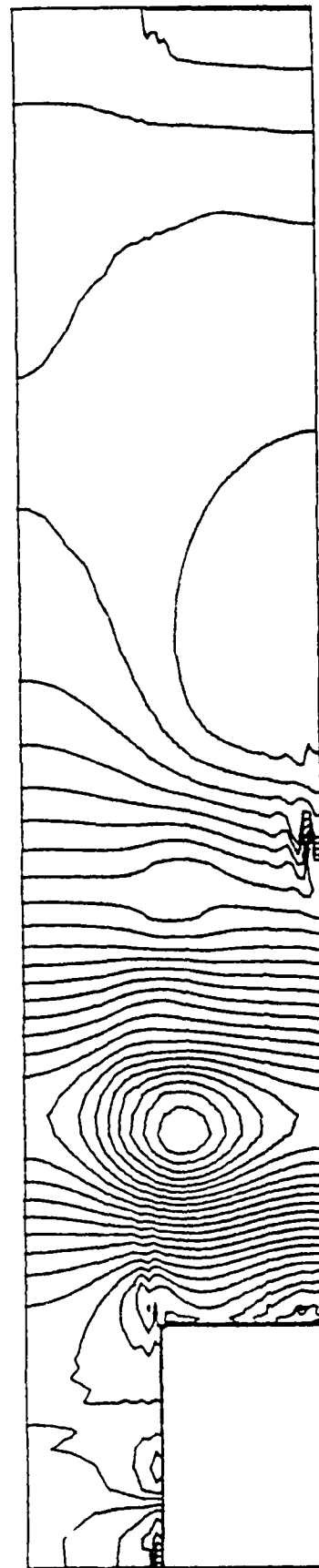
Figure 55d. Vorticity-Contour Plots for Case 6b of Table 7.



$N = 10,000$



$N = 20,000$



$N = 30,000$

Figure 55e. Pressure-Contour Plots for Case 6b of Table 7.

Numerical calculations of Case 6c are performed at a CFL number of 0.8, with all other conditions being identical to Case 6b. Figure 56 shows that the mass flow rate remains stable around 4.75 kg/s except for the fluctuations resulting from the eddies being washed off the outflow boundary starting at 28,000 DT and 38,800 DT. However, the large temperature fluctuations observed ( $\Delta T_{CFL} \sim 1/\sqrt{T}$ ) result from the particular choice of boundary conditions. Figure 57 shows the velocity vector plots and vorticity contour plots. The numerical solutions of Cases 6a to 6c show that the character of mass flow fluctuations and of the associated oscillatory behavior of the flowfield is a function of CFL number, as well as the relative location of the inflow and outflow boundaries. More important, the solution is nonphysical because of the large temperature fluctuations associated with the flowfield.

Cases 7a and 7b are modeled with the inflow conditions of Paragraph III.2.a(4) and outflow conditions involving split condition of Hasen<sup>44</sup> [see Paragraph III.2.b(3a)]. However, the split condition is modified for Case 7b as seen below:

$$P_{KL,j}^{n+1} = P_e \text{ if } j \leq 43 \text{ and } \frac{\partial P}{\partial x} = 0 \text{ if } j > 43. \quad (68)$$

The condition  $\partial P / \partial x = 0$  is restricted to the duct-wall boundary layer. The advantage of these boundary conditions is that they allow for the specification of inflow mass flow and have the desired reflection characteristics for the modeling of the unsteady flow behavior.<sup>37</sup>

Figures 58 and 59 show that the appearance of the reverse flow at the outflow boundary triggers mass flow oscillations starting with a fundamental frequency of  $\omega_{x1} \sim 128$  Hz. The establishment of the longitudinal oscillations is preceded by fluctuations in  $\Delta T_{CFL}$  for a short duration, starting from 17,700 DT to 19,700 DT. This appears to resemble the beating phenomenon of two harmonic waves of different amplitude and of slightly different frequencies. The thermal waves are restricted to a narrow

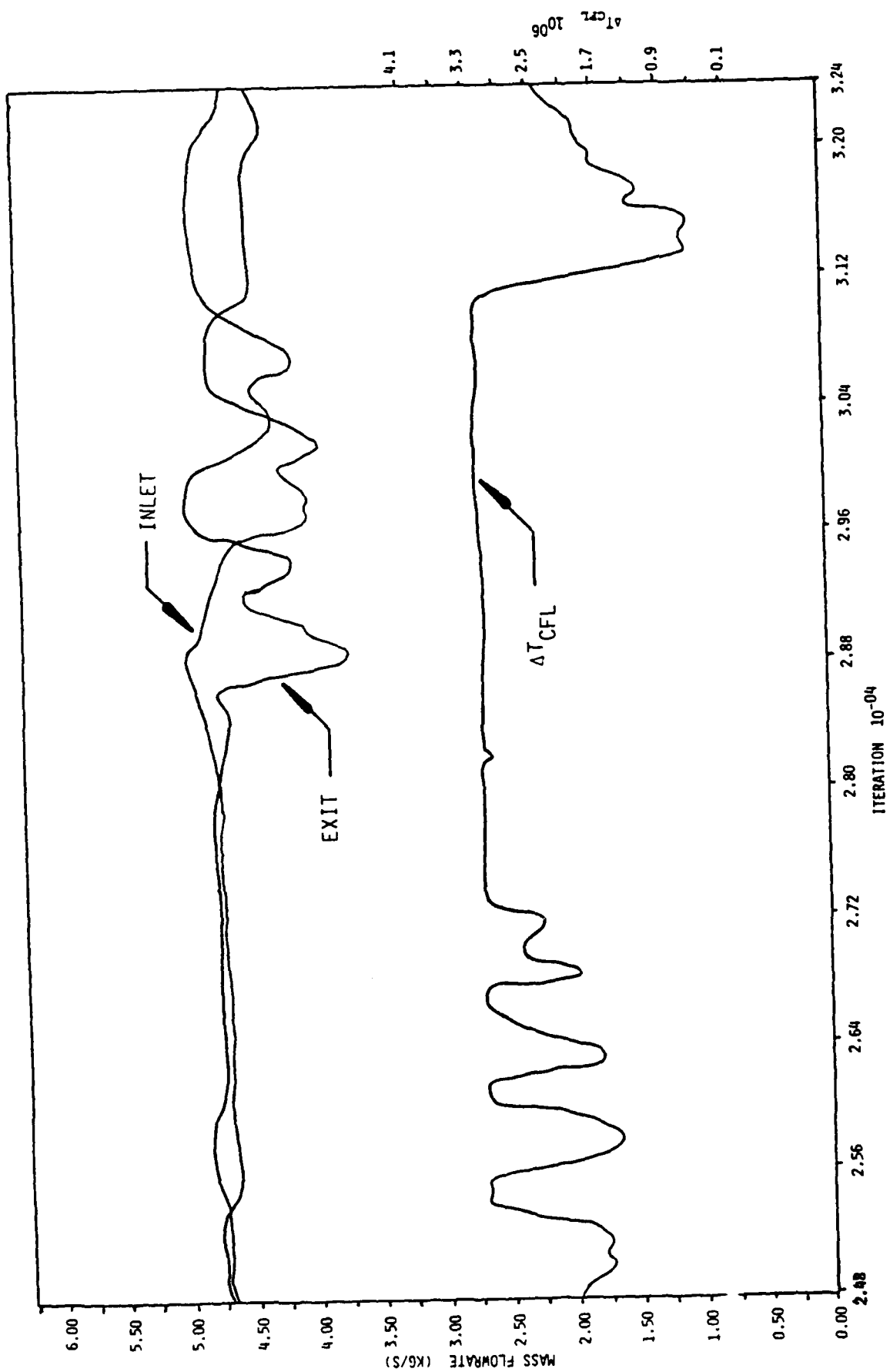


Figure 56a. Temporal Variation in Combustor Mass Flow and  $\Delta T_{CFL}$  for case 6c of Table 7.



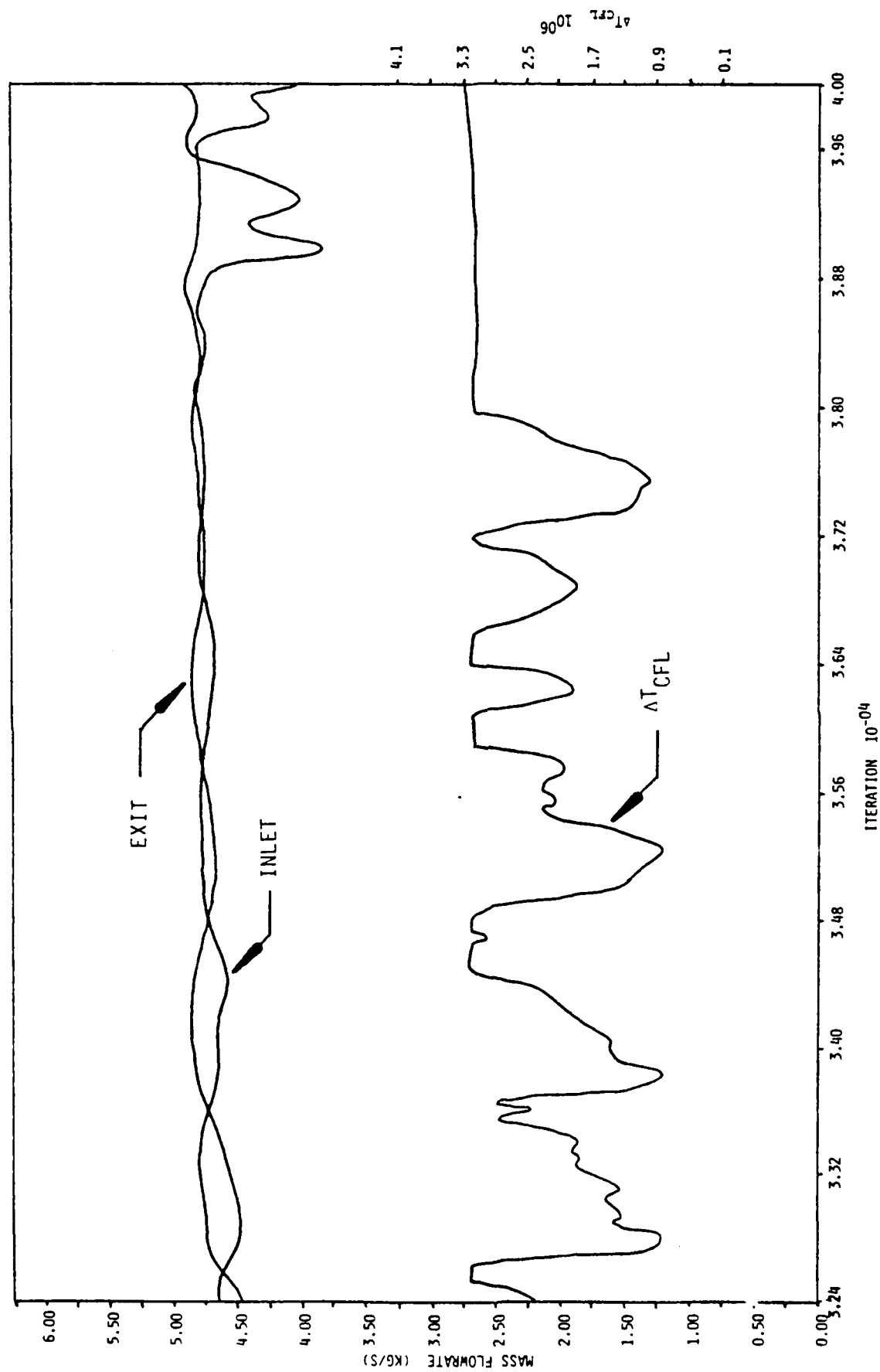
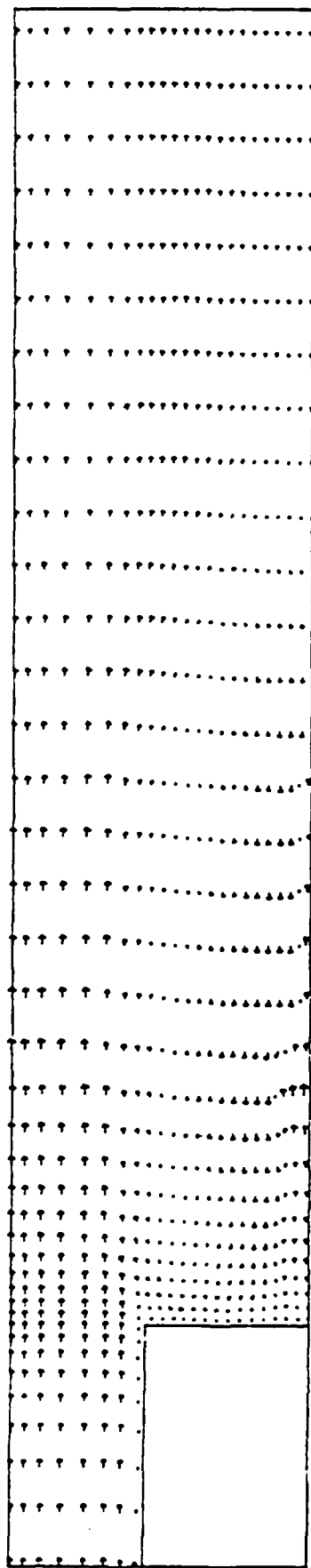
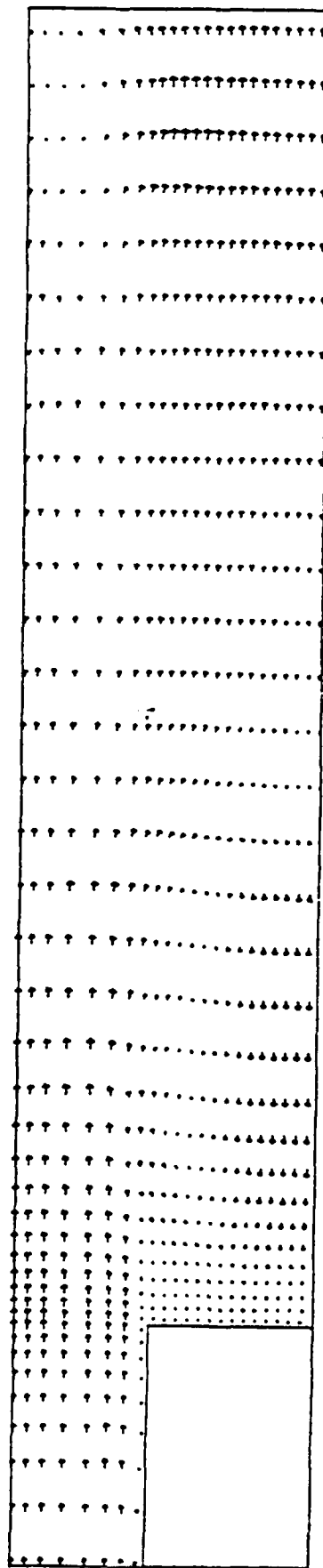


Figure 56h. Temporal Variation in Combustor Mass Flow and  $\Delta T_{CFL}$  for case 6c of Table 7.

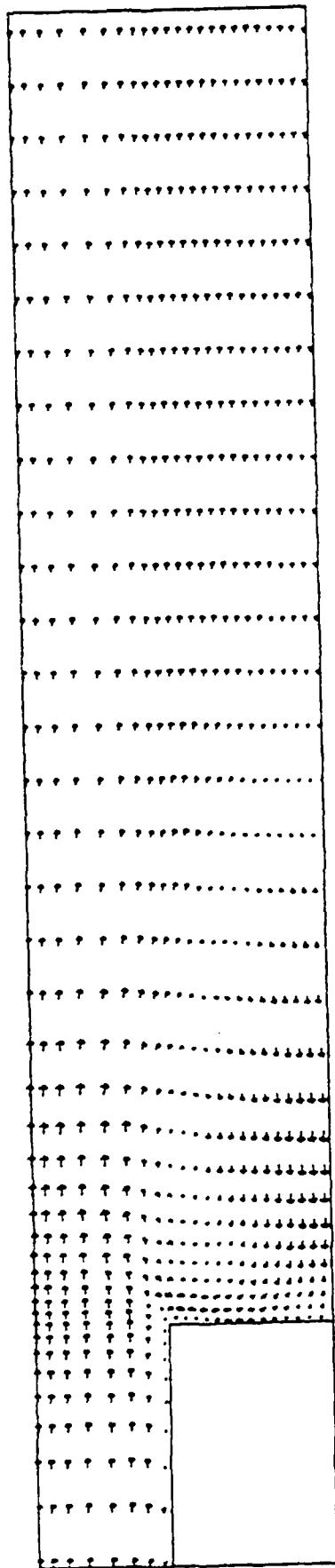


$N = 10,000$

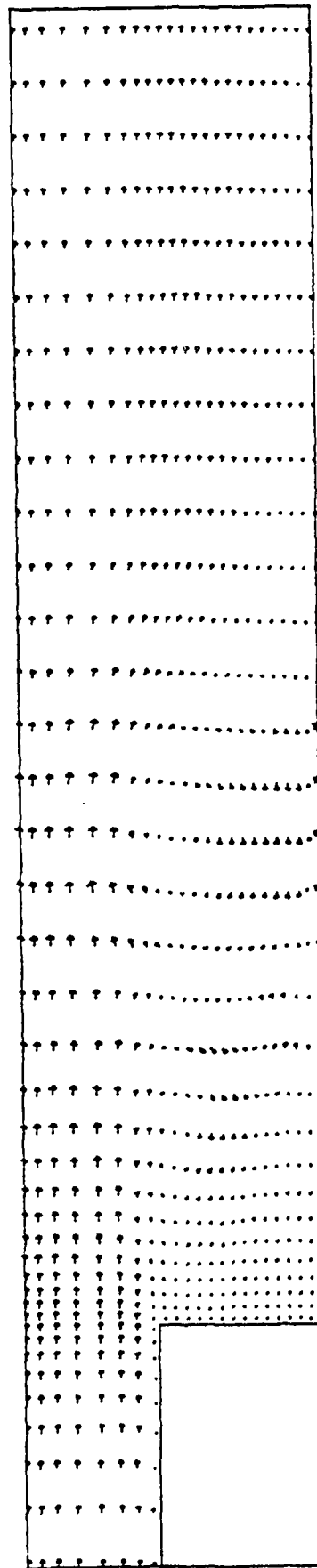


$N = 20,000$

Figure 57a. Velocity-Vector Plots for Case 6c of Table 7.



$N = 30,000$



$N = 40,000$

Figure 57b. Velocity-Vector Plots for Case 6c of Table 7.

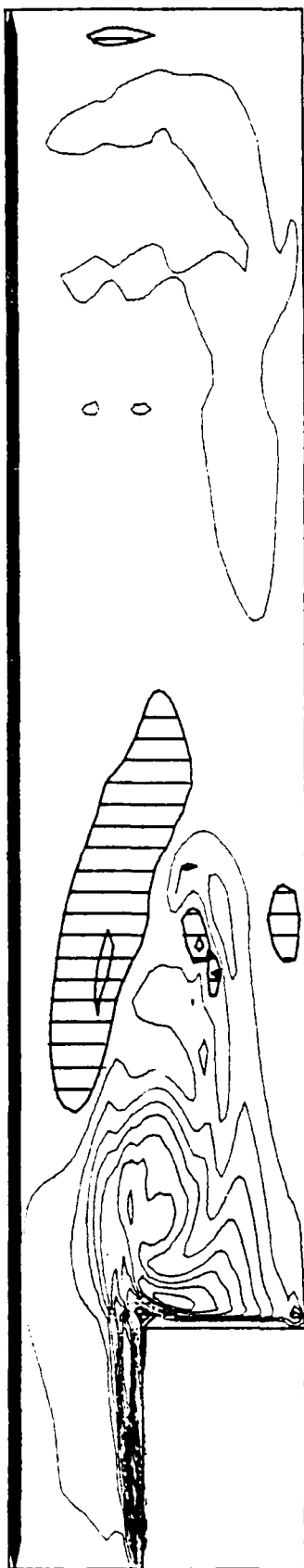


$N = 10,000$



$N = 20,000$

Figure 57c. Vorticity-Contour Plots for Case 6c of Table 7.

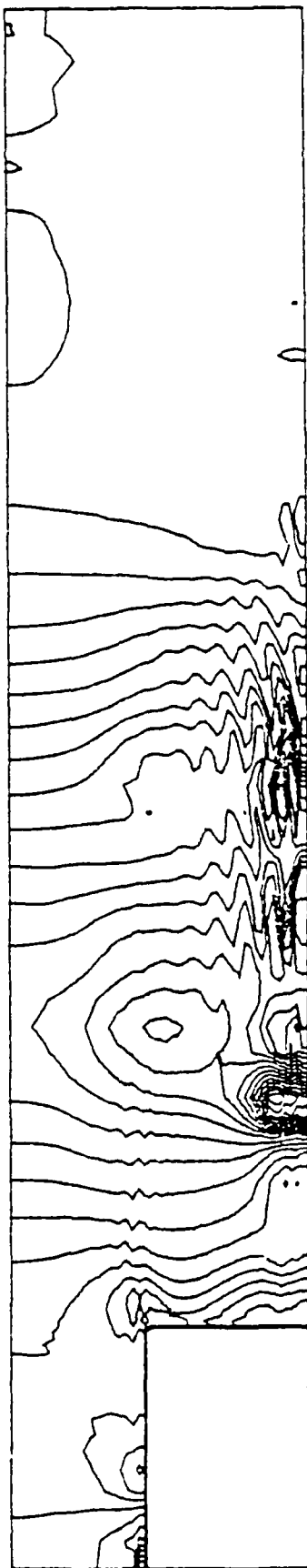


$N = 30,000$

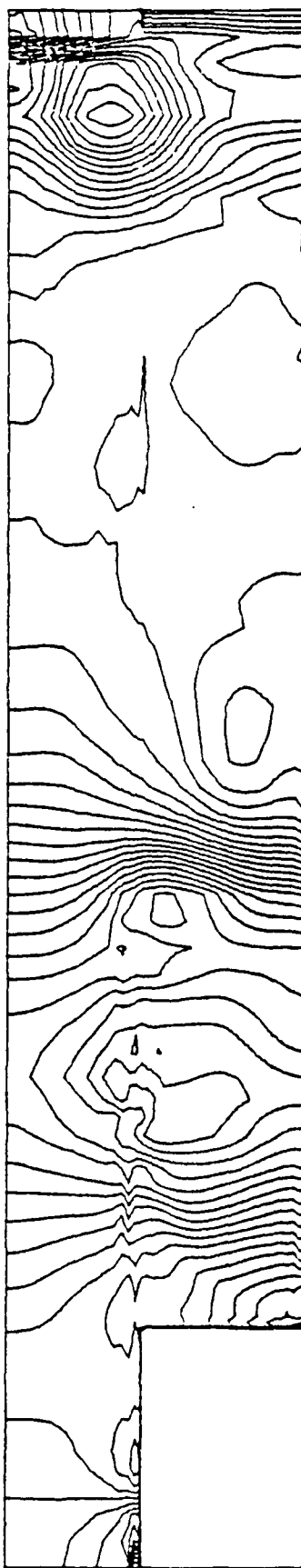


$N = 40,000$

Figure 57d. Vorticity-Contour Plots for Case 6c of Table 7.

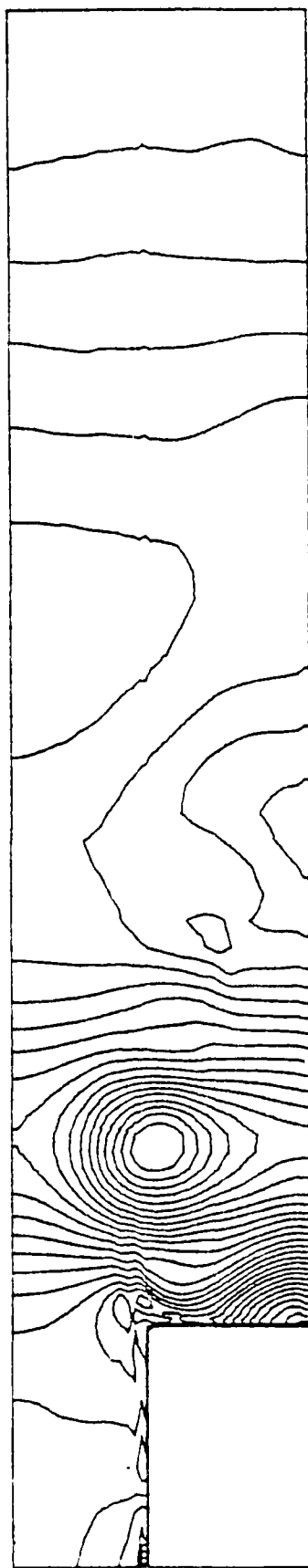


$N = 10,000$

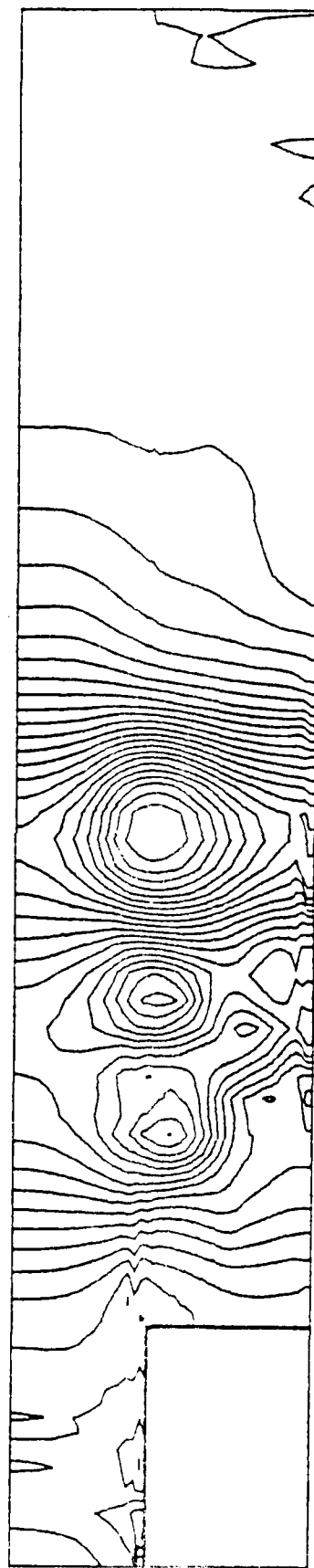


$N = 20,000$

Figure 57e. Pressure-Contour Plots for Case 6c of Table 7.



$N = 30,000$



$N = 40,000$

Figure 57f. Pressure-Contour Plots for Case 6c of Table 7.

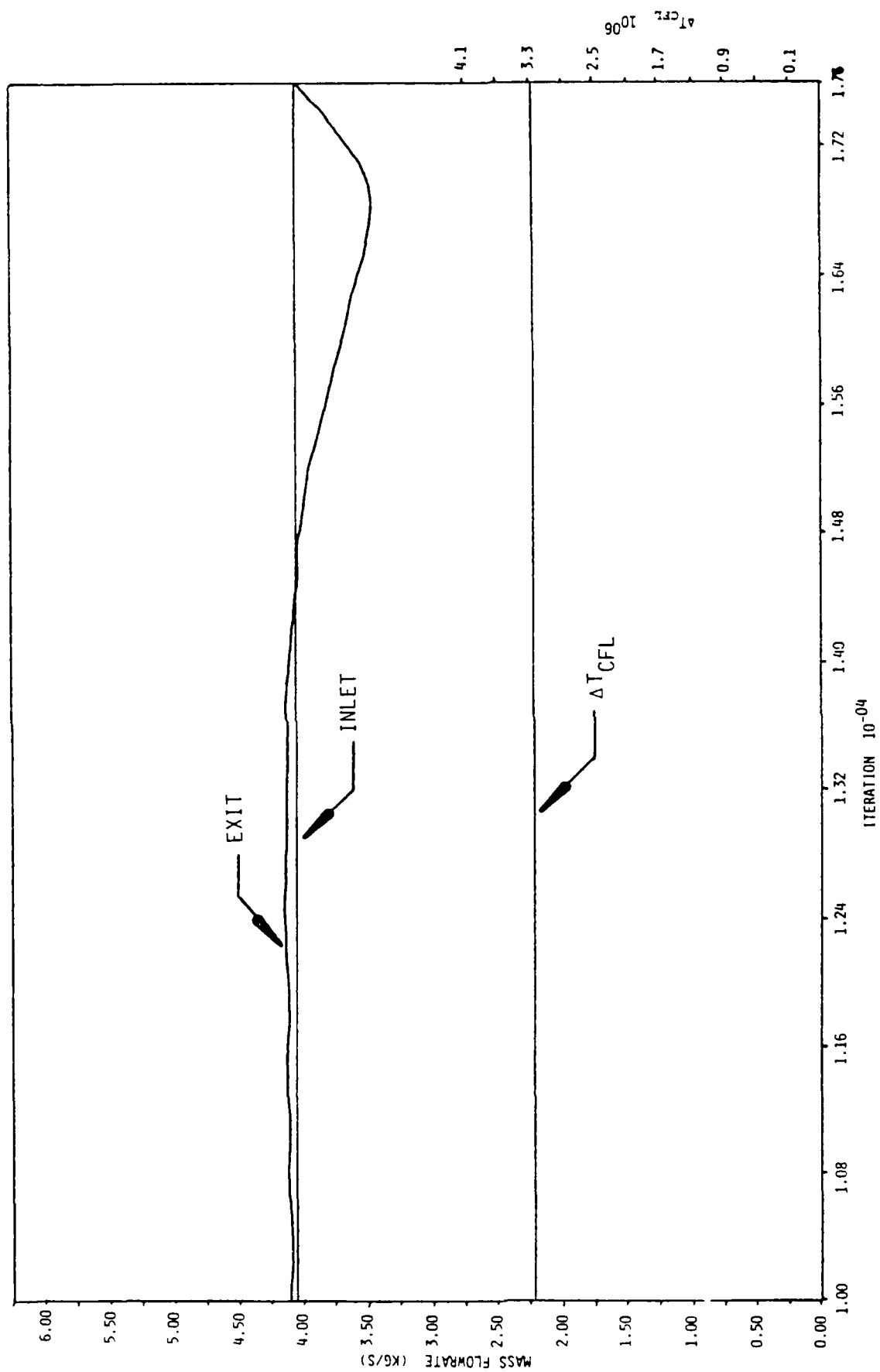


Figure 58a. Temporal Variation of Combustor Mass Flow and  $\Delta T_{CFL}$  for case 7a of Table 7.



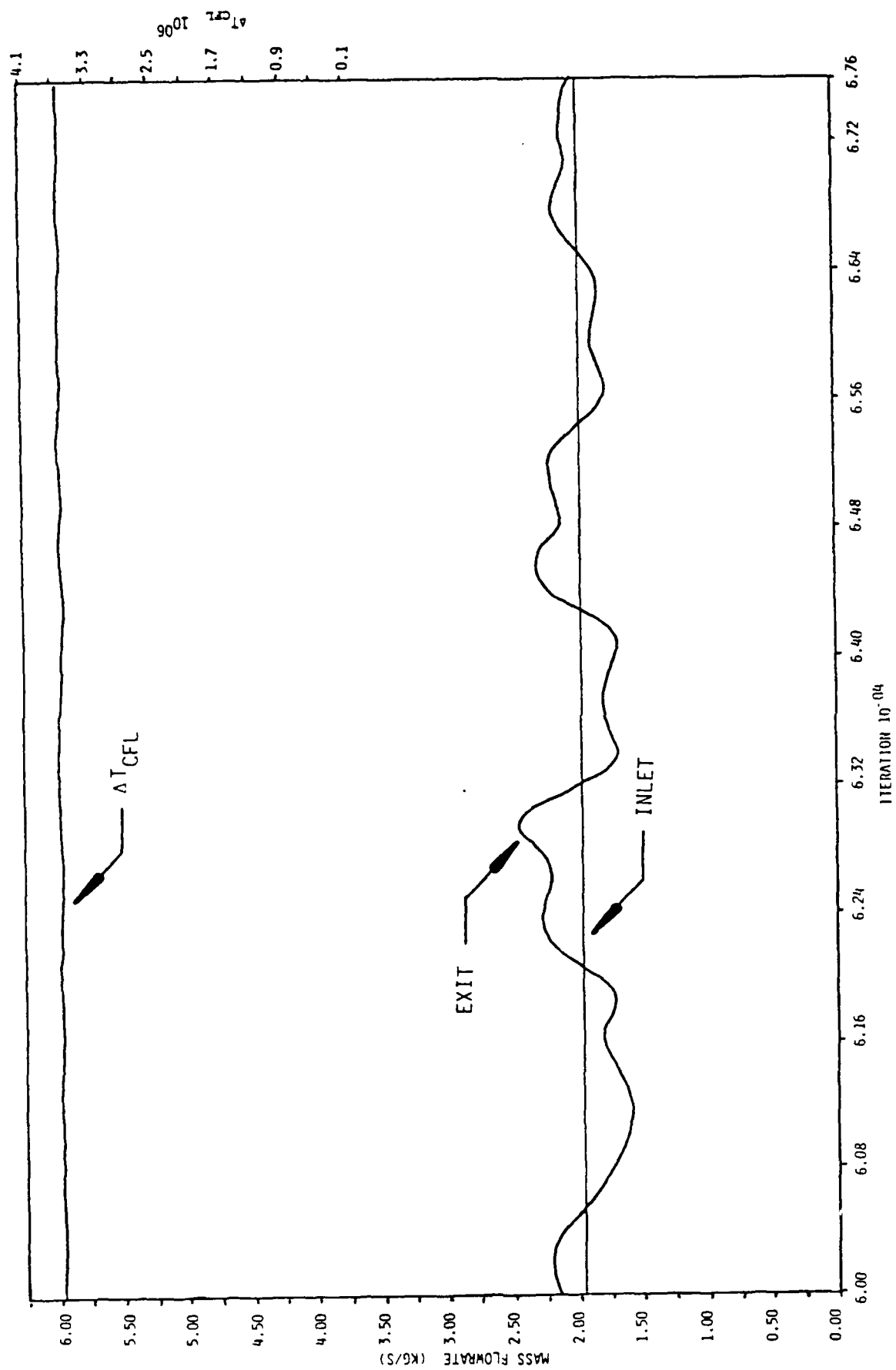


Figure 62c. Temporal Variation of Combustor Mass Flow and  $\Delta T_{CFL}$  for Case 8a of Table 7.

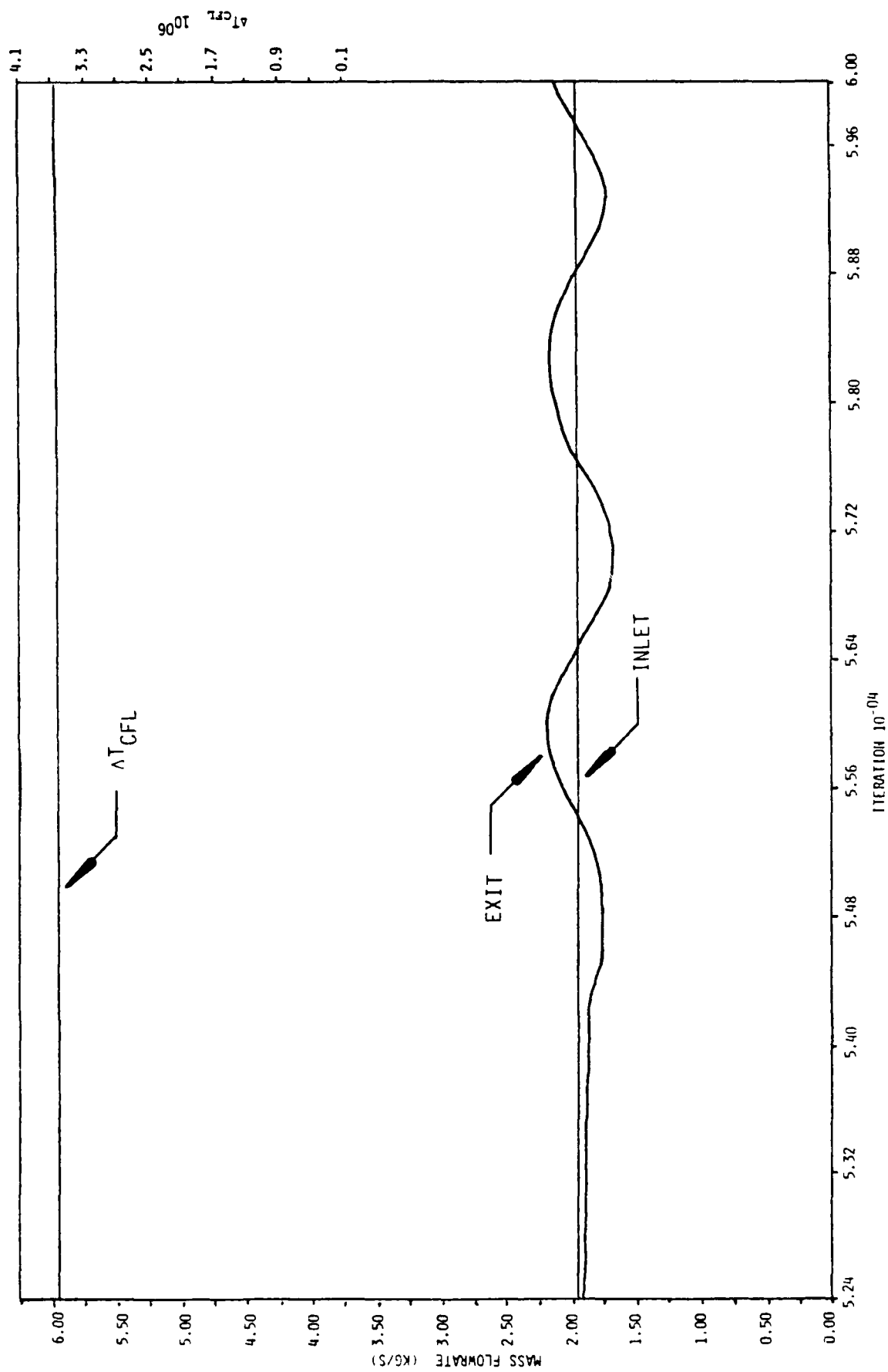


Figure 62b. Temporal Variation of Combustor Mass Flow and  $\Delta T_{CFL}$  for Case 8a of Table 7.

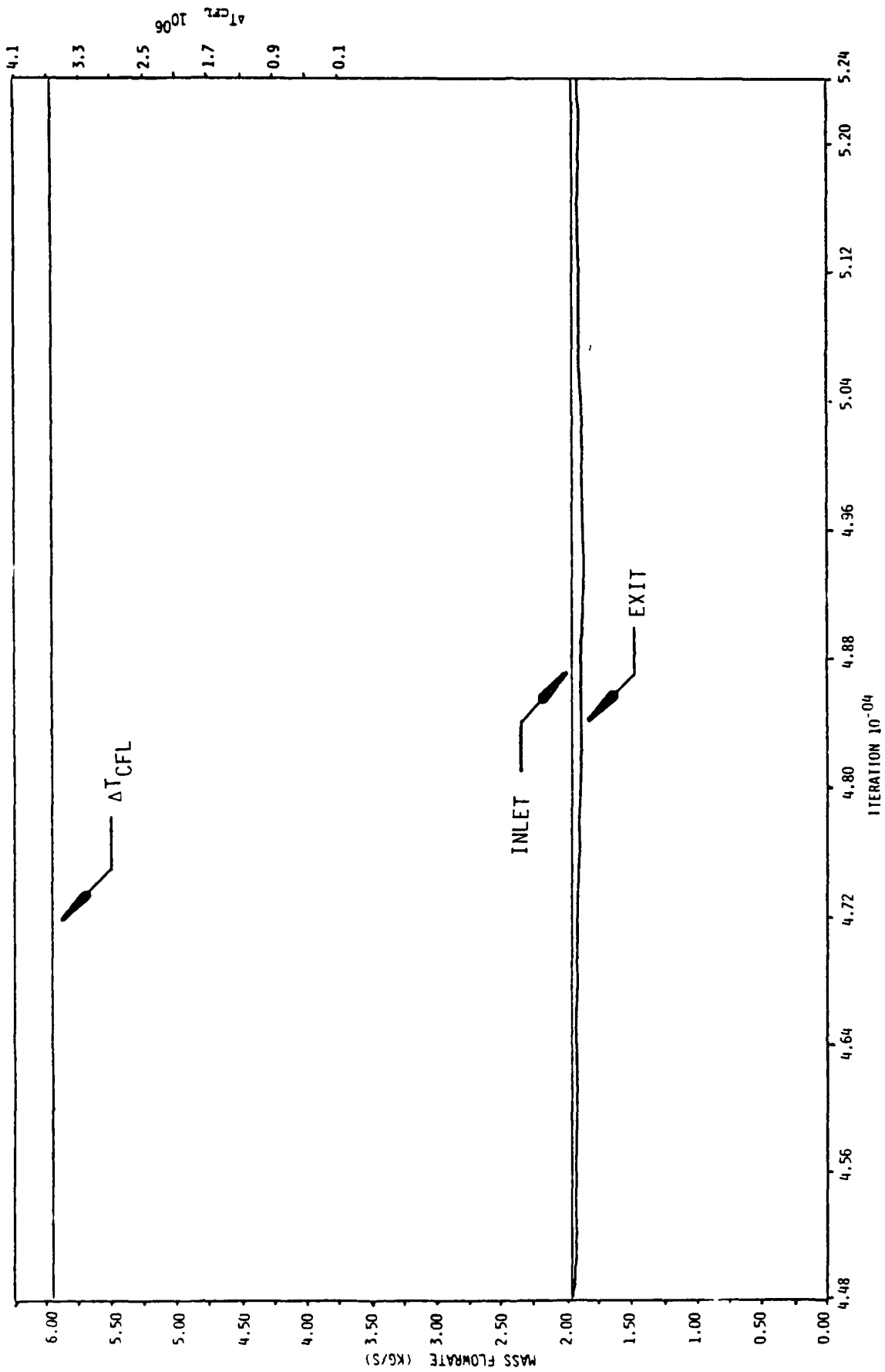
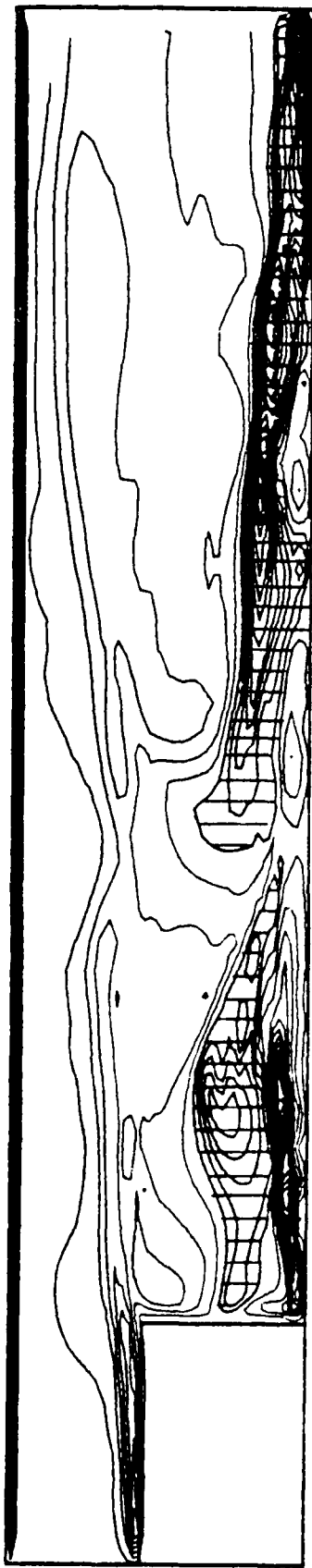


Figure 62a. Temporal Variation of Combustor Mass Flow and  $\Delta T_{CFL}$  for Case 8a of Table 7.



$N = 60,000$

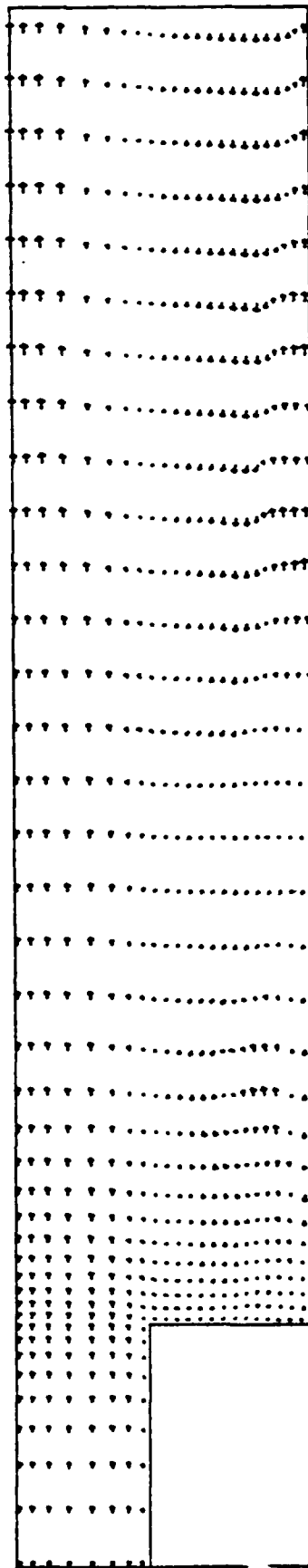
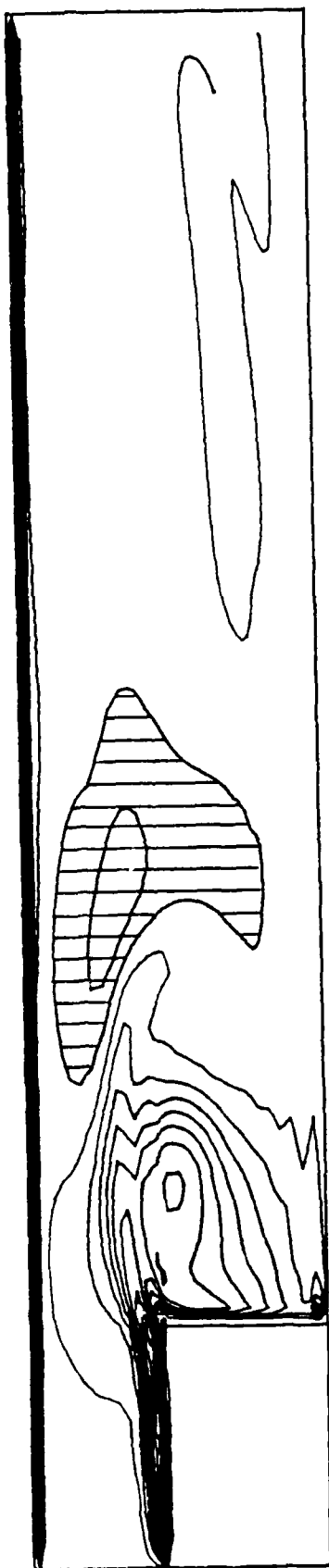
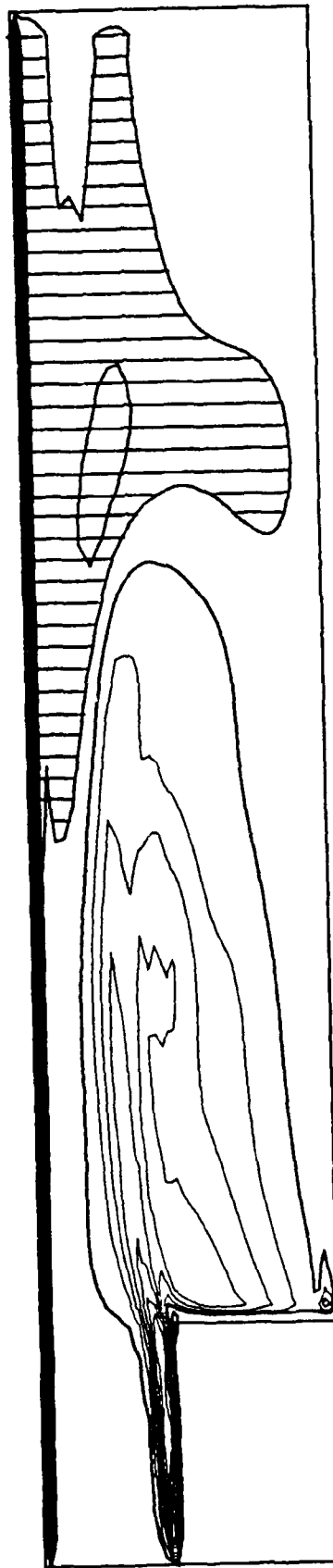


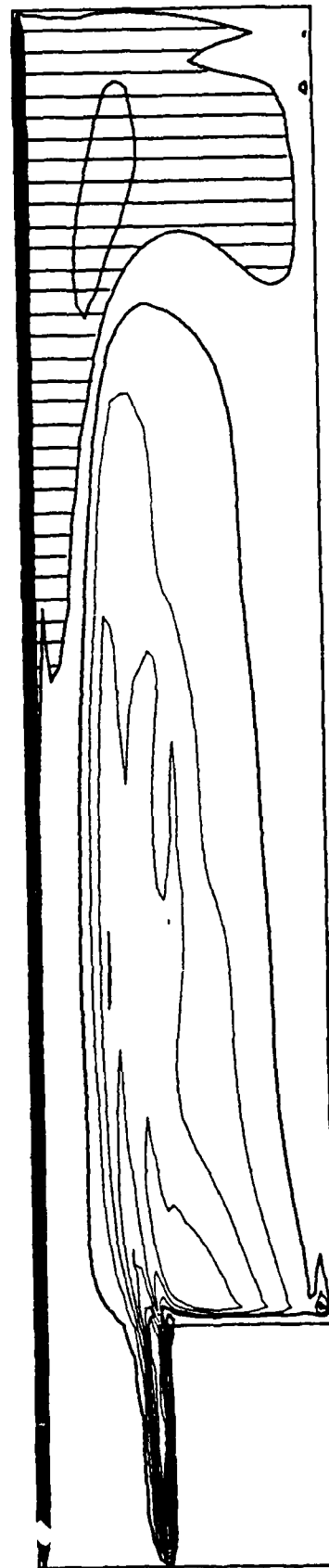
Figure 6lc. Vorticity-Contour and Velocity-Vector Plots for Case 7b of Table 7.



$N = 10,000$



$N = 20,000$



$N = 30,000$

Figure 6lb. Vorticity-Contour Plots Common to both Cases 7b and 8a of Table 7.

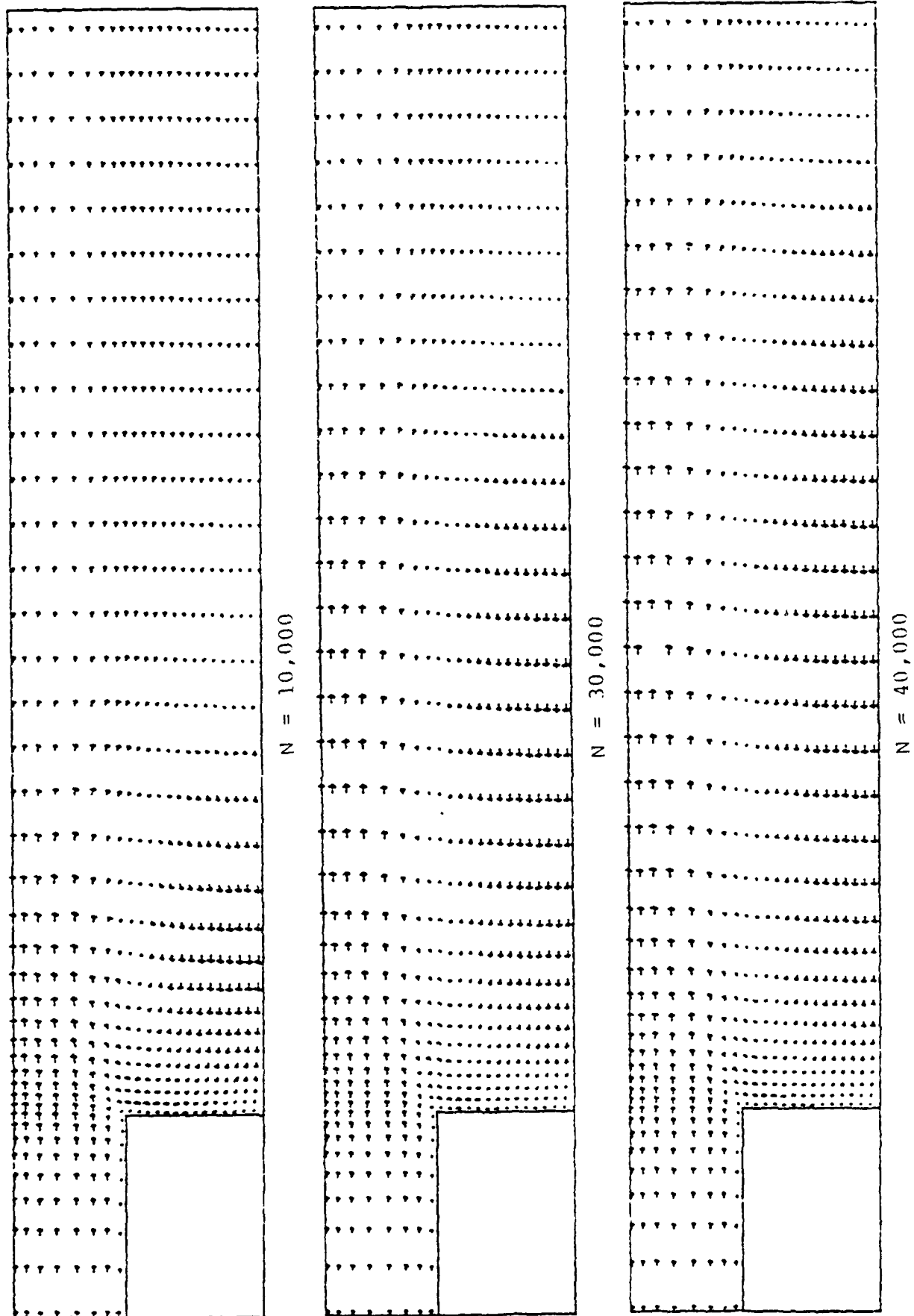


Figure 6la. Velocity-Vector Plots Common to both Cases 7b and 8a of Table 7.

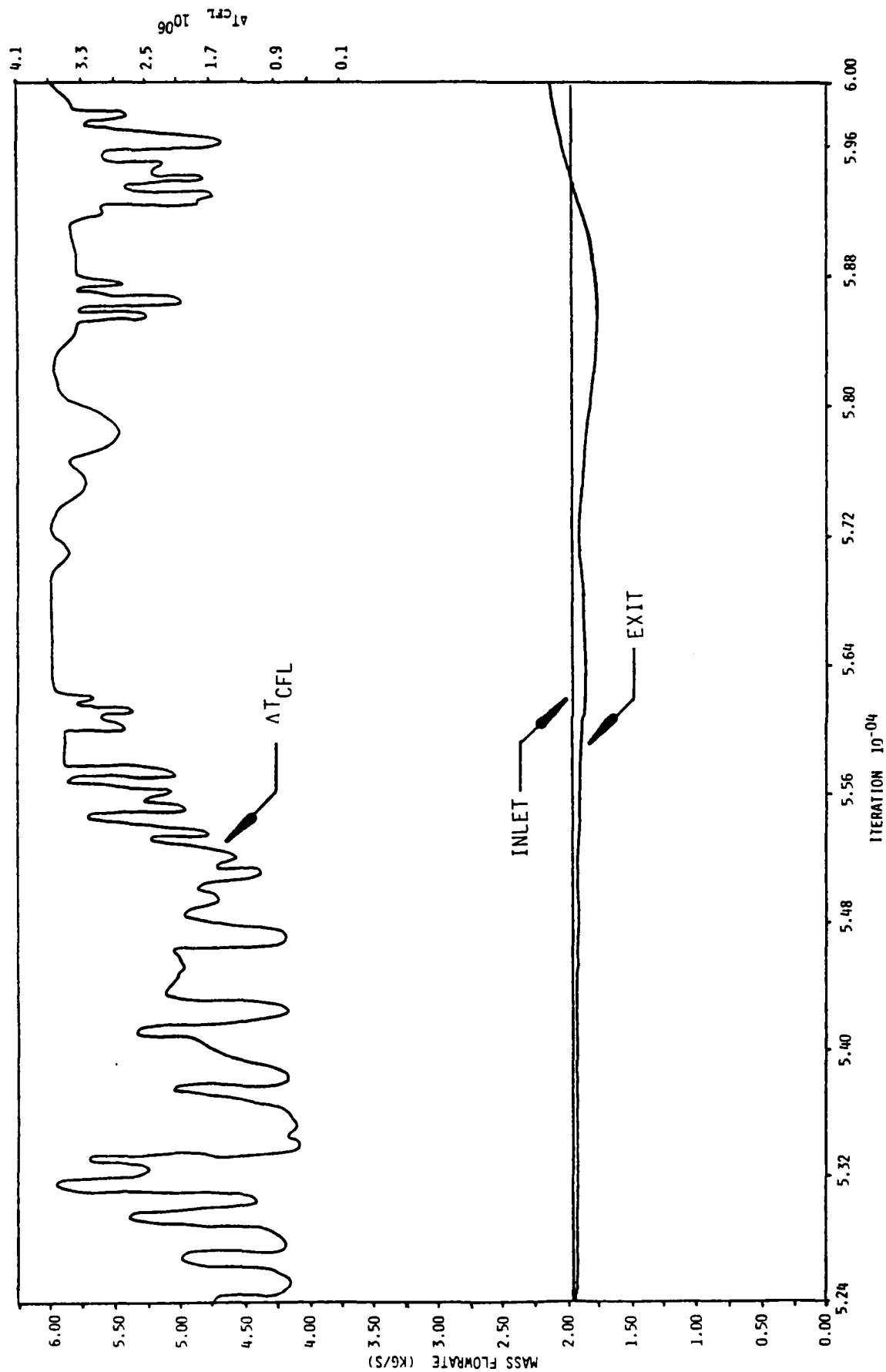


Figure 60b. Temporal Variation in Combustor Mass Flow and  $\Delta T_{CFL}$  for Case 7b of Table 7.

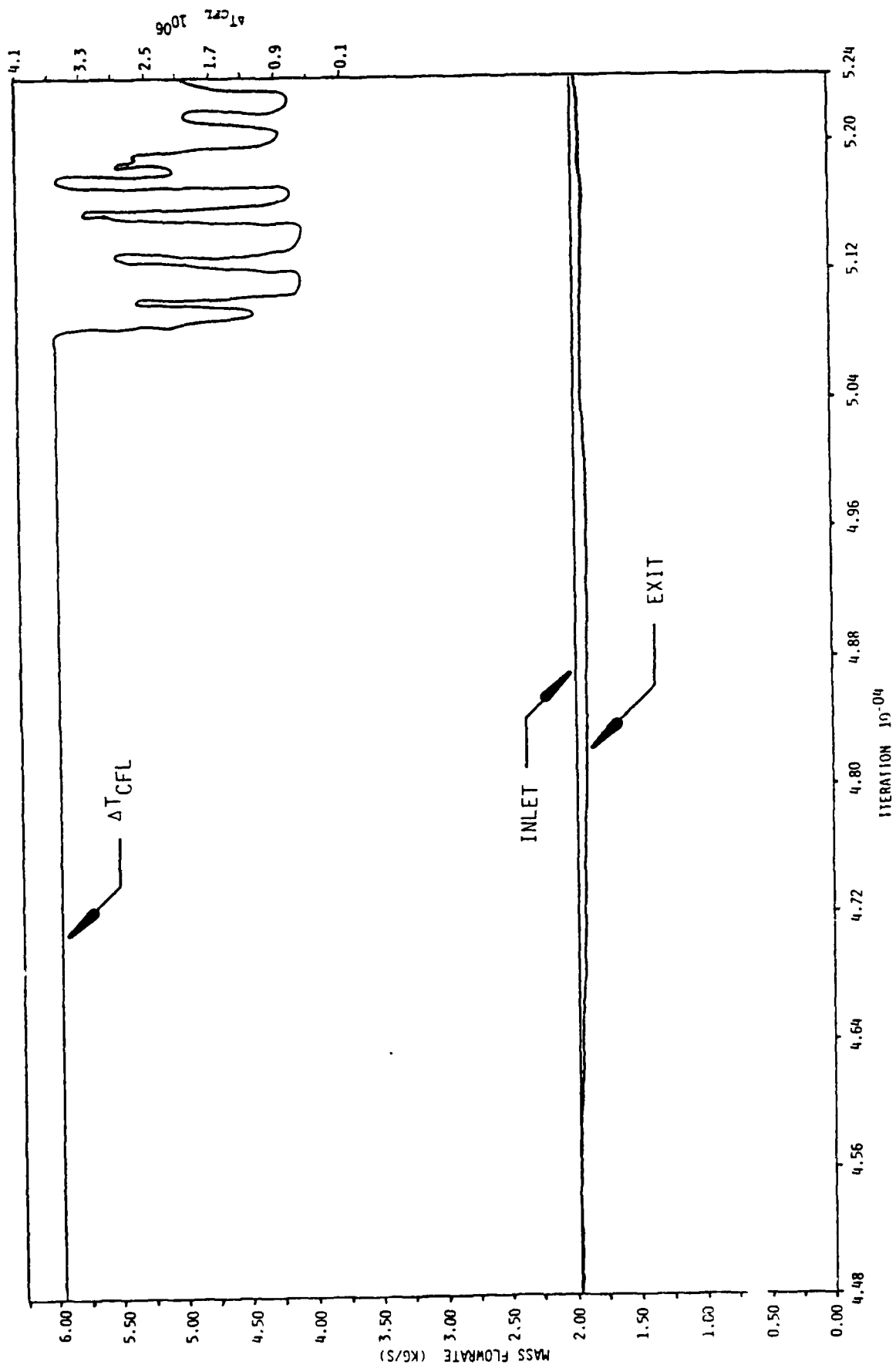


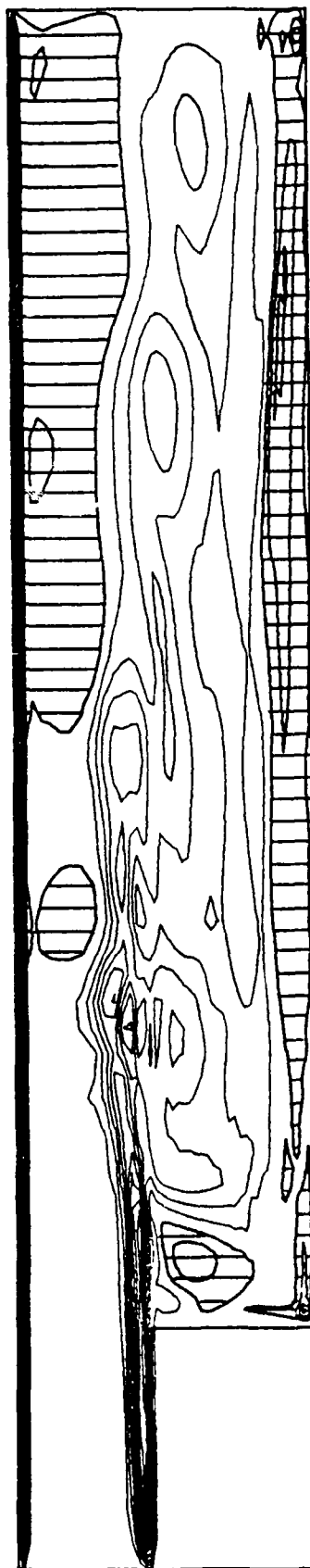
Figure 60a. Temporal Variation in Combustor Mass Flow and  $\Delta T_{CFL}$  for Case 7b of Table 7.



band of grid nodes near the reattachment point of the recirculation region. Figure 60 of Case 7b shows that the flow appears to be steady for the first 50,000 DT followed by temperature fluctuations even before the mass flow variations begin. Figure 61 shows the extending recirculation region before the numerical solution becomes unstable and nonphysical due to the reverse flow at the outflow boundary.

The outflow boundary conditions of Cases 8a and 8b involve specification of three variables, when there is a reverse flow at the boundary (see Paragraph III.2.b(5)). Unlike the numerical solutions of Cases 5 to 7 we studied, the  $\Delta T_{CFL}$  of Figure 62 remains invariant with time as it should be, even if the flowfield becomes unsteady. When the reverse flow appears at the outflow boundary around 54,000 DT, longitudinal oscillations are established at a definite fundamental frequency of  $\omega_{x1} = 128$  Hz with a time period of 7.92 milliseconds. This corresponds to the quarter-wave frequency of the resonator. As the time progresses, it excites the adjacent harmonics of frequency  $\omega_{x1}$ ,  $2\omega_{x1}$  ...,  $n\omega_{x1}$ . The bimodal frequency of the mass flow oscillations starting from 62,000 DT clearly appears to be qualitatively similar to the wave shown in Figure 63, which is a superposition of two simple harmonic waves,  $\{(2.0 - \frac{\omega t}{20}) \sin \omega t + (0.5 - \frac{\omega t}{40}) \sin 3\omega t\}$ . The two dominant frequencies of the flowfield correspond to  $\omega_{x1}$  and  $3\omega_{x1}$ . However, it takes approximately seven cycles for the longitudinal oscillations to attenuate before establishing a steady mass-flow rate. The velocity vector plots and vorticity contour plots for the first 40,000 DT of Figures 61 and 64 are identical and are not repeated in Figure 64. Figures 65 and 66 correspond to inflow mass rate of 4 kg/s of Case 8b and the results are similar to Case 8a.

Figure 67 shows the velocity-vector and vorticity-contour plots of Case 9. The outflow boundary conditions of Reference 45 allows for the reverse flow to appear at the outflow boundary without causing any oscillations in the mass flow rate but the results do indicate high temperature fluctuations.

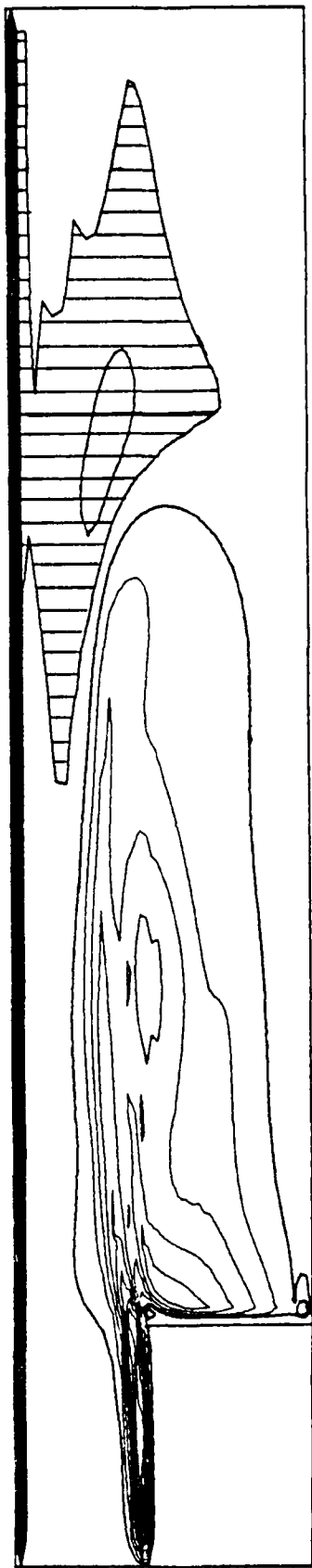


$N = 30,000$

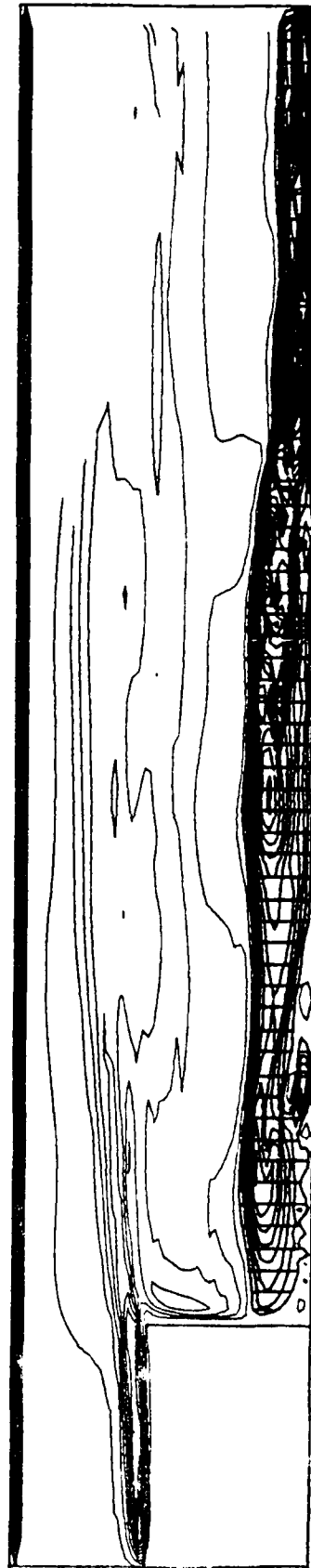


$N = 40,000$

Figure 59d. Vorticity-Contour Plots for Case 7a of Table 7.

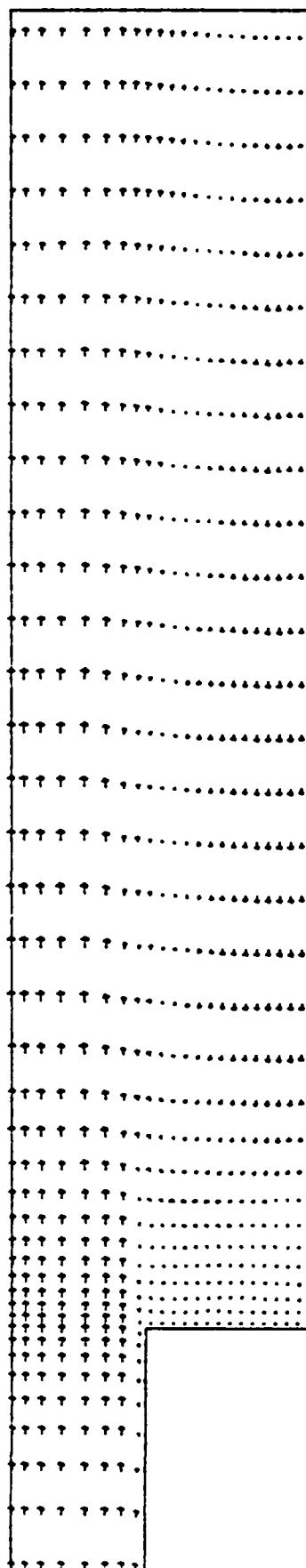


$N = 10,000$

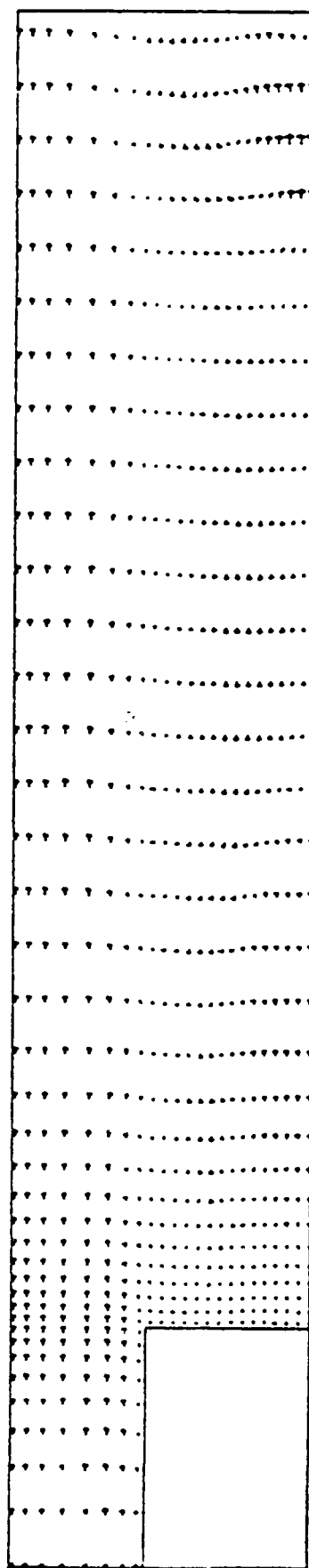


$N = 20,000$

Figure 59c. Vorticity-Contour Plots for Case 7a of Table 7.

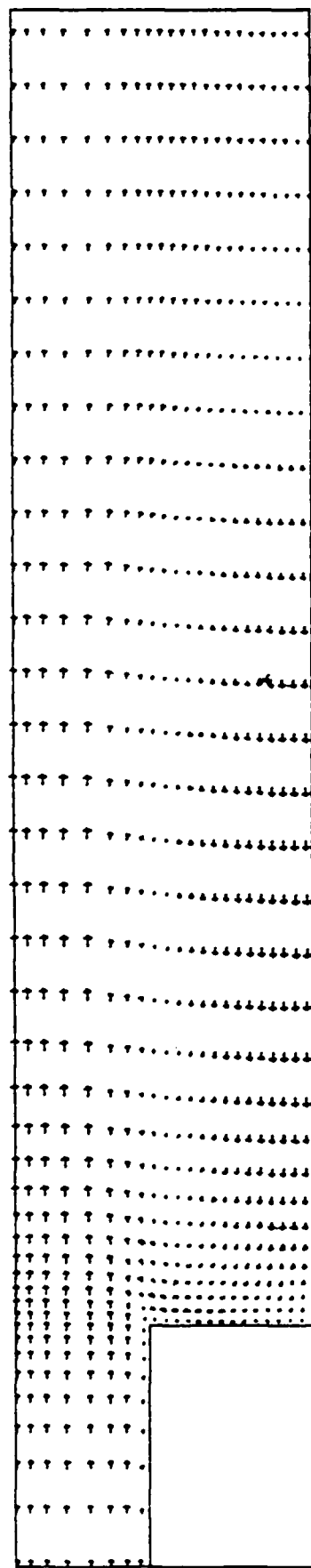


$N = 30,000$

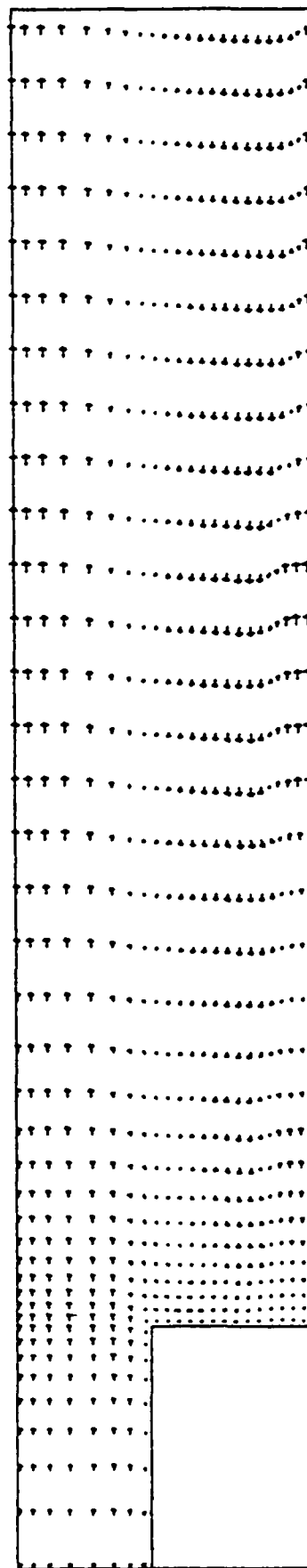


$N = 40,000$

Figure 59b. Velocity-Vector Plots for Case 7a of Table 7.



$N = 10,000$



$N = 20,000$

Figure 59a. Velocity-Vector Plots for Case 7a of Table 7.

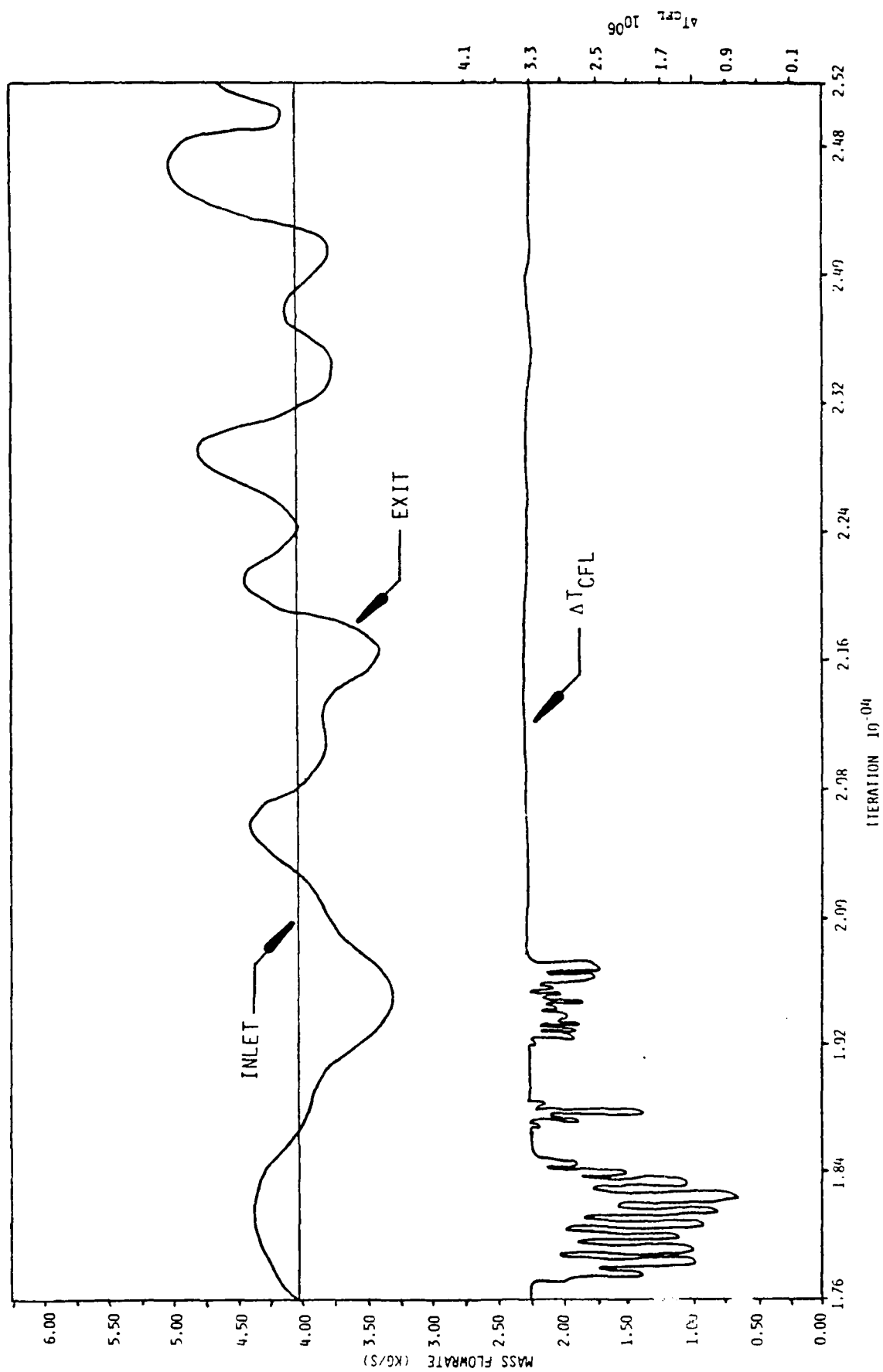


Figure 58b. Temporal Variation of Combustor Mass Flow and  $\Delta T_{CFL}$  for case 7a of Table 7.

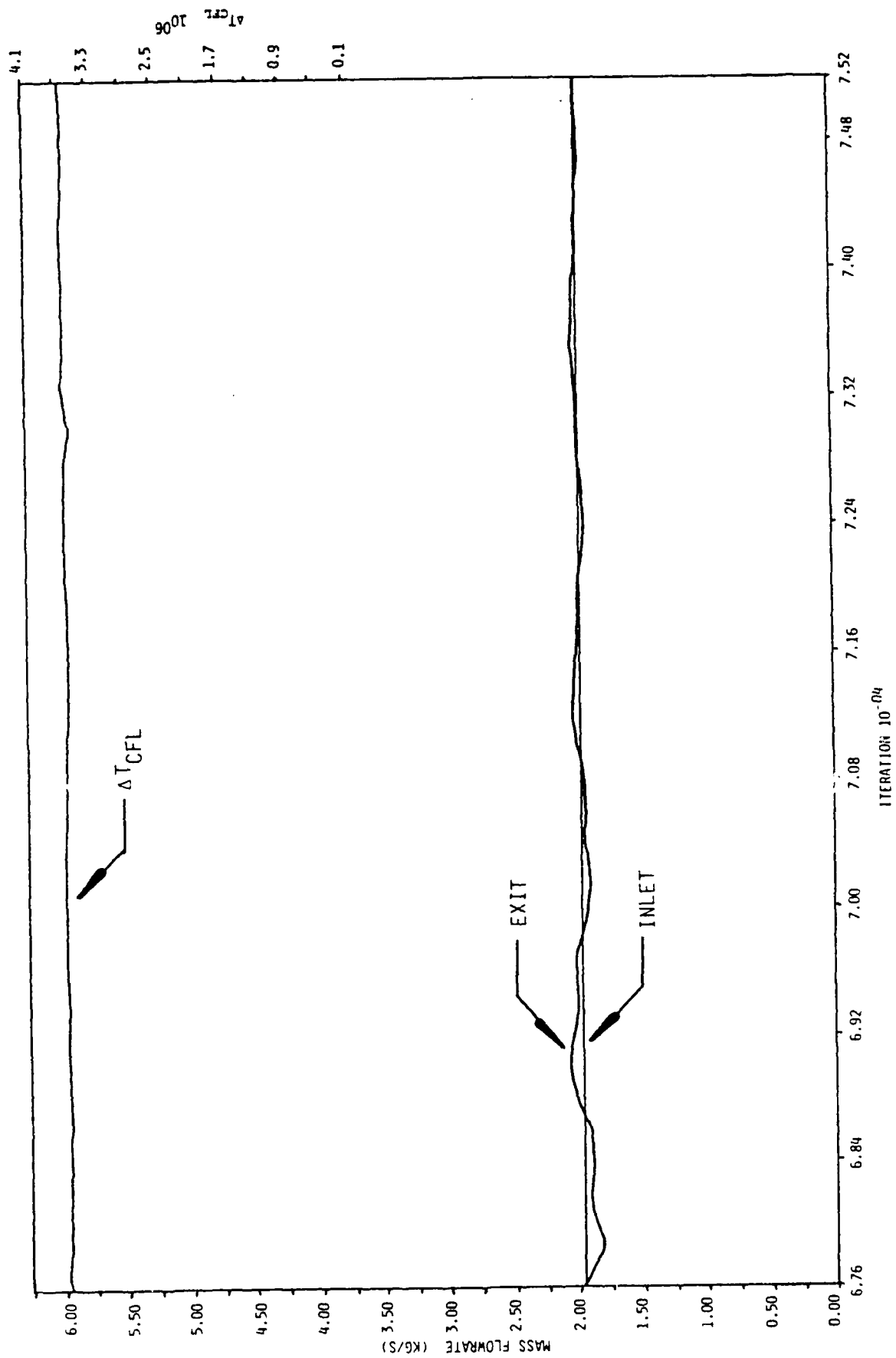


Figure 62d. Temporal Variation of Combustor Mass Flow and  $\Delta T_{CFL}$  for Case 8a of Table 7.

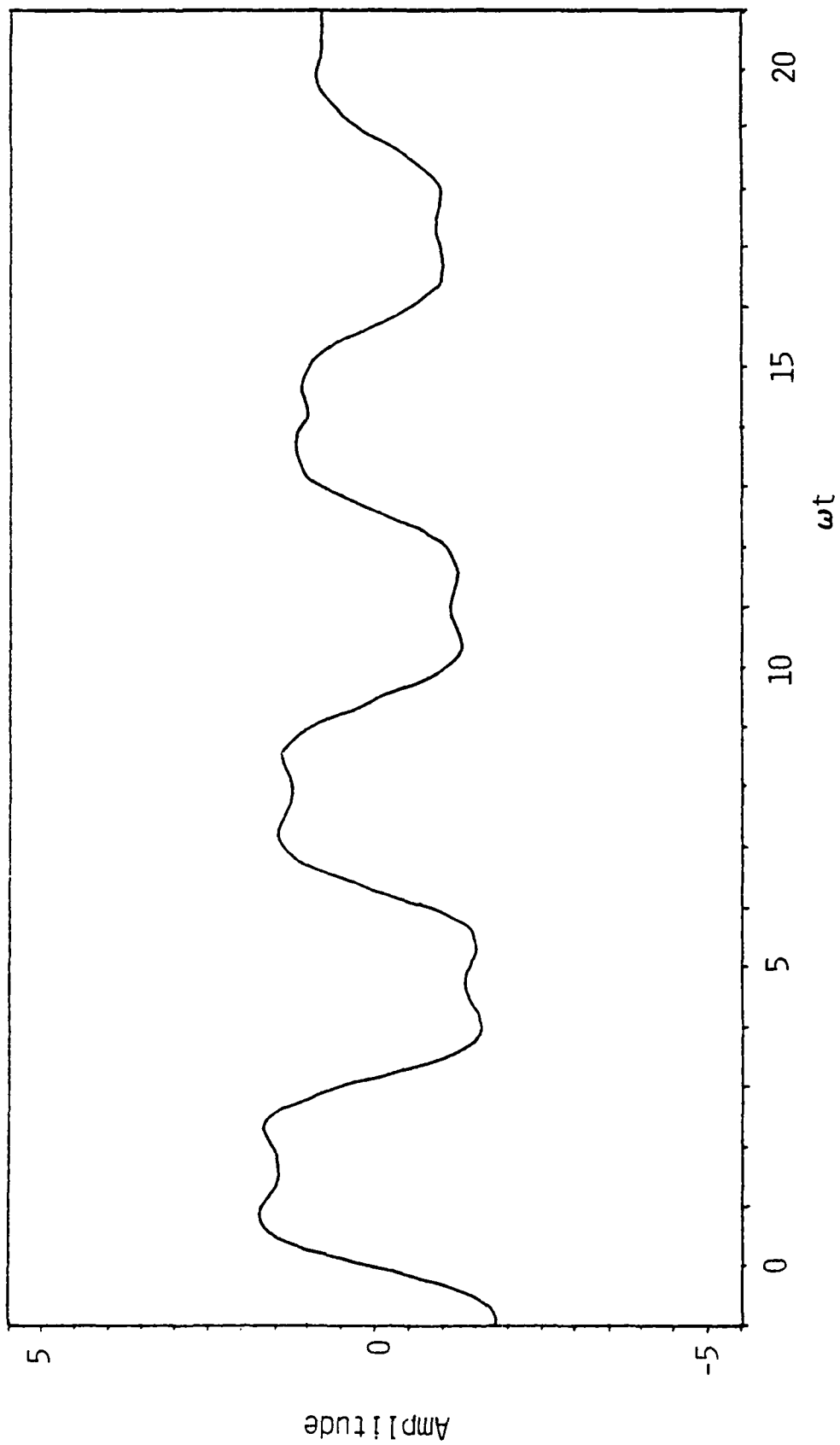
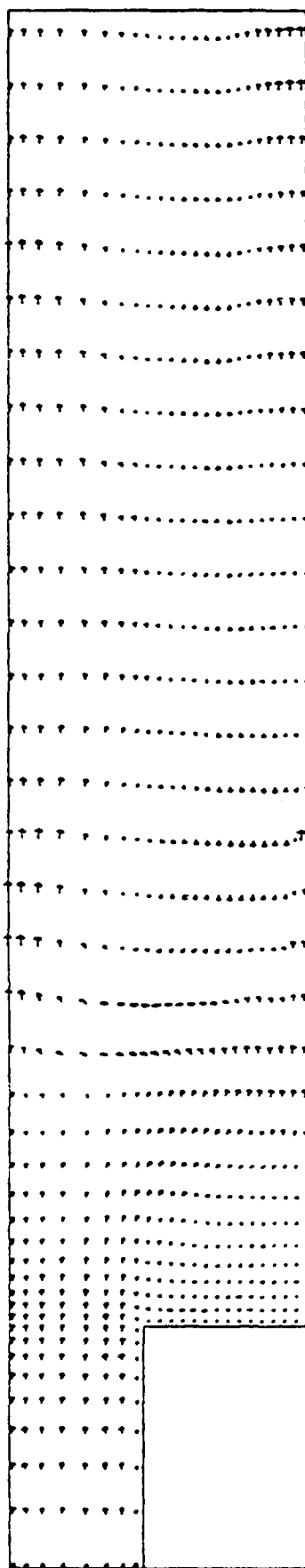
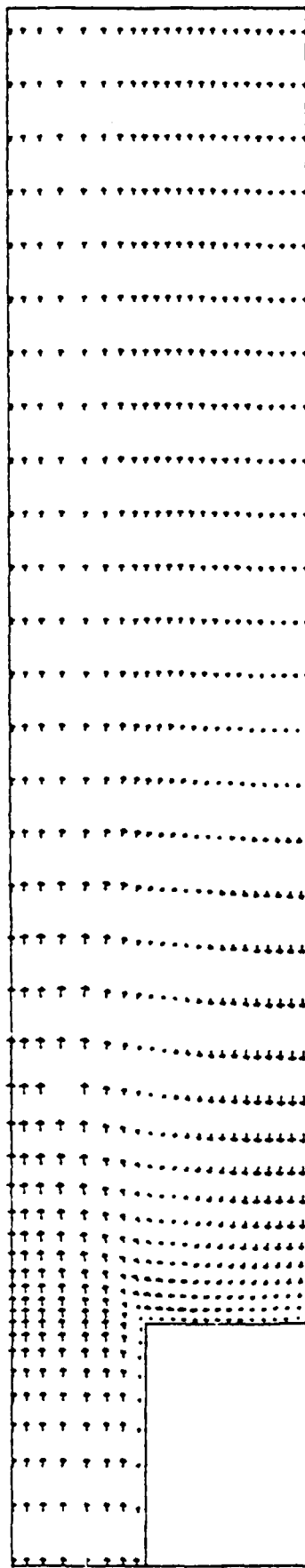


Figure 63. Superposition of Two Different Simple Harmonic Waves.

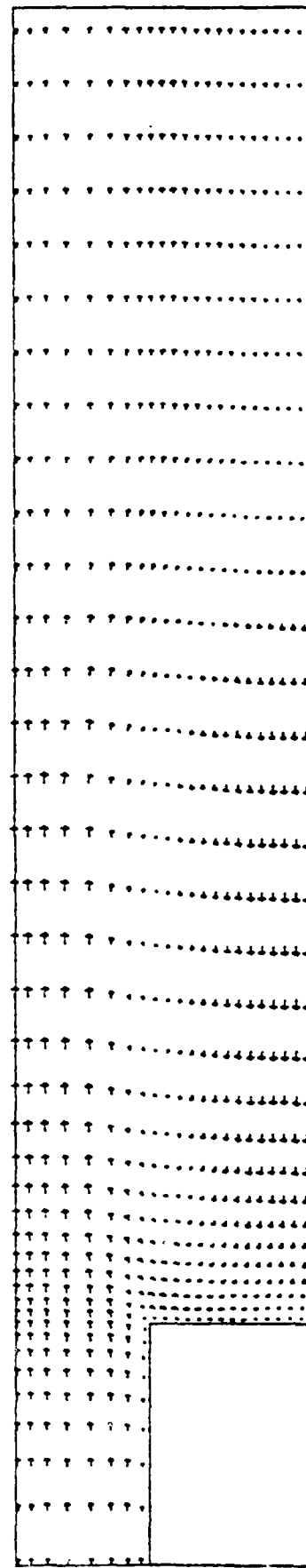




$N = 60,000$



$N = 70,000$

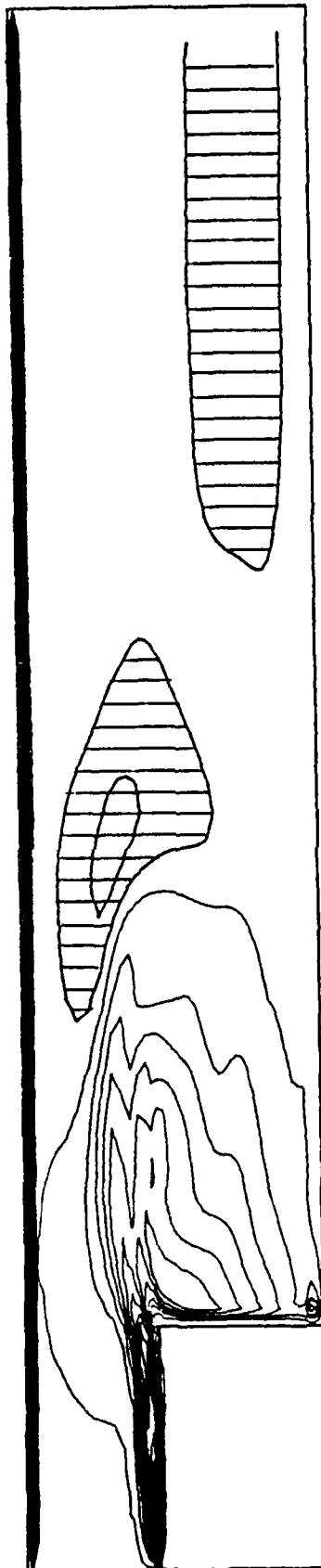


$N = 80,000$

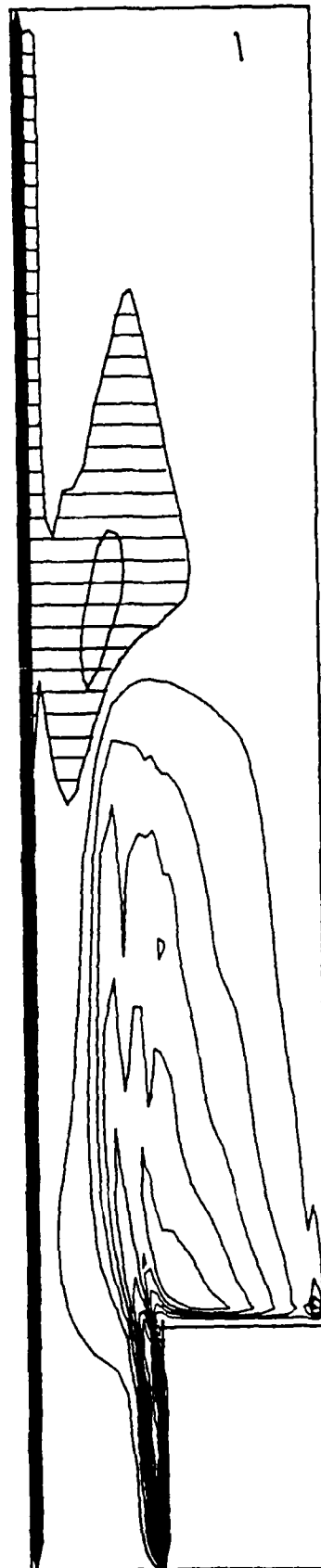
Figure 64a. Velocity-Vector Plots for Case 8a of Table 7.



$N = 60,000$



$N = 70,000$



$N = 80,000$

Figure 64b. Vorticity-Contour Plots for Case 8a of Table 7.

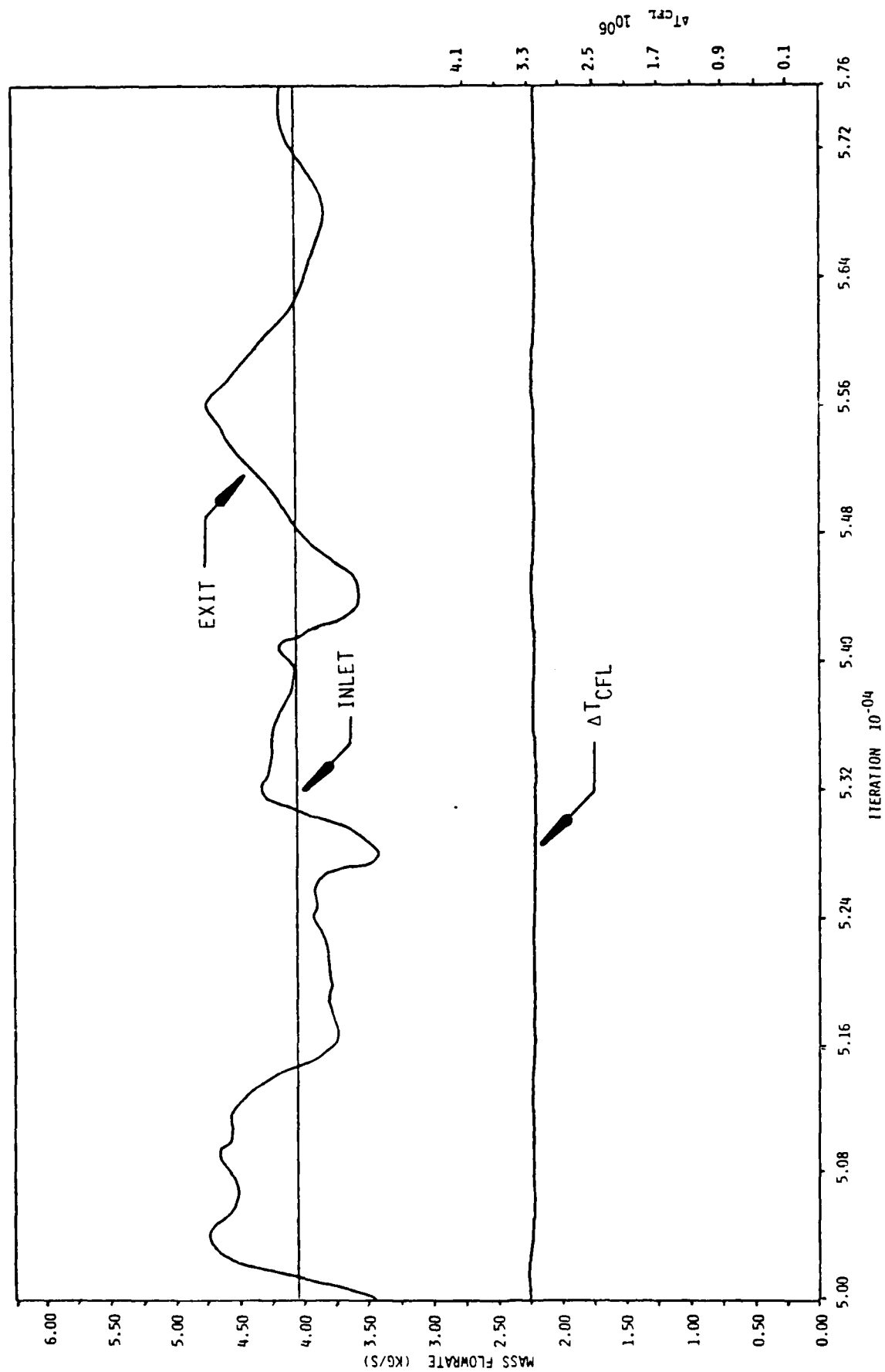


Figure 65a. Temporal Variation in Combustor Mass Flow and  $\Delta T_{CFL}$  for Case 8b of Table 7.

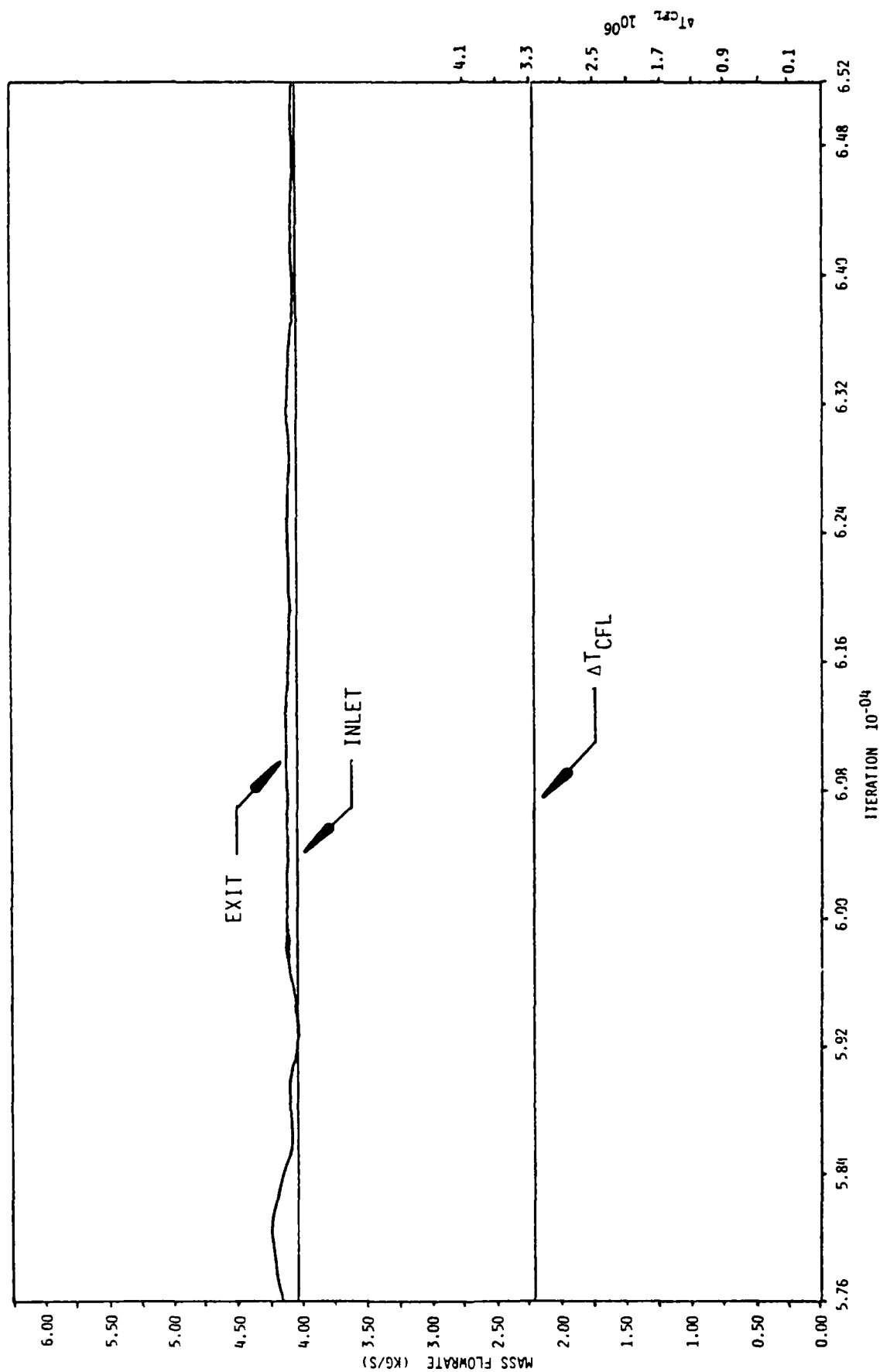
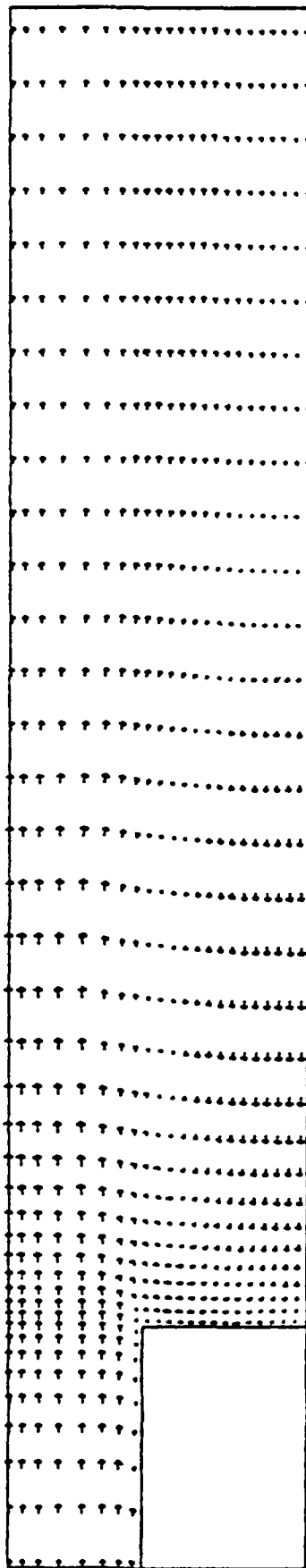
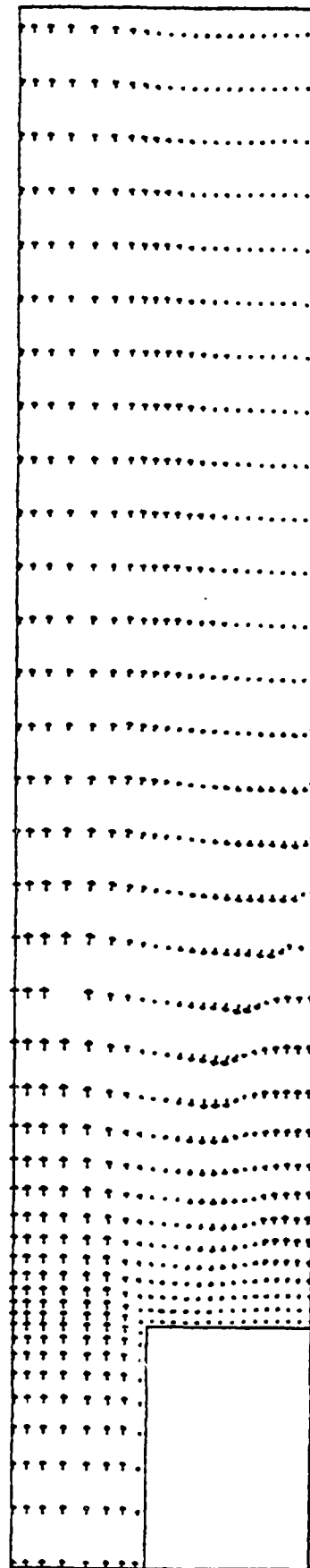


Figure 65b. Temporal Variation in Combustor Mass Flow and  $\Delta T_{CFL}$  for Case 8b of Table 7.

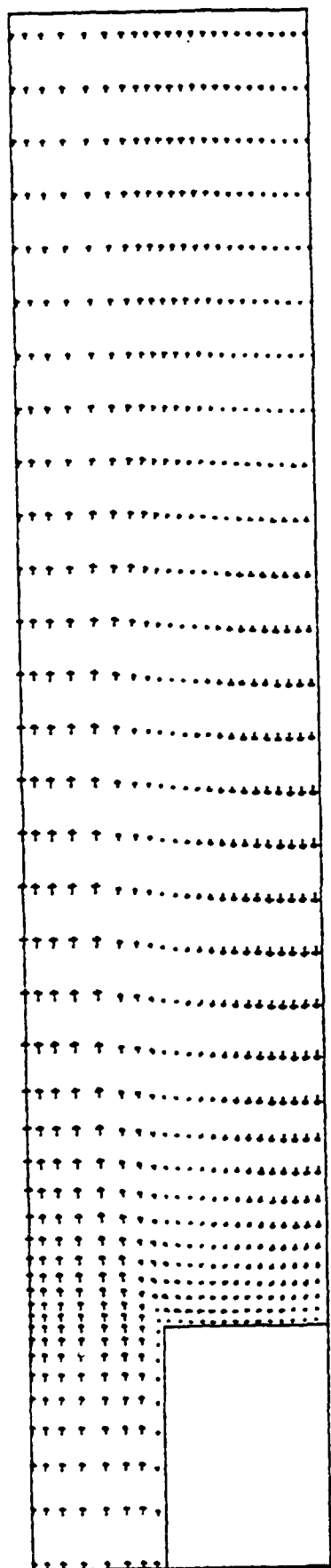


$N = 30,000$

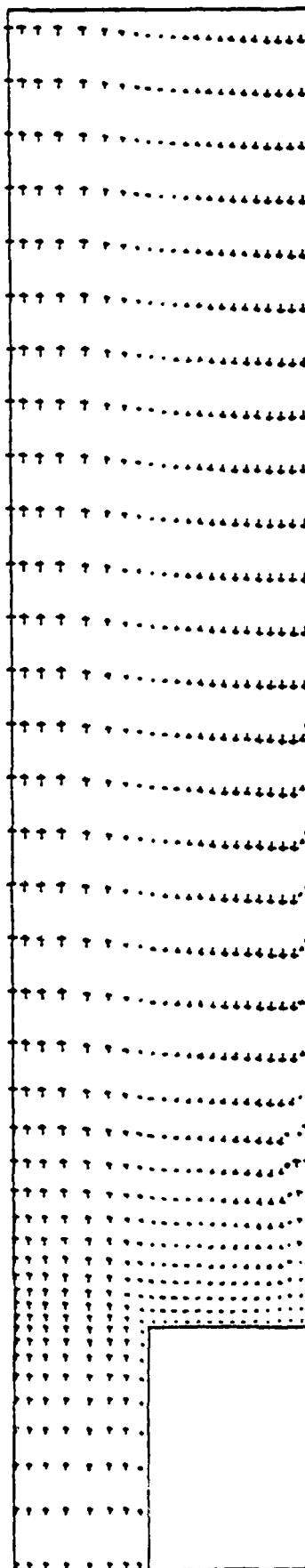


$N = 50,000$

Figure 66a. Velocity-Vector Plots for Case 8b of Table 7.

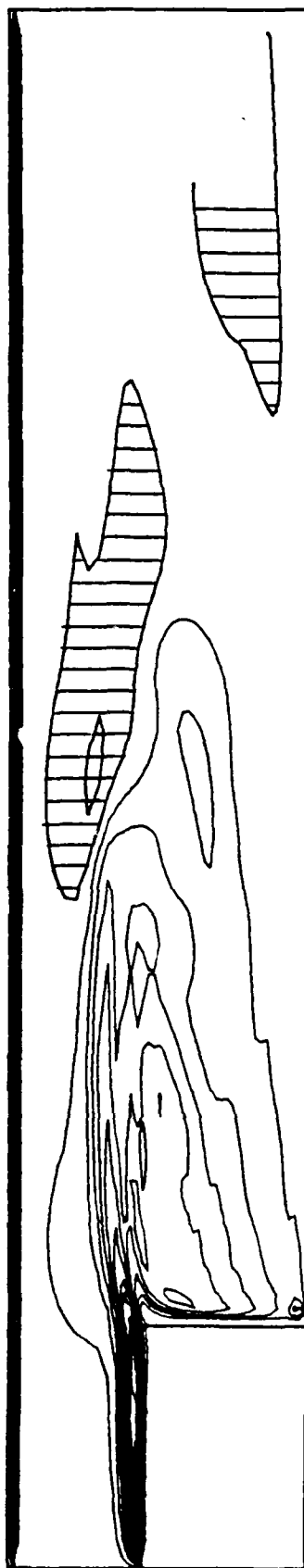


$N = 60,000$



$N = 70,000$

Figure 66b. Velocity-Vector Plots for Case 8b of Table 7.

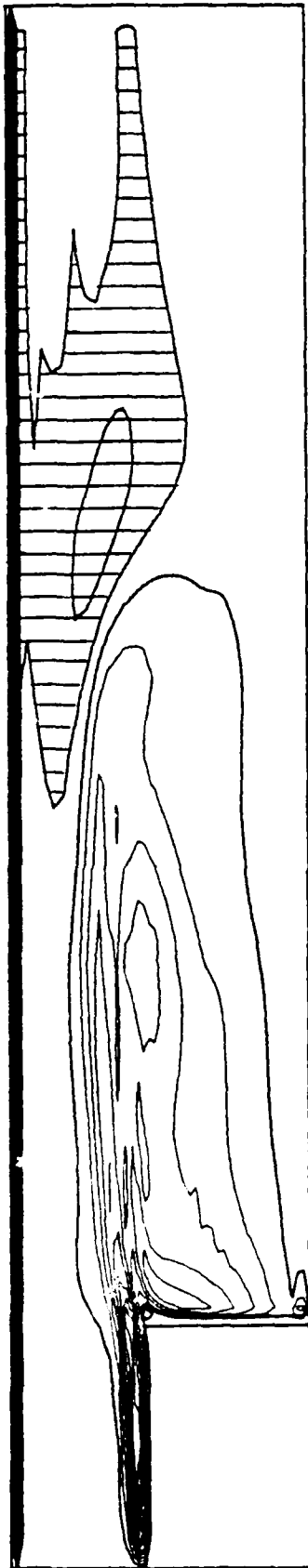


$N = 30,000$



$N = 50,000$

Figure 66c. Vorticity-Contour Plots for Case 8b of Table 7.



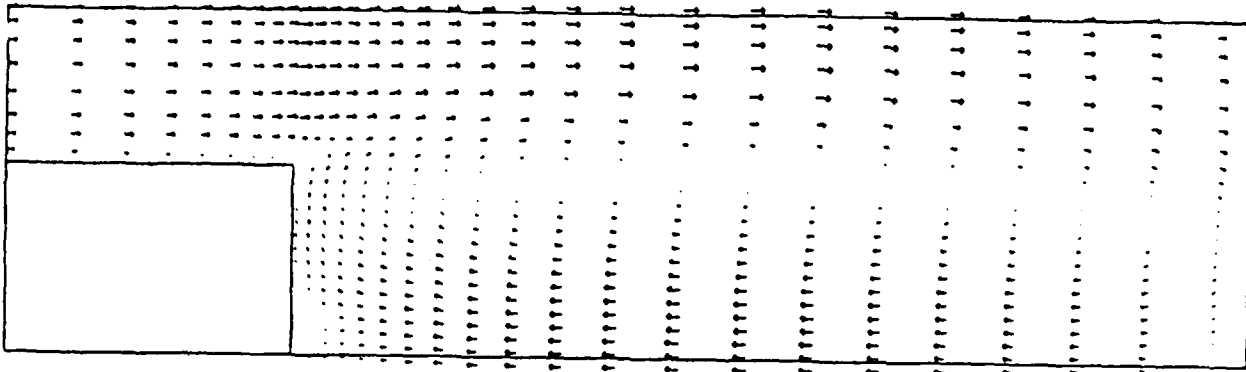
$N = 60,000$



$N = 70,000$

Figure 66d. Vorticity-Contour Plots for Case 8b of Table 7.





$N = 23,000$

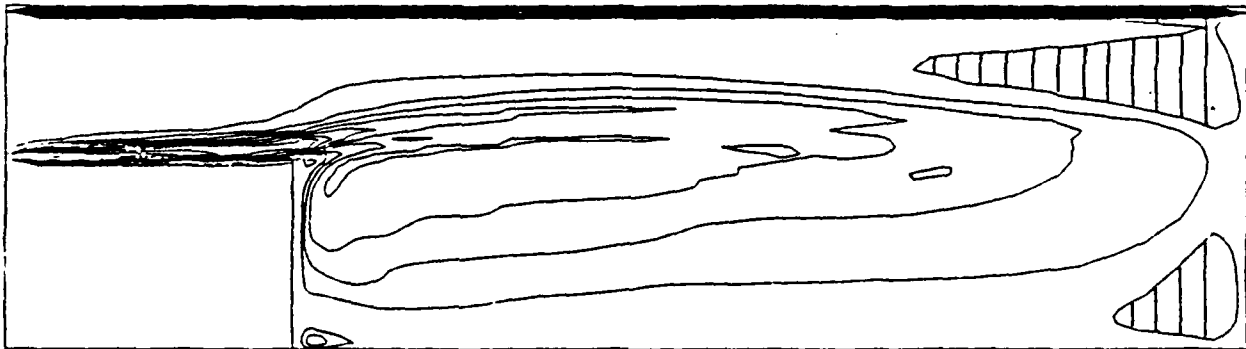


Figure 67. Velocity-Vector and Vorticity-Contour Plots for Case 9 of Table 7.

## SECTION IV

### CONCLUSIONS AND RECOMMENDATIONS

This section presents the main conclusions emerging from the numerical flowfield modeling of the centerbody combustor configuration, followed by recommendations for further activity.

#### 1. CONCLUSIONS

Numerical predictions of the turbulent recirculating flows in the centerbody combustor configuration have been made for nonreacting situations within the frameworks of both the Reynolds-averaged and time-dependent Navier-Stokes equations. The steady-state predictions with the Reynolds-averaged equations have examined both the large-scale and the small-scale CBCC, as well as the confined two-dimensional mixing layer. The turbulent eddy viscosity is computed by the  $k-\epsilon$  model and the calculations considered the effect of streamline curvature and the preferential influence of the normal stresses on the eddy viscosity. For the CBCC flowfields, the computational investigations address both the annular (air) and central ( $\text{CO}_2$ ) flows. The predicted results of the axial and radial distributions of the mean and fluctuating axial and radial velocity components are compared with the available experimental data.

The time-dependent calculations of the CBCC address the large-scale configuration with only the annular (air) stream present. No modeling of turbulence is included in the present calculations and the formulation accounts for the molecular viscosity only (except for the effects of artificial viscosity in the numerical computations). The predictive calculations with the time-dependent equations have examined the influence of the boundary conditions at the inlet and exit on the interior flowfield from the viewpoint of explaining the presence or the absence of a dynamic behavior.

Following are the major conclusions of this study:

- The numerical calculations of the Reynolds-averaged Navier-Stokes equations with the  $k-\epsilon$  turbulence model provide qualitatively correct predictions that are consistent with experimental observations in the confined two-dimensional mixing layer and the CBCC flowfields.
- The quantitative predictions in these configurations are generally good for the mean field and poor for the fluctuating field. This observation is characteristic of many complex turbulent flows and is largely due to the inadequacy of the standard  $k-\epsilon$  model (since it is an isotropic model and also does not account for the extra strain rates arising from interacting shear layers, large streamline curvature, etc.).
- Ad hoc modifications to the standard  $k-\epsilon$  model to account for the effects of large streamline curvature and the preferential influence of normal stresses emphasize the complex nature of the CBCC flowfields by exhibiting a parametric dependence on the geometric scale and flow rates. For example, the predictions of the small-scale CBCC with the standard  $k-\epsilon$  model and the improvements thereon due to streamline-curvature correction and dissipation-equation modification conform well to the behavior observed in several recirculating flows by other investigators. The predictions of the large-scale CBCC, however, exhibit trends that are considerably different, since the standard model appears to be the best overall, while the modifications overestimate the recirculation-zone lengths.
- The predictions of the vortex-center characteristics in the small-scale and large-scale CBCC's, on the other hand, demonstrate similar trends vis-a-vis the experimental data. Since the underprediction of the axial location of the vortex center by the standard model is consistent with the experience of other investigators, it suggests that either

the nature of the prediction is different in different regions of the flowfield, or the measurement of the centerline recirculation length in the large-scale CBCC is significantly affected by the LDA technique.

- Preliminary results appeared to demonstrate the capability of the computations with time-dependent Navier-Stokes equations to simulate the unsteady flow features in the CBCC. The physical realism of the predicted behavior is not clear, however, in view of the large axial extent of the recirculation region and the very large fluctuations in the mass flow rates and temperature. One possible source of this difficulty is the lack of an adequate turbulence model in the time-dependent computations.
- Comprehensive examination of the inflow and outflow boundary conditions in the time-dependent computations suggests an apparent lack of uniqueness in the numerical solutions of the unsteady flow. Several computational case studies appear to show that the time-dependent formulation yields a steady-state solution asymptotically. The fluctuations in the mass flow persist for a few thousand time steps before the mass flow becomes steady. It remains unchanged for some time and the fluctuations start to appear again. The only unsteady feature in the flowfield during the time the mass-flow rate remains steady is the slow axial propagation of the recirculation region toward the exit boundary (at a speed of approximately 10 ft/s). This process continues until the reverse flow reaches the exit boundary, thereby rendering the exit-boundary conditions incompatible. This inadequacy of the outflow boundary conditions to handle the reverse flow causes the flowfield to become unsteady, and nonphysical, breaks up the recirculation zone, and exhibits a shedding-like phenomenon as longitudinal oscillations in the mass-flow rate begin to appear with a definite fundamental frequency corresponding to a quarter-wave

AD-A153 682

TIME-AVERAGED AND TIME-DEPENDENT COMPUTATIONS OF  
ISOTHERMAL FLOWFIELDS IN. (U) DAYTON UNIV OH RESEARCH  
INST L KRISHNAMURTHY ET AL. DEC 84 UDR-TR-84-88  
AFMIL-TR-84-2081 F33615-82-K-2252

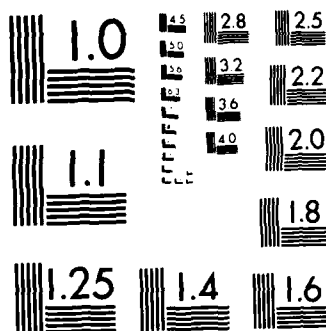
3/3

UNCLASSIFIED

F/G 20/4

NL





MICROCOPY RESOLUTION TEST CHART  
NATIONAL BUREAU OF STANDARDS 1963-A

resonator. It takes a considerable time for these longitudinal oscillations to attenuate before the flowfield attains a steady state. The whole process repeats again with the axial migration of the recirculation region as the calculations proceed further. Thus, it appears that the shedding-like behavior observed during the time period associated with the mass-flow fluctuations may be neither self-sustaining, nor physical. Therefore, a conclusive demonstration of the successful simulation of unsteady features of subsonic internal flows characteristic of the CBCC is not available at present.

## 2. RECOMMENDATIONS

In view of the foregoing conclusions, the present study offers the following recommendations for further activity in the time-averaged and time-dependent computations of turbulent mixing in subsonic internal flowfields.

- For predicting complex turbulent flows wherein large-scale unsteadiness is not significant, the time-averaged formulation (involving the Reynolds-averaged equations in constant-density flows and the Favre-averaged equations in variable-density flows, especially reacting flows) should be adequate, provided higher-level turbulence models are used. For flowfields wherein anisotropy is not significant, the standard  $k-\epsilon$  model should suffice. In the near-wake region of the CBCC where anisotropic effects are important, turbulence models involving the direct solution of the equations for the Reynolds stresses are worthwhile. A useful start in this direction would be the application of algebraic stress models.
- For the prediction of turbulent flows possessing unsteady features, the Reynolds-averaged formulation which retains the explicit time dependence should be considered. This approach should be adequate for the numerical simulation of those unsteady flows whose characteristic frequency of the

unsteady mean flow is much smaller than the characteristic frequency of the typical large eddies. Although it is instructive to regard the present time-dependent calculations with the full Navier-Stokes equations employing the laminar viscosity as a special subcase of the Reynolds-averaged simulation with zero turbulence, its relevance to the high-Reynolds-number flows in the CBCC is questionable. If the CBCC flowfield is representative of a cyclic unsteadiness with a single narrow-band frequency (which is much smaller than the typical eddy frequency) and no additional complications such as three-dimensional effect and free-stream turbulence are present, the axisymmetric Reynolds-averaged formulation should prove to be useful. Of course, the earlier remarks regarding the turbulence modeling still apply.

- It appears from the unpublished AFWAL/POSF data on the CBCC power spectra that this configuration involves a broad-band distribution of frequencies. Furthermore, the present experimental setup may not be entirely free from free-stream turbulence and three-dimensional effect. Thus, it may be necessary to consider the three-dimensional simulation with the Reynolds-averaged equations.
- Nevertheless, further research is clearly needed to ascertain the influence of the inflow and outflow boundary conditions on the successful simulation of unsteady features, or the lack thereof in subsonic internal flowfields.
- The numerical computation of turbulent flows through time-averaged Navier-Stokes equations presumes that the instantaneous flow variable can be decomposed into a well-defined mean component (which may be time-dependent) and a fluctuating component that is essentially random. Presently a viable theoretical framework to describe turbulent flows involving distinct quasi-deterministic,



large-scale structures (which occur in transitional flows and in flows which are younger and closer to their origin) does not exist. However, the approach based on large-eddy simulation with subgrid-scale turbulence modeling is computationally feasible and theoretically appealing, since the time-dependent, three-dimensional Navier-Stokes equations are used to calculate the eddies larger than a selected cutoff length and turbulence modeling is required only for the eddies that are smaller. While the available computer resources are not sufficient for this approach to simulate reacting flowfields in the CBCC, a start should be made with this approach for simpler flows which may be regarded as subsets of the CBCC.

## REFERENCES

1. W. M. Roquemore, et al., "Utilization of Laser Diagnostics to Evaluate Combustor Models," AGARD Propulsion and Energetics Panel on Combustion Problems in Turbine Engines, CPP-353, Cesme, Turkey, October 1983.
2. A. J. Lightman, P. D. Magill, and R. J. Andrews, "Laser Diagnostic Development and Measurement and Modeling of Turbulent Flowfields of Jets and Wakes, Part I: Two-Dimensional Laser Doppler Anemometer Measurements of Isothermal Flowfields in a Ducted Centerbody Combustor," Aero Propulsion Laboratory, Air Force Wright Aeronautical Laboratories, Wright-Patterson Air Force Base, Ohio, AFWAL-TR-83-2044, June 1983.
3. L. Krishnamurthy, et al., "Laser Diagnostic Development and Measurement and Modeling of Turbulent Flowfields of Jets and Wakes, Part II: Numerical Predictions of Isothermal Flowfields in a Ducted Centerbody Combustor," Aero Propulsion Laboratory, Air Force Wright Aeronautical Laboratories, Wright-Patterson Air Force Base, Ohio, AFWAL-TR-83-2044, June 1983.
4. Brum, R.D., Ikioka, L.M., and Samuelson, G.S., "Assessment of Candidate Combustor Configurations as Test Beds for Modeling Complex Flow," ASME-82-HT36, 1982.
5. L. Krishnamurthy, "Isothermal Flowfield Predictions of Confined Coflowing Turbulent Jets in an Axisymmetric Bluff-Body Near Wake," AFWAL-TR-81-2036, May 1981.
6. G. J. Sturgess and S. A. Syed, "Widely Spaced Co-Axial Jet, Diffusion-Flame Combustor: Isothermal Flow Calculations Using the Two-Equation Turbulence Model," AIAA-82-0133, 1982.
7. G. J. Sturgess and S. A. Syed, "Multi-Specie Isothermal Flow Calculations of Widely-Spaced Co-Axial Jets in a Confined Sudden Expansion with the Central Jet Dominant," "AIAA-82-1156, 1982.
8. L. Krishnamurthy and S. O. Park, "Isothermal Predictions of Recirculating Turbulent Flowfields of Confined Dual Coaxial Jets Behind an Axisymmetric Bluff Body," ASME-83-FE-14, Houston, Texas, June 1983.
9. L. Krishnamurthy, et al., "Similarity Considerations of Isothermal Turbulent Recirculating Flowfields in Axisymmetric Bluff-Body Near Wakes, AIAA-83-1203, AIAA/SAE/ASME 19th Joint Propulsion Conference, Seattle, Washington, June 1983.

10. A. D. Gosman and F. J. K. Ideriah, "TEACH-T: A General Computer Program for Two-Dimensional Turbulent Recirculating Flows," Imperial College, Department of Mechanical Engineering Report, June 1976.
11. B. E. Launder and D. B. Spalding, "The Numerical Computation of Turbulent Flows," *Comp. Meth. Applied Mech. and Engr.* 3, 1974, pp. 269-289.
12. A. K. Runchal, "Convergence and Accuracy of Three Finite-Difference Schemes for a Two-Dimensional Conduction and Convection Problem," *Int. J. of Numerical Methods in Engineering* 4, 1972, pp. 541-550.
13. P. Bradshaw, "Review-Complex Turbulent Flows," *J. Fluids Engng.* 97, 1975, pp. 146-154.
14. M. A. Leschziner and W. Rodi, "Calculation of Annular and Twin Parallel Jets Using Various Discretization Schemes and Turbulence-Model Variations," *J. Fluids Engng.*, 103, 1981, pp. 352-360.
15. W. M. Roquemore et al., "Influence of the Vortex Shedding Process on a Bluff-Body Diffusion Flame," AIAA-83-0335, 1983.
16. T. Carmody, "Establishment of the Wake Behind a Disk," *Journal of Basic Engineering*, 1964, pp. 869-882.
17. L. Krishnamurthy, "Combustor Modeling Assessment Studies," UDR-TR-79-111, December 1979.
18. L. M. Chiappetta, "User's Manual for TEACH computer Program for the Analysis of Turbulent, Swirling, Reacting Flow in a Research Combustor," NASA/Lewis Research Center Contract NAS3-22771, September 1983.
19. S. M. Masutani and C. T. Bowman, "A Fiberoptic Absorption Probe for Measurement of a Conserved Scalar in a Non-Premixed Turbulent Reacting Flow," Paper 82-62, Western States Section/The Combustion Institute, 1982 Fall Meeting, Livermore, California, October 1982.
20. S. V. Patankar, "Numerical Heat Transfer and Fluid Flow," Hemisphere Publishing Corp., McGraw-Hill, New York, 1980.
21. S. V. Patankar and D. B. Spalding, "A Calculation Procedure for Heat, Mass and Momentum Transfer in Three-Dimensional Parabolic Flows," *Int. J. of Heat and Mass Transfer* 15, 1972, pp. 1787-1806.

22. D. H. Wood and P. Bradshaw, "A Turbulent Mixing Layer Constrained by a Solid Surface. Part 1. Measurements Before Reaching the Surface," *J. of Fluid Mechanics* 122, September 1982, pp. 57-89.
23. Lightman, A.J., Richmond, R.D., Magill, P.D., Krishnamurthy, L., Roquemore, W.M., Bradley, R.P., Stutrud, J.S., and Reeves, C.M., "Velocity Measurements in a Bluff-Body Diffusion Flame," AIAA-80-1544, 1980.
24. A. J. Lightman and P. D. Magill, "Velocity Measurements in Confined Dual Coaxial Jets Behind an Axisymmetric Bluff Body: Isothermal and Combusting Flows," Aero Propulsion Laboratory, Air Force Wright Aeronautical Laboratories, Wright-Patterson Air Force Base, Ohio, AFWAL-TR-81-2018, 1981.
25. S. B. Pope and J. H. Whitelaw, "The Calculation of Near-Wake Flows," *J. Fluid Mech.* 73, 1976, pp. 9-32.
26. J. Militzer, W. B. Nicoll, and J. A. Alpay, 1977, "Some Observations on the Numerical Calculations of the Recirculation Region of Twin Parallel Symmetric Jet Flow," in *Proc. Turbulent Shear Flows 1 Symp.* University Park, Pennsylvania.
27. A. D. Gosman, E. E. Khalil, and J. H. Whitelaw, "The Calculation of Two-Dimensional Turbulent Recirculating Flows," in *Turbulent Shear Flows 1*, Springer-Verlag, 1979.
28. F. Durst and A. K. Rastogi, "Turbulent Flow Over Two-Dimensional Fences," in *Turbulent Shear Flows 2*, Springer-Verlag, 1982.
29. P. Bradshaw, "Effects of Streamline Curvature on Turbulent Flow," AGARDograph No. 169, 1973.
30. R. P. Bradley, W. M. Roquemore, J. S. Stutrud, C. M. Reeves, and C. A. Obringer, "Second Data Set for APL Research Combustor," Air Force Wright Aeronautical Laboratories, Aero Propulsion Laboratory, 1982.
31. J. A. C. Humphrey and F. Pourahmadi, "A Generalized Algebraic Relation for Predicting Developing Curved Channel Flow with a  $k-\epsilon$  Model of Turbulence," in *Proc. Turbulent Shear Flows 3 Symp.* Davis, California, 1981.
32. W. Rodi and G. Scheuerer, "Calculations of Curved Shear Layers with Two-Equation Turbulence Models," SFB80/T/211, University of Karlsruhe, 1982.
33. T. W. Davies and J. M. Beer, "Flow in the Wake of Bluff-Body Flame Stabilizers," Thirteenth Symposium (International) on Combustion, The Combustion Institute, 1971, pp. 631-638.

34. K. Kundu, et al., "On Flame Stabilization by Bluff Bodies," *J. of Engng. for Power*, 102, 1980, pp. 209-214.
35. S. Fujii and K. Eguchi, "A Comparison of Cold and Reacting Flows Around a Bluff-Body Flame Stabilizer," *J. of Fluids Engng.* 103, 1981, pp. 328-344.
36. N. W. M. Ko and W. T. Chan, "The Inner Regions of Annular Jets," *Journal of Fluid Mechanics*, 93, 1979, pp. 549-584.
37. A. T. Fedorchenko, "A Method for the Numerical Investigation of Unsteady Subsonic Flows of Viscous Gas in Ducts," *U.S.S.R. Comput. Maths. Math. Phys.*, 21, No. 5, 1981, pp. 143-159.
38. R. A. Serra, "Determination of Internal Gas Flows by a Transient Numerical Technique," *AIAA J.* 10, 1972, pp. 603-611.
39. J. N. Scott and W. L. Hankey, Jr., "Numerical Simulation of Cold Flow in an Axisymmetric Centerbody Combustor," *AIAA-83-1741*, AIAA 16th Fluid and Plasma Dynamics Conference, Danvers, Massachusetts, July 1983.
40. J. Oliger and A. Sundstrom, "Theoretical and Practical Aspects of Some Initial Boundary Value Problems in Fluid Mechanics," *SIAM J. Appl. Math.* 35, 1978, pp. 419-466.
41. J. Oliger and A. Sundstrom, "The Initial Boundary Value Problem for the Inviscid Eulerian Equations In Fluid Mechanics," to appear.
42. A. T. Fedorchenko, "Problems of the Numerical Modeling of Unsteady Spatial Viscous Gas Flows in Nozzles," *U.S.S.R. Comput. Maths. Math. Phys.* 22, No. 1, 1982, pp. 185-205.
43. D. H. Rudy and J. C. Strikwerda, "Boundary Conditions for Subsonic Compressible Navier-Stokes Calculations," *Computers and Fluids* 9, 1981, pp. 327-338.
44. G. Hasen, "A Navier-Stokes Solution for Cold Flow in an Axisymmetric Combustor," *AFWAL-TM-82-171-FIMM*, Air Force Wright Aeronautical Laboratories, W-PAFB, Ohio, March 1982.
45. K. Kailasanath, M. Fry, and E. Hyman, "Subsonic and Turbulent Reactive Flows," *SAI 84-128-WA*, Science Applications, Incorporated, 1710 Goodridge Drive, McLean, Virginia, April 1983.
46. W. L. Hankey, Private Communications, 1983.
47. J. S. Shang, "Oscillatory Compressible Flow around a Cylinder," *AIAA 82-0098*, AIAA 20th Aerospace Science Meeting, Orlando, Florida, January, 1982.

48. R. W. MacCormack, "Numerical Solution of the Interaction of a Shock Wave with a Laminar Boundary Layer," Lecture Notes in Physics 59, Springer-Verlag, 1971.
49. J. S. Shang, "Numerical Simulation of Wing-Fuselage Aerodynamic Interaction," AIAA 83-0225, AIAA 21st Aerospace Sciences Meeting, Reno, Nevada, January 1983.

APPENDIX A  
SCIENTIFIC PERSONNEL

L. Krishnamurthy, Senior Research Engineer  
Principal Investigator/Project Director

M. S. Raju, Associate Research Engineer

M. J. Creed, Chemical Engineering Undergraduate

J. N. Memering, Chemical Engineering Undergraduate

S. O. Park, Visiting Research Engineer (6/82 - 3/83)

J. N. Scott, Research Engineer (6/82 - 6/83)

K. Glaser, Mechanical Engineering Undergraduate (9/82 - 8/83)

D. R. Tappel, Mechanical Engineering Undergraduate (9/82 - 4/83)

## APPENDIX B

### LIST OF MANUSCRIPTS AND PRESENTATIONS

1. S. O. Park, D. R. Tappel and L. Krishnamurthy, "Numerical Calculations of a Confined Two-Dimensional Turbulent Isothermal Mixing Layer," AIAA (Day/Cin)-83-1-4, 9th Annual Minisymposium on Aerospace Science and Technology, Air Force Institute of Technology, Wright-Patterson Air Force Base, Ohio, March 22, 1983 (Full Paper and Presentation). (\*)
2. S. O. Park, L. Krishnamurthy, J. S. Stutrud and W. M. Roquemore, "Some Implications of Time-Averaged Recirculating Flowfields on Axisymmetric Bluff-Body Flame Stabilization," AIAA (Day/Cin)-83-1-3, *ibid.* (Abstract and Presentation).
3. J. N. Scott, "Numerical Simulation of Cold Flow in an Axisymmetric Centerbody Combustor," AIAA (Day/Cin)-83-13-9, *ibid.* (Abstract and Presentation).
4. L. Krishnamurthy, and S. O. Park, "Isothermal Predictions of Recirculating Turbulent Flowfields of Confined Dual Coaxial Jets Behind an Axisymmetric Bluff Body," 83-FE-14, ASME Fluids Engineering Conference, Houston, Texas, June 20-22, 1983. (Full Paper and Presentation). (\*\*)
5. L. Krishnamurthy, D. J. Wahrer, and H. S. Cochran, "Similarity Considerations of Isothermal Turbulent Recirculating Flowfields in Axisymmetric Bluff-Body Near Wakes," AIAA-83-1203, AIAA/ASME/SAE 19th Joint Propulsion Conference, Seattle, Washington, June 27-29, 1983. (Full Paper and Presentation). (\*\*\*)
6. J. N. Scott and W. M. Hankey, Jr., "Numerical Simulation of Cold Flow in an Axisymmetric Centerbody Combustor," AIAA-83-1741, AIAA 16th Fluid Dynamics, Plasma Dynamics and Lasers Conference, Danvers, Massachusetts, July 12-14, 1983. (Full Paper and Presentation).
7. L. Krishnamurthy, "Numerical Modeling of Some Complex Turbulent Flowfields," Invited Lecture at the 20th Annual Meeting of the Society of Engineering Science. University of Delaware, Newark, Delaware, August 22-24, 1983.
8. L. Krishnamurthy, and S. O. Park, "Streamline Curvature Effects in Confined Isothermal Recirculating Flowfields Behind an Axisymmetric Bluff Body: Numerical Calculations with the  $k-\epsilon$  Turbulence Model," Fourth Symposium on Turbulent Shear Flows, University of Karlsruhe, Karlsruhe, F. R. Germany, September 12-14, 1983. (Full Paper and Presentation).



9. J. N. Memering, "Time-Averaged Characteristics of the Vortex Center in Turbulent Recirculating Flows," AIAA (Day/Cin)-84-11-4, 10th Annual Minisymposium on Aerospace Science and Technology, Air Force Institute of Technology, Wright-Patterson Air Force Base, Ohio, March 20, 1984 (Full Paper and Presentation). Won the Best Undergraduate Student Paper Award of \$100.00.
  10. J. N. Memering, "Time-Averaged Characteristics of the Vortex Center in Turbulent Recirculating Flows," 34th AIChE North Central Regional Student Convention, Michigan Technological University, April 9-10, 1984 (Full Paper and Presentation).
  11. L. Krishnamurthy, "Computational Studies of Complex Turbulent Flowfields Relevant to Turbojet Combustors: An Overview," Invited Lecture at the AFOSR Supercomputing Meeting, "The Impact of Large-Scale Computing on Air Force Research and Development," Air Force Weapons Laboratory, Kirtland AFB, Albuquerque, New Mexico, April 4-6, 1984.
  12. J. N. Memering and L. Krishnamurthy, "Reynolds-Averaged, Isothermal Predictions of the Vortex-Center Characteristics in Axisymmetric, Turbulent Recirculation Zones," AIAA-84-1365, AIAA/SAE/ASME 20th Joint Propulsion Conference, Cincinnati, Ohio, June 11-13, 1984 (Full Paper and Presentation).
- (\*) A major part of the work represents the in-house contributions of AFWAL/POSF.
- (\*\*) Except for some of the results and preparation of the manuscript, the work represents contributions supported by Contract F33615-78-C-2005.
- (\*\*\*) Except for the preparation of the manuscript, the work represents contributions supported by Contract F33615-78-C-2005.

**END**

**FILMED**

6-85

**DTIC**